Université de Montréal

Étude des interactions entre les nanoparticules et les matrices biologiques par microscopie différentielle dynamique

Par

Pierre-Luc Latreille

Université de Montréal, Faculté de pharmacie

Thèse présentée en vue de l'obtention du grade de doctorat

en sciences pharmaceutiques, option technologie pharmaceutique

Août 2021

Université de Montréal

Faculté de pharmacie

Cette thèse intitulée

Étude des interactions entre les nanoparticules et les matrices biologiques par microscopie différentielle dynamique

Présenté par

Pierre-Luc Latreille

A été évalué par un jury composé des personnes suivantes

Davide Brambilla
Président-rapporteur

Xavier Banquy
Directeur de recherche

Patrice Hildgen
Codirecteur

Vincent A. Martinez
Codirecteur

Suzanne Giasson
Membre du jury

Marc Lavertu
Examinateur externe

Résumé

La nanomédecine repose essentiellement sur le développement de nouvelles formulations pour délivrer les médicaments à partir de nanotechnologies. L'idée principale est que l'encapsulation d'un principe actif par une nanoparticule (NP) pourrait lui permettre de s'accumuler dans des tumeurs, de pénétrer une barrière biologique ou bien pour cibler une composante biologique. Or, les performances de ces « nano-formulations » sont décevantes et, depuis quelques années, il a été remarqué que leur efficacité ne semble pas avoir évoluée dans le temps. De récentes hypothèses mettent de l'avant notre manque de connaissances vis-à-vis les interactions des nanotechnologies avec les éléments du vivant, et plus particulièrement, le manque de techniques robustes permettant de quantifier ces interactions.

Nous proposons donc dans cette thèse le développement et l'adaptation d'une nouvelle technique de microscopie, la microscopie différentielle dynamique (DDM), pour étudier les interactions entre les nanotechnologies et les matrices biologiques. Deux thématiques seront abordées, la première, les interactions des NPs avec les protéines des fluides biologiques et, la seconde, la capacité des NPs à diffuser dans des tissus interstitiels.

D'abord, nous avons revus les techniques de quantification permettant la mesure de l'adsorption de protéines à la surface des NPs. Nous avons ensuite identifié les questions fondamentales en lien avec cette adsorption. Deux phénomènes sont largement débattus dans la littérature, il s'agit de la formation de multicouches et de la réversibilité de l'adsorption. Une méta-analyse a donc permis d'orienter le développement de la technique par DDM pour mesurer l'adsorption de protéines, dans le but de répondre à ces interrogations. La méthodologie proposée pour la quantification de l'adsorption de protéines à la surface des NPs repose sur la mesure du signal de fluorescence de protéines fluorescentes adsorbées à la surface des NPs non fluorescentes. Cette méthodologie a été appliqué avec succès pour la quantification de l'adsorption des protéines du sérum, du lysozyme et de l'albumine. La technique a d'ailleurs permis de montrer que toutes les protéines étudiées s'adsorbaient en monocouches et que leur adsorption était réversible. Un

mécanisme d'adsorption atypique a été mis en évidence dans le cadre de nos expériences et un parallèle a pu être fait avec certaines hypothèses émises avec notre méta-analyse.

Ensuite, nous avons appliqué la DDM pour l'étude de la diffusion des NPs dans des matrices extracellulaires. La déformabilité des NPs a été étudiée afin de définir plus précisément sa contribution dans la diffusion à l'intérieur de milieux confinés. La diffusion des NPs « molles » a été comparée à celle des NPs « dures » dans un gel d'agarose, mimant la matrice extracellulaire. Les NPs molles ont été en mesure de diffuser jusqu'à 100 fois plus rapidement que les NPs dures de même taille. L'évaluation des contributions hydrodynamiques et électrostatiques a permis de déterminer que la taille des NPs molles, réduisant dans le gel, leur accordant un avantage diffusif par rapport aux NPs dures.

En sommes, ces travaux ont permis de mettre en évidence l'importance des techniques analytiques pour l'étude des nanotechnologies appliquées à la médecine et pour affiner notre compréhension de leurs interactions avec le vivant. Il est clair que la contribution de ces techniques à l'avancement de nos connaissances théoriques relatives aux nanotechnologies aura un impact direct sur leurs chances d'effectuer une transition vers la clinique.

Mots-clés : Nanoparticules, Nanomédecine, Diffusion, Propriétés mécaniques, Gels, Adsorption de protéines, Multicouches, Réversibilité, Effet Vroman, Microscopie différentielle dynamique.

Abstract

Nanomedicine is based primarily on the concept of drug formulation through nanotechnology. The main idea is based on the encapsulation of an active ingredient by a nanoparticle (NP) to allow it to accumulate in tumors, to penetrate a biological barrier or to target a biological component. However, the performance of these formulations is disappointing, and, in recent years, it has been noticed that their effectiveness has not improved in the last decade. Some recent hypotheses highlight our lack of knowledge about the interactions of nanotechnologies with living organism and more particularly the lack of techniques to quantify these interactions.

We therefore explore in this thesis the development and adaptation of a new microscopy technique, dynamic differential microscopy (DDM), to study the interactions of nanotechnologies with biological matrices. Two subjects are discussed, the first on the interactions of NPs with the proteins of biological fluids and, the second one, on the capacity of NPs to diffuse in interstitial tissues.

First, we reviewed quantification techniques that were allowing the measurement of protein adsorption at the surface of NPs. We then identified fundamental questions of this adsorption, namely, if it was generally structured in monolayers or in multilayers and if it was reversible or irreversible. A meta-analysis, based on these questions, could therefore guide the development of the DDM technique to measure protein adsorption and therefore answer these questions. The methodology proposed for the quantification of protein adsorption is based on the measurement of the fluorescence signal which comes from fluorescently tagged proteins adsorbed on non-fluorescent NPs. This methodology was successfully applied for the quantification of the adsorption of lysozyme, albumin and serum proteins. The technique demonstrated that all the proteins studied adsorbed in monolayers and that their adsorption was reversible. An atypical adsorption mechanism which was also hypothesized in our meta-analysis was evidenced by DDM as well.

Next, we applied DDM to study the diffusion of NPs in extracellular matrices. The contribution of deformability has been a parameter studied in terms of its relation to improve their diffusion within these confined environments. The diffusion of "soft" NPs was compared to that of "hard" NPs in an agarose gel, mimicking the extracellular matrix. Soft NPs have been observed to diffuse up to 100 times faster than hard NPs of the same size. Evaluation of the hydrodynamic and electrostatic contributions determined that the soft NPs shrinks in the gel, boosting their diffusion in comparison to hard NPs.

In summary, this work highlights the important contribution of analytical techniques to the field of nanotechnologies applied to pharmacy and to our understanding of their interactions with living organisms. It is clear that the contribution of these techniques to our detailed understanding of nanomedicine properties has a direct relation with their clinical translation potential.

Keywords : Nanoparticles, Nanomedecine, Diffusion, Mechanical properties, Gels, Protein adsorption, Multilayers, Reversibility, Vroman effect, Differential dynamic microscopy.

.

Table des matières

Liste des tableaux

Liste des figures

Annexe 2

Annexe 3

Liste des sigles et abréviations

ABBRÉVIATION	DÉFINITION	DÉFINITION anglaise
AF4	Fractionnement par flux de champ d'écoulement asymétrique	Asymmetric flow field flow fractionation
AUC	Ultracentrifugation analytique	Analytical ultracentrifugation
AuNPs	Nanoparticules d'or sphériques	Spherical gold nanoparticles
BAM	N-tert-butylacrylamide	N-tert-butylacrylamide
BCA	Acide bicinchoninique	Bicinchoninic acid
BET	Modèle de Brunauer-Emett-Teller	Brunauer-Emett-Teller model
BSA	Albumine de serum bovin	Bovine serum albumin
CCM-FBS	Milieu de culture cellulaire supplémenté de sérum bovin	Cell culture medium supplemented with fetal bovine serum
CD	Spectroscopie par dichroïsme circulaire	Circular dichroism spectroscopy
CP - PC	Couronne de protéine	Protein corona
cryo-EM	Microscopie électronique à transmission cryogénique	Cryogenic electron microscopy
DCS	Sédimentation par centrifugation différentielle	Differential centrifuge sedimentation
DDLS	DLS par dépolarisation de la lumière	Depolarized DLS
DLS	Diffusion dynamique de la lumière	Dynamic light scattering
DDM	Microscopie différentielle dynamique	Differential dynamic microscopy
DSC	Calorimétrie différentielle à balayage	Differential scanning calorimetry
ELISA	Méthode immuno-enzymatique	Enzyme-linked immunosorbent assay
ESI	Ionisation par électronébulisation	Electrospray ionization
EPR	Augmentation de la perméation et la rétention	Enhanced permeation and retention

FBS	Sérum foetal bovin	Fetal bovine serum
FCS	Spectroscopie de correlation de fluorescence	Fluorescence correlation spectroscopy
FTIR	Spectroscopie infrarouge à tranformée de Fourier	Fourier-transform infrared spectroscopy
HCA	Anhydrase carbonique humaine	Human carbonic anhydrase
HDX	Échange Hydrogen-Deuterium	Hydrogen-Deuterium exchange
HSA	Albumine sérique humain	Human serum albumin
IR	Infrarouge	Infrared
ITC	Titration Calorimétrique Isotherme	Isothermal titration calorimetry
LC	Chromatographie liquide	Liquid chromatography
LC-MS/MS	Chromatographie liquide et spectroscopie de masse en tandem	Liquid chromatography tandem mass spectrometry
LSPR	Résonance plasmonique de surface localisée	Localized Surface Plasmon Resonance
MS	Spectrométrie de masse	Mass spectrometry
MUS	Sulfonate de mercaptoundecane	Mercaptoundecane sulfonate
NIPAM	N-isopropylacrylamide	N-isopropylacrylamide
NP	Nanoparticule	Nanoparticle
NSAF	Facteur d'abondance spectrale normalisée	Normalized spectral abundance factor
OT	Octanethiol	Octanethiol
PCS	Spectrocopie à corrélation de photon	Photon correlation spectroscopy
PEG	Polyéthylene glycol	Polyethylene glycol
PEG-COOH	Acide carboxilyque en fin de chaîne d'un polyéthylène glycol	Carboxylic acid end group on polyethylene glycol
PLGA	Acide Polylactique-*co*-glycolique	Polylactic-*co*-glycolic acid
PS	Polystyrène	Polystyrene

PS-COOH	Acide carboxylique en bout de chaîne d'un polystyrène	Carboxylic acid end group on polystyrene
PSS	Sulfonate de polystyrene	Polystyrene sulfonate
QCM-D	Microbalance à quartz avec suivi du facteur de dissipation	Quartz crystal microbalance with dissipation monitoring
QELSS	Spectroscopie de la diffusion quasi-élastique de la lumière	Quasi-elastic light scattering spectroscopy
RMN - NMR	Résonance magnétique nucléaire	Nuclear magnetic resonance
SANS	Diffusion de neutrons aux petits angles	Small-angle neutron scattering
SAXS	Diffusion des rayons X aux petits angles	Small-angle X-ray scattering
SERS	Spectrométrie Raman exaltée de surface	Surface enhanced Raman spectroscopy
SOLEXSY	Spectroscopie à échange de solvant	Solvent exchange spectroscopy
SpC	Compte spectral	Spectral count
SPR	Résonance plasmonique de surface	Surface plasmon resonance
SRCD	Synchrotron radiation circular dichroism spectroscopy	Synchrotron radiation circular dichroism spectroscopy
TEM	Microscopie électronique à transmission	Transmission electron microscopy
TGA	Analyse thermogravimétrique	Thermogravimetric analysis
TMV	Virus mosaique du tabac	Tobacco mosaic virus
UV	Ultraviolet	Ultraviolet

Je dédie cette thèse à ma famille

Remerciements

Je tiens d'abord à remercier mon directeur de recherche, le Pr Xavier Banquy pour m'avoir proposé ce fabuleux et ambitieux projet de doctorat en lien avec cette toute nouvelle technique de microscopie. Nos riches discussions scientifiques, nos longues réunions pour tenter de résoudre des problèmes et tes nombreuses suggestions ont grandement contribué à l'aboutissement du travail qui est présenté dans cette thèse. Je tiens aussi à remercie le Pr Patrice Hildgen d'avoir accepté de me co-diriger dans ce projet de doctorat, malgré l'imminence de sa retraite. Merci pour les discussions stimulantes et les judicieux conseils que tu m'as apportés.

Un merci tout particulier au Dr Vincent A. Martinez pour sa collaboration et pour ses activités de co-supervision au projet. Merci pour sa patience, à Édimbourg, à me montrer le fonctionnement de la « DDM », à répondre aux questions et, bien sûr, à revoir et commenter tous mes articles. Merci pour toutes ces discussions enrichissantes, ces idées et cet enthousiasme pour la DDM et pour la science.

J'aimerais aussi remercier les différents membres du jury pour leur temps consacré à la lecture de cette thèse, le Pr Davide Brambilla, le président du jury, le Pr Marc Lavertu, examinateur externe et la Pre Suzanne Giasson, membre du jury.

Je tiens aussi à remercier les membres du 4^{e} étage, de l'axe analyse et formulation du médicament, professeurs, étudiants et anciens étudiants. Un merci tout spécial à mes anciens collègues et amis, Jimmy et Augustine, pour leurs idées, leur soutien, les entraînements aux gym et les soirées de AoE2. Malgré la distance, je vous dis merci pour votre support et votre amitié. Je pense aussi à « Alex », Hugo et Mirza pour les 5 à 7 Super Smash Bros qui nous faisaient oublier les résultats qui ne fonctionnaient pas.

Enfin, ce travail n'aurait jamais vu le jour sans l'apport de chacun des co-auteurs des articles publiés, en révision et en préparation. Merci pour vos nombreuses relectures et révisions scientifiques.

Un merci plus particulier à mes anciens colocataires Maxime et Simon pour m'avoir enduré pendant toutes ces années à travailler à des heures pas possibles et pour toutes ces heures passées à jouer à Super Smash Bros et à Zelda autour d'un bon scotch.

À ma famille, qui m'encourage et m'écoutent de loin depuis déjà un bon moment, merci à vous. Plus particulièrement, merci à mes parents, merci de m'avoir montré à persévérer, et à m'encourager malgré cette folie académique. C'est toujours un plaisir revenir vous voir en Abitibi!

Enfin, j'aimerais remercier ma complice, ma coloc et ma copine, Daphné, qui m'inspire à chaque jour à me dépasser, qui m'a accompagné et enduré malgré les frustrations engendrées par la rédaction de cette thèse. Merci pour le temps passé à essayer de comprendre mes idées. Merci pour tout.

Chapitre 1 – Introduction

Le développement et l'évaluation de l'efficacité d'un nouveau médicament ou d'une nouvelle thérapie pharmaceutique est un processus excessivement coûteux. De récentes analyses ont montrées que les coûts moyens associés au développement d'un nouveau médicament, de la conception en laboratoire jusqu'aux approbations réglementaires, s'élèvent maintenant à plus d'un milliard US$[1]. Jusqu'à tout récemment, la classe thérapeutique pour laquelle les coûts totaux moyens de développement par nouvelle entité moléculaire étaient les plus onéreux (entre 2009 et 2018), en moyenne 4.4 milliards US$, est celle des anticancéreux et des agents immunomodulateurs[1]. Même si les conclusions peuvent varier d'une étude à l'autre, ces études montrent néanmoins une croissance des coûts moyens de développement [1, 2]. Cette augmentation de coûts peut s'expliquer en partie par une difficulté croissante à découvrir de nouvelles cibles thérapeutiques et à améliorer les thérapies déjà commercialisées. En effet, le développement de nouvelles thérapies à base de petites molécules (ou principes actifs) visant une cible thérapeutique s'est grandement complexifié dans les dernières décennies[3]. Cela a eu pour effet de contribuer à la diversification des approches employées pour générer de nouvelles thérapies efficaces. Par exemple, les biothérapies, impliquant des molécules biologique, *e.g.* peptides, protéines, anticorps monoclonaux et enzymes, ont rapidement gagné en popularité dans les dernières années[4]. La communauté scientifique a d'ailleurs démontré un intérêt marqué pour le développement de nouvelles formulations dans le but d'accroître à la fois l'efficacité de certains traitements et de rendre possible leur utilisation pour différentes thérapies. Par exemple, dans les années 50-70 on a vu le développement d'implants à base de biomatériaux pour la libération contrôlée de principes actifs [5]. Il s'agit de la période durant laquelle les mécanismes de libération et d'interaction des matériaux avec les fluides biologiques ont été pour la première fois étudiés. Ensuite, se sont diversifiés puis complexifiés les matériaux à usage pharmaceutique. Deux tendances bien distinctes ont émergé de cette révolution. D'une part, les outils macroscopiques incluant les biomatériaux[6], les implants polymériques[7] et les timbres transdermiques[8], ont permis un meilleur contrôle de la libération et de l'administration des principes actifs. D'autre part, les «

réservoirs » miniatures, *i.e.* les micro- et les nanoparticules, pour encapsuler les molécules peu solubles ou rapidement métabolisées ont permis d'améliorer leur efficacité d'administration et prolonger leur durée d'action[9, 10]. Cette miniaturisation a mené graduellement à l'incorporation des « nanotechnologies » à la conception de nouvelles formulations de produits pharmaceutiques[11]. De cette fusion est né un engouement pour la nanomédecine, science qui étudie et développe des formulations en prenant avantage de certaines propriétés propres aux nanotechnologies.

1.1 La nanomédecine : les hypothèses

Pour illustrer le concept de la nanomédecine, on peut se représenter des « réservoirs » ayant une taille caractéristique de 1 à 100 nanomètres[12] constitués de polymères ou de matériaux biocompatibles et biodégradables encapsulant des principes actifs. La nanomédecine cependant ne se limite pas à l'encapsulation de principes actifs, elle s'étend aussi aux sphères du diagnostic et de l'imagerie en passant par les vaccins et même les antibiotiques[13]. Les nanoparticules (NPs) possèdent en fait plusieurs propriétés spécifiques les différenciant des autres matériaux macroscopiques (ex. : biomatériaux, implants), soit une surface très large par unité de volume (grande aire spécifique), pour certaines des propriétés optiques uniques (*e.g.* points quantiques[14], NPs d'or[15]), en plus de permettre des modifications structurelles et chimiques à leur surface. Ainsi, l'utilisation de NPs dans le domaine des sciences pharmaceutiques a mené à des observations qui ont soulevé plusieurs hypothèses concernant les effets potentiels des NPs dans diverses applications.

1.1.1 La nanomédecine pour traiter le cancer

L'utilisation des nanoparticules dans le but de transporter des principes actifs pour traiter les tumeurs repose en partie sur les observations de Matsumura & Maeda. Ces derniers ont noté une augmentation de la perméabilité et de la rétention (de l'anglais *Enhanced Permeability and retention effect* ou effet « EPR ») de larges macromolécules, par rapport aux petites molécules, dans les tumeurs vascularisées chez la souris[16]. L'effet EPR est généralement décrit comme un phénomène permettant l'accumulation de NPs préférentiellement dans les tumeurs. Cette accumulation est causée par la forte fenestration des capillaires sanguins à proximité des

tumeurs, couplée à une réduction du drainage lymphatique[17]. La taille des fenestrations des capillaires sanguins, coïncidant aux tailles des nanotechnologies (environ 100-1000 nm), favoriserait donc leur accumulation dans les tumeurs[18, 19]. Cette observation a mené par la suite à l'hypothèse que l'utilisation de NPs encapsulant des molécules anticancéreuses permettrait de transporter préférentiellement la charge thérapeutique à son site d'action, *i.e.* la tumeur depuis la circulation sanguine. En augmentant la concentration du principe actif à l'intérieur de la tumeur, il est attendu que l'effet EPR conduise à une augmentation de l'efficacité thérapeutique, voire une diminution de la dose efficace. Cependant, le concept de l'effet EPR demeure controversé[20, 21]. Depuis plusieurs années, les échecs des essais cliniques se basant sur cet effet spécifique à la nanomédecine se multiplient. Ceci suggère que l'effet EPR observé pour certains types de tumeurs provoquées chez les souris ne serait peut-être pas transposable à la réalité observée chez les patients en clinique. Même si l'amélioration de l'efficacité thérapeutique n'est pas toujours observée, la diminution des effets indésirables et des effets hors cibles des molécules anticancéreuses reste un rôle important que peut jouer la nanomédecine. L'encapsulation de principes actifs dans des NPs a aussi été utilisée afin de modifier leur pharmacocinétique et leur biodistribution, ainsi que dans certains cas, accroître leur solubilité dans le milieu physiologique pour permettre leur administration par la voie intraveineuse. Ces paramètres peuvent par la suite être modifiés en contrôlant la chimie de surface des NPs. Par exemple, afin de prolonger la durée de circulation des NPs dans le sang, il est possible d'attacher du poly(éthylène glycol) (PEG) à la surface de ces dernières[22, 23]. Dans ce cas-ci, la présence de PEG aura pour effet de modifier les propriété biophysiques et physicochimiques des NPs[24].

Il est bien connu que le cancer est une maladie à multiples facettes, pouvant évoluer dans le temps. Une préoccupation actuelle en lien avec le traitement du cancer est l'apparition des phénomènes de résistance aux traitements. En effet, il est possible d'observer l'émergence d'une résistance multiple aux anticancéreux. Plus spécifiquement, il a été remarqué que les cellules cancéreuses ont tendance à surproduire des pompes à efflux (*eg* P-gp) à leur surface, ce qui contribuerait à l'expulsion des agents antinéoplasiques hors de la cellule[25]. La surexpression de ces pompes à efflux aura donc pour effet de limiter l'exposition des cellules aux molécules actives et ainsi réduire leur efficacité. Pour pallier ce problème, la nanomédecine propose des solutions

qui se veulent simples. Ces approches consistent soit à camoufler les molécules anticancéreuses à l'intérieur des NPs pour les protéger des pompes à efflux ou bien à charger des NPs d'une combinaison de plusieurs molécules (*eg* divers antinéoplasiques et inhibiteurs de pompes P-gp) pour offrir un effet à « large spectre »[9, 26, 27]. De manière générale, l'hypothèse que la nanomédecine puisse surmonter le défi posé par la résistance multiple aux agents antitumoraux se base sur les caractéristiques fondamentales de la nanomédecine, dont l'effet EPR et la possibilité de modifier une NP pour cibler activement les tumeurs (détaillé dans la prochaine section).

1.1.2 La nanomédecine pour les thérapies ciblées

Une caractéristique propre aux nanotechnologies est leur capacité à être adaptées pour produire des effets bien spécifiques *via* une modification de leurs nombreux paramètres physicochimiques (taille, chimie de surface, matériaux, structure, etc). Par exemple, il est possible d'ajouter, à la surface des NPs, des molécules qui auront une affinité pour un élément en particulier dans un organe, un tissu lésé, ou encore à la surface d'une cellule. Ce mécanisme de ciblage, aussi communément appelé « ciblage actif », implique la reconnaissance d'un récepteur par un ligand. Ce dernier est différent de l'effet EPR, aussi appelé « ciblage passif », qui est spécifique à la physiologie des tumeurs et pour lequel la taille favorable des NPs permet leur accumulation, sans nécessiter d'interactions spécifiques. Les protéines, les peptides, les anticorps, les acides nucléiques et les petites molécules sont tous des exemples d'éléments pouvant être inclus dans la « décoration » des NPs pour améliorer le ciblage de cellules, d'organes ou encore de tumeurs[28]. Certains récepteurs cellulaires surexprimés par les cellules cancéreuses (alpha intégrine[29], Her-2[30], transferrine[31, 32]) ont déjà été envisagés pour du ciblage actif. Puisque ces récepteurs sont surexprimés à la surface des cellules tumorales, et non des cellules normales, il est attendu que les NPs à ciblage actif permettront d'accroître la concentration d'antinéoplasiques dans la tumeur et d'offrir une meilleure efficacité thérapeutique. Cependant, l'obtention de cette accumulation n'est pas toujours possible puisqu'elle dépend de multiples facteurs (clairance, localisation de la cible). Or, aujourd'hui, on associe plutôt le ciblage actif à une caractéristique propre aux nanotechnologies qui permet d'accroître leurs interactions avec leur cible sans nécessairement y changer radicalement leur biodistribution[28]. Enfin, le ciblage actif permet d'accroître la flexibilité

du design des NPs, d'en améliorer la personnalisation pour différentes applications et d'améliorer leurs propriétés de ciblage pour ultimement maximiser les chances de succès thérapeutique.

1.1.3 La nanomédecine pour administrer les acides nucléiques

En plus des avantages que proposent les NPs dans un contexte de thérapie ciblée, les interactions ligand-récepteur peuvent mener à la capture et à l'internalisation des NPs par les cellules. En exploitant le potentiel des interactions avec les cellules, de nouveaux concepts favorisant la pénétration des différentes barrières biologiques ont été imaginés. En effet, l'utilisation de la nanomédecine est de plus en plus répandue dans la recherche sur les thérapies visant à moduler l'expression génique [33-37]. La thérapie génique a pour objectif de livrer du matériel génétique sous forme d'acides nucléiques à l'intérieur des cellules pour introduire un gène absent ou altéré sous forme d'ADN. De manière semblable, la livraison d'ARN peut à la fois apporter les instructions pour produire une protéine (ARN messager) ou moduler son expression (siARN, microARN). Initialement, la thérapie génique a été développée en se basant sur la transfection de gènes à l'aide d'un vecteur viral[38], afin de bénéficier de leur capacité à pénétrer des cellules spécifiques du corps. Cependant, plusieurs éléments freinent l'utilisation de cette technique, notamment la pathogénicité de certains vecteurs viraux ainsi que la complexité de leur développement[36]. L'utilisation des nanotechnologies dans ce contexte a donc été évalué en misant sur l'approche du ciblage actif, afin de favoriser l'internalisation cellulaire de NPs et la livraison du matériel génétique à l'intérieur de la cellule. Ainsi la nanomédecine pourrait devenir une plateforme hautement personnalisable de thérapie génique qui permettrait de s'affranchir des inconvénients des vecteurs viraux, tout en permettant de faire pénétrer à travers la barrière cellulaire, les molécules hydrophiles, volumineuses, chargées électroniquement, et sensibles à la dégradation que sont les acides nucléiques (ADN ou ARN).

1.1.4 La nanomédecine pour pénétrer les barrières biologiques

Il a été démontré que les NPs internalisées dans une cellule appartenant à une couche cellulaire barrière peuvent traverser la cellule par le biais de mécanismes de trafic vésiculaire intracellulaires. Plusieurs chercheurs ont constaté que les NPs seraient en mesure de traverser des barrières cellulaires, telles que la barrière hémato-encéphalique[39, 40]. Les cellules possèdent

plusieurs voies d'internalisation, dont certaines leur permettent de capter des molécules pour ensuite les excréter[41, 42]. Il est donc possible, en exploitant ces mécanismes, d'optimiser l'interaction des NPs avec certains ligands de récepteurs membranaires clés (folate, transferrine, insuline)[41] dans le but de stimuler l'endocytose (ou la transcytose) permettant ainsi aux NPs de traverser des barrières biologiques. Ce mécanisme jumelé au ciblage actif de la nanomédecine, est une idée qui a eu d'importantes répercussions dans les domaines de recherche pour lesquels la cible thérapeutique est difficile d'accès. Notamment, l'accessibilité des NPs ou des principes actifs antitumoraux reste limité à l'intérieur de la tumeur dû à une panoplie de facteurs d'ordre hydrodynamique[43, 44]. L'accessibilité au cerveau est un enjeu important pour les thérapies contre le glioblastome ou la maladie d'Alzheimer, par exemple. L'accès au cerveau est principalement limité par l'herméticité de la barrière hémato-encéphalique[45]. Cette dernière est constituée de trois mécanismes de protection limitant le passage de molécules vers le cerveau. D'abord, des jonctions serrées (<1 nm) limitent le transport passif des petites molécules et des plus larges. Ensuite, les pompes à efflux (P-gp, mdr1, etc) qui expulsent les petites molécules du cytoplasme de l'endothélium vers le sang. Finalement, de multiples couches de cellules (endothéliales, péricytes, astrocytes) doivent être traversées afin d'atteindre le cerveau[45]. Ces mécanismes limitent fortement l'exposition du cerveau aux petites molécules et, de ce fait, aux agents thérapeutiques. La nanomédecine permettrait potentiellement de pénétrer cette barrière hémato-encéphalique pour atteindre le cerveau et ouvrir la porte à de nouveaux traitements.

1.2 La nanomédecine : les constats

Les différentes hypothèses présentées témoignent du potentiel et la versatilité de la nanomédecine. Bien que ces hypothèses aient été largement étudiées chez les animaux et, pour la majorité, reproduites dans des études strictement contrôlées, la réalité clinique n'est toutefois pas aussi simple. Les NPs utilisées dans un contexte médical sont des matériaux complexes qui interagissent différemment avec les milieux biologiques que les petites molécules chimiques. La complexité des interactions entre les NPs et les milieux biologiques doit évidemment être considérée lorsque vient le temps de développer une telle technologie, et ainsi d'en maximiser les chances de succès.

Bien que les nanotechnologies destinées à un usage médical auront rapidement suscité un intérêt marqué de la part de la communauté scientifique dès les années 80, c'est seulement en 1995 que la première thérapie issue de la nanomédecine, le vecteur liposomal de doxorubicine Doxil®, aura été approuvé par la FDA[46]. Y. Barenholz, un des principaux scientifiques associé au développement de ce produit, a décrit dans une revue de la littérature la complexité du développement de Doxil® et les différents obstacles qui ont dû être surmontés pour permettre l'obtention d'un design optimal et efficace[46]. Le design final a mis l'emphase sur les propriétés pharmacocinétiques ainsi que l'efficacité de la formulation. L'utilisation de poly(éthylène glycol) (PEG) pour recouvrir partiellement les liposomes a été un élément clé dans la réduction de la clairance des liposomes et la diminution de la taille des liposomes (100 nm). Cette diminution de taille des liposomes a, en outre, permis d'exploiter le phénomène EPR, mis en évidence pour la première fois chez l'humain[23]. À la suite de cette approbation, s'en est suivie un engouement pour le domaine de la nanomédecine, menant à l'approbation de plusieurs vecteurs liposomaux développés avec une approche similaire à celle du Doxil®. En effet, si on se base sur des données récentes, les liposomes constituent la majorité des NPs approuvées et en développement[17, 47, 48]. Cependant, le nombre suspension colloïdales à base de liposomes approuvés par la FDA entre 1995 et 2021 est de seulement 8, soit environ une formulation tous les 3 ans[47]. Ce faible taux de réussite, contrastant l'optimisme généré par les nombreuses possibilités imaginées de la nanomédecine, soulève plusieurs interrogations.

Une récente méta-analyse sur l'efficacité des liposomes chargés de doxorubicine comme le Doxil®, a montré que l'utilisation de vecteurs liposomaux ne permet pas de produire des effets thérapeutiques supérieurs à ceux obtenus avec la doxorubicine seule[21]. Les avantages de la formulation liposomale, se limitent plutôt à la réduction des risques. Il a été noté une réduction de la clairance, une limitation de la biodistribution qui ont contribué à limiter certains effets secondaires graves, comme la cardiotoxicité induite par la doxorubicine[23, 46]. Cette méta-analyse a donc mis en doute les fondements même de la nanomédecine sur le plan de l'efficacité.

En fait, depuis quelques années, on peut remarquer l'absence de translation clinique dans le domaine de la nanomédecine, plus particulièrement pour son application contre les tumeurs solides en oncologie. Alors que seulement 8 formulations à base de liposomes ont été approuvées

par la FDA depuis 1995, les nanoformulations à base de NPs polymériques n'ont, jusqu'à ce jour, jamais connues de réel succès. Le même constat a été fait pour les NPs destinées au ciblage actif de tumeurs[19]. Ce manque flagrant de résultats concluants est au cœur des critiques de la nanomédecine. Par exemple, le professeur Kinam Park explique qu'il s'agit d'une balance complexe entre la proportion de la dose administrée au patient se retrouvant dans les tumeurs et celle qui se distribue ailleurs dans le corps[5, 19]. En effet, bien que les nanotechnologies puissent permettre l'acheminement d'une quantité 5 fois plus importante (par exemple, 5% vs 1%) d'agents antitumoraux en comparaison avec les approches de formulations classiques au niveau de la cible, il n'en reste pas moins qu'environ 95% de la dose se retrouve dans les autres organes. Ainsi, dépendamment de la vitesse de libération du principe actif, cette proportion « hors-cible » de la dose administrée pourrait contribuer à la production d'effets systémiques indésirables. K. Park suggère donc d'exploiter ces 5% théorique ciblant les tumeurs et d'optimiser le design de la formulation pour en améliorer la dose administrée. Cependant, l'estimation de 5% d'efficacité de ciblage de la nanomédecine pour cibler les tumeurs s'est avérée être une surestimation. Selon une récente méta-analyse, il a été mis en évidence qu'en moyenne, seulement 0,7% de la dose s'accumulait dans les tumeurs[49]. En plus de souligner un ciblage sous-optimal des tumeurs par la nanomédecine, les auteurs ont aussi constatés l'absence de progrès entre 2005 et 2015 en lien avec cette efficacité de ciblage. De manière assez intéressante, ce constat illustre bien les raisons menant au faible taux de réussite des nanotechnologies à effectuer une transition en clinique, expliquant par le fait même, la faible quantité de nanoformulations disponibles sur le marché. Les conclusions de cette étude pointent vers un manque de compréhension en ce qui a trait aux phénomènes pouvant nuire ou affecter les NPs utilisées pour l'administration de principes actifs. Par exemple, il a été observé que le choix des matériaux, la stratégie de ciblage (actif ou passif), le rayon hydrodynamique et la forme sont tous des paramètres influençant, à divers degrés, l'accumulation de NPs dans les tumeurs[49]. Ainsi, comprendre les fondements des interactions entre les NPs et les systèmes biologiques, *i.e.* interactions nano-bio, permettrait d'extraire des tendances et d'orienter le design des NPs en fonction des propriétés désirées.

Outre les controverses générées par l'effet ou l'absence de l'effet EPR dans le traitement des tumeurs solides, d'autres approches auront permis à la nanomédecine d'innover et d'établir de

nouveaux standards. Un exemple de cette innovation est le Patisiran (ONPATTRO®), développé par Alnylam et approuvé par la FDA dans le traitement d'une maladie rare, l'amyloïdose héréditaire à transthyrétine, pour lequel aucun traitement thérapeutique n'existait avant l'approbation de ce médicament[50, 51]. Issu de la thérapie génique, Patisiran est un nanovecteur lipidique encapsulant des petits ARN interférents (siARN) permettant de contrôler (réduire) l'expression de la protéine transthyrétine dans le foie. De plus, ce nanovecteur a été conçu afin de cibler spécifiquement le foie par le biais d'une affinité forte des NPs lipidiques pour la protéine ApoE. On ne peut passer sous silence les récents développements de la nanotechnologie dans la vaccination, notamment pour l'immunisation contre le coronavirus induisant le syndrome respiratoire aigu sévère (SRAS-CoV-2). Par exemple, des nanovecteurs lipidiques développés par Moderna et Pfizer-BioNTech ont été utilisés pour transporter un ARNm encodant pour la protéine S du virus à SRAS-CoV-2[52]. Administrés par injection sous-cutanée, les NPs transfectent les cellules musculaires et tendent à favoriser la production de la protéine S, générant ainsi une réponse immunitaire contre celle-ci. Ces vaccins, bien que développés en un peu moins d'un an[52], offrent une excellente protection contre la souche originale et ses variants[53]. Enfin, NBTXR3 (Hensify®), développé par Nanobiotix et approuvé en 2019 par les agences réglementaires européennes, propose une voie d'administration différente de l'injection intraveineuse qui est la voie « classique » pour le traitement local des sarcomes avancés des tissus mous[50]. En effet, les NPs crystallines à base d'oxyde d'hafnium sont injectés directement dans la tumeur pour ensuite agir à titre de potentialisateurs pour la radiothérapie classique. En somme, ces divers exemples illustrent bien l'importance que constitue le choix des composantes des nanotechnologies et rappellent les rôles que peuvent jouer les nanotechnologies dans l'innovation des produits thérapeutiques.

1.3 Les phénomènes à la base des interactions nano-bio

Les interactions nano-bio peuvent être de natures diverses. Pour illustrer cette idée, il est possible d'imaginer le parcours classique des NPs de leur entrée dans un organisme, à l'atteinte de leur cible. Tout d'abord, les NPs, suspendues dans une solution saline iso-osmotique ou un tampon à pH contrôlé, sont injectées dans un vaisseau sanguin. Dès lors, elles se retrouvent dans une solution visqueuse concentrée en protéines et cellules sanguines. Les NPs sont ensuite

transportées par le flux sanguin jusqu'à leur site d'action, par exemple la tumeur. Sous l'effet du phénomène EPR, une partie des NPs s'accumulent en périphérie de la tumeur par extravasation, par le biais de la diffusion, pour finalement pénétrer à l'intérieur de la tumeur. De ce trajet hypothétique, on peut identifier deux composantes clés pouvant influencer l'efficacité des nanoformulations : 1) les interactions avec les fluides biologiques et 2) la capacité des NPs à diffuser dans des matrices biologiques denses. Il s'agit des deux composantes sur lesquelles se concentrera le projet de recherche. Bien entendu, d'autres interactions peuvent contribuer à affecter l'efficacité des nanotechnologies. Les interactions avec des organes contribuant à leur clairance (reins[54], foie[55]) et le système phagocytaire mononucléé[56] sont des exemples d'interactions nano-bio importantes pour comprendre les mécanismes impliqués dans la pharmacocinétique des NPs, mais ces interactions ne seront pas abordées dans le cadre de ce travail[49].

Afin de mieux comprendre les fondements de ces interactions, des techniques spécialisées dans la quantification de phénomènes d'interaction entre les NPs et les fluides biologique ou l'étude du transport des NPs dans les matrices biologiques sont essentielles.

1.3.1 Les interactions avec les fluides biologiques

À l'entrée dans la circulation sanguine, les NPs sont immédiatement mises en contact étroit avec une grande quantité de protéines. On reporte qu'environ 3000 protéines différentes sont en circulation dans le sang[57], possédant une large variété de structures tri-dimensionnelles, fonctions et affinités. De ce fait, il est très probable que certaines protéines interagissent avec les NPs et soient portées à recouvrir la surface de ces dernières, formant ainsi une couronne de protéine (CP). Cette CP aura pour principal effet d'altérer les interactions cellulaires des NPs[58, 59] limitant, dans certains cas, la reconnaissance de récepteurs par ciblage actif[32]. Dans d'autres cas, cette modification de la surface des NPs pourrait aussi être responsable de ciblage non intentionnel, d'une altération de la pharmacocinétique et même d'une reconnaissance par les macrophages[60]. Il est donc primordial de bien comprendre l'impact que la CP peut avoir sur le comportement des NPs, *in vivo,* et de démystifier les mécanismes d'adsorption ainsi que les éléments pouvant les influencer.

Un large éventail de méthodes analytiques sera nécessaire pour bien caractériser la CP et comprendre son impact sur le comportement des NPs. La composition du sang étant très diversifiée, un grand nombre de protéines devront être analysées dans le but de déterminer la composition de la CP. Il est donc nécessaire d'employer des techniques d'analyses protéomiques, telle que la chromatographie liquide par spectrométrie de masse en tandem (LC-MS/MS), pour la caractériser[61]. Des corrélations ont été réalisées afin de mesurer la relation entre la composition de la CP et les interactions cellulaires[58, 59, 62], la toxicité et la pathophysiologie[63] ainsi que les interactions avec le système immunitaire[64, 65]. L'idée principale de cette aire de recherche est de pouvoir prédire et contrôler les différentes interactions ainsi que la biodistribution des NPs en analysant et optimisant la composition de la CP[60].

Pour contrôler les interactions des NPs avec les fluides biologiques, plus particulièrement avec les protéines, il est primordial d'identifier les mécanismes impliqués afin de mieux comprendre les fondements de ces interactions. Un moyen d'y parvenir consiste à mesurer l'affinité des protéines individuelles aux NPs en y mesurant l'influence de certains paramètres, tels que le choix du matériau[66-70], la forme des NPs[71] et la température[72]. Pour mesurer cette affinité, des techniques pour quantifier l'adsorption de protéines aux NPs doivent être employées. Préférablement, les NPs doivent rester dans leur milieu initial de manière à éviter les perturbations de l'équilibre des complexes protéines-NPs[73]. Certaines techniques le permettent indirectement, en se basant sur la changement du rayon hydrodynamique des NPs comme la diffusion dynamique de la lumière (DLS)[74], la spectroscopie à corrélation de fluorescence (FCS)[66], la résonnance magnétique nucléaire (RMN)[75]. Toutefois, ces dernières sont limitées en résolution par la taille et la stabilité des NPs. Le titrage calorimétrique isotherme (ITC) est une alternative employée pour évaluer l'affinité de l'interaction protéines-NPs en plus d'en tirer des paramètres thermodynamiques de la réaction d'adsorption. Cependant, la sensibilité de l'ITC est généralement limitée et dépendante du type d'interaction[76]. D'autres techniques permettent d'estimer l'affinité des interactions protéines-NPs au prix de certaines limitations, telle que la nécessité d'extraire les NPs de leur milieu. C'est dans le but de s'affranchir des limitations des techniques existantes que de nouvelles techniques pour mesurer les interactions protéines-NPs ont été développées (cytométrie de flux[77] et l'ultracentrifugation analytique[78] en sont des exemples).

1.3.2 Les phénomènes de diffusion et de transport dans les tissus denses

Une fois que les NPs atteignent leur cible, que ce soit une tumeur ou un organe, elles doivent y pénétrer afin d'y livrer leur contenu (principe actif ou matériel génétique), idéalement, de manière uniforme. Tel que discuté un peu plus tôt, un grand enjeu dans le développement de nanotechnologies est leur capacité à pénétrer des barrières biologiques. Dans le cas des tumeurs, plusieurs barrières s'élèvent contre la pénétration de molécules et de macromolécules. Premièrement, une pression hydrostatique élevée par rapport aux vaisseaux sanguins s'oppose à l'entrée de molécules dans la tumeur[43, 44, 79]. À l'intérieur de cette dernière, se trouve également une matrice extracellulaire désorganisée constituée de fibres de collagène et d'autres protéines structurales limitant la diffusion des NPs, la diffusion étant effectivement un de leurs principaux moyens de transport[80].

Pour améliorer la pénétration tumorale, on pourrait donc être porté à croire que réduire la taille soit un avantage, car la diffusion D est inversement proportionnelle au rayon R des NPs, soit $D \sim 1/R$. De manière intéressante, cette tendance mène à un certain paradoxe. En effet, les molécules actives transportées par les NPs sont beaucoup plus petites (~1 nm) que leur cargo (~100 nm) et diffuserons donc beaucoup plus vite (~100x) que les NPs que l'on tente d'optimiser pour pénétrer des structures biologiques denses. Cependant, les petites molécules perdent l'effet EPR dû à leur petite taille et cela a pour effet de limiter leur accumulation tumorale, justifiant l'utilisation de vecteurs plus larges[16, 81]. L'option de réduire la taille des NPs rend toutefois ces dernières plus susceptibles à la clairance rénale, d'autant plus lorsqu'elle est inférieure à 8 nm[54]. Les deux constats sont que les NPs trop petites (<8 nm) auront des clairances plus élevées et que les NPs trop grandes (>100 nm) auront une diffusion limitée. Ce sont principalement ces observations qui ont mené à la détermination des tailles critiques en nanomédecine.

Ces limitations complexifient l'optimisation de vecteurs capables de pénétrer facilement les milieux denses des tumeurs. Il est donc nécessaire d'étudier l'effet de certains paramètres (*eg* taille, propriétés de surfaces, forme, élasticité) sur la diffusion des NPs dans ces milieux. Bien qu'il soit possible d'évaluer la pénétration *in vivo* de NPs, ces études nécessitent l'utilisation de systèmes d'imagerie complexes et coûteux, qui seront généralement sensibles aux erreurs et rarement adaptés pour la réalisation de larges études comparatives.

Il est possible de mimer les tissus biologiques à l'aide de gels de différentes compositions, de sorte à pouvoir y mesurer la diffusion de NPs et de macromolécules[82, 83]. Mesurer la diffusion dans ces milieux turbides et hétérogènes est en réalité un défi. Il est possible de mesurer la diffusion de NPs fluorescentes dans des gels par FCS[84-86] ou par recouvrement de la fluorescence après photoblanchiment (FRAP)[82, 83]. Cependant, avec ces techniques il est difficile d'observer la dépendance spatiale de la mesure de diffusion, un paramètre souvent oublié[87]. En effet, la diffusion dans un milieu hétérogène, comme les gels, peut dépendre de l'aire de la région observée. Par exemple, à l'intérieur d'un pore, la diffusion sera rapide, mais pour une région ayant plusieurs pores interconnectés, elle sera plus lente. On observe alors un phénomène de diffusion « anormale », ou plus précisément, de « sous diffusion ». La technique de localisation et de suivi multiple de NPs (de l'anglais, « *Multiple Particle Tracking* », MPT) permet une meilleure résolution spatiale, à condition d'obtenir une résolution claire des NPs et de sélectionner le meilleur algorithme d'analyse, sachant que ce dernier peut influencer le résultat obtenu[88]. Par exemple, dans plusieurs études, la diffusion de NPs de tailles supérieures à 100 nm a été mesurée par MPT dans des fluides biologiques, tel que le mucus pulmonaire[89], vaginal[90, 91] et gastro-intestinal[90, 92], afin d'optimiser leur pénétration dans ces milieux. Ce type d'étude, dans des modèles *in vivo* ou *in vitro* de tissus (gels), est beaucoup plus rare pour les petites NPs (<100 nm). Le manque d'études pourrait permettre d'expliquer la faible compréhension des paramètres affectant la pénétration tissulaire et tumorale pour les petites NPs employées en nanomédecine. Or résoudre ce besoin technologique pourrait pallier ce manque de connaissance en favorisant l'accélération de l'étude des paramètres influençant la diffusion des NPs dans ces milieux complexes.

1.4 La microscopie différentielle dynamique

On peut remarquer un engouement pour le développement de nouvelles techniques de caractérisation et de quantification des interactions nano-bio. Cette observation n'est pas surprenante sachant que les nanotechnologies ne sont pas des formulations dites « classiques » et qu'elles présentent des caractéristiques bien distinctes (ratio surface/volume, importante réactivité de surface, instabilité colloïdale, etc.). Ainsi, il est normal que lorsqu'on expose ces

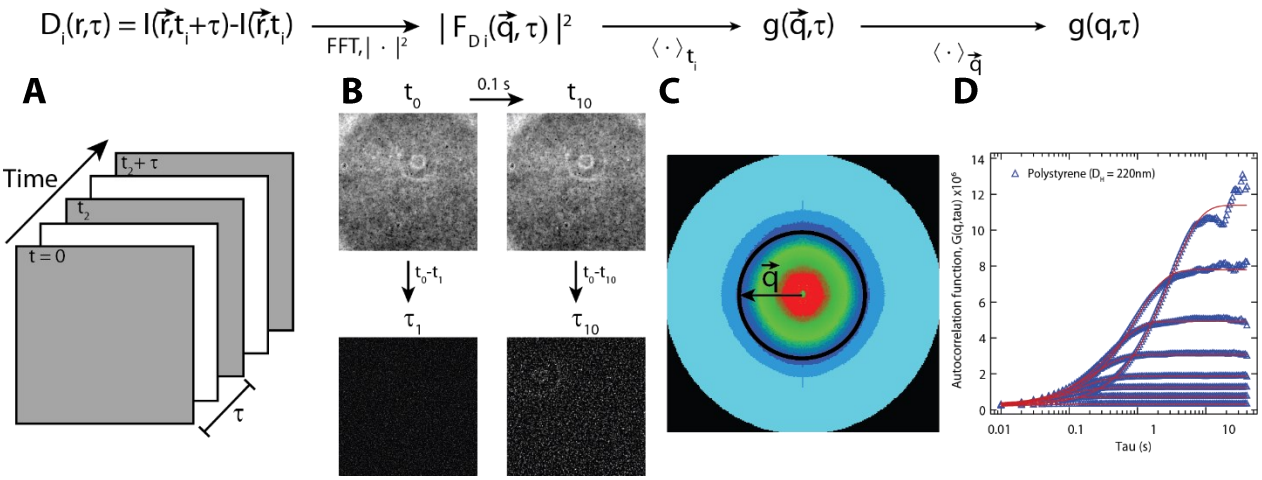

Figure 1.1. Représentation du processus de calcul de la fonction d'autocorrélation en DDM à partir d'une série temporelle d'image. D'abord on fait l'acquisition d'une série d'image (A). Ensuite on prend des images pour différents intervalles de temps t et on y soustrait les valeurs d'intensité pour obtenir l'image différentielle D_i (B). L'image différentielle peut être vue par les images sombres notées τ_1 pour les temps de délais très courts, et τ_{10} pour des temps de délais plus grand. Le spectre de puissance, résultant de la transformée de Fourier des images différentielle, produit une apparence circulaire pour les dynamiques isotropes (C). La moyenne azimutale en q permet de générer les fonctions d'autocorrélations $g(q,\tau)$ et d'extraire les dynamiques browniennes (D). La série d'équation représente la procédure mathématique pour reproduire les étapes B à D.

nanoformulations à la complexité du vivant, les techniques, couramment utilisées pour caractériser les interactions des petites molécules avec les milieux biologiques, ne soient pas optimales.

Une technique d'analyse récemment développée par Cerbino et Trappe pour mesurer la diffusion de nanoparticules à partir d'un microscope à champ clair a particulièrement attiré notre attention[93]. Avec l'aide uniquement d'un microscope à champ clair équipé d'une caméra à haute vitesse d'acquisition (~100 ips), les auteurs ont été capables de mesurer la dynamique de NPs de polystyrène de 73 nm de diamètre et d'en extraire correctement le coefficient de diffusion[93]. En effet, il s'agit de la première technique d'analyse vidéo capable de mesurer la dynamique des NPs

sans avoir besoin de résoudre avec précision la position des NPs dans le champ optique. Cette technique fut nommée la microscopie différentielle dynamique (de l'anglais, « *differential dynamic microscopy* », DDM). De plus, un support visuel accompagnant les données quantitatives extraites des vidéos, permet de faciliter l'interprétation des résultats et d'assurer l'exactitude des analyses.

La DDM se base sur un principe de mesure des fluctuations d'intensité lumineuse à partir d'une série temporelle d'image. En effet, les NPs en déplacement génèrent des fluctuations d'intensité lumineuse qui sont enregistrées par la caméra. Chacun des pixels de la caméra mesure les fluctuations d'intensité causées par le mouvement brownien des NPs en suspension. En soustrayant les intensités de deux images séparées par un temps τ, on élimine les contributions de tout ce qui est statique et on se retrouve avec uniquement la composante dynamique du système, soit le mouvement des NPs. Ces différences d'image, D_i , sont calculées pour chaque temps de délai, τ, et position dans l'image, $\vec{r}$, à partir de chacune des images de la vidéo enregistrée de sorte que le résultat obtenu à partir de l'équation 1.1 produira une image différentielle, semblable à celle illustrée à la Figure 1.1A.

$$D_i(\vec{r}, t_i) = I(\vec{r}, t_i + \tau) - I(\vec{r}, t_i) \quad (1.1)$$

Plus le temps de délai sera long, plus l'intensité de l'image différentielle va croitre puisque la grande majorité des NPs auront eu le temps de se déplacer. Afin de quantifier ce signal différentiel et son évolution dans le temps, on utilisera la transformée de Fourier spatiale afin de travailler dans l'espace fréquentiel. La fréquence spatiale *q* sera défini par la longueur caractéristique *L*, où $q=2\pi/L$. On obtient le spectre de puissance, qui est la valeur absolue au carré de la transformée de Fourier. La moyenne est calculée pour chacun des temps initiaux t_i et on obtient la fonction de corrélation des différences d'images (DICF)

$$g(\vec{q}, \tau) = \langle |I(\vec{q}, t + \tau) - I(\vec{q}, t)|^2 \rangle \quad (1.2)$$

où $I(\vec{q}, t)$ est la transformée de Fourier de $I(\vec{r}, t_i)$. Si la dynamique mesurée est isotropique comme le mouvement brownien de NPs, le spectre de puissance aura alors une apparence circulaire (Figure 1.1C) et la moyenne azimutale peut être calculée de sorte que $\vec{q} = |q|$ et finalement, on obtient

$$g(q,\tau) = \langle |I(q,t+\tau) - I(q,t)|^2 \rangle. \quad (1.3)$$

En considérant que les fluctuations d'intensités sont reliées aux fluctuations de densité de particules, il a été montré que $g(q,\tau)$ est relié à la fonction de diffusion intermédiaire (ISF) par[94]

$$g(q,\tau) = A(q)[1 - f(q,t)] + B(q), \quad (1.4)$$

où A(q) est un préfacteur qui dépend du système optique, du nombre, de la forme et de la structure de la suspension de particules et B(q) dépend du bruit provenant de la caméra. L'ISF dépend du type de déplacement des objets et pour une dynamique brownienne elle prend la forme[94-97]

$$f(q,t) = \langle e^{-i\vec{q}\left(\vec{r}(t+\tau)-\vec{r}(t)\right)} \rangle = e^{-Dq^2\tau} \quad (1.5)$$

pour des sphères monodisperses avec un coefficient de diffusion *D.* Ainsi à partir de vidéos acquises d'une suspension de sphères browniennes, sur la base de la mesure des fluctuations d'intensité enregistrées par chacun des pixels de la caméra il est possible de mesurer le coefficient de diffusion de ces sphères. De plus, la quantité mesurée en DDM, $g(q,\tau)$ permet d'extraire l'ISF, qui peut aussi être obtenue par DLS[95]. Cette réalisation a permis de généraliser la DDM à d'autres types de mouvements, par exemple le mouvement balistique et diffusif des bactéries[94, 96, 98] et à des dynamiques présentant des anisotropies[97, 99]. L'utilisation de la DDM a d'ailleurs été étendue à d'autres modes d'illuminations et de microscopie comme le contraste de phase[94, 96, 97], la fluorescence[100], le champ sombre[101] en lumière polarisée[102] et à la microscopie confocal[98]. Cette adaptation à divers modes d'imagerie rend cette technique beaucoup plus versatile et plus accessible que les autres techniques de ce genre.

Un autre paramètre important sur lequel repose la DDM est l'amplitude du signal $A(q)$. Ce dernier dépend du nombre n_o et de l'intensité I_o de l'objet dans le champ d'observation pour chaque dynamique observable, selon l'équation[97]

$$A(q) = n_o {I_o}^2 P(q) S(q) T(q) \quad (1.6)$$

où $P(q)$ est le facteur de forme, $S(q)$ est le facteur de structure des suspensions de NPs et $T(q)$ est la fonction de transfert optique du microscope dépendant du système d'imagerie utilisé. Il est possible de découpler les différentes dynamiques d'un système. Par exemple, cela permet

d'identifier avec précision la dynamique diffusive de suspensions bidisperses de NPs ayant des tailles de 50 et 1000 nm[103] ou bien d'identifier les fractions motiles et non motiles d'une population de bactéries[94]. Cette approche pourrait être étendue à la caractérisation de l'adsorption de protéines sur des NPs. L'utilisation de protéines fluorescentes et de NPs non-fluorescentes produirait en DDM des contributions dynamiques différentes pour les protéines libres et les protéines adsorbées. Si la taille des NPs est suffisamment grande par rapport à celle des protéines, par exemple 200 nm *vs* 6 nm en diamètre, cela permettrait d'extraire l'intensité du signal A(q) des protéines adsorbées à la surface des NPs. On réalisera qu'en fluorescence, uniquement l'adsorption de protéines fluorescentes à la surface des NPs contribuera à l'intensité du signal de la dynamique attribuable aux NPs. De cette manière, l'amplitude du signal $A(q)$ de l'équation 1.6 mettra en relation la quantité de protéines fluorescentes adsorbées par NPs, Γ, et l'intensité de la fluorescence des protéines, I_p, par $I_o=I_p\,\Gamma$. Ce type d'approche par DDM n'a cependant jamais été exploré et devra donc être validé pour une telle utilisation.

1.5 Hypothèse et objectifs

Le développement de techniques permettant la caractérisation des interactions entre les NPs et les milieux biologiques a été identifié comme un facteur d'importance dans le développement du domaine de la nanomédecine. L'idée principale véhiculée par cette approche est qu'une meilleure caractérisation de ces interactions permettrait de mieux comprendre les avantages et limitations de la nanomédecine. Les récents développements relatifs à la DDM ont montré que la technique permet de mesurer des dynamiques dans des milieux denses[104], turbides[98] et confinés[105], ayant une complexité se rapprochant de celle du vivant. Ainsi, il serait possible d'envisager l'utilisation de la DDM pour caractériser divers aspects de la nanomédecine. Les différents paramètres mesurés par la DDM, tels que l'amplitude du signal A(q) et le coefficient de diffusion D, pourraient donc permettre d'évaluer les interactions des NPs à la fois avec les fluides biologiques et les tissus interstitiels.

1.5.1 Hypothèse de recherche

L'hypothèse centrale de ce projet est donc la suivante:

> *« La DDM permet d'investiguer les diverses interactions des nanoparticules dans des milieux biologiques simulés. Dans un premier temps, les interactions des NPs avec les protéines des fluides biologiques, et dans un deuxième temps, les paramètres affectant la diffusion des NPs dans un modèle de tissu interstitiel.»*

Les interactions entre les NPs et les protéines seront traitées dans les chapitres 2,3, et 4. L'influence des paramètres de diffusion des NPs dans les matrices biologiques sera abordée dans les chapitres 5 et 6.

1.5.2 Objectifs de recherche

Afin de valider cette hypothèse de recherche, l'objectif principal commun aux deux thématiques est de :

> « *Développer, valider et appliquer la DDM à des systèmes de NPs d'intérêt en nanomédecine pour lesquels les techniques actuelles ne permettent pas une quantification optimale*. »

Premièrement, nous développerons la DDM afin d'évaluer sa capacité à quantifier l'adsorption de protéines à la surface des NPs *in vitro* et *in vivo*. La DDM sera ensuite employée pour mesurer la diffusion de NPs dans des modèles de matrices extracellulaires. Le contexte et les approches envisagées pour l'atteinte de ces deux objectifs de recherche seront davantage détaillés dans les prochains chapitres.

Dans le chapitre 2 sera introduit les interactions entre les nanoparticules et les protéines issues des fluides biologiques dans un contexte de nanomédecine. D'une part, nous détaillerons certaines problématiques associées à ce domaine de recherche et, d'autre part, introduirons notre hypothèse de recherche associée à cette thématique qui sera explorée dans cette thèse.

Le chapitre 3 s'intéressera à la relation entre les techniques analytiques et certaines mesures controversées de la CP. Cette revue de la littérature fait l'objet d'une publication, présentement

en cours de révision, dans le journal ACS Nano : Latreille, PL.; Le Goas, M.; Salimi, S.; Robert, J.; De Crescenzo, G.; Boffito, D.; Martinez, V.A.; Hildgen, P.; Banquy X., ***Scratching the Surface of the Protein Corona: Challenging Measurements and Controversies*****.** *ACS Nano* **2021.**

Le chapitre 4 portera sur le développement de la méthode par DDM et la caractérisation de la CP *in situ*. Nous tenterons, par DDM, d'apporter des explications à certaines interrogations soulevées dans le chapitre 3. Nous montrerons aussi la capacité de la DDM à effectuer une mesure de la désorption de la CP *in vivo*. Ces travaux font l'objet d'un article en préparation : Latreille, PL., Rabanel, JM., Le Goas M., Salimi S., Arlt J., Patten S.A., Poon W.C.K., Ramassany C., Hildgen P., Martinez V.A., Banquy X. ***Deciphering in vitro and in vivo the protein corona formation and dynamics by differential dynamic microscopy*****.** À soumettre à Science Advance, **2021**.

Dans le chapitre 5, nous aborderons la thématique de la dynamique des colloïdes et de leur diffusion dans les tissus interstitiels. Cette section mettra en relation la mesure de la diffusion et la pénétration des NPs dans les tissus. Nous y détaillerons notre hypothèse de recherche et les objectifs spécifiques reliés à cette thématique.

Le chapitre 6 s'intéressera à l'étude des propriétés mécaniques des NPs et de l'influence de ces dernières sur la diffusion des NPs dans des matrices extracellulaire modèles. Nous montrerons, entre autres, l'avantage des NPs déformables à diffuser dans les milieux confinés contrairement aux NPs « dures ». Ces travaux ont fait l'objet d'une publication dans « *Nature Communications* » : Latreille, P.-L.; Adibnia, V.; Nour, A.; Rabanel, J.-M.; Lalloz, A.; Arlt, J.; Poon, W. C. K.; Hildgen, P.; Martinez, V. A.; Banquy, X., ***Spontaneous shrinking of soft nanoparticles boosts their diffusion in confined media.*** Nature Communications. **2019**, 10 (1), 4294.

Le chapitre 7 présentera une discussion détaillée des travaux présentés dans les chapitres précédents. Nous mettrons en perspective nos différentes observations, en se rapportant à nos hypothèses de recherche, et évaluerons leur impact scientifique.

Enfin, le chapitre 8 permettra de conclure sur les travaux présentés dans cette thèse. Nous soulèverons des questions en lien avec nos recherches et nous identifierons les possibilités offertes par le développement de la DDM pour l'étude des nanotechnologies en médecine.

Chapitre 2 – Interaction protéines-NPs dans le contexte de la biodistribution

Nous avons précédemment établi que l'adsorption de protéines est une barrière au contrôle et à l'efficacité de la nanomédecine. En effet, les protéines que l'on retrouve dans le sang ont tendance à s'adsorber à la surface des NPs, modifiant leurs propriétés de surface qui a leur tour modifieront la biodistribution et le devenir des particules dans l'organisme. En effet, les protéines plasmatiques ont une affinité non-spécifique pour les NPs. Cette affinité est principalement médiée par les propriétés physicochimiques de surface des NPs *e.g.* chimie de surface[24, 67, 68], charge[69, 106] ainsi que la taille[107-109]. Ainsi, des NPs de composition, structure et chimie de surface différentes produiront des interactions de nature diverses avec les protéines constituantes du sang contribuant à générer des CP de compositions différentes[63, 108]. Bien que certaines de ces protéines ont des rôles biologiques bien définis, il peut être difficile de prédire l'impact de la CP sur le devenir des NPs. Par exemple, dans certaines études, on note que la CP peut avoir un effet perturbateur sur la capacité des NPs à cibler des récepteurs membranaires de cellules[32], alors que dans d'autres cas, elle semble n'avoir aucun effet[110]. D'autres analyses révèlent que certaines protéines de la CP favorisent l'internalisation des NPs dans des cellules, alors que d'autres la réduisent[58, 59]. De la même manière, certaines protéines agissant comme dysopsonines et permettant de retarder ou d'éviter la reconnaissance par le système immunitaire par opsonisation, se sont retrouvées adsorbées à la surface de NPs PEGylées. Il a été démontré que ces dysopsonines étaient responsables de l'effet camouflage du polymère PEG[65] en plus de prolonger le temps de circulation des NPs faiblement PEGylées[111]. Ces démonstrations tendent à montrer que la CP est un important déterminant de la biodistribution des NPs et que la composition en protéine dicte l'identité biologique de ces dernières[60].

Bien que certaines tendances générales reliées à la CP aient été vérifiées et répétées indépendamment, certaines tendances sont moins claires, tel que l'effet perturbateur de la CP sur le ciblage des NPs mentionné précédemment. Cet exemple n'est pas unique et les résultats

opposés proviennent, selon nous, principalement des défis analytiques rencontrés lors de l'étude des interactions protéines-NPs. En effet, deux paramètres clés des interactions protéines-NPs font objet d'observations contradictoires: la présence de multicouches de protéines et la réversibilité de l'adsorption des protéines à la surface des NPs.

2.1 Observations divergentes : les multicouches

Les premières observations de protéines adsorbées en multicouches ont été reportées entre 2010-2012[31, 112, 113] et se sont par la suite multipliées. Cependant, des résultats contradictoires ont été rapportés. Ainsi, pour certains systèmes identiques (ou très semblables), la présence tantôt de monocouches, tantôt de multicouches, a été rapportée. Un exemple bien documenté est l'adsorption de la transferrine à la surface de NPs constituées de polystyrènes sulfatés[31, 70]. Ces observations soulèvent ainsi une question complexe quant à l'existence réelle de multicouches et ce qu'elles représentent. En effet, pour que des multicouches de protéines puissent se constituer, il est nécessaire qu'elles se forment via des interactions protéines-protéines. Or, les protéines du plasma sont très stables, *i.e.* les protéines plasmatiques ne coagulent pas spontanément. Ainsi, pour que des interactions protéines-protéines soient suffisamment fortes pour générer des multicouches, une forte dénaturation ou fibrillation doit avoir lieu[73, 114]. Il est aussi intéressant de noter que certains auteurs présentent l'adsorption en multicouche comme inévitable[115-117], alors que d'autres rapportent ne jamais avoir observé ce phénomène[73, 118]. Certaines hypothèses ont été avancées pour expliquer cette division parmi les chercheurs travaillant sur cette thématique. Étant donné le défi analytique que constitue la détection de multicouches, il est possible que certains biais analytiques proviennent de la technique choisie[118]. La composition du fluide biologique[113] et la taille des NPs[117, 119] sont des paramètres qui ont aussi été identifiés comme pouvant avoir un impact sur la formation de multicouches de protéines. Ces hypothèses pourraient permettre d'expliquer pourquoi certaines études observent des multicouches alors que d'autres non, et d'ainsi unifier ces observations *a priori* opposées.

2.1 Observations divergentes : la réversibilité de l'adsorption

Un concept important qui revient souvent dans les études portant sur l'effet de la CP sur les NPs est celui de couronne « dure » et de couronne « molle ou faible ». Ce concept a été introduit par K. Dawson et coll. en 2008. L'idée repose sur la supposée existence au sein de la CP d'une couronne de protéines dite « dure » (de l'anglais, « *hard corona* », HC) qui interagit fortement et de façon stable voire irréversible avec la surface des NPs, ainsi que d'une couronne de protéines dite « molle » (de l'anglais, « *soft corona* », SC) dont l'absorption est réversible et est le produit d'interactions faibles et de courte durée avec les NPs[107]. Ces deux couronnes sont souvent représentées en couches successives, à la manière de multicouches[31]. Cependant, la pertinence et l'existence de ce modèle est remise en question puisqu'il n'apporte ni solutions ni explications aux phénomènes observés en lien avec la CP en plus d'y créer de la confusion[120, 121].

La réversibilité de l'adsorption de protéines est aussi sujette à des études contradictoires. En effet, sur des NPs d'or, il a été rapporté dans certaines études que l'adsorption de l'albumine bovine sérique (ou BSA) est irréversible[113, 122, 123] alors que d'autres rapportent qu'elle peut être réversible et même déplacée par d'autres protéines[124, 125]. Dans le même ordre d'idée, pour des NPs différentes, mais possédant des chimies de surface semblables, une étude a fait l'observation d'une dynamique d'échange de protéines au sein de la CP[63] alors qu'une autre y démontre l'absence de désorption par dilution pour les protéines du sérum[69]. L'ensemble de ces observations *à priori* contradictoires contribuent à souligner l'importance de mieux comprendre les interactions protéines-NPs et d'optimiser les techniques permettant leur analyse. Déterminer si la CP est un ensemble dynamique ou plutôt statique aura des répercussions importantes sur les applications futures des NPs, tel que le développement d'outils diagnostiques[126].

2.2 Hypothèse et objectifs spécifiques : les interactions protéines-NPs

Tel que discuté dans la section précédente, il existe un engouement pour le développement de nouvelles techniques afin de pallier les lacunes des techniques déjà existantes. Il est possible que les observations divergentes proviennent de ces lacunes analytiques. Ainsi nous croyons que l'utilisation de la DDM pourrait permettre de s'affranchir de certaines problématiques

technologiques qui sont intrinsèques aux autres techniques et résoudre certaines divergences reliées à l'adsorption de protéines.

Afin de tester notre hypothèse de recherche, nous avons procédé en deux temps :

Nous avons d'abord procédé à une revue exhaustive des techniques de caractérisation de la CP, leurs principes, avantages et limitations. Ensuite, grâce à une méta-analyse, nous avons évalué l'impact des techniques analytiques, et de certains paramètres physicochimiques, sur la récurrence de l'observation de multicouches ainsi que de la réversibilité de l'adsorption de protéines. À l'aide d'analyses statistiques, nous avons tenté d'expliquer certains phénomènes et de résoudre les incohérences observées dans ces études.

Ensuite, nous avons expérimentalement développé une nouvelle technique de quantification de la CP par DDM afin de tenter de répondre aux problématiques identifiées. Nous avons choisi d'utiliser des systèmes modèles, soit des NPs simples à base de polystyrène et des protéines simples, telles que le lysozyme et l'albumine, pour établir la validité de l'approche. Graduellement, nous avons étudié des systèmes plus complexes de protéines comme le sérum bovin contenant un ensemble varié de protéines. Finalement, la technique a été appliquée dans un système *in vivo*, chez le poisson zèbre. Enfin, à l'aide de l'analyse préalable de la problématique et des mesures expérimentales mettant en œuvre la DDM nous tentons de répondre à certaines questions et controverses entourant la structure et la dynamique de la CP.

Les travaux proposés font l'objet de deux publications scientifiques.

La méta-analyse de la CP a été soumise dans le journal ACS Nano (en révision) :

Latreille, PL.; Le Goas, M.; Salimi, S.; Robert, J.; De Crescenzo, G.; Boffito, D.; Martinez, V.A.; Hildgen, P.; Banquy X., *Scratching the Surface of the Protein Corona: Challenging Measurements and Controversies*. *ACS Nano* **2021.**

L'article scientifique dans lequel le développement de la DDM pour la caractérisation de la CP est présenté sera soumis pour publication sous peu.

Latreille, PL., Rabanel, JM., Le Goas M., Salimi S., Arlt J., Patten S.A., Poon W.C.K., Ramassany C., Hildgen P., Martinez V.A., Banquy X. *Deciphering in vitro and in vivo the protein corona formation and dynamics by differential dynamic microscopy*. À soumettre à Science Advance, **2021**.

Chapitre 3 – "Scratching the Surface of the Protein Corona: Challenging Measurements and Controversies"

Pierre-Luc Latreille[1], Marine Le Goas[1], Sina Salimi[1], Jordan Robert[1], Gregory De Crescenzo[2], Daria C. Boffito[2], Vincent A. Martinez[3†], Patrice Hildgen[1] and Xavier Banquy[1†]

1) *Faculty of Pharmacy, Université de Montréal, PO Box 6128, Succursale Centre-ville, Montréal, Québec H3C 3J7, Canada*
2) *Department of Chemical Engineering, Polytechnique Montréal, Montreal, Canada*
3) *School of Physics and Astronomy, The University of Edinburgh, Peter Guthrie Tait Road, Edinburgh, EH9 3FD, UK*

Dans cette revue, nous avons exploré à la fois les fondements des méthodes pour la caractérisation de la CP et leur performance à caractériser deux phénomènes particuliers de la CP : l'adsorption en multicouches et la réversibilité de l'adsorption.

Étant donné l'ampleur de ce travail, les deux parties de la revue ont été scindées pour en faire deux publications. L'analyse et la revue des concepts de quantifications de la CP sera soumise dans un journal pour publication, par exemple, « Journal of Controlled Release » ou encore « Biomacromolecules ».

La partie de la méta-analyse en lien avec l'adsorption de protéines en multicouches et sa réversibilité a été soumise au journal ACS Nano. À cet instant, l'article de revue révisé par les pairs nécessitera des corrections mineures.

En **Annexe 1**, se retrouvent les informations supplémentaires (de l'anglais « *supplementary informations* », SI) cités dans le cadre de ce chapitre.

3.1 Introduction

Nanomedicine has undergone unprecedented changes in the recent years. Despite a setback from the disappointing and controversial observation of its dubious efficacy to treat malignant tissues in the literature of the last decade[49], new challenges have motivated studies towards the understanding of nanoparticles (NPs) interactions with biological media[60, 116, 121]. Identifying nano-bio interactions is critical for the design and application of nanomedicine, as they have been shown to vastly influence NPs fate *in vivo*[60]. The use and control of these interactions is a multidisciplinary and multidimensional challenge at the interface of nanoscience, biology, medicine and physics. Considering the complex nature of physiological fluids as well as NPs' large palette of attributes (such as size, shape and surface chemistry), a variety of different phenomena should be expected to occur from nano-bio interactions.

In 2007, Cedervall *et al.* observed that proteins were completely covering the NPs' outer surface, from which the term "protein corona" was coined[127]. From this observation, the study of NPs interactions with proteins has been rapidly expanding to identify mechanisms of formation, as well as their roles and actions in the host environments. From there, it was hypothesized that, since nano-bio interactions are mostly mediated through the surface of NPs, adsorption of proteins onto NPs would alter the biological identity of the NPs by modifying their surface properties. For instance, it was observed that the protein corona could modulate or even screen the active targeting of NPs, a strategy that consists in attaching organ- or cell-specific moieties onto NPs[32]. Tenzer *et al.* further described the process of protein corona formation around NPs as a "natural functionalization", which was reported to happen in less than a minute.[63] The composition of this natural functionalization was found to depend on the type of NPs (material, surface coating, size, surface charge)[63, 107, 108], and was also correlated to different pathophysiological responses to NPs[63]. Likewise, the protein corona was also found to impact the pharmacokinetics of NPs[111]. Many observations suggest that the proteins adsorbed on the NPs surface are in fact the material interacting with cells, therefore dictating the NPs biological identity[60, 112]. As a result, there is a critical need to understand the mechanisms and processes of

protein adsorption on NPs to better control and predict the resulting biological behavior of nanomedicines.

The early physical concepts describing the adsorption of biomolecules onto nanomaterials were reminiscent of macroscopic biomaterials. However, the nanoscopic size of NPs, their surface energy, surface-to-volume ratio and mobility are all orders of magnitude different compared to macroscopic biomaterials constituting implants for example, which makes NPs a widely different system to study. Indeed, the size of NPs can range from that of a protein to hundreds of times larger, thus introducing new challenges in terms of both measurement and prediction of important parameters such as colloidal stability, composition and structure of the protein corona, and reversibility of adsorption. Even though the small size of NPs grants them unique properties, it also makes them very difficult to observe in solution and even more difficult to distinguish from proteins themselves.

Despite these issues, quantification of protein adsorption on NPs has been enabled through the use of already available techniques, *e.g.* dynamic light scattering (DLS)[113], fluorescence correlation spectroscopy (FCS)[66], mass spectrometry-based proteomics[107], differential centrifugal sedimentation (DCS)[128] and isothermal titration calorimetry (ITC)[127]. The concept of "hard" and "soft coronas" has emerged from these quantitative measurements of protein adsorption[31, 107, 113]. The hard corona is typically described as a "long-lived" or irreversibly adsorbed layer of proteins, whereas the soft corona is described as a loosely adsorbed layer[107] that is interchangeable with other molecules present in the medium[129]. Because of the weak adsorption and fast equilibrium dynamics of the soft corona, it was hypothesized to be almost exclusively observed *in situ*[107] as well as to potentially form multilayers atop of a hard corona[31]. However, both the dynamics of the protein corona and its thickness (mono- or multilayers) are still subjects of debate. Many have claimed to observe protein coronas structured in multilayers around NPs[31, 113, 117, 130], while others have also reported the formation of monolayers using similar experimental approaches and *in situ* techniques[69, 70, 75, 78]. Concerns have been raised that some techniques may not always be suited for such quantifications[73, 106, 120, 130, 131]. As the field is

growing rapidly, there has not been a clear resolution of these contrasting observations yet and barely any attempt has been made to unify them.

In this review, we aim to address these concerns by first giving an overview of the techniques used for protein corona characterization and the quantification of its key attributes. A detailed description of the underlying physical phenomena and operating principles is provided for all the techniques, in order to identify both their advantages and limitations. Complementary techniques that assess the structure of the proteins and protein corona are also detailed. In a second part, we perform a statistical analysis of a large number of reported data to provide answers to both debates of mono- vs multilayers and reversible vs irreversible protein adsorption. With this analysis, we detect potential biases linked to experimental parameters, such as the choice of the technique or the type of protein solution used to study the protein corona, and to extract meaningful trends that could advance this field of research.

3.2 The classical approaches for understanding and quantifying the adsorption process

3.2.1 The nature of the adsorption phenomena

The adsorption of proteins (P) on a NP surface site (S) is a dynamic process, often described as a reversible process $P + S \leftrightarrow PS$ that eventually reaches equilibrium. The physical concepts used to describe protein adsorption on a NP surface are often borrowed from enzymology, biochemistry and surface chemistry, as the observed physical phenomenon is considered as similar. In the context of protein adsorption on NPs, the reversible reaction can be described via its kinetics constants (k_{on} and k_{off}) or its thermodynamic constants (K_A or K_D):

$$K_A = \frac{1}{K_D} = \frac{k_{on}}{k_{off}} = \frac{[PS]}{[P][S]} \quad (3.1)$$

where square brackets […] denote a concentration, K_A and K_D are the association and dissociation thermodynamic constants, respectively, while k_{on} is the second-order rate constant of binding and k_{off} the first-order rate constant of the desorption of the protein from the NP. Here, K_A is

expressed as M^{-1}, the kinetics constant k_{on} in $M^{-1}s^{-1}$ and k_{off} in s^{-1}. Subsequently, the Langmuir isotherm can be derived, which describes the surface coverage ratio θ of the NPs at equilibrium:

$$\theta = \frac{K_A[P]}{1+K_A[P]} \quad (3.2)$$

The Langmuir model, originally derived to describe gas adsorption on surfaces[132], is based on the assumptions that binding sites are finite and identical, that adsorbed molecules as well as free molecules do not interact with each other, and that only a monolayer of molecules is formed at the surface[133]. As protein adsorption on NPs is often not as simple or ideal, more elaborated models are required to describe the adsorption process more adequately. For instance, the Hill adsorption isotherm is based on the same laws of mass action as the Langmuir isotherm, but also considers that an integer number *n* of molecules can simultaneously occupy one adsorption site. This then leads to a modified Langmuir isotherm:

$$\theta = \frac{K_A[P]^n}{1+K_A[P]^n} \quad (3.3)$$

However, the Hill isotherm is only an approximation of cooperative adsorption as the model assumes that sites can only be either fully occupied or empty, but not partially occupied. As a consequence, the Hill factor *n* is now interpreted as an indication of cooperative ($n>1$) or anti-cooperative ($n<1$) binding that can take non-integer values[133, 134] and that yields the Langmuir isotherm when $n=1$. The Hill isotherm is now broadly used to characterize protein interaction with NPs and other objects[134].

In the context of multilayered protein adsorption, another modification of the Langmuir isotherm is used. The Brunauer-Emett-Teller (BET) model considers that the second and subsequent layers form at the top of the first layer with a different affinity $K_{A\text{-multi}}$ from the first layer[133]. Every layer still respects the Langmuir model individually which results in:

$$\theta = \frac{K_A[P]}{(1-K_{A-multi}[P])(1+(K_A-K_{A-multi})[P])}. \quad (3.4)$$

The latter expression diverges to infinity when [P] increases, thus indicating that the formation of multilayers does not lead to saturation. Along with the two previous isotherms (Equations 3.2-3.4) relies on the assumption that adsorption is a reversible process, as do most of the technique-

dependent models used to characterize the adsorption process of proteins on NPs. It is important to note that isotherms different from the three presented here may provide additional information to describe the association of protein-NPs systems but may also rely on different assumptions and parameters[133, 135].

3.2.2 The challenges related to quantifying protein adsorption onto NPs surfaces

Even though the adsorption of proteins on surfaces has been extensively studied on macroscopic surfaces, the complexity and difficulty to characterize this phenomenon dramatically increases when it comes to mixtures of proteins adsorbing onto nanoscopic surfaces. In 1962 Vroman reported that adsorption of proteins on macroscopic surfaces led to a peculiar phenomenon (later called the Vroman effect) where competition of proteins for a finite surface would lead to dynamic and static enrichment along with a displacement of different proteins[136]. Following reports confirmed this phenomenon, and it is now acknowledged that fast diffusive proteins adsorb first but are gradually replaced by slower proteins with a higher affinity to the surface[137]. As a result, in a biological fluid, composition, affinity, concentration and time are all relevant parameters that can influence the formation of the protein depot on macroscopic biomaterials, and could also by extension apply to nanomaterials[63, 138].

To quantify the adsorption of proteins on nanoscale surfaces, numerous methodologies have been developed to either measure the affinity of proteins for NPs or quantify the density of proteins on NPs surface, for example by measuring the change of NP radius in presence of a protein solution. These strategies often rely on the measurement of the NPs diffusion coefficient D, which is related to the hydrodynamic radius R_H by the Stoke-Einstein equation $R_H = k_B T/6\pi\eta D$ (where k_B is the Boltzmann constant, T the temperature and η the viscosity). An increase of R_H in a protein solution is attributed to the adsorption of proteins on the NPs. For example, the adsorption of a protein having an average diameter of 6 nm is expected to produce an increase of R_H on the order of 6 nm at full coverage. The increase in NP radius as a function of the number of adsorbed proteins N can be estimated by a simple relationship $R_H(N) =$

$R_0(1+\frac{V_P}{V_{NP}}N)^{1/3}$ with V_P/V_{NP} being the volume ratio of the proteins to the NP and R_0 being the initial NP radius. By substituting the the Hill adsorption isotherm in the previous equation, it is possible to establish the relationship between the change in NP radius and the affinity of the proteins to the NP surface that can be written as[118]:

$$R_H = R_0\left(1+\frac{\frac{V_P}{V_{NP}}N_{max}}{1+\left(\frac{K_D'}{[P]}\right)^n}\right)^{1/3} \quad (3.5)$$

where N_{max} is the maximum number of proteins per NP and K_D' the concentration at half coverage, which is also related to the thermodynamic dissociation constant as follows: $K_D = K_D'^{1/n}$, with *n* being the Hill factor. As many techniques are using this framework to study protein-NP interactions, it is crucial to understand the limitations of this approach. Since the measurement of R_H is key to derive both N_{max} and K_D, it is imperative to take great care in the measurement of R_H, as small errors may lead to large variations in the calculated parameters, this being more prominent for large NPs. Assuming that typical experimental errors on radius determination range from 1 to 10%[139], the maximum increase of R_H due to protein adsorption in Equation 3.5, *i.e.*, for a protein monolayer, the ratio $(R_H-R_0)/R_0$ at equilibrium (or $2R_{Protein}/R_0$), requires to be substantially larger than the relative error of the measurement. For instance, for adsorption of human serum albumin (HSA, $R_{Protein} \approx 3.5$ nm) on NPs of $R_0 = 100$ nm, the ratio $2R_{Protein}/R_0$ is 7%, which is not large enough if intrinsic variations in the NP size are of the order of 1-10%. On the other hand, for smaller NPs ($R_0 = 5$ nm) the same ratio would be in the range of 140%, which is far superior to any possible systematic variability of the measurement. As a result, the sensitivity of this approach is greater for small NPs than for large NPs, making small NPs more appropriate to investigate.

An alternative approach for the quantification of protein adsorption on NPs is based on the measurement of the mass of adsorbed proteins. Here, the total mass of adsorbed proteins is measured and the total surface area per unit volume $S_{NP}=\pi R_0^2 C_{NP}/m_{NP}$ is related to the radius of NPs, R_0, their mass concentration C_{NP} and the mass of one NP m_{NP}. Dividing the total mass by the total surface area gives the surface mass density of adsorbed proteins Γ (often expressed in

μg/cm²). By substituting $\theta = \Gamma / \Gamma_{max}$ into one of the previously described isotherms and evaluating Γ at equilibrium for different concentrations of proteins, the equilibrium constant K_A and Γ_{max} can be derived. It is also possible to estimate Γ_{max} from known parameters. From the assumption that the protein is a sphere that occupies an area $S_p = \pi R_{Protein}^2$ on the NPs surface and from geometric considerations, the theoretical value of Γ_{max} for a monolayer of proteins is then:

$$\Gamma_{max} = \frac{MW\ (R_0 + R_{Protein})^2}{S_p\ {R_0}^2\ N_A} p \qquad (3.6)$$

where N_A is the Avogadro number, *MW* the molecular weight of the protein and *p* the packing parameter (from 0.78 to 0.91 for square or hexagonal packing). The number of proteins on NPs, the packing density and the presence of mono-or multilayers can also be determined. However, it is important to estimate the possible error on the quantification of Γ_{max}. Small errors on the NP size and the protein radius have a large impact on Γ_{max} as both parameters are to the power two in Equation 3.6. Moreover, the assumption that the projected area of the protein S_p is a circle may not be accurate for structures deviating from a sphere (*e.g.* rod-like[140], prolate ellipsoid[141], triangular prism[66]). Such error analysis has been reported for polyethylene glycol (PEG) surface coverage and layer thickness measurements and we recommend this literature to the reader for further details[142].

3.3 How to quantify protein adsorption on nanoparticles?

3.3.1 *Ex situ* quantification methods

The methods to quantify proteins adsorbed onto NPs can be classified as *ex situ* or *in situ*, depending on whether the technique requires physical separation of the protein solution surrounding the NPs or if the measurement can be performed directly in the suspension. *Ex situ* techniques usually require one extra preparation step, often called purification of the NPs. Reviews or studies dealing with the efficiency, advantages or caveats of various NPs purification methods already exist and contain further details[61, 120, 131, 143]. Magnetic isolation and centrifugation can specifically isolate magnetic NPs and NPs denser than proteins, respectively. Gel filtration and asymmetric flow field-flow filtration (AF4) are based on size separation, while

capillary electrophoresis depends on the charge-to-mass ratio. It has been shown that the NPs purification method can impact the protein corona, specifically the amount of weakly adsorbed proteins. Harsh purification methods such as centrifugation have been shown to alter the corona composition compared to more gentle techniques such as AF4[120]. Therefore, *ex situ* measurements of protein adsorption are often regarded as adequate for the hard corona, while removing the soft corona (or multilayers). Furthermore, the time to achieve purification can significantly impact the composition of the protein corona, making time-resolved measurements of the protein corona even more challenging[61].

UV-vis spectroscopy-based methods

UV-vis spectroscopy is one of the techniques that has been used to study protein adsorption on NPs. Two main approaches can be found in the literature: quantification of adsorbed or free protein concentration, and localized surface plasmon resonance (LSPR) in the case of metallic NPs.

The quantification of adsorbed or free protein concentrations can be achieved in two distinct ways, one from the intrinsic UV signature of proteins and the other from a chemical reaction with proteins (*e.g.* bicinchoninic acid assay - BCA, or Coomassie). For both techniques, separation of the NPs-proteins complexes from free proteins is mandatory, quantification of proteins bound to NPs being either direct or indirect (*i.e.*, dosing proteins remaining in solution) as shown in Figure 3.1A and B. Adsorption isotherms can be constructed for a given protein-NP system by preparing samples with different protein concentrations.

Absorbance readout at 280 nm (due to the aromatic sidechains of tryptophan and tyrosine, as well as disulfide bridges between cysteine residues)[144] is often used to quantify protein adsorption. For example, Kumar *et al.* studied the adsorption of lysozyme on silica NPs using this approach (Figure 3.1A)[145]. According to their results, at saturation conditions, 90 and 270 lysozyme molecules were adsorbed per silica NPs with R_H equal to 8 and 12.5 nm, respectively. As shown in Figure 3.1A, increasing the protein concentration over 0.1 wt % decreased the adsorption considerably. This behavior was explained by the aggregation of NPs observed by

small-angle neutron scattering (SANS). Using the same UV-based approach, differences between the adsorption of cationic lysozyme and anionic bovine serum albumin (BSA) proteins on anionic silica NPs were also observed[146]. While lysozyme adsorbed strongly on NPs and both the Γ_{max} and K_A displayed particle size dependence, BSA failed to adsorb, owing to the electrostatic repulsion between anionic proteins and silica NPs. Using the same measurement approach, the authors also investigated the effects of salt concentration[141] and pH[147] on the same NPs-proteins systems.

The presence of other types of molecules that adsorb at the same wavelength could interfere with the determination method. In that regard, the BCA assay may be of interest (Figure 3.1B). The BCA assay relies on two chemical reactions: first Cu^{2+} reduction into into Cu^{+} by the peptide bonds followed by the chelation of Cu^{+} by the bicinchoninic acid, resulting in a complex strongly absorbing in the visible range. The BCA assay measures the number of peptide bonds and thus the number of proteins[148]. Several alternatives to the bicinchoninic acid exist; they exploit different absorption wavelengths, reaction mechanisms and incubation times.

The fast and efficient approach of the BCA assay has been used to various ends, similarly to the standard UV protein quantification. For instance, Walkey *et al.* used the BCA assay to study the effect of gold NPs (AuNPs) size and PEG grafting density on serum proteins adsorption[109], whereas Eren *et al.* investigated the affinity of lysozyme for silica NPs via an adsorption isotherm[149]. Its scalability was highlighted by a more recent example where Walkey *et al.* characterized the adsorption of serum proteins using the BCA assay for a library of 105 surface-modified AuNPs featuring three NP sizes and a variety of surface properties[58]. The authors isolated the bound proteins and quantified them for each type of NP of their library. Based on their experiments, an algorithm was developped to determine the predicting factors for NP-cell association from a large pool of parameters. However, BCA assays can only generate information regarding the total amount of adsorbed proteins (*e.g.* equivalent BSA), independently of the type of protein. This limited information may explain the rather weak correlation with NP-cell association. In another study, Mohammad-Beigi *et al.* used an elegant approach based on the BCA assay to quantify the serum-induced hard and soft coronas on silica and polystyrene NPs[150]. After isolating the hard corona, the authors used click chemistry to trap softly bound proteins

upon a second exposure to serum. Despite the potential errors arising from this approach, by coupling this analysis to mass spectrometry, the authors concluded that the surface was not oversaturated with proteins, hence suggesting that both the hard and the soft coronas are directly interacting with the surface of the NP, and not in a layered structure. Other examples for the applications of the BCA assay can be found elsewhere[151-153].

The second approach to quantify protein adsorption with UV-vis spectroscopy involves monitoring the signal of NPs, rather than the proteins' one. In the case of metallic NPs, their localized surface plasmon resonance (LSPR) signal could reveal information regarding protein adsorption. LSPR arises from the collective oscillation of the conduction electrons across metallic NPs upon exposure to light[154]. This phenomenon leads to an absorbance spectrum characterized by a resonance peak located at a characteristic wavelength. When metallic NPs are exposed to a protein solution, this LSPR band is typically expected to shift in the red spectrum due to the change in the refractive index of the NPs-proteins complex. The extent of the shift can be related to the amount of adsorbed proteins.

Piella *et al.* used this method to study the formation of the protein corona on citrate-stabilized AuNPs (3.5-150 nm) in cell culture medium supplemented with fetal bovine serum (CCM-FBS)[117]. By monitoring the LSPR shift over time, they observed changes up to 48 hours until reaching a plateau. The smaller the size of NPs, the sooner the LSPR band reaches the plateau. Of interest for the scope of this review, the largest redshift was observed for the smallest particles, but it was not correlated to a higher protein adsorption (as demonstrated by DLS measurements), as the extent of the redshift also depends on other factors such as the NP size and adsorbed macromolecules composition/chain length [117, 155]. These observations highlight that the interpretation of the LSPR is non trivial; however such a high sensitivity could be exploited to fine tune the application of NPs to target quantitatively and qualitatively protein-specific bonds. Interestingly, the LSPR method is also sensitive to aggregation that translates into a significant redshift and broadening of the LSPR peak, *e.g.* from ~520 to ~650 nm[156], an asset to test metallic NP stability before studying protein corona formation[117]. However, this method is not comprehensive for studying aggregation and complementary techniques such as small-angle

neutron scattering (SANS) could provide more details such as the fractal structure of aggregates, building block size and effective particle radius[145].

Fluorescence spectroscopy

Fluorescence spectroscopy uses a beam of light that excites the electrons of the analytes, which results in the emission of photons with a longer wavelength (due to the energy loss through molecular vibrations) while returning to the ground state. Accordingly, quantifying the intensity of emission allows to obtain the concentration of analytes[157]. Researchers have used fluorescence spectroscopy to quantify and investigate adsorption of proteins to different surfaces, including NPs[158, 159]. In proteins, three aromatic amino acids (phenylalanine, tyrosine, and tryptophan) are intrinsically fluorescent. However, they are rather not so abundant in proteins making the protein structure only weakly fluorescent[157]. Thus, in most protein adsorption studies using this technique, researchers have conjugated proteins with fluorescent tags[160].

Similar to UV-vis spectroscopy, in order to calculate the number of adsorbed proteins on NPs, fluorescence spectroscopy can also indirectly quantify the amount of bound proteins from subtracting the measured free protein concentration it from the total protein concentration (Figure 3.1C). Indeed, this straightforward approach is a valuable asset for a routine analysis of nanomaterials interaction with proteins, as shown by Rabanel *et al.*[24], though it suffers from similar drawbacks as UV-vis spectroscopy with additional requirements (*e.g.* linking a fluorescent tag). To avoid the need of separation prior to the analysis, environment-sensitive fluorophores can also be used, so that free proteins are distinguishable *in situ* from adsorbed ones. For instance, Welsch *et al.* studied the adsorption of fluorescein-conjugated proteins to polystyrene-poly(*N*-isopropylacrylamide) microgels[161]. Fluorescein shows a pH-dependent emission, which made the quantification possible *in situ*. Indeed fluorescent emission would decrease upon the adsorption of proteins, due to a lower pH in the microgel network (and also to self-quenching as a result of the increased local fluorescein concentration), Accordingly, the amount of unbound proteins was quantified by adding the microgels to the protein samples and measuring the

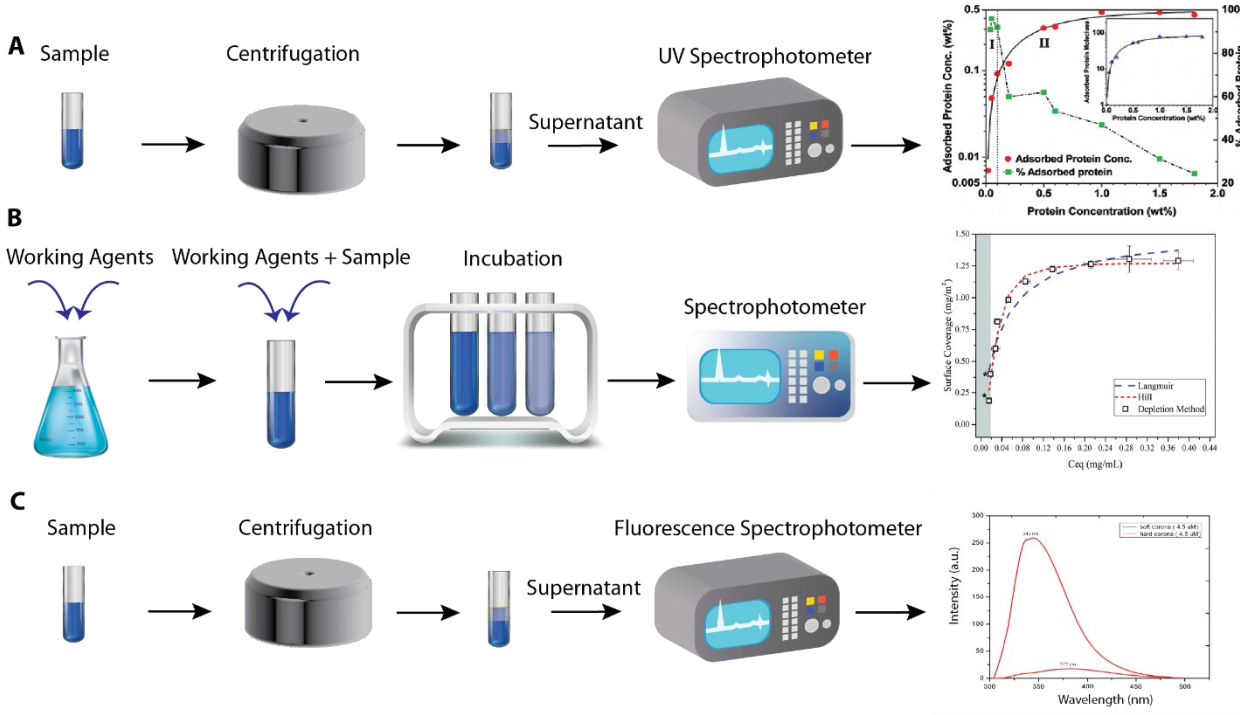

Figure 3.1. Spectroscopy-based procedures to investigate the adsorption of proteins on NPs. (A) UV-vis spectroscopy to obtain the adsorption isotherm of lysozyme proteins on silica NPs (16 nm). (B) BCA assay to study the adsorption of serum proteins on AuNPs. (C) BSA protein corona on silver NPs analyzed by a fluorescence spectrophotometer. Graphs in panels A, B and C were adapted with permission from [145, 109] and [162] respectively.

remaining fluorescence intensity, that is related to the concentration of free proteins. The authors also used fluorescence spectroscopy to study the dynamics of competitive protein adsorption to soft polymeric layers surrounding NPs[161]. By adding an equimolar amount of unlabeled lysozyme to the microgel particles loaded with labeled lysozyme, they were able to detect a sharp increase in the fluorescence intensity over time, indicating the desorption of labeled proteins from the microgels, and thus the reversibility of lysozyme adsorption. Moreover, competitive adsorption experiments were performed, adding either cytochrome c or b-D-glucosidase to the microgel particles loaded with labeled lysozyme. Subsequently, adding b-D-glucosidase proteins resulted in a stronger fluorescence response from further increasing the

lysozyme desorption, which the authors interpreted as an indication of its higher affinity towards the microgel surface.

Two other fluorescence spectroscopy-based techniques, namely fluorescence correlation spectroscopy (FCS) and fluorescence quenching, have been widely used by researchers for protein adsorption studies. These techniques provide additional insight regarding the protein corona and are discussed in more details in further sections.

Mass spectrometry-based proteomics

Mass spectrometry techniques (MS) are now recognized as a pillar of pharmaceutics and proteomics analysis. Their sensitivity and selectivity coupled with liquid chromatography (LC) make it a powerhouse to identify and quantify molecules, peptides and proteins in biological samples. Liquid chromatography tandem mass spectrometry (LC-MS/MS) is commonly used to identify proteins in different matrices.

In a typical proteomic analysis, proteins are digested using trypsin, which breaks them into smaller peptides. The resulting solution is injected through an eluent into a LC-MS/MS over several hours to separate the different peptides produced from the protein digestion. The peptides are separated in a chromatographic column, then ionized, typically through electrospray ionization (ESI). The first quadrupole (Q1) selects the ionized parent compounds; the collision cell (Q2) fragments them and the third quadrupole (Q3) detects them by mass/charge ratio, m/z. The resulting m/z spectrum of the mixture of peptides is matched through databases, where a deconvolution of the spectrum is performed to obtain the relative abundance of proteins. This relative abundance or “normalized spectral abundance factor” (*NSAF*) is given by:

$$NSAF_k = \frac{\frac{SpC_k}{MW_k}}{\sum_{i=1}^{n}(\frac{SpC_i}{MW_i})} \tag{3.7}$$

where SpC_k is the spectral count of the protein *k* of molecular weight *MW*, which is compared to the total of detected proteins *i*. Statistical analysis must be performed to assess the reliability and sensitivity of the analysis and the identified proteins.

To assess the protein corona composition, a few sample preparation steps must be performed prior to protein digestion (Figure 3.2A). Unbound proteins must be removed as this technique is not suited for *in situ* analysis of the protein corona. Any contaminant's trace influences the *NSAF* and leads to erroneous identification of proteins in the protein corona. Therefore, a thorough purification process must be developed to ensure that identified proteins only come from the isolated protein corona. However, as mentioned by many authors[61, 63, 120, 121], this process very likely removes weakly bound proteins and hinders testing for the so-called soft corona or multiple layers. Moreover, the amount of proteins adsorbed on NPs cannot be calculated as the analysis only provides a relative abundance of the proteins on the surface of the NPs. This inability to quantify the total amount of proteins adsorbed makes this method inadequate for distinguishing between mono- or multilayers.

Despite these limitations, this technique has proven quite powerful to analyze the composition of the protein corona. It led for instance to the identification of 60+ proteins in the corona of surface-functionalized polystyrene (PS) NPs, in a study by Lundqvist *et al*.[107] The authors identified few proteins whose presence in the corona was independent of the surface functionalization of the NPs. In fact, the protein corona composition of small NPs had more in common with their equivalent-size counterparts, despite a different surface functionalization, than with large NPs with the same surface functionalization[107]. Tenzer *et al.* also furthered these studies by following the adsorption of 125 proteins on silica NPs of different sizes, ranging from R_H=4 to 62 nm[108]. In this study, the authors did not find any correlation with surface charge, although all their NPs were negatively charged. It was observed, however, that different NPs sizes would result in slightly modified protein corona compositions, even with differences in particle size as small as 5 nm in radius. Unfortunately, no correlation was found for any type of protein enriched or depleted with increasing NPs size. The effect was also reproduced on PEGylated gold nanorods and nanostars by García-Álvarez *et al.*[163] Both rods and stars had a distinctive corona

composition with a significant amount of proteins that were not shared among them, changing according their size and shape. For instance, 20 nm radius gold stars adsorbed much more proteins with MW < 20 kDa and had a higher protein diversity than gold rods. However, the behaviour was reversed for larger radius (70 nm), gold rods were the ones with more different types of proteins.

To rule out the impact of the purification procedure over these findings, Monopoli *et al.* showed that centrifugation, size exclusion chromatography and magnetic isolation were all valid methods that resulted in similar protein coronas[143]. However, other soft methods of purification such as asymmetric flow field flow fractionation (AF4) have been producing significantly different protein maps of the protein corona when compared to centrifugation[120], at odds with the previous study. Clusterin and Apo-A1 (both apolipoproteins) were found at much higher ratio in the protein corona after purification by centrifugation (30 and 11%) rather than AF4 (< 1%). Though, discrepancies in the presence of Apo-A1 in the protein corona of NPs have been observed in key studies using mass spectrometry to identify the composition of the protein corona. Indeed, it is usually thought that Apo-A1 is enriched on hydrophilic NPs[65, 109, 164] and positively charged NPs[63, 164]. However, reports showed the opposite trend for hydrophilicity with microgel particles of N-isopropylacrylamide/N-tert-butylacrylamide (NIPAM/BAM) particles[127] and for positive charge with functionalized PS NPs[65]. These discrepancies highlight the difficulty in untangling rationales in a multiparametric problem such as protein adsorption. Nonetheless, clever approaches exist to evidence both the enrichment of proteins and its biological importance. For example, Bertrand *et al*. correlated the pharmacokinetics of NPs to the composition of their protein corona by changing their surface hydrophilicity[111]. Indeed, the authors observed that hydrophobic NPs were preferentially enriched with ApoE, and then further demonstrated that this enrichment would slow down clearance in comparison to a ApoE knockout mouse model. Similar observations were also made for clusterin, both are known to decrease phagocytic recognition, further confirming their biological relevance in the protein corona.

Even if the identification of proteins by mass spectrometry does not provide any critical information regarding the quantity of proteins adsorbed per NP or the presence of multilayers,

the time evolution of the ratio of proteins adsorbed on NPs provides information on the dynamics of the protein corona (Figure 3.2B). Indeed, using fast purification methods of the proteins-NPs complexes (< 0.5 min), several studies have converged towards the same phenomenological adsorption mechanism[63, 64, 165]. Initially, proteins adsorb very quickly on NPs. The total mass of adsorbed proteins then remains constant, whereas the ratio of adsorbed proteins significantly changes over time, a typical signature of the Vroman effect, where groups of proteins could adsorb preferentially compared to others. The Vroman effect was reported to occur for periods longer than 7 days, as equilibrium was still not reached[64]. Interestingly, within the time frame of these experiments, almost all proteins detected within the first minutes were also found at the end of the experiment, hours later. This observation derived from mass-spectrometry proteomics experiments led to the term “fingerprint” of the protein corona, which conveys the idea that the protein corona initially formed on NPs represents its biological identity. This novel concept propelled protein corona research into the diagnostic field, where the identification of groups of proteins in the corona could lead to the early identification and monitoring of chronic diseases and cancer[126].

From this emergent idea of the protein corona fingerprint, its impact on cellular uptake or interaction was also greatly studied through mass spectrometry-based proteomics. Early studies showed that differences in the protein corona composition could result in significant shifts in NPs-cells interactions and cellular uptake[166], even in the case of small changes induced by protein deglycosylation[167]. More recent studies however focused on predicting the biological interactions based on the identification of the protein corona. Through a bioinformatics-based modeling of the NP-cell interaction, Walkey *et al*. showed that the protein fingerprint of the NPs measured by mass-spectrometry, and more specifically “some proteins”, were more predictive for NP-cell interaction[58]. Ritz *et al*. later confirmed this trend through the identification of 20 proteins that were positively or negatively correlated with cellular uptake[59]. Naturally, cellular uptake was found to increase when NPs were covered with some positively correlated proteins (ApoH) prior to cell exposition, and to decrease in the case of negatively correlated ones (ApoA4 and ApoC3). Interestingly, protein coronas were also found for viruses, notably the tobacco

mosaic virus (TMV), whose corona was dominated by complement proteins and immunoglobulins[168]. It could be indeed very interesting to see if the disruptive effect of the protein corona over biological interactions of nanomedicines is translated to the interaction of viruses with their host.

It is important to consider that even though MS-based proteomics is an extremely sensitive technique, reproducibility is a known challenge in the field. It depends on the apparatus used, user control, sample preparation and analytical method[169-171]. Reproducibility in the identification of a protein in proteomics studies can oscillate between 35 and 60%[169], which impacts mostly the identification of peptides (or proteins) of low abundance and the accuracy of the quantification of more abundant peptides (or proteins). These variations are being tackled by a large effort to improve MS reproducibility across studies, which aims to reduce the impact of human errors by harmonizing protocols intra- and inter-laboratories[169, 172-175]. In order to identify new biomarkers of diseases within the protein corona of NPs, one study demonstrated that automation of the workflow and optimization of the purification protocol allowed to achieve 22% coefficient of variation for 2000 proteins detected [171].

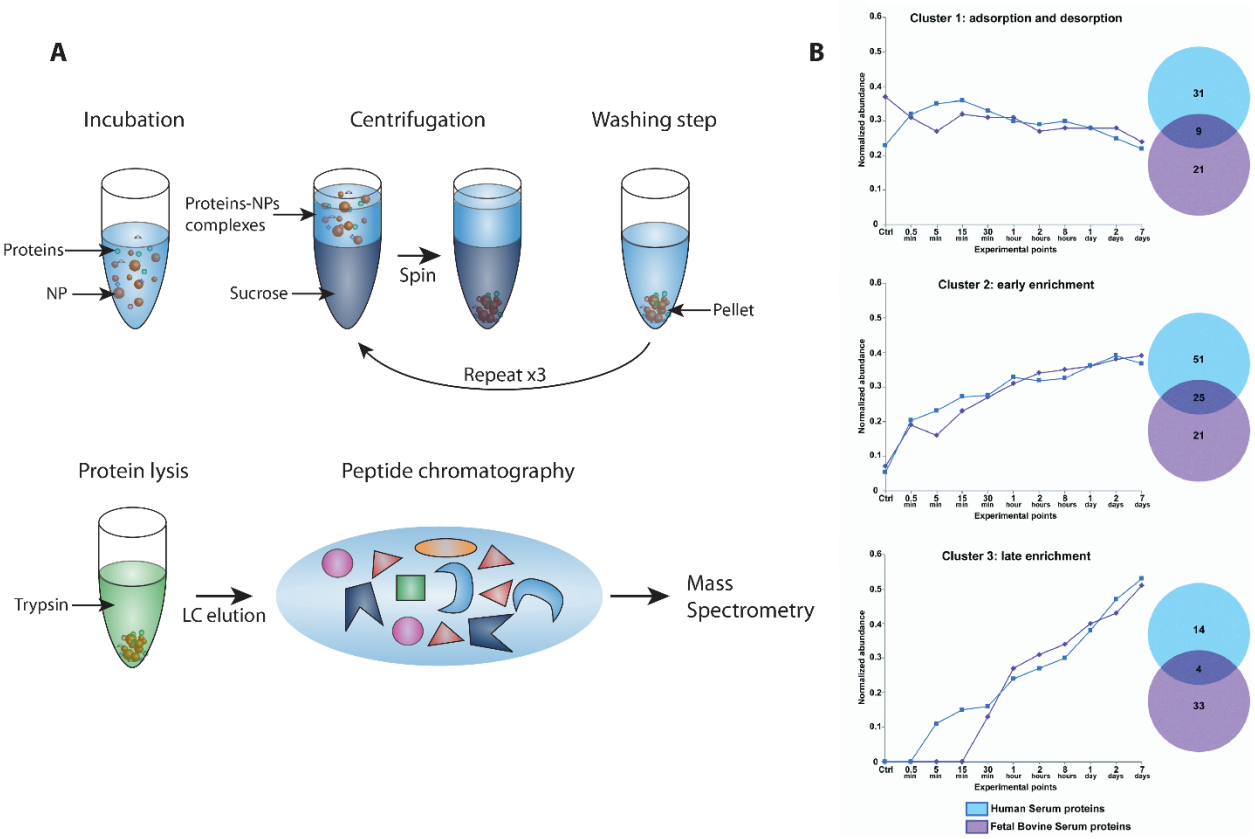

Figure 3.2. Mass spectrometry-based proteomics procedure for the quantitative study of the protein corona. (A) Representation of the extensive purification process required for proteomics studies of the protein corona and the preparation steps before the mass spectrometry analysis. The sequence starts by incubating proteins and NPs. Then, the resulting NPs-proteins complexes are purified with 3 consecutive centrifugations over a sucrose cushion. Proteins in the pellet are digested with trypsin, eluted on a chromatographic apparatus and then analysed by mass spectrometry. (B) Representation of the dynamic composition of the protein corona as observed from time-resolved mass spectrometry studies for different behaviors. Panel B was adapted with permission from [64].

Thermogravimetric analysis

Thermogravimetric analysis (TGA) measures the time evolution of a sample mass during a controlled temperature program. The set-up consists of a precise micro-balance connected to a pan inside a closed furnace with a controlled atmosphere (Figure 3.3A). TGA provides information about a variety of physical transformations (phase transitions, absorption, desorption) or chemical transformations (thermal decomposition, solid-gas reactions). Information on sample composition can be derived from the weight loss in a certain temperature range[176].

TGA enables to extract the total amount of adsorbed proteins by comparing TGA data obtained for protein-coated NPs to native NPs. Any additional weight loss observed with protein-coated NPs above 100-150°C (to discard the weight loss due to adsorbed water)[177, 178] and below the evaporation temperature of NPs is attributed to the thermal decomposition of adsorbed proteins and is therefore used to calculate the total mass of the protein corona (Figure 3.3B). This technique has been used in a study using magnetic NPs, where the additional weight loss observed from 200 to 330°C for NPs pre-incubated with serum was attributed to adsorbed proteins[177]. Quantitative characterization of adsorbed proteins onto silica NPs after exposure to supplemented culture medium has also been achieved using TGA[179]. From TGA measurements performed using pure BSA, the authors determined that the mass loss from 100 to 550°C corresponded to adsorbed proteins. The TGA technique has been used in a variety of other studies, to quantify adsorbed proteins for different surface chemistries and various types of NPs such as magnetic NPs[178, 180], mesoporous silica NPs[181, 182] and even graphene oxide[183].

To obtain finer details of the composition of the protein corona, combination of TGA data to LC-MS/MS analysis can be performed, using the following equation:[184, 185]

$$W_k = NSAF_k \times W_{tot} \quad (3.8)$$

where W_k is the amount of an individual protein *k* adsorbed per amount of particles, typically in µg mg^{-1}, $NSAF_k$ the normalized spectral abundance factor for protein *k* taken from LC-MS/MS analysis, and W_{tot} the total amount of proteins adsorbed onto the particles as determined by TGA. This allows to identify composition trends in the protein corona (Figure 3.3C).

TGA is a rather straightforward technique to quantify the protein corona of NPs. Although the separation of the NPs from the medium is required, complex media containing a mixture of proteins can be used. Small amounts of material are theoretically required (> 5 µg of dry NPs for most recent setups), but sensitivity can be limited by the fact that adsorbed proteins may represent a very small amount of the total weight of NPs. Weight loss attribution after exposure to biological media may also be more complicated than assumed, as other molecules can adsorb to NPs (*e.g.* the "metabolite corona")[186] and NPs can experience different degradation processes, such as ligand exchange[187].

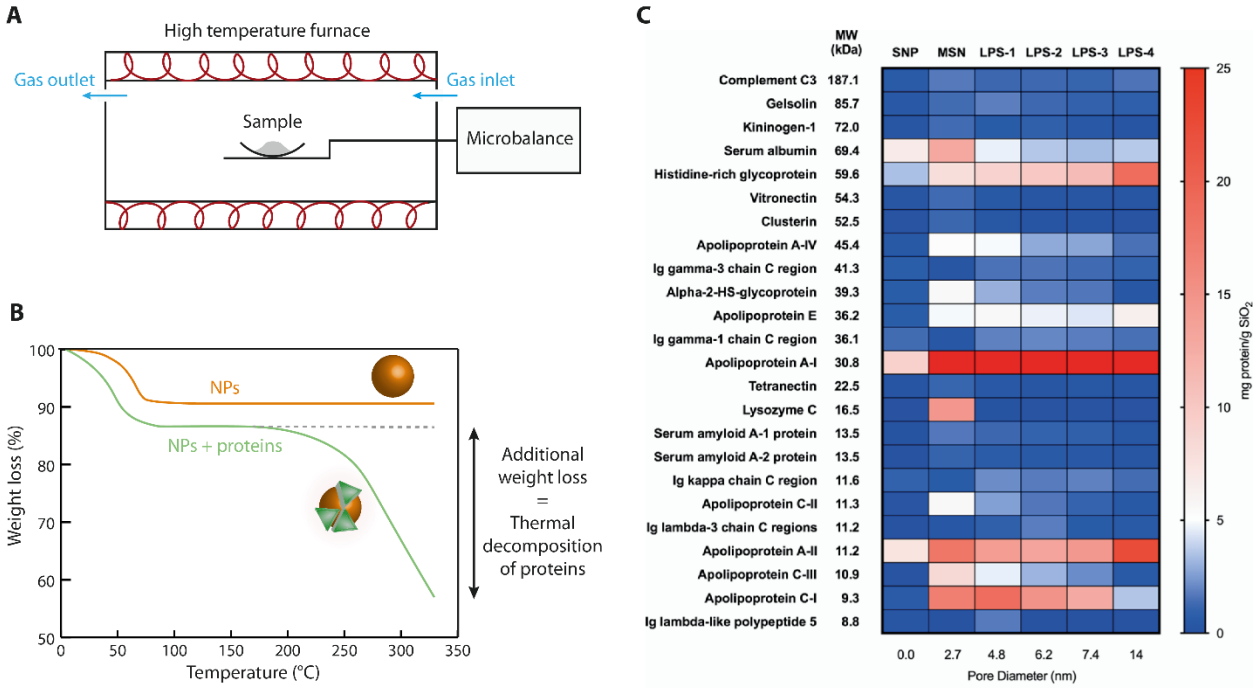

Figure 3.3. TGA to quantify the protein corona. (A) Schematic of a typical setup used in TGA. (B) Example of weight loss as a function of temperature for protein-coated NPs and native ones. The additional weight loss above 100-150°C is attributed to adsorbed proteins. (C) Quantification of individual proteins as a function of pore diameter of silica NPs, obtained by combining TGA data with LC-MS/MS analysis. Panel C was adapted with permission from [185].

Analytical ultracentrifugation

Analytical ultracentrifugation (AUC) is a powerful label-free technique to characterize small NPs. As correlation-based techniques, AUC can assess the protein corona on NPs of size equivalent to proteins. The principle of the technique is to expose particles to a centrifugal force – ranging from few g's to a million times gravity – which will induce separation of the particles from the proteins solution based on their difference in mass and density. Thus, AUC is mainly used with metallic NPs, which have a significantly higher density than proteins. When submitted to high centrifugal forces, particles are subjected to an accelerated sedimentation rate proportional to the difference between the mass and the buoyancy of the NP, and inversely proportional to its hydrodynamic radius[188]. Therefore, measurement of differences in hydrodynamic radius allows to obtain the protein corona thickness. The main physical parameter obtained from AUC and used to determine the particles' hydrodynamic radius is the radial concentration distribution (Figure 3.4B). The sample is injected in different cells (sample and reference) equipped with a detection window designed for the determination of the concentration distribution as a function of the radial distance from the point of injection (Figure 3.4A). The concentration distributions are acquired at time intervals ranging from minutes to hours through different detection systems. Three optical techniques are commercially available with AUC: UV absorbance, optical interference and fluorescence emission, depending on the particles and proteins used[78]. The sensitivity of these detectors to scattering and turbidity explains why AUC is mainly used for small NPs. Two different modes of experiments can be performed: sedimentation velocity or sedimentation equilibrium[78, 188, 189]. The first mode operates at high centrifugal speed for a few minutes. Size, shape or shell thickness can then be extracted using hydrodynamic theory. The second is used to determine molecular weight, stoichiometry and dissociation constants at very low centrifugal force in order to maintain the equilibrium between the centrifugal force and Brownian diffusion[188].

Assuming that the NPs are not aggregated, AUC allows to determine the concentration distribution of the sample as a function of time and distance from the rotor center, $c(t, r)$. This

concentration distribution is then used to obtain sedimentation (*s*, in seconds) (Figure 3.4C) and diffusion coefficients (*D,* in $m^2\ s^{-1}$) using Lamm equation: [78]

$$\frac{\partial c}{\partial t} = D\left(\frac{\partial^2 c}{\partial r^2} + \frac{1}{r}\frac{\partial c}{\partial r}\right) - s\omega^2\left(r\frac{\partial c}{\partial r} + 2c\right) \quad (3.9)$$

where ω is the angular velocity (in s^{-1}), and both *D* and *s* coefficients can be determined numerically. This equation serves as a basis to generate models that require the accurate knowledge of molecular weight and extinction coefficients of both particles and proteins in the specific case of protein adsorption on NPs. Bekdemir *et al.* developed for instance a Hill-Langmuir adsorption model (derived from Equations 3.3 and 3.5) where the sedimentation coefficient is expressed as a function of K_D, N_{max} and *n*:[78, 190]

$$s(C_{NP}) = \frac{2}{9\,\eta_S}\sqrt[3]{\frac{9}{16\pi^2}}\ \frac{(\rho_{NP}-\rho_S)\,V_{NP} + N_{max}\frac{2}{1+\left(\frac{K_D}{C_{NP}}\right)^n}(\rho_P-\rho_S)\,V_P}{\left(V_{NP} + N_{max}\frac{1}{1+\left(\frac{K_D}{C_{NP}}\right)^n}V_P\right)} \quad (3.10)$$

where C_{NP} is the concentration of NPs, η_S and ρ_S are the viscosity and density of the solvent, respectively, and ρ_{NP}, V_{NP} and ρ_P, V_P are the density and volume of NPs or proteins (P). Then, it is possible to numerically solve Equation 3.9 using the experimental distribution concentration function $c(t, r)$ to obtain the sedimentation coefficients. Plotting these sedimentation coefficients as a function of protein concentration (Figure 3.4D) yields the adsorption isotherm where N_{max} is extracted by fitting with Equation 3.10. This method to quantify adsorbed proteins is not restricted to one type of AUC detection and can be generalized to other detectors[78, 190, 191].

As previously mentioned, AUC has been used to quantify the protein corona at the surface of NPs and to assess the stealth properties of coated NPs in protein solutions. Spherical AuNPs between 1.6 and 3.3 nm in radius were coated with a mixture of hydrophilic polymeric coating (mercaptoundecane sulfonate, MUS) and hydrophobic ligand (octanethiol, OT) designed to modulate protein adsorption[190]. Measurements of N_{max} from AUC ranged from 4 to 7 HSA proteins/NP for NPs with a hydrophilic coating (MUS:OT ratio of 8:1) with a linear relation to AuNPs surface area. On the other hand, the slightly hydrophilic coating (MUS:OT ratio of 2:1) had

no linear impact relative to the AuNPs surface area on N_{max}. The authors suggested that this non-linearity emerged from a non-homogeneous shell of hydrophobic and hydrophilic ligands arranged in a patchy distribution. A subsequent study confirmed these results by showing that 7 nm MUS-coated AuNPs had similar N_{max} values with BSA and HSA[78]. Citrate-coated AuNPs showed a different behavior with N_{max} value of 36 BSA proteins adsorbed on 12.6 nm AuNPs.

Using interference AUC, Schaefer *et al.* showed that CeO_2 NPs exhibited different values of N_{max} with BSA proteins, depending on the composition of the NPs[191]. When lithium was detected in the CeO_2 NP of 5.8 nm in radius, N_{max} increased from 13 (without lithium) to 35 equivalent proteins per NP (assuming an average M_W=100 kDa for proteins). The authors also showed that protein adsorption does not occur with negatively charged SiO_2 NPs. This was also pinpointed by Bekdemir *et al.* with 5 nm ethylene glycol-coated AuNPs, which did not exhibit any protein corona formation in HSA solution[190]. The authors also showed that protein adsorption does not occur with negatively charged SiO_2 NPs.

As demonstrated in all these studies, AUC is a promising tool to characterize the protein corona on small metallic NPs using label-free proteins, but some limitations remain, as listed in Table 3.1. The accurate knowledge of the NPs and proteins parameters (density and volume) are mandatory to extract quantitative information. Also, AUC is more suited to characterize high density materials such as metallic NPs, as highlighted by Equation 3.10, where a large density difference between water and the proteins or the NPs is preferable to achieve higher resolution on the measurement.

Differential centrifugal sedimentation

Differential centrifugal sedimentation (DCS) shares numerous similarities to AUC since it takes advantage of the centrifugal force to assess the protein corona. The principle of the method is to expose NPs suspensions to small centrifugal forces (few g's force) to induce the slow sedimentation of particles in a medium with a viscosity gradient (Figure 3.4E). A spectroscopic detector is used to quantify particles' concentration profile (Figure 3.4F). The main parameter

obtained from DCS measurement is the sedimentation time, t_s. It is related to the spherical particles' hydrodynamic radius through:

$$t_s = \frac{B}{4\left(\rho_{eff,\,NP} - \rho_g\right) R_H^{\,2}} \tag{3.11}$$

where $\rho_{eff,NP}$ is the effective density of NPs-proteins complexes, ρ_g is the average density of the viscosity gradient, and B a constant calculated from solution viscosity and cell geometry. Note that it is possible to analyze particles with a shape other than spherical by using the equivalent radius approximation. The effective particle density is required to solve Equation 3.11 and its value can be challenging and time-consuming to find, due to the presence of the protein corona. One simple approximation is to consider the effective NP density as the density of the core NP, knowing that the density of the corona is very low compared to the core. A more accurate approach is to use a core-shell model where the NPs-proteins complexes effective density is decomposed between a core and a shell of thickness δ:[192]

$$\rho_{eff,\,NP} = \frac{8R_0^{\,3}\rho_{NP} + \left((2R_0+2\delta)^3 - 8R_0^{\,3}\right)\rho_P}{(2R_0+2\delta)^3} \tag{3.12}$$

Additionally, the shell thickness of NPs functionalized with ligands can be studied by decomposing $\rho_{eff,\,NP}$ between a core, a ligands' shell and a proteins' shell adsorbed on top of the first ligands layer. Davidson *et al.* showed that the main uncertainty in the calculation of δ is the protein corona density value (ρ_P)[192]. Indeed, a protein corona is not homogeneously packed around NPs due to solvent hydration, the proportion of which may vary depending on the proteins' hydrophobicity. In response to this issue, the authors used a shell density value of 1.15 g/cm^3 for BSA protein corona, assuming a water content of 70%. Ultimately, the mass of proteins on NPs could be deduced from the protein corona thickness.

DCS quantification of the protein corona thickness and adsorbed mass has been performed on a large variety of NPs materials such as PS[112], Au[192, 193], Ag[193] and silica NPs[112, 138, 193]. Wang *et al*. showed that DCS can quantify protein adsorption on mixtures of NPs of different sizes (Figure 3.4G)[193]. The authors measured the protein corona thickness of six AuNPs ranging from 10 to 50 nm in radius. Very weak BSA adsorption was detected for all AuNPs at concentrations below 10$^-$

^{8} M (δ < 1 nm). By increasing BSA concentration up to 10^{-3} M, AuNPs from 10 to 30 nm showed a shell thickness between 3 and 4 nm, while it reached 10 nm for larger AuNPs of 40 and 50 nm, therefore highlighting the impact of NP size. Walczyk *et al.* observed a similar trend for PS-COOH NPs incubated in human blood plasma, with thicknesses of 6.6 nm and 10.6 nm for silica NPs of 25 nm and 50 nm radius, respectively[112]. Davidson *et al.* used DCS to study the influence of surface chemistry. They showed that 5.5 nm citrate-stabilized and carboxylic acid-polyethylene glycol (PEG-COOH)-functionalized AuNPs exhibited similar δ values as bare AuNPs[192]. Interestingly, the authors observed that AuNPs coated with inert PEG did not exhibit any protein corona formation, which agrees with studies on stealth properties of PEG layer[193].

DCS is a powerful tool for protein corona studies in complex biological media, since it does not require any labeling of the proteins nor the NPs. Unlike AUC, polymeric NPs with low density can be studied by DCS in presence of proteins solution. Major advantages of DCS are the ability to filter out NPs aggregates from the measurements and to have a high enough resolution to quantify the protein corona in a mixture of NPs of different sizes. DCS has also limitations (listed in Table 3.1), the main one being the necessity to determine the protein corona density and hydration shell layer thickness.

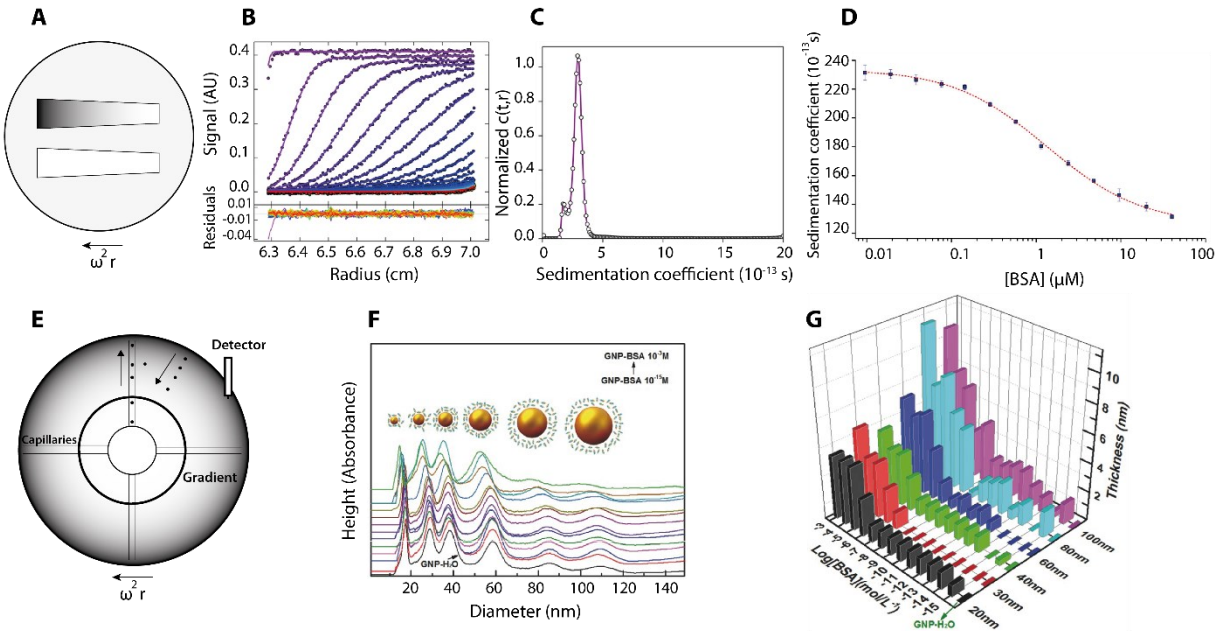

Figure 3.4. NP radius characterization using centrifugal force techniques. (A) Schematic of an AUC disc showing the positions of the measurement and reference cells. (B) Typical sedimentation velocity experiments showing concentration profiles. (C) Resulting sedimentation coefficient distribution. (D) AUC measurements of sedimentation coefficient are plotted against BSA concentration. The red curve is a fit from Equation 3.10. (E) Schematic of a DCS disc showing the positions of the capillaries and spectroscopic detector. (F) Raw data and (G) resulting protein corona thicknesses as a function of protein concentration obtained with DCS for BSA-AuNPs complexes. Panels B-C, D and F-G were adapted with permission from[194], [78] and [193], respectively.

3.3.2 *In situ* quantification methods

Dynamic light scattering

Dynamic light scattering (DLS), also referred to as quasi-elastic light scattering spectroscopy (QELSS), or photon correlation spectroscopy (PCS), has been used extensively for the study of proteins interactions with NPs. The principle of DLS to measure the diffusion coefficient of an object is straightforward[95]. A coherent monochromatic light (laser) impinges on a solution. Particles in suspension partially scatter the light to a detector positioned at an angle θ_{DLS} from the light source's emission direction. Then adetector (photomultiplier or avalanche photodiode) collects the scattered light intensity over time (Figure 3.5A and B). The scattered intensity fluctuates over time due to the (Brownian) motion of the particles. An autocorrelator then calculates the normalized intensity-intensity correlation function $g(q,\tau)$ (or ICF), which represents the main parameter measured by DLS:

$$g(q,\tau) = \frac{\langle I(q,t)\, I(q,t+\tau)\rangle}{\langle I(q)\rangle^2} - 1 \qquad (3.13)$$

with $\langle \dots \rangle$ denoting average over time and where $I(q,t)$ and $I(q,t+\tau)$ are the intensities measured at time t and time delay τ, respectively, for the scattering vector $\vec{q}$, which in turn depends on the angle of the detector θ_{DLS}, the wavelength λ of the laser and the refractive index of the sample n_1 through $q = 4\pi n_1/\lambda \ sin(\theta_{DLS}/2)$. Under appropriate conditions[95], $g(q,\tau)$ is related to the normalized electric-field autocorrelation function $f(q,\tau)$ via the Siegert relation:

$$g(q,\tau) = C|f(q,\tau)|^2 \qquad (3.14)$$

with C the coherence factor, an experimental constant determined by the ratio of the speckle area to the detector area. For non-interacting monodisperse particles,

$$f(q,\tau) = \exp(-q^2 D\tau) \qquad (3.15)$$

Fitting measured ICF using Equation 3.14-3.15, or by replacing Equation 3.15 with the cumulant expansion or using CONTIN algorithm (a regularization method based on the inverse Laplace transform[195]) to extract the average diffusion coefficient of the particles.

In the context of the measurement of proteins adsorption on NPs, as introduced previously in section 3.2.2, DLS can measure changes in D, which in turn provides an estimation of K_D as well as the maximum number of adsorbed proteins N_{max} when D is measured as a function of the protein concentration. This analysis procedure is illustrated in Figure 3.5C and D for FCS measurement, but the procedure is applicable to DLS as well. Measurement of the diffusion coefficient can also provide information about the formation of multilayers on NPs in the case that the measured protein layer exceeds the dimensions of one protein.

Because all molecules in the suspension can *a priori* scatter light, proteins and NPs simultaneously contribute to the total scattered intensity reaching the detector. When proteins are smaller than NPs, they create a characteristic fast decay of the correlation function due to their higher diffusion coefficient. Depending on the proteins and NPs size, as well as on their respective concentration and refractive index, this first decay will be more or less pronounced but will strongly affect the value of D if a single global average diffusion coefficient is assumed for the whole NP/protein mixture. Then, only a method that does not assume a single D (*e.g.* the CONTIN algorithm or a double exponential model) should be used, at the price of being more sensitive to noise[196] or of introducing potential errors to the calculated parameters N_{max} and K_D. This approach was used by Waghmare *et al.* to study BSA adsorption on silver NPs of R_H=24.0±2.5 nm[162]. A strong signal arising from the high concentration of free BSA forced the authors to account for the free protein contribution in the autocorrelation function. As a result, the NPs' radius increased by ΔR_H=10.1±1.1 nm and was attributed to the formation of multiple layers of BSA around the NPs based on the side-on orientation of BSA and Equation 3.5.

Since the scattered intensity is highly dependent on the particle radius ($I \sim R^6$), it is possible to minimize the protein signal contribution to the autocorrelation function using large particles. By doing so, the scattering signal of the proteins will remain small compared to the particles, effectively reducing its relative contribution to the autocorrelation function. However, this procedure has a significant downside, as it decreases the sensitivity to the change of R_H produced by protein adsorption (already discussed in details in section 3.2.2). Hence, increasing R_0 makes the quantification of small variations of R_H more challenging, or even impossible.

One notable source of error in the measurement of *D* by DLS originates from the instability of the NP suspension. NP aggregation is challenging to assess by DLS as it tends to decrease the overall diffusion coefficient of the suspension, depending on the structure of the aggregates. Since large particles or aggregates scatter light much more than small ones, a small fraction of aggregated NPs may affect the measurements by skewing the correlation function towards lower *D* (larger R_H), which could be interpreted as protein adsorption. Control experiments to verify if aggregation occurs should involve analyzing the *q*-dependence of the scattering intensity *I*(*q*) and the diffusion coefficient *D*(*q*). There are many instances where DLS observed an increase of NP radius exceeding the diameter of the proteins, which was sometimes attributed to the formation of protein multilayers[74, 113, 117, 119, 162] and other times to aggregation[74, 123, 197-199], therefore highlighting the critical aspect of this control experiment.

To date, DLS characterization has been a major actor in the studies of the protein corona. The importance of surface chemistry was highlighted by Cui *et al.* using AuNPs of R_H=21-25 nm[74]. In this case it was found that adsorption of BSA, fibrinogen and transferrin was almost consistently supressed with 2kDa or 5kDa PEG-coated NPs, whereas other coatings of citrate, carboxylate and cysteine resulted in either strong aggregation or adsorption with K_D'=9.5-266 μM and generally a Hill coefficient $n > 1$. Surface curvature was also largely studied by Puntes and coworkers, where larger NPs were found to be more consistently covered by multilayers of proteins[117, 119]. Other studies have also characterized the dynamic nature of the protein corona using DLS. One study showed that by sequentially incubating NPs in HSA and then in fibrinogen (or inversely) the radius of the NPs was changing differently over time, *e.g.* the sequence HSA-to-fibrinogen produced an increase of NP radius while the sequence fibrinogen-to-BSA produced a decrease[124].

Zeta potential measurements are also frequently used alongside DLS to study proteins-particles interactions as it uses the same equipment and provides additional information. Zeta potential is measured via the electrophoretic mobility of the NPs, which depends on the NP surface charge density, its size and the ionic strength of the medium[200]. Thus, zeta potential is a surface property that will be mostly influenced by the surface composition of the NPs, and therefore by the presence of proteins. Indeed, using a combination of the simultaneous measurement of R_H and

zeta potential and extensive purification of protein-NPs complexes, it was observed that the serum protein corona was "hardening" over time[113]. Measurements of the zeta potential are also less size-sensitive. Cai and co-workers have used zeta potential measurements to explore the protein corona formation using NPs (R_H=60-100 nm) made of both polylactic-*co*-glycolic acid (PLGA) and polystyrene sulfonate (PSS) polymers in presence of lysozyme[201]. Zeta potential change with protein concentration closely matched the protein adsorption isotherm measured from a BCA assay. Though aggregation of the NPs occurred close to the point of NPs surface potential neutralization, the zeta potential value was still highly sensitive to the adsorbed amount of proteins. The destabilizing effect of protein adsorption prevented further analysis of the adsorption from the size of NPs.

Efforts to minimize the limitations of standard DLS for the study of biological interactions with the nanoscale are ongoing. With that intent, Balog *et al.* proposed an alternative approach to standard DLS, which takes advantage of the optical anisotropy and localized surface plasmon resonance (LSPR) of metallic NPs. Under light scattering conditions, the coupling of these two phenomena results in a depolarized speckle pattern. By selectively measuring the depolarized intensity autocorrelation function[199], this variant of DLS, called depolarized dynamic light scattering (DDLS), effectively suppresses the biological media contribution in the scattering spectrum. With short measurement times, the authors were able to characterize the adsorption kinetics of BSA and FBS proteins on AuNPs. Within those conditions, the signal-to-noise ratio was drastically improved compared to standard DLS. Yet, DDLS signal relies on the optical anisotropies of the NPs (*e.g.* geometry, internal structure), therefore limiting its use.

Fluorescence correlation spectroscopy

As we previously discussed, the major criticisms regarding the use of DLS to study proteins-NPs interactions come from its limitations and potential biases (*e.g.* scattering of free proteins, high sensitivity to aggregation). Fluorescence correlation spectroscopy (FCS) is another correlation-based technique that is analogue to DLS and allows to specifically isolate the scattering contribution of a fluorescent species and measure its diffusion coefficient *D*. FCS can be

performed on a standard DLS setup as well as on a microscope (Figure 3.5A). The detailed theoretical background of FCS can be found elsewhere[66, 73, 95, 202, 203]; here only the basic approach of FCS will be covered. In a standard setup, a laser tuned at the excitation wavelength of the labeled NPs or proteins is focused on a sample that contains the fluorescent objects. The objects in the illumination volume emit fluorescence and the intensity is recorded by a photomultiplier tube detector. The resulting intensity is analyzed in an autocorrelator. The normalized intensity autocorrelation function in FCS is defined as:

$$G(\tau) = \frac{\langle I(\tau) I(t+\tau) \rangle}{\langle I(t) \rangle^2} - 1 \tag{3.16}$$

where $I(t)$ is the fluorescence intensity measured by the detector at a given time, and τ is the delay time. In a FCS experiment, the signal fluctuations arise from the concentration fluctuations of the fluorescent molecules in-and-out of the illumination volume (see Figure 3.5B). Therefore, the signal-to-noise ratio is proportional to the inverse of the square root of the illumination volume and to the inverse of the square root of the average number of fluorescent molecules $1/\langle N_{fluo} \rangle^{1/2}$ [95]. As a consequence, FCS experiments are preferably performed on either very small volumes (~10^{-15} L) or very dilute suspensions (~10^{-9} M of particles). The illumination volume also affects the autocorrelation function. In the case of a light beam with a gaussian intensity profile that is typically found on a microscope, the autocorrelation function takes the form:

$$G(\tau) = \frac{1}{\langle N_{fluo} \rangle} \left[1 + \frac{\tau}{\tau_R}\right]^{-1} \left[1 + \left(\frac{r_0}{z_0}\right)^2 \frac{\tau}{\tau_R}\right]^{-1/2} \tag{3.17}$$

where r_0 and z_0 are the radial and axial profiles of the illumination volume and τ_R is the relaxation time of the measured dynamics. The relaxation time is related to the diffusion coefficient D through $D = {r_0}^2/4\tau_R$ [66, 118], which provides the intensity averaged diffusion coefficient in the illumination volume. Then, it is possible through Stokes-Einstein equation to extract the hydrodynamic radius R_H and, using Equation 3.5, to obtain the maximum number of adsorbed proteins N_{max}, the dissociation constant K_D and the Hill coefficient n, as illustrated in Figure 3.5C and D.

One of the key advantages of FCS is that it can be performed on a standard confocal microscope, allowing to study the dynamics of small objects in complex matrices. For instance, FCS has been successful in studying the dynamics of nano-objects in cells' cytoplasm[204] or the dynamics of lipid rafts in cell membranes[205]. The study of proteins-NPs interactions is also an important contribution of this technique.

To detect proteins-NPs interactions FCS selectively isolates the dynamics of fluorescent molecules. Using fluorescent NPs, free proteins will not have any contribution in the autocorrelation function of the fluorescent light, so that the measure of *D* is highly specific to the NPs. Additionally, as mentioned previously, FCS measurements must be performed at a very diluted concentration of NPs to optimize the signal-to-noise ratio and to minimize NPs aggregation, potentially preventing 2 biases commonly observed in DLS measurements. However, prevention of aggregation cannot always be guaranteed, and the precision of FCS measurements will, just as in DLS, be defined by its capacity to accurately measure R_H variations of the order of a protein diameter.

FCS can provide valuable information about protein conformation at NPs surface. In a study led by Nienhaus group, Röcker *et al*. demonstrated that HSA adsorption on CdSe/ZnS NPs (R_0 = 5.6±0.2 nm) led to a radius increase ΔR_H = 3.3 ± 0.3 nm which corresponds closely to a specific orientation of HSA on the NPs[66]. HSA has a structure reminiscent of a triangular prism of 8.4 nm sides and 3.15 nm thickness, corroborating that HSA adsorbs face down on the NPs and produces only a monolayer. A strong dependence on temperature was reported in a separate study, where the incubation medium was either cooled, warmed or left at room temperature[72]. Significant decrease of K_D', N_{max} and corona thickness in some instances was reported, which was attributed to different denaturation or conformational changes of the proteins upon binding to the NPs. Further studies making use of FCS have shown that orientation changes are not only triggered by temperature fluctuations but also by chemical modifications (succinylated or aminated)[206] of the protein. Treuel *et al.* described that adsorption of native HSA led to a ΔR_H=3.3±0.6 nm on CdSe/ZnS NPs with HSA facing down on NPs, while succinylated HSA led to ΔR_H=8.1±0.6 nm,

suggesting that the base of the prism is likely the anchorage point of the protein on the NPs.Aminated HSA led to ΔR_H=4.6±0.1 nm, which the authors identified as a random or unknown orientation, or a volume expansion of the protein due to its amination. Also, surface modification of polymer-coated FePt NPs with either glucose or 0.75 to 10 kDa PEG showed that the affinity of HSA for the NPs was almost unaffected in comparison to bare NPs[68]. Conversely, the number of adsorbed proteins N_{max} and the Hill coefficient n were strongly affected by these modifications. A similar trend with fibrinogen adsorption on bare NPs and PEGylated NPs (PEG 10kDa) was reported where K_D' changed by a factor of 5, while the ratio at saturation of adsorbed proteins/NP decreased by a factor of 10 and the Hill coefficient by a factor of 2. Pelaz *et al.* explained these findings by mentioning that n decreased due to the steric hindrance generated by the PEG chains that proteins have to overcome in order to adsorb on the NP surface. Since most of the surface is occupied by PEG chains, the number of proteins is concomitantly decreased (low N_{max}), without necessarily changing the affinity of the protein for the NP surface.

In most protein adsorption studies using FCS, the formation of a protein monolayer on the NP is reported, even when $\Delta R_H > 2R_{Protein}$[66, 69, 70, 73, 118]. However, one study by Milani *et al.* reports the formation of protein multilayers[31]. The authors used an alternative quantification method of the adsorbed protein corona, labeling the proteins instead of the NPs and using Equation 3.17. Adsorbed proteins on NPs are drastically slowed down, making possible the quantification of free and bound proteins from the autocorrelation function. Adsorption of up to 3 layers of the transferrin protein was found using this quantification method on sulfonate PS NPs (R_0 = 48.6 nm). However, this methodology was heavily criticized due to its high sensitivity to aggregation[207] and to the fact that the fluorescent dye used to label the protein may alter its adsorption profile[207].

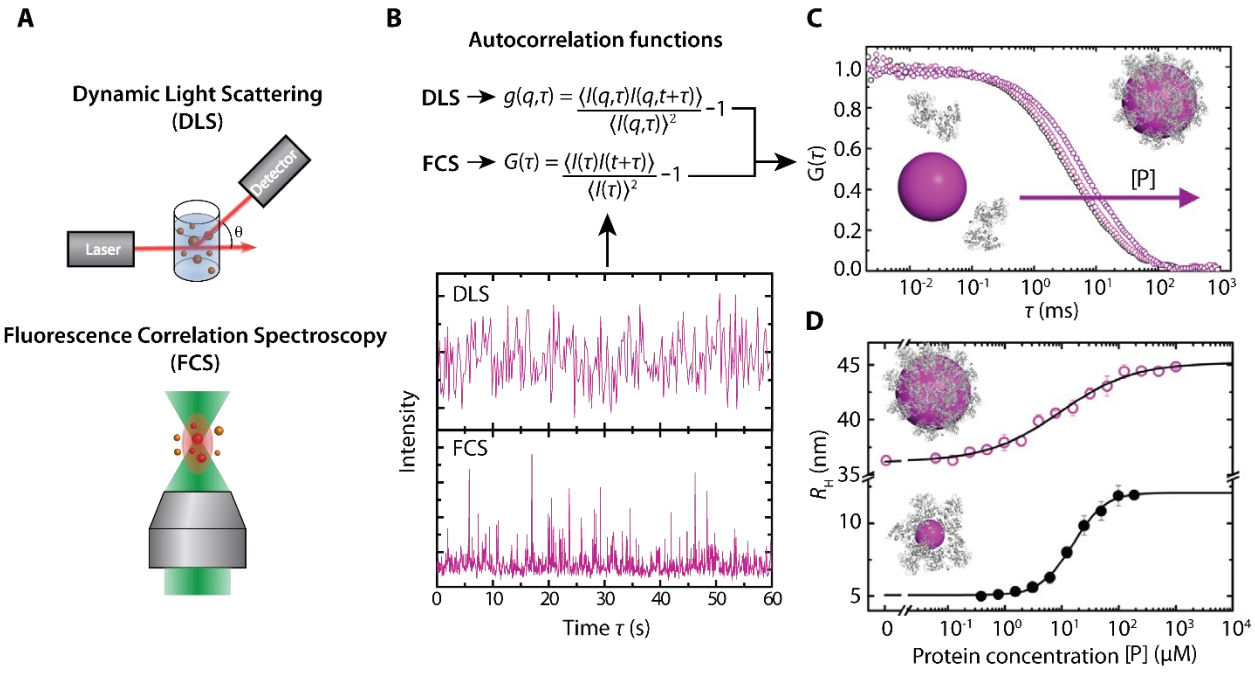

Figure 3.5. Correlation-based techniques for the determination of protein adsorption in situ. (A) Schematics of dynamic light scattering (DLS) and fluorescence correlation spectroscopy (FCS). (B) Recording of the scattered intensity signal for DLS and emitted intensity for FCS. (C) Evolution of the autocorrelation functions obtained from FCS with increasing protein concentration in the medium. (D) Measurement of the radius of NPs-proteins complexes with increasing protein concentrations for 2 distinct NP sizes from FCS autocorrelation functions. Black curves in panel D are a fit from Equation 3.5. Panels C and D were adapted with permission from [118].

Fluorescence quenching

The quenching of fluorescence is a commonly used phenomenon in biochemistry and molecular biology to study interactions of proteins with molecules or surfaces[157]. The quenching process of a fluorophore *F* requires a molecular interaction with a quencher *Q* that could result from different sources. These interactions can stem from direct physical or chemical bonds arising from molecular collisions, intermolecular rearrangements, and from complex formation or even resonance energy transfer[157]. These interactions inhibit or recapture the fluorescence generated by the fluorophore, decreasing the total fluorescence intensity *I*, as depicted in Figure 3.6A. Depending on the quenching mechanism, the quenching rate k_q may decay differently as a

function of the distance between the fluorophore and the quencher ($r_{Q\text{-}F}$). For energy transfer, the quenching efficiency decays as $k_q(r_{Q\text{-}F}) \sim r_{Q\text{-}F}^{-6}$ while for direct electron cloud interactions, the quenching efficiency often decays faster $k_q(r_{Q\text{-}F}) \sim \exp(-r_{Q\text{-}F})$ due to the exponentially decreasing density of electron clouds. Therefore, in some cases (*e.g.* resonance energy transfer), efficient quenching may happen quite far from the quenching molecule, more than 10 nm of distance, not requiring the formation of a complex.

Interpretation of fluorescence quenching experiments are frequently based on the Stern-Volmer equation[157]:

$$\frac{F_0}{F} = 1 + K_{sv}\,[Q] \tag{3.18}$$

where F_0 is the fluorescence intensity without quenching, F the quenched fluorescence intensity and K_{sv} the Stern-Volmer constant. In the case of a dynamic quenching, *i.e.* from molecular collisions, $K_{sv} = k_q \tau_0$, where k_q is the constant of a diffusion-controlled reaction based on Smoluchowski equation and τ_0 the fluorophore lifetime. As a result of dynamic quenching, the fluorophore lifetime decreases with quenching $F_0/F=\tau_0/\tau$ as an additional rate process that dynamically depopulates fluorescent molecules. However, this type of quenching is not directly correlated to physical adsorption of molecules. In the case of physical or chemical adsorption of molecules, a static quenching occurs.

Static quenching is interpreted and derived from the equilibrium constant of Equation 3.1 of the reaction $F + Q \leftrightarrow FQ$, where *FQ* is the complex between the fluorophore *F* and the quencher *Q*. Incidentally, substituting the total concentration of the fluorophore $[F]_{tot}=[F]+[FQ]$ in Equation 3.1 also results in Equation 3.18. Therefore, it is impossible to identify whether a quenching process is the result of adsorption or molecular collision from a Stern-Volmer plot. However, there are key differences between both phenomena that can differentiate them. For static quenching, the fluorophore lifetime is not affected ($\tau_0/\tau=1$), whereas for collisional quenching, the fluorophore lifetime is proportional to the fluorescence quenching ($F_0/F = \tau_0/\tau$). Collisional quenching also depends on the mobility of both molecules, as described by Smoluchowski equation, with $K_{sv} \sim T/\eta$, where T is the temperature and η the medium viscosity. For static

quenching, dependency over T and η are controlled by the thermodynamics of Q and F association.

It also frequently happens that both quenching mechanisms (collisional and static quenching) are significant in one same system. If the system is quenched via resonance energy transfer (long-range), there is a chance that the system exhibits 2 quenching mechanisms. The Stern-Volmer plot for two simultaneous quenching processes is described by the quadratic function[157]:

$$\frac{F_0}{F} = (1 + K_{sv1}[Q])(1 + K_{sv2}[Q]) \quad (3.19)$$

where indices 1 and 2 refer to collisional and static quenching. The resulting Stern-Volmer plot will then be marked by an upward curve, a key feature of two simultaneous quenching mechanisms. In the case of proteins-NPs interactions, failing to account for both phenomena could then lead to significant errors in the measurement of K_{sv} and to the erroneous interpretation that $K_{sv} = K_A$, which is only valid in the case of static quenching.

Another popular analysis of fluorescence quenching experiments is derived from the Hill adsorption isotherm and Equation 3.18:

$$\log\left(\frac{F_0 - F}{F}\right) = log\ K_D + n\ log[Q] \quad (3.20)$$

This representation is shown in Figure 3.6B. In this situation, if Q is the NP, the measurement of n is actually the inverse Hill coefficient, whereas if Q is the protein, then n is the Hill coefficient[208]. However, to make sure this analysis is suitable, one needs then to rule out the possibility of two quenching mechanisms, as Equation 3.19 is bound to falsely generate $n > 1$ if analyzed with Equation 3.20. Temperature-dependent measurement and/or lifetime measurement of the fluorophore are required to rule out the contribution of both quenching mechanisms and truly measure the Hill coefficient and the equilibrium constant. When these parameters are considered, it is then possible to extract from Van't Hoff plots ($\ln K_A = -\frac{\Delta H}{RT} + \frac{\Delta S}{R}$) different thermodynamic parameters such as enthalpy ΔH and entropy ΔS changes. When K_A is measured at different temperatures, a complete thermodynamic description of the adsorption process can be obtained[209-212]. Thermodynamic parameters measured by fluorescence quenching have been

compared to other techniques (notably isothermal titration calorimetry, ITC) for the interaction of ultrasmall AuNPs with HSA and transferrin[209]. Fluorescence quenching and ITC were found to generally agree, with positive ΔH and ΔS for HSA, and negative ΔH and positive ΔS for transferrin. From these values, the authors concluded that the protein adsorption was entropy-driven, hence arising from hydrophobic interactions. Indeed, the characterization of the adsorption thermodynamics can also help identify the interaction driving the adsorption process[213]. For instance, electrostatic interaction was identified as the leading mechanism of the adsorption of a β-sheet forming peptide reminiscent of amyloid-beta on AuNPs[211], whereas interaction between graphene oxide-silver nanocomposites and BSA was found to be driven by Van der Waals forces and hydrogen bonding[214]. Electrostatic (HSA, transferrin, β-sheet forming peptide)[211, 212, 215], Van der Waals (BSA)[214], hydrophobic (HSA, γ-globulins, transferrin)[210, 212] and hydrogen bonding (BSA)[214] have all been identified as driving mechanisms of protein adsorption on small NPs (R_0 < 15 nm). The adsorption mechanism was found to change notably as a function of the protein[209, 212] and surface charge of the NPs[215].

Despite the straightforward approach of fluorescence quenching to quantify proteins-NPs interactions, the approach is subject to high uncertainties. For instance a review from Hühn *et al.* on the measurement of the equilibrium constant K_A of protein adsorption on NPs showed that most techniques were able to observe a dependency of K_A on the zeta potential of the NPs, which was not the case for fluorescence quenching measurements[106]. This finding supports the rising concern about the validity of the approach of fluorescence quenching and the 6-7 orders of magnitude difference obtained for K_A, compared with other techniques[208, 216].

Another completely different approach using fluorescence quenching is to take advantage of time-resolved experiments. Time-resolved fluorescence quenching can provide very useful insight into the dynamics of protein adsorption on NPs and the equilibrium constant of the reaction. This overcomes many of the already discussed issue of “steady-state” fluorescence quenching. A typical experiment will use fluorescent NPs quenched by a quencher-labeled protein. Both are rapidly mixed in a fluorescent spectrometer which records fluorescence

intensity over time. Upon adsorption, proteins will quench the signal of the NPs, resulting in a decrease of the fluorescence intensity over time, represented in Figure 3.6C. Then, the kinetics of protein adsorption can be modeled from the time-dependent fluorescent intensity, assuming a pseudo first-order kinetics:[66]

$$F(t) = F_0 \exp\left(-t/\tau_D\right) \tag{3.21}$$

with τ_D being the characteristic decay time of the fluorescence intensity, related to the adsorption kinetics of the proteins *via* a linear relation:

$$\tau_D{}^{-1} = k_{on} + [Q]k_{off} \tag{3.22}$$

with k_{on} and k_{off} the rates of adsorption and desorption of proteins, respectively. From these experiments it is then possible to obtain k_{on}, k_{off}, and the equilibrium constant from Equation 3.1. The relation between Equations (3.21) and (3.22) arise from the assumption of a pseudo first-order kinetics ([*Q*]>>[*F*]), in other words, when the quantity of proteins is in large excess over the number of total sites. However, the criteria of this assumption are not always met and need to be carefully evaluated. The complete methodology was however only used once by Röcker *et al*.[66] For HSA on CdSe/ZnS NPs, the measured desorption rate constant k_{off}=(9 ± 2) × 10^{-3} s^{-1} and the adsorption rate constant k_{on} = (2.4 ± 0.5) × 10^3 $mol^{-1}Ls^{-1}$ were in good agreement with the affinity constant of HSA obtained through the adsorption isotherm methodology. Alternatively, competition experiments can be performed between two proteins by monitoring the adsorption kinetics of both proteins labeled with different fluorescent labels (see Figure 3.6C)[125]. Though such system is more complex than single protein experiments, it provides an indication on the time needed for the system to reach equilibrium.

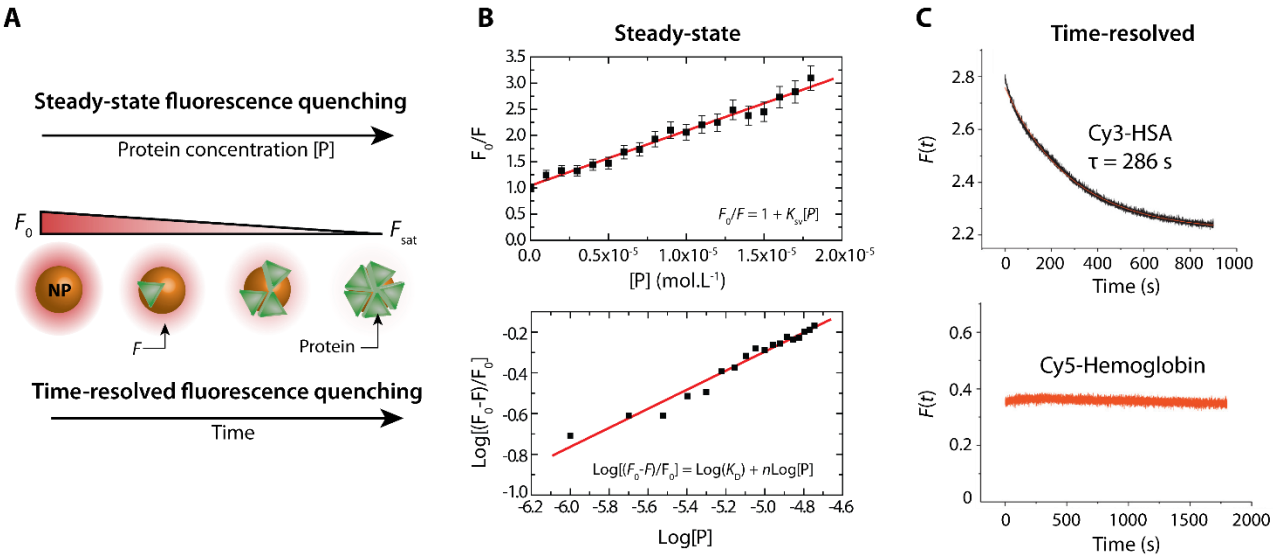

Figure 3.6. Fluorescence quenching techniques to study protein-NPs interactions. (A) Schematics of the measured fluorescence intensity in the two different modes of fluorescence quenching: (B) steady-state fluorescence quenching and (C) time-resolved fluorescence quenching obtained for 2 competing proteins on NPs surfaces, where curves are fit from model Equation 3.21. Panel C was adapted from [125].

Flow cytometry

Flow cytometry is an emerging technique in the protein corona field. Its tremendous developments within the last few years have increased its sensitivity to smaller objects, positioning it as a very powerful and versatile technique for the characterization of cells and viruses[217], extracellular vesicles (*e.g.* exosomes[218]) as well as for high-throughput enzyme-linked immunosorbent assay (ELISA) assays[219]. These recent improvements are also paving the way to a novel approach to analyze the protein corona. Although in its infancy, the ubiquity of flow cytometer in biological laboratory facilities could position the technique as one of the most common tools for the study of proteins-NPs interactions.

A flow cytometer is typically designed to study the expression of proteins in transfected cells or to detect the presence of proteins on cells by using a fluorescent marker. Therefore, it is usually equipped with many light sensitive detectors. A suspension collected by the flow chamber is

slowly pumped through a microchannel where fluorescence multiwavelength detectors are carefully placed along with a light scattering detector, as represented in Figure 3.7. When a large object (*e.g.* cells, large NPs) goes through the laser, the object will induce a short burst of scattered light to the detector, where the intensity of the signal depends on the size and the refractive index of the material (assuming shape and orientation are constant). Simultaneously, if the object is fluorescent, the fluorescence detectors will also record a spike of fluorescence with its corresponding light scattering amplitude. The fluorescence signal depends on the quantum efficiency of the fluorescent probe and its concentration through the light path. Therefore, a graph of scattered light vs fluorescence can be plotted for each individual pulse recorded by the flow cytometer throughout the experiment. However, boundaries over the resulting signal must be carefully and objectively placed in order to selectively remove noise signal. Then, the fluorescence signal can be quantified and averaged. For proteins-NPs analysis, the typical experiment would use non-fluorescent NPs and fluorescent proteins in order to quantify the adsorption. Non fluorescent proteins can also be used but need to be subsequently revealed by a fluorescently labeled antibody targeting the desired protein (see Figure 3.7). The latter approach was used by Lo Giudice *et al.* to demonstrate that flow cytometry was capable of resolving and quantifying protein adsorption on NPs[77].

The pioneering work from Liptrott *et al.* in 2014 is, to our knowledge, the first report making use of flow cytometry to semi-quantitatively assess the protein-NP interaction[220]. It is also one of the few studies that demonstrated solid drug NPs interaction with fibrinogen, albumin and transferrin proteins from plasma. Flow cytometry has also been used to quantify covalently-linked BSA[221] as well as to identify and sort subpopulations of the protein corona on microbubbles[222].

Currently, the critical limitation of this approach is its inability to detect individual scattering events of small objects (usually R_H < 250 nm). Yet, by using the "swarm regime" to capture the scattering signal of multiple NPs and counting them as a single event, Lo Giudice *et al.* were able to reliably quantify protein adsorption on NPs as small as R_H=25 nm. Even though sensitivity can

be improved in this way[77], more sensitive detectors or strategies will be required to cover the full spectrum of NPs sizes.

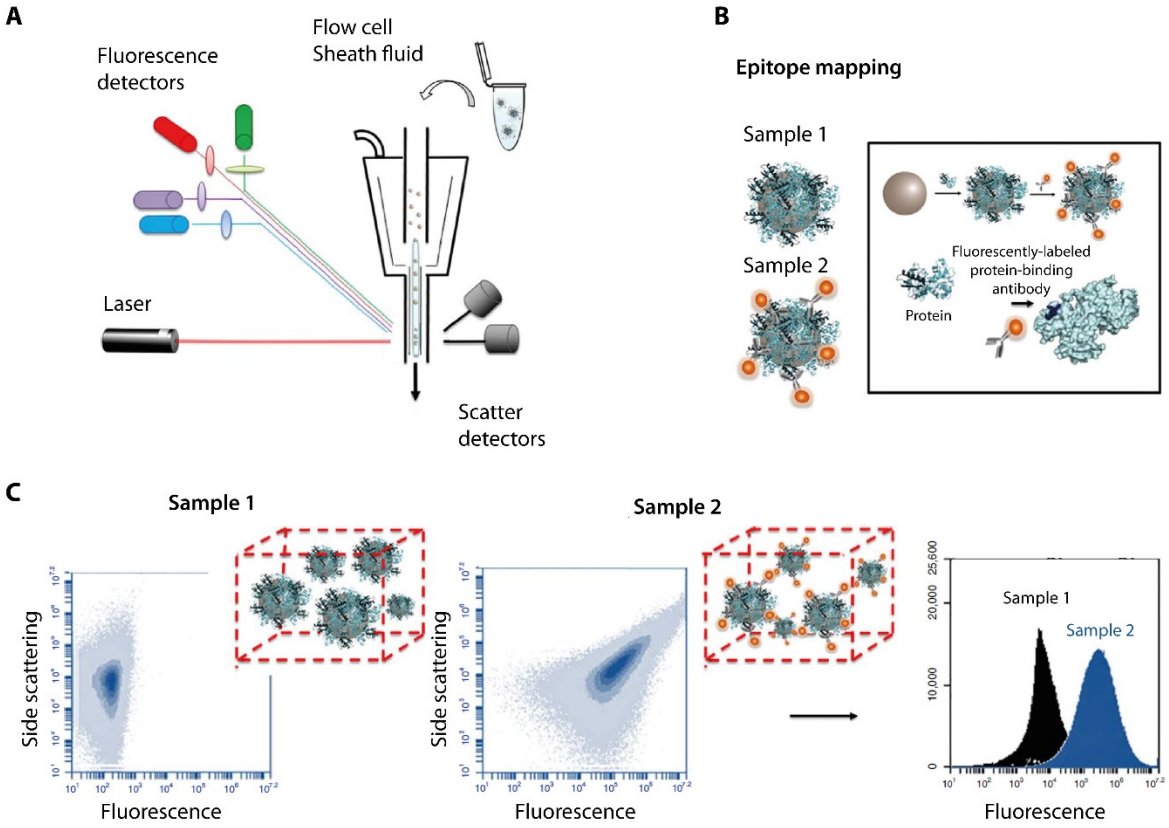

Figure 3.7. Representation of flow cytometry experiments designed to quantify protein adsorption. (A) Schematics of the detection chamber of the flow cytometer. (B) Principle of epitope mapping for protein corona detection. NP-protein complexes are incubated with fluorescently labeled protein-binding antibodies (sample 2). Control experiment corresponds to no incubation with protein-binding antibodies (sample 1). (C) Examples of flow cytometry results for both control and fluorescently labeled samples. Reproduced and adapted from [77] with permissions.

Nuclear magnetic resonance spectroscopy

Nuclear magnetic resonance (NMR) spectroscopy is a powerful technique that has been widely used to study proteins-NPs interactions, as reviewed by Assfalg *et al.* in 2016[223]. NMR observes the perturbation of nuclear spins when placed in a powerful magnetic field and mesures the resulting electromagnetic signal. NMR analysis of proteins is mainly based on ^{1}H, ^{13}C and ^{15}N nuclei signal. In a typical NMR experiment, three main parameters can be extracted to give information about the studied species: the chemical shift ν, which is affected by the local chemical environments of the nuclei, the signal intensity *I*, which is related to the number of nuclei resonating at a given frequency and the linewidth, which depends on the rotational correlation time of the analyzed species, which in turn is linked to their size (Figure 3.8A). NMR signals of proteins are expected to be disturbed by the presence of NPs, depending on the nature of their interactions and the properties of the NPs. This technique enables to characterize the orientation, structure and dynamics of proteins adsorbed onto NPs, but can also be used to quantify them.

Proteins-NPs interactions are often characterized when adsorption and desorption reach a dynamic equilibrium. Proteins analyzed by NMR in presence of NPs can therefore be detected in two distinct states: bound or unbound. The shape of the NMR spectrum will depend on the regime of the chemical exchange. k_{ex} being the exchange rate and Δν the chemical shift difference between the two states bound and unbound, three regimes can be distinguished, as described in Figure 3.8A. The slow exchange regime ($k_{ex} << \Delta\nu$) is the only one where signals from both states are distinct. When bound to NPs, proteins will adopt the rotational diffusion coefficient of the NPs, which is higher due to their larger size. NMR signals of adsorbed proteins will therefore be negligible, due to their broadening beyond the detection limit (Figure 3.8A), which means that NP-bound proteins will not be detected if the exchange regime is slow enough. It is then possible to quantify protein adsorption based on the decrease of the integrated NMR signal of unbound proteins. Wang *et al.* applied this technique to a set of 6 proteins, in order to quantify the number of proteins bound per AuNP, using the integrated amid signal of proteins (Figure 3.8B):[224]

$$N = \left(1 - \frac{Integrated\ signal_{with\ NPs}}{Integrated\ signal_{without\ NPs}}\right) \frac{C_{\mathrm{P}}}{C_{\mathrm{NP}}} \quad (3.23)$$

where C_P is the total protein concentration, C_{NP} the total NP concentration and N the number of proteins bound per NP. The same group then extended this quantification to a set of AuNPs of varying size (from 14 to 86 nm)[225]. One benefit of this technique is that it is not affected by NPs aggregation, as it measures selectively the unbound proteins concentration.

However, this method is limited to the quantification of one specific protein. To quantify the competitive binding of two proteins, the same group developed a new method based on the isotopic labeling of the proteins by either ^{13}C or ^{15}N [226]. Adsorption of each protein was quantified independently, via the method described above, by filtering the signals of either ^{13}C- or ^{15}N-attached protons.

NMR also enables to measure the diffusion coefficients of the analyzed species, and thus to obtain information about their hydrodynamic radius. The diffusion measurements are based on pulsed-field gradient experiments, where the signal intensity decay is fitted to extract the diffusion coefficient[227]:

$$I = I_0\, e^{-D\,Z} \quad (3.24)$$

where I is the observed intensity, I_0 the reference intensity and Z a factor set by the experimental parameters and the characteristics of the observed nucleus. A large range of diffusion coefficients can be measured, from 10^{-7} to 10^{-14} $m^2\ s^{-1}$, which corresponds to hydodynamic diameters ranging from a few picometers to tens of micrometers. To characterize the protein corona, this technique has been used in combination with fluorine (^{19}F) labeling of the NPs[75, 228]. This avoids any interference from the background, thanks to the natural absence of fluorine in biological fluids. Measurements could be performed in complex biological environments such as full culture medium, plasma and blood. Furthermore, the use of NPs with different ^{19}F-labeled ligands led to differentiated chemical shifts and enabled to simultaneously measure their hydrodynamic radii[229].

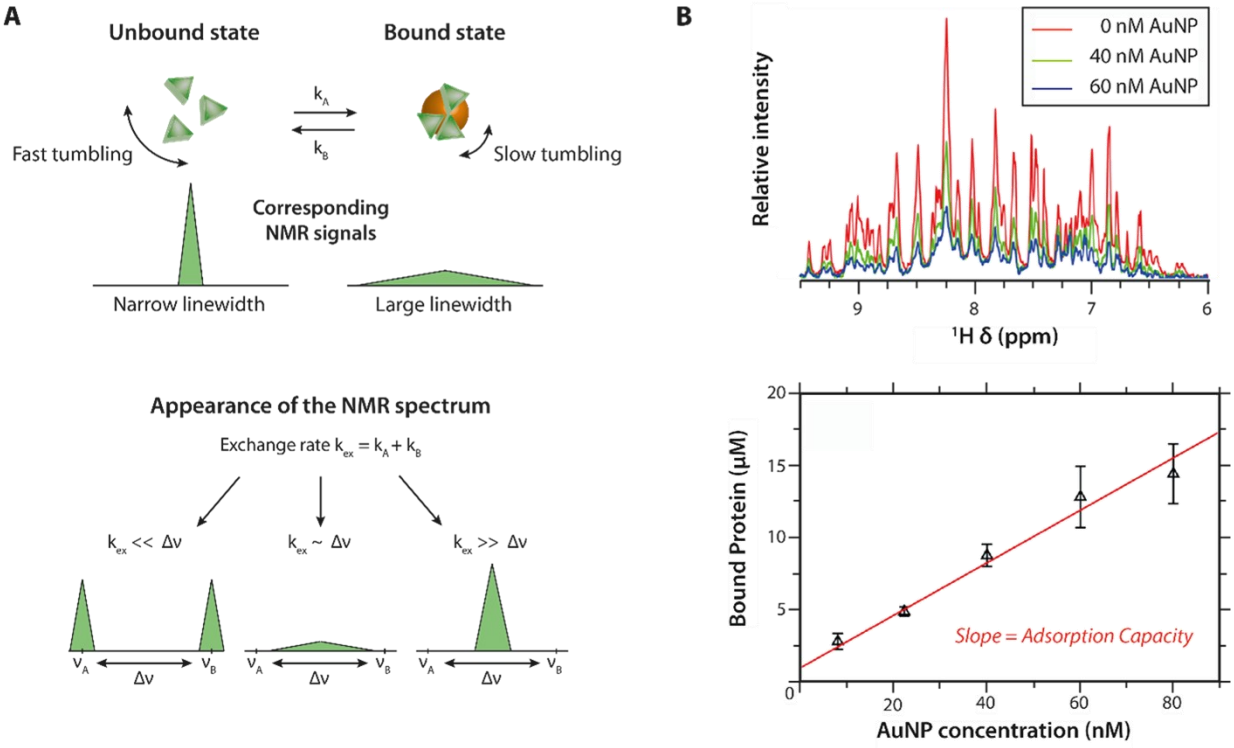

Figure 3.8. NMR approach to quantify adsorbed proteins. (A) Comparison of NMR signals obtained for bound and unbound proteins as well as for the three exchange regimes. (B) Protein quantification is obtained through the decrease of the integrated NMR signal of unbound proteins in the presence of NPs. The adsorption capacity can be calculated from the evolution of the concentration of bound proteins as a function of NPs concentration. Panel B was adapted from [224] with permission.

Surface plasmon resonance

Plasmonic techniques exploit the properties of surface plasmons generated at the interface between a metal and a dielectric medium. The most common method is the attenuated total reflection in a prism, with two possible configurations (Kretschmann or Otto). Grating, wave-guide and interferometer are other methods used with SPR devices. Surface plasmons are a collective movement of electrons generated through the interaction of metal with light. When a metallic interface is excited at the plasmon wavelength, resonance of the conduction electrons appears, inducing oscillation waves (surface plasmons) that propagate parallel to the metal

surface. Surface plasmon resonance (SPR) uses a flat metallic sensor surface while localized surface plasmon resonance (LSPR) uses either NPs deposited on a flat surface or in suspension (Figure 3.9A). SPR devices are designed with flow channels running buffers and proteins solutions on the surface of the sensor film, while detection relies on the use of a light beam of fixed wavelength. During a measurement, the intensity of the light beam reflected by the sensor surface is decreased for a specific reflection angle, called the SPR angle, ϑ_{SPR} (Figure 3.9A). From the electromagnetic theory, ϑ_{SPR} is derived as a function of both media (n_1, n_2) and metallic (n_m) refractive indexes for the Kretschmann configuration:

$$\vartheta_{SPR} = \sin^{-1}\left(\frac{1}{n_1}\sqrt{\frac{n_2^2\, n_m^2}{n_2^2+n_m^2}}\right) \tag{3.25}$$

When proteins are adsorbed or desorbed near the surface of the sensor, n_2 and n_m change, which leads to a change in ϑ_{SPR} (Figure 3.9B). SPR experiments monitor ϑ_{SPR} shift over time to analyze adsorption-desorption of proteins in a sensorgram (Figure 3.9C).

In most LSPR setups, the flat metallic surface is replaced by immobilized metallic NPs forming a 2-dimensional array. The main advantage is that the sensing volume is significantly smaller compared to a flat gold film, which increases sensitivity. The shift of maximal plasmon wavelength $\Delta\lambda_{max}$ obtained in LSPR experiments is, as ϑ_{SPR}, related to the refractive indices of the medium and the NPs array. Once the sensorgram is recorded, there are different methods to extract the quantity of proteins adsorbed on NPs. Multi-parametric SPR, using two incident wavelengths, was proposed by Kari *et al.* to numerically resolve surface plasmon vectors equations through the two-wavelength method, and to obtain the protein corona thickness[230]. In this study, the authors focused on serum proteins adsorption on liposomes with and without PEG coating. As proteins adsorbed on the particles, a shift of ϑ_{SPR} towards larger angles was observed. The corona thickness δ was calculated between 9.6 nm and 16.4 nm for charged liposomes of R_H = 20 and 28 nm, respectively. The protein corona formed on non-PEGylated charged liposomes was thicker compared to PEGylated charged (δ = 4.6 - 8.6 nm) and non-charged non-PEGylated ones (δ = 7.6 - 13 nm). Finally, the authors showed that the protein

corona of charged liposomes was more densely packed, as refractive index values were higher compared to other studied liposomes.

Fehran *et al.* used numerical calculations to mathematically link the plasmon wavelength shift $\Delta\lambda_{max}$ to δ with a LSPR device composed of gold-coated nanodisks array:[154]

$$\overline{\Delta\lambda_{max}}=\Delta n\left[1-\left(\frac{R^*}{R^*+\delta}\right)^5\right] \quad (3.26)$$

where Δn is the refractive index change after protein adsorption and R^* is a characteristic distance between nanodisks and proteins. The authors studied adsorption of HSA proteins on gold nanodisks of 120 nm in diameter, coated with either titania or silica. They measured $\Delta\lambda_{max}$ of 1.4 nm and 0.9 nm, respectively. However, when normalized by their corresponding bulk sensitivity, both coatings showed a similar $\Delta\lambda_{max}$. Thus, by using Equation 3.26, a protein layer thickness δ = 1.5 nm was calculated. Zen *et al.* used numerical methods to model the optical response of an array of 50 nm carbon-coated gold nanodisks in presence of BSA or fibrinogen[231]. The authors calculated a protein corona thickness of 3.2 nm with fibrinogen solution. However, with BSA, they found that hydrogen-doped carbon-coated NPs exhibited a δ of only 1.8 nm compared to 2.3 nm for amorphous carbon-coated NPs. Finally, the authors estimated the density of BSA to be around 2.3 mg m^{-2} for both coatings. In the same line, Miclaus *et al.* used numerical methods to model the optical response of a LSPR array of coated silver nanocubes in FBS solution[232]. The protein mass density was found to reach a plateau at 3% FBS up to 10% with a density of 2.7 mg m^{-2} of FBS proteins on 35 nm polyvinylpyrrolidone-coated silver nanocubes. When 1% FBS proteins solution was running, the density was reported to be 0.9 mg m^{-2}.

SPR devices represent an attractive alternative to UV spectroscopic techniques since a large variety of NPs can be studied when bound to the sensor chip. SPR sensing is a label-free technique, allowing real time monitoring of adsorption, even in complex proteins solutions. It

consumes small quantities of sample and can extract kinetic binding constants. However, SPR sensing has some limitations that are listed in Table 3.1.

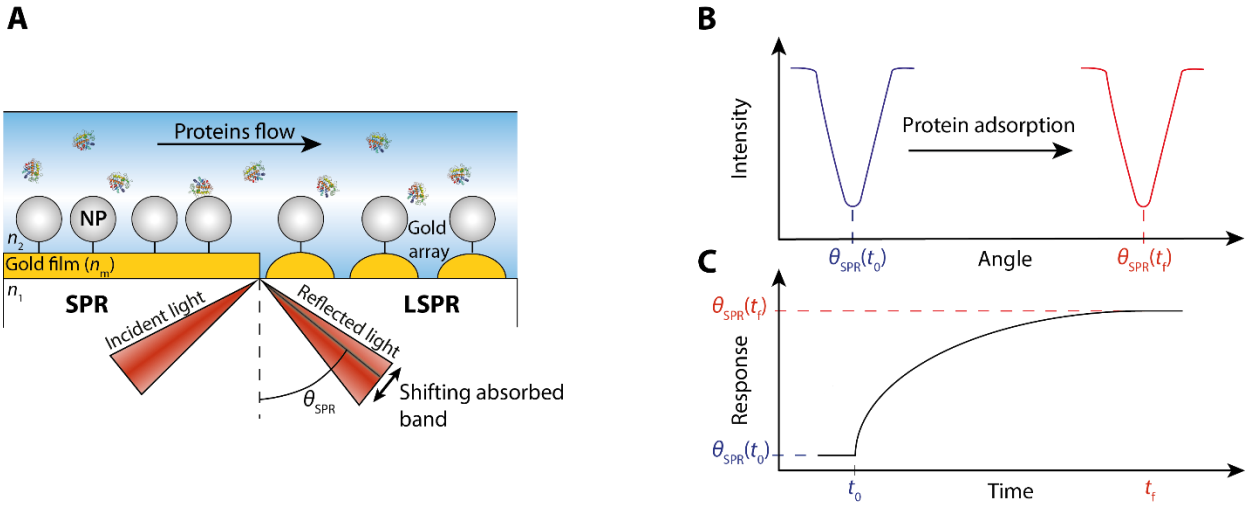

Figure 3.9. Overview of the SPR measurements for protein adsorption. (A) Schematic representation of SPR and LSPR detection systems in presence of proteins. (B) Representation of the SPR angular shift due to binding events on NPs. (C) Corresponding response as a function of time, giving access to adsorption kinetics.

Isothermal titration calorimetry

Another *in situ* technique used to study protein adsorption is isothermal titration calorimetry (ITC). This technique measures the heat exchange caused by molecular interactions between NPs and their environment. It allows to extract analytical thermodynamic parameters without immobilization, modification or labeling of the particles and the proteins. These parameters include enthalpy change (ΔH), equilibrium constant (K_A) and binding stoichiometry (N)[233]. Finally, these parameters could be used to calculate the Gibbs free energy (ΔG), entropy change (ΔS), heat capacity change (ΔC_P), and the number of proteins adsorbed on the surface of particles as well as their affinity[127, 234].

Figure 3.10A shows a schematic of a typical ITC instrument. The setup consists of two cells (reference and sample) placed in an adiabatic jacket with an approximate volume of 0.5–1.5 mL each. Cells are heated up to the set point temperature and a feed-back control system maintains

the temperature constant throughout the experiment. Injection of aliquots of the solution into the sample cell and the resulting molecular interactions cause transient heat generation and transfer. The thermogram is obtained from the applied power needed to maintain the temperature of the cells constant over time. It is constituted of different peaks, each indicating one injection. Importantly, the heat due to dilution of the protein should be quantified via control experiments and subtracted from the raw data[234]. This could be done by injecting the protein solution in the buffer alone (reference run) and measuring the heat of dilution. Consequently, integrating the normalized data using a proper model ends up with quantifying the number of adsorbed proteins and the related thermodynamic properties[233, 235].

For instance, Figure 3.10B illustrates results of ITC experiments obtained after titration of HSA proteins in a suspension of NIPAM/BAM NPs[127]. The thermograms presented in Figure 3.10B (upper graphs) show that the adsorption of HSA on the surface of NPs is exothermic (negative peak values indicate heat release) and that the amount of released heat due to the adsorption decreases over time (height of each peak), as the binding sites become saturated,[236] until reaching a constant value, corresponding to the heat of dilution.

Moreover, as mentioned earlier, titration isotherms can be fitted using adequate models to extract information regarding the thermodynamics of the system. For protein-NP interactions, a one-site binding isotherm is usually used to extract thermodynamic parameters[237]. This model assumes that no inter-protein interaction occurs and each protein is adsorbed on one site without cooperativity effects (Langmuir type isotherm)[127]. The equation representing this model is:

$$Q_{\mathrm{c}} = \frac{V_{\mathrm{cell}}\, C_{\mathrm{NP}}\, N\, \Delta \mathrm{H}}{2}\left(1 + \frac{C_{\mathrm{P}}}{N\, C_{\mathrm{NP}}} + \frac{1}{K_{\mathrm{A}}\, N\, C_{\mathrm{NP}}} - \sqrt{\left(1 + \frac{C_{\mathrm{P}}}{N\ C_{NP}} + \frac{1}{K_{\mathrm{A}}\, N\, C_{\mathrm{NP}}}\right)^2 - \frac{4\, C_{\mathrm{P}}}{N\, C_{\mathrm{NP}}}}\right) \quad (3.27)$$

where Q_{c} is the cumulated heat generated by the adsorption of proteins on the surface of NPs and V_{cell} the cell volume. Indeed, performing an iterative fitting via standard Marquardt methods leads to the extraction of N, K_{A}, and ΔH. More details of Equation 3.27 and the related procedure have been presented elsewhere[238, 239]. An example of using the above-mentioned model is illustrated in Figure 3.10B (lower graphs)[127], which compares the effect of particle size and

hydrophobicity on the adsorption of HSA. According to the results obtained using this model, the number of adsorbed proteins on more hydrophobic NPs was almost six times higher than hydrophilic NPs. Also, increasing the size of NPs from 70 nm to 200 nm increased the number of adsorbed proteins proportionally to the surface area of the NPs.

In addition to the one-site model, researchers have also used two-sites models to explain protein adsorption on NP surface and fit the titration data obtained by ITC[240-242]. For instance, Nasir *et al.* reported that the heat profiles of human carbonic anhydrase (HCA) adsorption on 26 nm PS NPs required a two-site binding model to obtain a proper fitting[242]. However, for larger NPs (49 and 94 nm), one-site binding model was found to be the best choice. Thus, selecting a proper model for fitting the results of ITC experiments is key to extract reliable thermodynamic parameters of the system. From their ITC results, the authors observed an inverse relation between the size of hydrophobic PS NPs and the number of HCA proteins adsorbed per surface area. They hypothesized that the higher curvature reduced protein-protein repulsive interactions, therefore increasing the density of adsorbed proteins on the surface. They concluded that the balance between protein stabilization at the surface and the inter-protein interactions determines the equilibrium coverage of proteins.

Interestingly, the results of ITC experiments could reveal the origin of non-covalent protein-NP interactions based on their thermodynamic signatures. Indeed, spontaneous interactions occur when the Gibbs free energy associated is negative ($\Delta G < 0$). Accordingly, its sign depends on both magnitude and signs of enthalpy and entropy changes ($\Delta G = \Delta H - T\Delta S$). The magnitude of the enthalpy of interaction depends on the bond lengths and angles (*e.g.* in hydrogen bonding) while its negative sign illustrates the favorability of interactions between proteins and NPs[235] that is generally achieved in case of non-covalent bonds[76]. Besides, two contributions are included in the entropy change, *i.e.* the solvation entropy change and the conformational entropy change. In the case of hydrophobic interactions, the solvent entropy is positive because of the desolvation of water, while conformational entropy change is negative due to a decrease in the rotational freedom and the relative disorder of the system[243]. Indeed, the balance between these

two contributions decides if the entropy of reaction is favorable (positive). Therefore, the driving force of protein adsorption to the surface of NPs differs case by case.

Chakraborti *et al.* studied the interactions of polyethyleneimine-functionalized ZnO NPs with BSA by ITC[244]. They reported a favorable enthalpy change (negative value) showing possible weak van der Waals and/or electrostatic interactions between proteins and NPs, while the contribution of entropy was negligible. In another study by Henzler *et al.*, they investigated the adsorption of β-lactoglobulin on spherical polyelectrolyte brushes[245]. According to the ITC results fitted by a two-sites binding model, the adsorption process was only driven by entropy as it was endothermic ($\Delta H > 0$) and $\Delta S < 0$. Indeed, they explained it by proposing a mechanism where the counterions of the protein and the polyelectrolyte were released upon the adsorption of proteins. Other studies on the investigation of protein interactions with NPs by ITC can be found elsewhere[76, 233, 237, 246, 247].

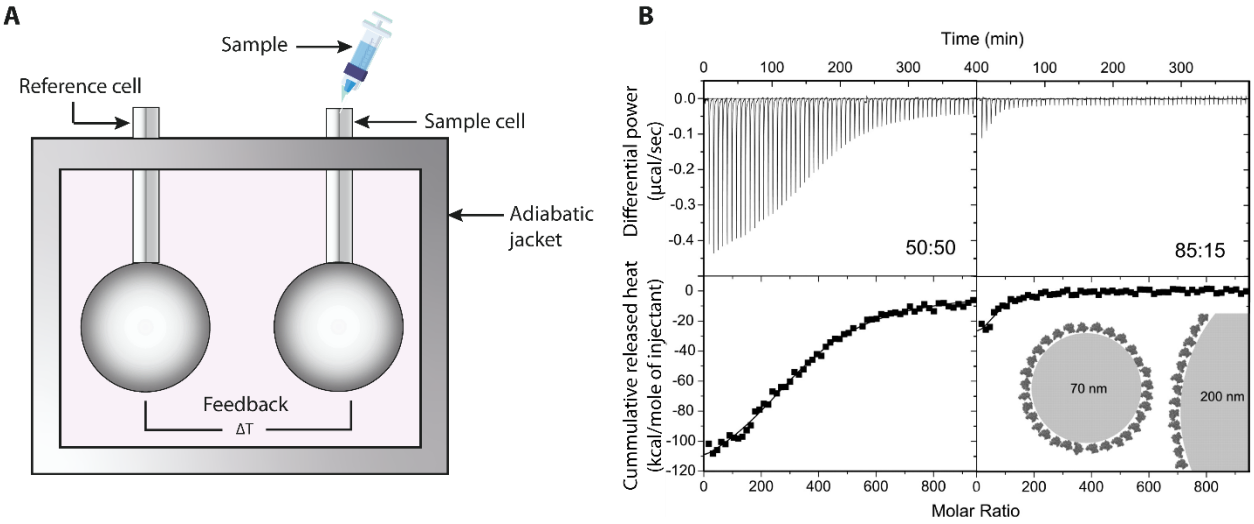

Figure 3.10. ITC for studying protein adsorption on NPs. (A) Schematic of an ITC instrument; aliquots of the solution are injected into the sample cell via a syringe. (B) Example of data obtained by ITC; HSA protein titration in the mixture of NIPAM/BAM NPs with different compositions. Upper graphs represent raw data and lower ones the integrated heats fitted with the one-site binding model from Equation 3.27. Panel B was adapted with permission from [127].

Although ITC enables to extract thermodynamic parameters and investigate the protein-NP interactions, interpretation of results could be complex in some cases. Indeed, in addition to the non-covalent interactions, other phenomena such as solvent reorganization as well as protein reconfiguration, aggregation, and denaturation could contribute to the overall heat signal measured by the technique[237]. As a result, it would be tough to specify the relative contribution of each phenomenon to the calculated Δ*H* and Δ*S*. Thus, cautious analysis is required to accurately shed light on the origin of interactions between proteins and NPs.

Table 3.1. Summary of quantitative techniques

Technique	Extracted parameters	Sample	NP size (nm)	Advantages	Drawbacks
Ex situ techniques					
UV-vis spectroscopy	A_0, K_A	100-1000 µL	Any	Easy-to-use Quantifies the extent of aggregation	Incapable of detecting multilayers
Fluorescence spectroscopy		~100 µL	Any	Easy-to-use	Requires fluorescence
Mass Spectrometry-Based Proteomics	$NSAF_k$	10-100 µL	Any	Identifies proteins within the corona Highly sensitive Produces large amounts of information Use in complex media	High experimental variability Relies on large databases and statistical analysis Relies on optimized separation process Very specialized and expensive equipment
TGA	W_{tot}	Dry state - µg to mg	Any	Easy and accessible Use in complex media	Assumptions made about the interpretation of weight loss Low sensitivity for large NPs and few adsorbed proteins
AUC	c(t,r), N_{max}	< 500 µL	< 50	Label-free proteins Additional measurement of size, molecular mass and kinetic constants	Requires reversible adsorption Requires an accurate evaluation of NPs and proteins parameters Limited to high density materials
DCS	t_s, δ	~100 µL	5-1000	Use in complex media Unaffected by aggregation Mixture of NPs of different sizes	Difficult to determine $\rho_{eff,NP}$ Requires reversible adsorption
In situ techniques					
Dynamic Light Scattering	R_H, K_D, n	1 mL	$R_{NP} \sim R_{Prot}$	Easy implementation Quantitatively relates change in R_H with protein structure and orientation on NPs Alternative techniques: Zeta Potential & DDLS	Very sensitive to aggregation Sensitive to free proteins Not suitable for large NPs
Fluorescence Correlation Spectroscopy	R_H, K_D, n	<1 mL	$R_{NP} \sim R_{Prot}$	Specific for fluorescent objects and remove the non-fluorescent background Sensitive to very low concentrations Quantitatively relates change in R_H with protein structure and orientation on NPs	Sensitive to aggregation Not suitable for large NPs Requires fluorescence
Fluorescence Quenching	F/F_0, K_{SV}, k_{on} & k_{off}	~1 mL	Any	Straightforward and only requires a spectrofluorometer Static and dynamic measurements possible Offers insight about reversibility of protein adsorption Extraction of thermodynamic parameters	Many potential issues on the measurement Unexplained large discrepancy of K_{SV} compared to other techniques Difficult interpretation May require labeling
Flow Cytometry	N, K_D, n	<0.1mL	> 50	Multiplexing potential Very small volumes Quantification of functional epitopes	Requires antibody reporter binder May require optimization to improve detection limit and precision
NMR	N, protein structure	< 1 mL	$R_{NP} > R_{Prot}$	Unaffected by aggregation Non optical (can be used in turbid environments)	Specific proteins (no mixture) Limited to small proteins Slow exchange processes only
Diffusion NMR	R_H	< 1 mL	$R_{NP} \sim R_{Prot}$	Non optical (can be used in turbid environments) Use in complex media Multiplexing	Isotopic labeling
SPR LSPR	θ_{SPR} λ_{max}	2-400 µL	Any	Large variety of NPs Label-free proteins Real time monitoring – Kinetic constants	Sensitive to motion and temperature Limited sensitive area
ITC	N, K_A, ΔH	170 -1400 µL	Any	Extraction of thermodynamic parameters	No detection for entropy-driven adsorption Limitation for the sample concentration due to aggregation

3.4 Protein and corona structure at the NP interface

3.4.1 Protein conformation at the NP interface

Several techniques allow to retrieve information on the conformation of adsorbed proteins. One of the most common ones is circular dichroism spectroscopy (CD), which relies on the absorption of polarized light. In the case of proteins, the CD signal is generated by their secondary structure. For instance, α-helices and β-sheets produce characteristic CD signals[248]. This property has been used in many studies to detect and quantify structural changes of proteins upon adsorption onto NPs[246, 249-255]. Recently, the high photon flux provided by synchrotron radiation CD (SRCD) has enabled to access a broader spectral range and higher sensitivity[256-258]. SRCD has also proven useful for *in situ* analyses of NP-bound proteins, as it revealed destabilization of weakly bound proteins (soft corona)[259].

FTIR also allows to study the secondary structure of proteins. When the sample is subjected to infrared radiation, chemical bonds get excited and therefore vibrate at certain frequencies. Protein bonds are characterized by specific absorption frequencies. In particular, amide bands are used to monitor the conformation of both the backbone and side chains of proteins. FTIR has been used to discern changes between α-helices and β-sheets structures due to protein corona formation[260-264]. In addition, relative quantification between α, β and random coils can be studied[261].

With a similar approach, Raman spectroscopy is sensitive to molecular bonds by measuring the frequencies at which the sample absorbs. Raman spectroscopy and surface-enhanced Raman spectroscopy (SERS) monitor amide bands characteristic of either α-helices or β-sheets[265, 266]. At the surface of plasmonic NPs, the Raman signal is enhanced due to surface plasmons. Taking advantage of this phenomenon, SERS has been used to discern qualitative changes in proteins secondary structures at low concentrations[267].

Specific NMR experiments also enable to get structural information. In particular, 2D chemical shift mapping and hydrogen-deuterium exchange (HDX) experiments allow to detect the number and location of amino acid residues affected by the binding to NPs, and therefore to identify the

regions in the protein that interact with NPs, as well as potential conformational rearrangements[268-270]. Solvent exchange spectroscopy (SOLEXSY) experiments can further be used to test the presence of additional layers of weakly bound proteins, which would undergo structural modifications on a faster time scale[270].

Fluorescence resonance energy transfer or Förster resonance energy transfer (FRET) has also been used to to monitor conformational changes of adsorbed proteins. This technique is based on the distance-dependent energy transfer from an excited donor fluorophore to an acceptor. Therefore, the use of site-specific labeling, for instance by attaching two different fluorophores to opposite ends of a same protein, allows to probe its folding[271]. With this approach, Raoufi *et al.* found that fibronectin underwent more pronounced conformational changes on bare AuNPs than on NPs that had been pre-coated with different proteins[272]. In case the NP acts as an acceptor or donor itself, only one protein site needs to be labeled, as demonstrated by Qu *et al.*, who studied the affinity and adsorption orientation of HSA on quantum dots[273].

Other techniques have occasionally been used to study protein conformation. For example, small-angle neutron scattering (SANS) has helped to determine if the shape of adsorbed proteins was maintained[274-276], while differential scanning calorimetry (DSC) has revealed structure loss and destabilization of adsorbed proteins[277].

3.4.2 Structure of the protein corona

Apart from the protein conformation, the structure of the corona itself (thickness, morphology, organization,) can be characterized through various techniques. First, all the correlation-based techniques already described in this paper can be used to determine the thickness of the adsorbed protein layer (see section 3 and Table 3.1).

As an imaging technique, TEM allows to visualize the protein corona and therefore to get information about its shape, thickness, density and homogeneity[278-281]. Negative staining techniques are often used for these purposes. Recently, cryo-EM has offered even higher resolution and enabled to quantify individual adsorbed proteins and to determine their orientation on the surface[246, 259]. Immuno-mapping strategies with antibody-labeled AuNPs have

also allowed to identify the spatial organization (orientation and position) of adsorbed proteins[128, 282].

Small-angle X-ray and neutron scattering (SAXS and SANS) have helped to characterize the structure of the protein corona in terms of thickness and uniformity[276, 283]. In the case of NPs coated with polyelectrolyte brushes, SAXS has even enabled to characterize the amount and distribution of adsorbed proteins as a function of time[284, 285]. Aggregation phenomena in proteins-NPs systems have also been studied via these techniques, to obtain the size and morphology (mass fractal dimension) of the aggregates[286-288].

Information about the layer conformation can also be gained through quartz crystal microbalance with dissipation monitoring (QCM-D). Real-time monitoring of both the shifts in frequency and energy dissipation have indeed allowed to determine the thickness of the layer, its dynamic organization, whether it was fluid or rigid/compact, and to distinguish between hard and soft coronas[289-292].

Finally, evaluation of the protein corona morphology can be performed through AUC by calculating the frictional ratio, which compares the friction due to sedimentation of the studied particle to the friction of an ideal sphere. Thus the asymmetry of a particle can be determined when the frictional ratio deviates from 1 [78].

3.5 Are protein multilayers the exception or the rule?

After more than a decade of research on the protein corona formation and structure, many studies have tried to tackle the mono- *vs* multilayer hypothesis. The hypothesis of multilayer adsorption stems from the concept of the existence of “hard” and “soft” coronas. Though this denomination was meant to describe the long- and short-lived interactions between proteins and NPs (“hard” and “soft” corona, respectively)[107, 127], this concept reinforced the hypothesis of multilayered protein adsorption. Indeed, it has been hypothesized that upon adsorption of a sufficiently hard (long-lived) protein corona, a subsequent protein layer with a weaker affinity (soft corona) could adsorb on top of the initial protein layer through protein-protein interactions[31]. Even though protein-protein interactions can be observed *in vivo*, serum proteins

are considered as colloidally very stable. Without significant denaturation of the proteins (or fibrillation[114]), it would therefore be surprising to see proteins "aggregating" preferentially around NPs[73, 118]. Since weak protein-protein interactions give rise to soft (and multilayered) protein corona, protein multilayers have been thought to be easily perturbed by purification steps and, as a result, very difficult to characterize[120]. Many attempts aiming to reveal the presence of the soft corona have been reported[31, 113, 120, 130, 232], but these still remain challenged by other reports[70, 73, 118]. Hence, the question regarding the structure of the protein corona layer(s) has no clear answer yet and is up for scientific debate.

In an attempt to resolve this issue, we have analysed the results of 88 research articles explicitly dealing with mono- or multilayer adsorption, which corresponded to a total of 308 different NP-protein systems. (we here define a NP-protein system as a NP of a given size and chemical composition that was incubated in a solution containing a known protein, a known mixture of proteins or a biological extract (*e.g.* serum, blood)). Statistical analysis of this set of publications allows to graphically represent the reported occurrence of protein mono- and multilayers across all systems, and to extract trends depending on the measurement technique, separation technique, type of protein solution, and NP radius (see Figure 3.11). Details of the research methodology and the criteria used to define the occurrence of a mono- or multilayer are provided in the supporting information section, and all extracted data are available in the supplementary Table.

3.5.1 Characterization techniques have a minimal impact on multilayer occurrence

To determine if the occurrence of mono- vs multilayers depends on the experimental technique, we represented the distribution of mono- and multilayers for 13 characterization techniques (see Figure 3.11A). The occurrence of multi- and monolayer systems reported a significant prevalence of monolayers over multilayers for most of the techniques, with exception made of DCS, SPR, fluorescence spectroscopy, and fluorescence quenching, which represent ~13% of all the NP-protein systems analyzed. Overall, about 75% of reported protein coronas appear as monolayers, which contrast with reports claiming that multilayers are more frequently observed[121]. Some

techniques such as FCS, UV-vis AUC, CD and NMR (constituting ~28% of the NP-protein systems investigated so far) report less than 5% of multilayers systems.

Since the dataset studied across all techniques (308 systems for 13 techniques) can still be considered as modest, the previous analysis may be subject to variation due to small sample size for each technique. To address this issue, techniques were grouped according to their type of measurement of protein adsorption and the physical phenomenon on which they are based. Techniques were divided into 4 different categories, namely radius-based techniques, UV and fluorescence spectroscopy, other spectroscopic techniques and the remaining techniques (ITC, TEM, ICP-MS, SANS, QCM and AFM) to generate Figure 3.11B. As a result, the percentage of multilayers converges towards ~26%, except for UV and fluorescence spectroscopy (14.3%), but differences between groups of techniques are not statistically significant based on an analysis of variance (ANOVA). Therefore, it appears that the type of technique used does not critically influence the occurrence of multilayers observation, independently of the NP-protein system considered. This leads to the conclusion that techniques were overall equally appropriate, and that none of the groups of techniques was more proficient in the observation of multilayers.

It is important to note that one study used the BCA quantification assay to assess protein adsorption on 105 NPs-serum systems of AuNPs with different coatings, that all resulted in a monolayer corona (see supporting information)[58]. To preserve other studies' significance, only 9 systems were included in our analysis, *i.e.* the 3 core sizes the authors tested with 3 representative coatings each (neutral, anionic and cationic). As a consequence, with the consideration of these systems, the difference for the detection of multilayers between UV and the other groups of techniques could be significant.

Despite the minimal influence of the quantification method on the detection of protein mono- or multilayers, it has been reported that purification of the proteins-NPs complexes has a great impact on the composition of the protein corona and the observation of weakly bound proteins[120, 131, 293]. Therefore, a second analysis was performed, where techniques were this time classified into two categories, namely as *in situ* and *ex situ* techniques. Remarkably, it appears that techniques requiring physical separation of proteins (*ex situ* category) are as likely to detect

multilayers as techniques that do not require separation (*in situ* category), as demonstrated by the minimal difference in their respective percentage of multilayers (24 and 27% respectively, see Figure 3.11C). This analysis indicates that despite the significant efforts invested to design techniques capable of quantifying protein adsorption *in situ*, there is still only a small number of systems exhibiting multilayers. This observation seems to contradict the current thinking and may demonstrate that either *in situ* techniques are not as efficient as we suppose or, alternatively, multilayer adsorption is not affected by the separation process.

On one hand, one must keep in mind that the protein corona literature is constantly evolving, with a few hundred publications each year. *In situ* techniques (*e.g.* flow cytometry[77], NMR[75]) have made significant progress to improve their sensitivity to distinguish soft corona and multilayers. Recent technical advances do not yet have a significant impact in the present analysis, but they are expected to have one in the next few years, as more systems will be explored.

On the other hand, experimental studies have shown contradictory results regarding the impact of the separation technique on the protein corona composition and structure. One study showing differences in the protein corona composition using AF_4 or centrifugation[120] separation techniques seems to contradict another one mentioning no significant impact between separation techniques[143]. Interestingly, in our analysis, the category of techniques with the lowest occurrence of multilayers is UV and fluorescence spectroscopy, in which the studies were found to frequently use harsh centrifugation protocols for purification. In most cases, between 1 and 3 centrifugation steps are performed to ensure proper separation of NPs and proteins[58, 109, 113, 141, 150, 246]. Therefore, this seems to strengthen the hypothesis that only harsh purification protocols (*e.g.* centrifugation) can significantly disrupt weakly adsorbed proteins, while softer separation techniques (*e.g.* AUC, DCS, capillary electrophoresis, AF_4) may leave the protein corona relatively undamaged. Therefore, pooling both soft and harsh separation techniques in the same technique categories might have diluted the impact of the latter in our analysis. A statistical analysis could have been performed using separation techniques as criteria, but the small dataset (~ 85 systems) and the large predominance of centrifugation for these studies would not have produced information with a high enough statistical power. Therefore, the global conclusion that the

multilayers occurrence does not depend on the category of *in situ* or *ex situ* should be interpreted with caution.

3.5.2 Mixtures of proteins do not promote multilayer formation

Another parameter that is usually considered important is the type of protein solution. Not only may proteins exhibit different behaviors when studied alone, but studies of the Vroman effect have demonstrated that mixtures of proteins can sometimes cause surprising phenomena. It is often assumed that solutions containing different proteins, such as serum, are more likely to produce multilayers. One of the hypothesized scenarios is that a first layer of proteins irreversibly adsorbs on NPs (often simultaneously exhibiting conformational changes), then facilitating the subsequent formation of protein multilayers through protein-protein interactions[113, 116]. Therefore, increasing the variety of proteins in the solution might increase the likelihood of such scenario. In the following analysis, we divided our pool of protein-NP systems into two different categories: those using protein mixtures (containing two or more different proteins) and those using single protein solutions. As shown in Figure 3.11D, both categories share very similar proportions of protein monolayers (75% and 71% respectively). The small difference in ratio observed between the two categories is not statistically significant. This result implies that the richness of proteins interactions and the complexity of serum or proteins mixtures do not specifically favor multilayers formation, as previously hypothesized.

Interestingly, single protein studies largely dominate the protein corona field of research (>75%). Simplicity is obviously more attractive when designing protein adsorption experiments, as more parameters can be controlled, making the process of identifying multilayers more robust. Yet, the orientation of the adsorbed protein affects its monolayer mass density and dismissing this effect may result in misleading conclusions, even for single protein studies. Multiple thicknesses of protein corona monolayers have indeed been reported for a same protein, either ApoA-1 (2.5-8 nm)[69], HSA (3.2-8.4 nm)[66, 206] or fibrinogen (5-45 nm)[68]. Protein mixtures are even more difficult to assess as not all proteins have the same size (therefore surface coverage), mass, amino-acid composition and 3D structure. They require more complex analysis and extensive control experiments. For instance, accurate surface coverage calculations can require the combination of

BCA assay (total protein mass adsorbed) with a detailed mass-spectrometry analysis of the relative abundance of proteins[150].

3.5.3 The occurrence of protein multilayers is positively correlated with NP radius

The NP radius has also been hypothesized to influence the occurrence of multilayers formation in many reports[117, 119, 252]. Piella *et al*. suggested that proteins perceive large NPs as flat surfaces and are therefore subjected to greater conformational changes upon adsorption, leading to the formation of multiple layers. On the contrary, small NPs exhibit smaller contact surface with proteins, thus inducing fewer rearrangements upon adsorption[117]. Bibliographic data were analyzed to determine if there is a correlation between the NP radius and the detection of mono- or multilayers in the protein corona. The box plot in Figure 3.11E shows the distribution of protein-NPs systems exhibiting mono- or multilayers as a function of NP radius, while Figure 3.11F represents the evolution of the multilayers detection ratio as a function of NP radius. This analysis shows that the probability of finding multilayers increases with the NP radius, with a threshold located around 20 nm. There is indeed a strong prevalence of monolayers for small NP radii: 97% for NP radii similar to proteins' or smaller ($R \leq 3$ nm), more than 90% for radii < 10 nm and more than 80% for radii < 20 nm, whereas for larger NPs the probability fluctuates around 45%. This general trend is consistent with what has been observed in past studies covering a wide range of NP sizes[117, 119, 252].

However, the higher number of studies reporting the use of small NPs may introduce a slight bias in this analysis. In the present dataset, 60% of the systems studied include NPs with a radius inferior to 20 nm (40% with R < 10nm). The statistical significance of our analysis therefore decreases when the NP radius increases. This discrepancy between small and large NPs could be explained by the limitations of the techniques used to study the protein corona. As discussed in section 3.2.2, all the radius-based techniques suffer from a low precision for large NPs, as the thickness of the protein corona becomes almost negligible compared to the NP radius. Spectroscopic techniques are also challenging to implement for large NPs due to strong NP scattering and absorption. Finally, high concentrations of large NPs are generally difficult to

manipulate without aggregation and/or precipitation, which can be detrimental for techniques with low sensitivity. Based on our literature analysis, only SPR, DCS, ITC and DLS have been used to determine the presence of mono- or multilayers in the protein corona for the largest NPs (R > 50 nm for ~15% of the dataset). DLS and DCS frequently observed multilayers for large radius (R > 50 nm). Since both techniques are radius-sensitive, they are more prone to variations in the case of large radii. On the other hand, SPR and ITC, which are not size-dependent, have shown opposite results: SPR studies frequently report multilayers formation for almost any NP size, in contrast to ITC, which did not report any multilayers above R > 50 nm up to 200 nm. This seemingly contradictory result might originate from the lower sample size for these two techniques. Overall, even considering the potential bias from DLS and DCS for large NPs, the correlation of multilayers with NP radius remains.

This correlation was further confirmed by performing an analysis by groups of techniques, type of measurements and type of protein solution using the previously observed threshold of R = 20 nm to define small NPs (R ≤ 20 nm) and large NPs (R > 20 nm). Again, a strong correlation between multilayer occurrence and NP size was observed. On average, for each category, multilayers were detected on large NPs (~15% and ~45% multilayers were observed for small and large NPs, respectively), with the exception of one category of techniques (category: other) exhibiting no clear trend. Considering the coherence of this analysis with the previous one, the result highlights the pivotal role of NP size for the occurrence of multilayers in the protein corona. Even though a complete elucidation of the adsorption mechanisms is still needed to fully explain and predict these observations, protein conformational changes induced by low surface curvature upon adsorption may appear as a reasonable explanation.

In light of these results, future studies should focus on refining our knowledge of protein adsorption onto larger NPs by improving the current measurement techniques or developping new ones that are more sensitive for larger NP sizes. We also suggest future studies to have a special focus towards the mechanisms of adsorption, in an attempt to unify contradictory findings. Only then will the impact of NP size and other parameters on the occurrence of mono- or multilayers be truly determined.

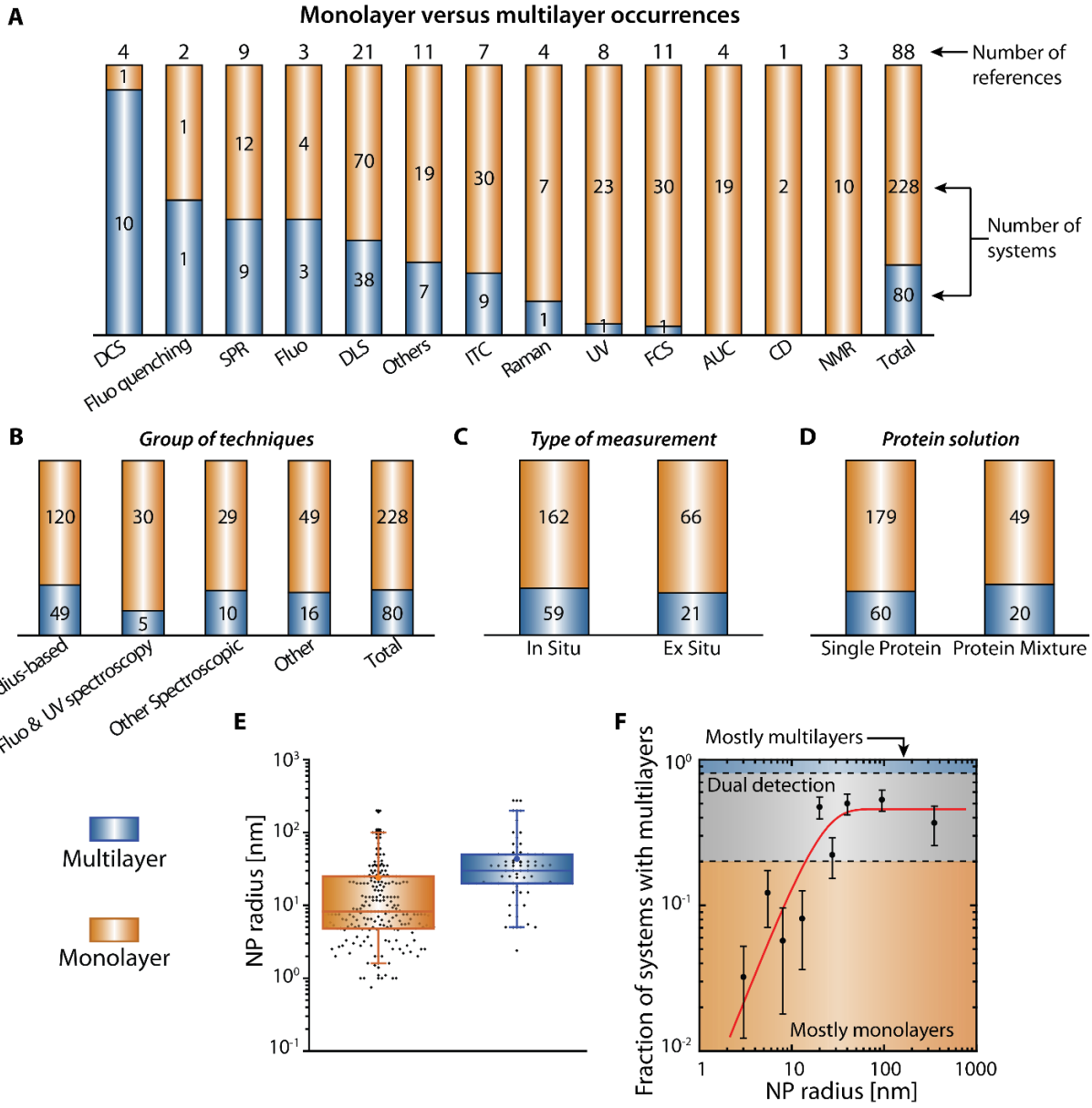

Figure 3.11. Dataset analysis of mono- (orange) and multilayers (blue) in the protein corona. Occurrence of proteins-NPs systems exhibiting mono- vs multilayers as a function of (A) the technique, (B) the group of techniques, (C) the type of technique used, (D) the type of protein solution, (E) and (F) the NP radius. Error bars in panel F represent the standard deviation calculated for a binomial distribution, the red line is a fit of a single exponential decay to highlight the general observation and the datapoints represent the largest NP size of their group.

3.6 Is protein adsorption on NPs a reversible or irreversible phenomenon?

Reversibility of protein adsorption has become a subject of debate among researchers. Indeed, several studies have reported that the protein corona consists of two parts; a “hard” corona that includes the proteins irreversibly bound to the surface of NPs, and a secondary layer called “soft” corona that describes loosely attached proteins that undergo dynamic exchange with the medium[31, 113, 120, 127]. Since the protein corona is considered as the fingerprint of NPs in a biological environment[58], it is essential to analyze how this corona evolves with time in terms of composition and structure, in order to have a better understanding of its influence over the biodistribution and the pathophysiology of nanomedicines[294]. For instance, the overall concept of the protein corona as a (bio)fingerprint of NPs is somehow at odds with the dynamic picture supported by the Vroman effect. In that regard, without reference to the hard and soft corona, an analysis of the dynamics of exchange in the protein corona is required. Accordingly, a total of 67 articles combining 210 different proteins-NPs systems were analyzed to determine the impact of the technique, type of protein solution, NP size and experimental design used (see Figure 3.12). Details of the research methodology and the criteria used to define the occurrence of reversibility or irreversibility are provided in the supporting information section. All extracted data are available in the supplementary Table.

3.6.1 Techniques proficiency to assess the protein corona dynamics

NPs-proteins systems from the bibliographic dataset were at first categorized by the characterization technique. In Figure 3.12A, the number of occurrences of reversible and irreversible protein adsorption are compared for each technique. According to this Figure, SPR, ITC, flow cytometry, LC-MS/MS, fluorescence quenching, and DCS techniques have mostly reported reversible protein adsorption. Our analysis could demonstrate the limitation or the potential of some techniques to detect the dynamics of protein adsorption. In Figure 3.12A, the number of references and systems is in general quite low for each technique, which makes technique-by-technique comparison quite difficult. However, a global analysis of the observations can be made. For several experimental approaches (SPR, DCS, protein assays, AUC, fluorescence

quenching, LC-MS/MS, ITC and flow cytometry), reversibility was predominantly found (>80% reversible). In some fewer cases (FCS, UV and fluorescence), occurrence of reversibility was much less predominant (40-60%), whereas DLS, Raman and FT-IR techniques and "Others", have mainly reported irreversible protein adsorption (<40% reversible). Combining all observations of reversible and irreversible systems yields a total of 35% of systems being characterized as irreversible while 65% displayed a reversible or dynamic behavior.

To examine the impact of techniques on the occurrence of adsorption reversibility, all techniques were sorted into categories based on the physical phenomena used to assess adsorption reversibility (Figure 3.12B), as previously established in section 3.5.1. Two categories (radius-based and other spectroscopic techniques) converge towards 45% of systems showing irreversible adsorption throughout our pool of studies. However, the two other groups of techniques, UV and Fluorescence spectroscopy along with "Other" both observe less frequently irreversible adsorption, with ~25% and ~15% respectively. An analysis of variance (ANOVA) showed that differences were statistically significant between categories (p-value < 0.01). This classification was therefore inefficient to eliminate the large differences between techniques presented in Figure 3.12A. Hence, protein corona reversibility may appear as technique-dependent and some categories of techniques may be more proficient in the observation of dynamic exchange, even though there is no theoretical basis (to our knowledge) that would justify such a large array of findings.

Regardless of the impact of the quantification technique on the occurrence of dynamic exchange in the protein corona, we may also expect a large influence of the type of protocol, either *in situ* or *ex situ*. Indeed, *ex situ* measurements imply an additional separation step that could remove weakly bound proteins and leave only strongly bound proteins, as seen in Section 3.1. Therefore, an increased number of reversible systems can be expected for *in situ* measurements. Surprisingly, the opposite trend is observed. Figure 3.12C indicates a statistically significant difference (p-value<0.01) in the occurrence of reversibility between *ex situ* and *in situ* measurements, showing respectively 19% and 39% of irreversible systems. This apparent impact of *in situ* or *ex situ* measurement on the occurrence of reversibility is not easily explained. Section 3.6.5 furthers the analysis by introducing the impact of experimental design.

3.6.2 Mixtures of proteins solutions do not impact the reversibility of the corona

Another parameter that is expected to have an influence on the protein corona dynamics is the composition of the protein solution, *i.e.* whether it is composed of a single protein or of a mixture of proteins. Indeed, as previously stated in section 3.5.2, it is often assumed that serum solutions are more likely to produce multilayers through the formation of a first layer of irreversibly bound proteins. In Figure 3.12D, both protein mixtures and single protein solutions exhibit around 65% of reversible NPs-proteins systems. Hence, it appears that protein mixtures do not exhibit a higher tendency to irreversibly adsorb on NPs, an observation that is in line with our previous analysis on the occurrence of multilayers in protein mixtures. Unsurprisingly, a large variety of observations is present in the literature, showing no clear trend of the impact of proteins mixture on the protein corona exchange dynamics[69, 117, 123, 161].

3.6.3 Adsorption time is crucial

Another important aspect that may explain the data shown in Figure 3.12 is the chosen time window of the experiments. Indeed, several studies have reported that proteins tend to form a loosely bound corona around NPs as soon as they are in contact with the particles[31, 113]. However, as time goes by, this reversible so-called soft corona may convert to an irreversible hard corona. This evolution more likely results from noncovalent interactions between the adsorbed proteins and the NPs that can induce orientation and conformational changes of proteins, therefore strengthening their adhesion over time[31, 113]. Unfortunately, it is impossible to assess this parameter in this review because of the lack of experimental details in the literature. Moreover, only limited data exists regarding the evolution of the desorption kinetics as a function of the incubation time[113].

Yet, the desorption constant k_{off} also contains important information regarding the adsorption process, as it is related to the average lifetime of a binding event. A lower desorption constant implies a lower probability of simultaneous release of all the interacting segments of the protein[295], therefore a longer mean residence time of the proteins on the NPs. For instance, a desorption constant of 10^{-2} s^{-1} corresponds to 1 minute of residence time on the surface of a NP,

while one of 10^{-5} s^{-1} is about 1 day. Thus, as the desorption constant decreases, assessing the reversibility of protein adsorption becomes more challenging, since longer experiments are required. In the context of nanomedicine, a k_{off} lower than 10^{-5} s^{-1} is often considered as irreversible, since the corresponding half-life of the protein-NP complex is much longer than the time it takes for NPs to be cleared from the bloodstream (hours to a few days)[296]. Figure 3.12E represents the desorption constants obtained for metallic NPs only, but with different proteins, all characterized by SPR. A very large distribution of k_{off} (5 to 6 orders of magnitude) is observed, showing a strong influence of the protein-NP system. Such large variation of k_{off} from one system to another is expected to impact the occurrence of protein adsorption reversibility. Interestingly, this k_{off} distribution shows a potential dependence on the size of NPs, where small NPs have larger k_{off} values than large NPs. Note, however, that the sample size covered by this study is rather small and the large distribution of k_{off} could as well be the result of different NP surface chemistries, protein-protein interactions, and the different protein conformational flexibility to provide steric stabilization to the NPs[297].

3.6.4 Larger NP size tend to facilitate reversibility of protein adsorption

Particle size affects protein conformation[298] and density[109] on NPs, which in turn affect the reversibility of adsorption. Studies were able to assess protein conformation on NPs surfaces over time and suggested that a gradual loss of secondary or tertiary structure was occurring when proteins adsorbed on NPs[260, 263, 266]. Nevertheless, this change of structure does not appear to be systematically correlated with adsorption irreversibility. On one hand, Basu *et al.* observed that structural changes of proteins adsorbed on PLGA NPs could occur without affecting the reversible nature of the adsorption process[261], on the other hand, Lehman *et al.* have demonstrated that thiolated proteins adsorbed on silica NPs had conformational changes and their adsorption was found irreversible[179]. Figure 3.12F illustrates the correlation between the occurrence of irreversible protein adsorption and the NP radius, as derived from our bibliographic dataset. For NP radii smaller than 50 nm, approximately 40% of systems were found to be irreversible. In contrast, larger particle radii produced mostly reversibility, at odds with the common hypothesis that larger NPs induce more conformation changes to the proteins that in turn make the adsorption process irreversible, but in line with Cristian *et al.* observation[260]. However, as

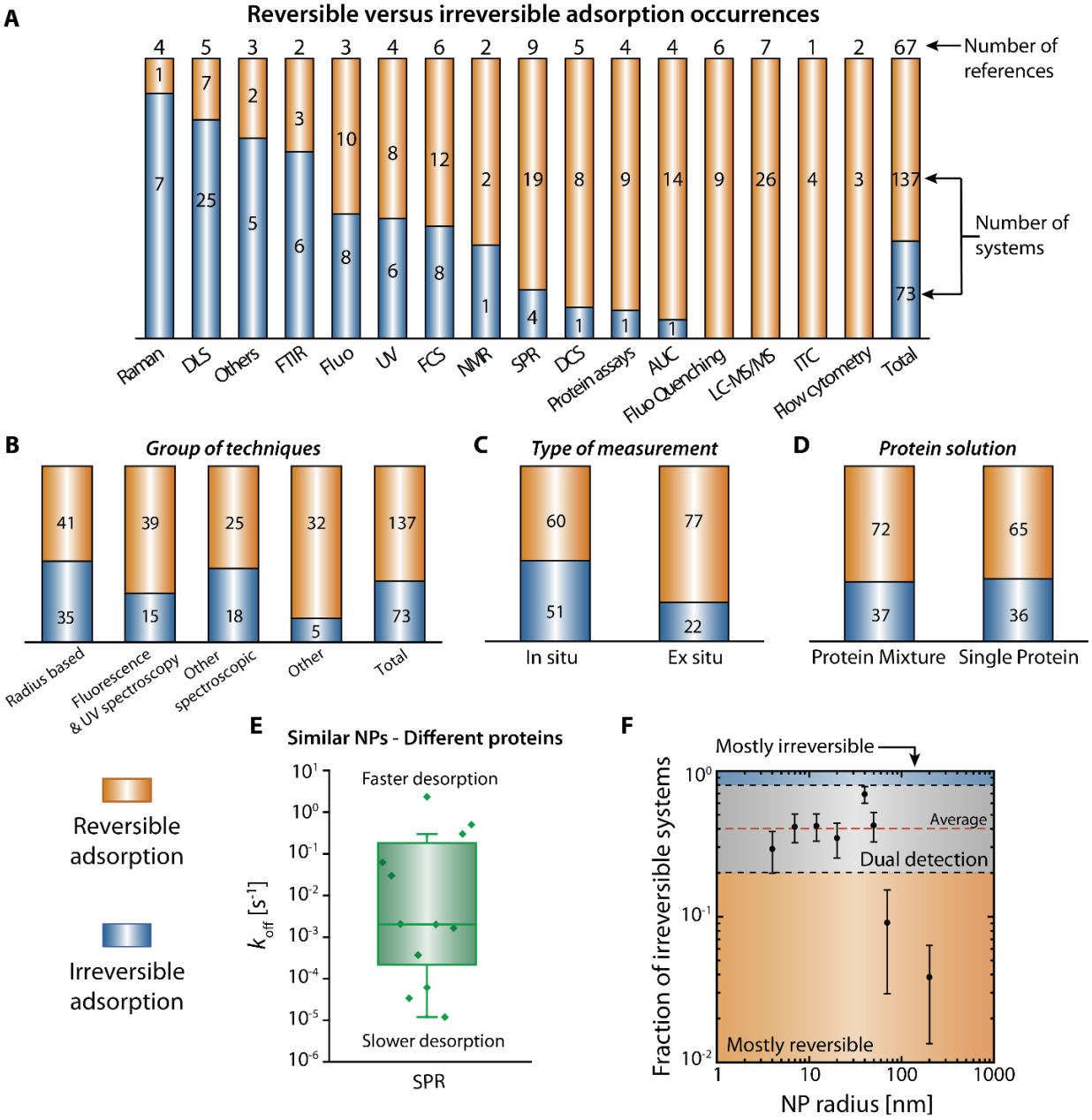

Figure 3.12. Dataset analysis of reversible (orange) vs irreversible (blue) adsorption. Occurrence of proteins-NPs systems exhibiting reversible or irreversible adsorption as a function of (A) the technique, (B) the group of techniques, (C) the type of measurement, (D) the type of protein solution. (E) Desorption constants obtained by SPR technique for systems composed of similar NPs but different proteins. (F) The distribution of the fraction of irreversible systems as a function of NP radius. Error bars in panel F represent the standard deviation calculated for a binomial distribution and the datapoints represent the largest NP size of their group.

observed in section 5, only a handful of experiments were directed towards larger NPs, so more studies will be needed to confirm this trend.

3.6.5 The dynamics of the protein corona is critically affected by the experimental design

The significant differences found across techniques and *in situ* or *ex situ* experiments do not seem in line with any theoretical basis or hypothesis that have been discussed in the published literature. We further the analysis of the bibliographical dataset using two new categories related to different experimental designs: the first category regroups reversibility studies performed by diluting the proteins-NPs, and the second category corresponds to studies where competition experiments (*i.e.* introducing a competing protein or molecule) were performed to test the exchange dynamics of the protein corona (see Figure 3.13A). The occurrences of reversible and irreversible adsorption for both categories are presented in Figure 3.13B. A great difference is observed between the dilution and the competition experiments, with ~45% and ~10% of irreversibility respectively. Statistical analysis demonstrates a highly significant difference (p-value < 0.00001), highlighting the non-trivial impact of the experimental design over the assessment of the reversibility of protein adsorption.

The literature is relatively scarce regarding the fundamental principles of reversibility and exchange dynamics of the protein corona[66, 69, 70, 113]. Both the dilution and competition approaches rely on the perturbation of the adsorption equilibrium. Assuming that the adsorption mechanism can be modeled by Langmuir or Hill's equations, as depicted in section 3.2.1, both experimental approaches may be equivalent in terms of assessing the reversibility of protein-NP binding. However, in a more realistic scenario where proteins undergo conformational changes or simply switch orientation upon adsorption, the equilibrium and kinetics of the adsorption process become strongly dependent on the experimental design used to assess them[299, 300]. In competition experiments, the presence of multiple species competing for the NPs surface may limit conformational or orientational changes at the NP surface, therefore favoring the exchange of the initially adsorbed proteins. As a result, competition experiments are more prone to detect

changes of the composition of the protein corona (dynamic exchange), while, for a dilution experiment, the same proteins would not (or very slowly) desorb from the NPs (Figure 3.13A). For the latter case, the protein binding would be categorized as irreversible, therefore creating the illusion of a static protein corona[300]. From our bibliographical data analysis (see Figure 3.13B), we found that about 10% of the protein-NP systems are truly irreversible, 55% undergo a simple adsorption process similar to the description provided in section 3.2.1 and the remaining systems (35%) are experiencing multi-step adsorption process.

Interestingly, this observation provides insights into the contradictory observations of the existence of a protein fingerprint and the omnipresence of the Vroman effect. Indeed, protein corona composition can evolve with time in a complex fluid but separating NP-protein complexes from free proteins or diluting a NP suspension may not always remove adsorbed proteins from the NP surface. No desorption does not imply irreversibility *per se*, rather, the adsorption mechanism could be more complex than expected.

3.6.6 Unification of opposing observations

We evaluated whether the aforementioned difference between dilution and competition experiments could impact the results for the categories evaluated in Figure 3.12: group of techniques, type of measurement, type of protein solution and NP size. We plotted the fraction of dilution experiments as a function of the fraction of irreversible systems (Figure 3.13C). A linear fit with a high coefficient of determination (R^2=0.912) could be drawn, indicating that the previously observed statistical differences mostly result from the use of competition *vs* dilution experimental designs. This observation suggests that the measurement of the protein corona dynamics is not correlated to any of the categories previously evaluated (*i.e.* the group of techniques, *in situ* or *ex situ* measurement and the type of proteins solutions), but mostly to the experimental design. The only deviation to this correlation was observed for large NPs of R > 50 nm exhibiting only ~6% of irreversible systems (for ~42% of dilution experiments). This once again corroborates the previous observation of a marked decrease of the occurrence of irreversible adsorption after the 50-nm radius threshold. Interestingly, small NPs (R < 50 nm) did not show this deviation, with ~40% irreversible systems assessed by 70% of dilution experiments. This tends

to suggest that the NP size or its radius of curvature may also influence the adsorption mechanism (as explained is section 3.5.3) in a way that has not been assessed so far, making large NPs more likely to exhibit reversibility. Up to now, all the evidence suggest that the adsorption mechanism is key to understand the protein corona dynamics. Yet, studies aiming to experimentally unravel the adsorption mechanism on NPs are still scarce. A better understanding of such phenomena will be particularly crucial for predicting the biological behavior of nanomedicines and maximizing their biological impact.

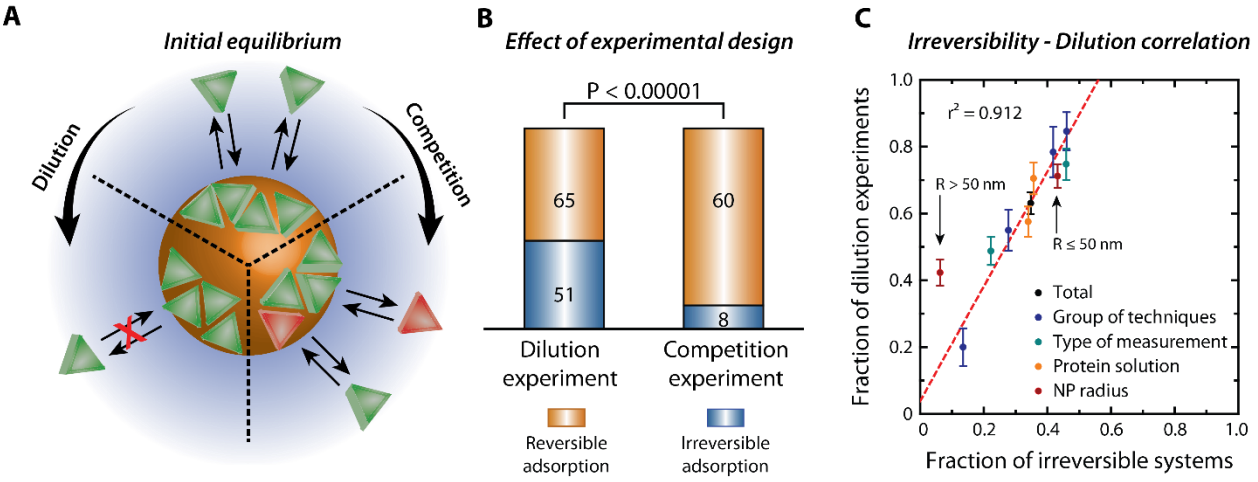

Figure 3.13. Impact of the experimental design on the reversibility experiment outcome. (A) Graphical representation of the dichotomous observations regarding the design of reversibility experiments. (B) Occurrence of systems exhibiting reversible or irreversible adsorption as a function of the experimental design. (C) The experimental design (dilution or competition) shows a strong correlation with the detection ratio of irreversibility Red line in C is a linear fit.

3.7 Outlook and conclusion

We here provided an overview of the techniques currently used in protein corona research, enabling us to draw a critical comparison of their advantages and limitations. We then used a large dataset of systems extracted from references published in the field during the past fifteen years to perform a statistical correlation analysis in an effort to identify potential experimental biases regarding key properties of the protein corona. The experimental design (*i.e.*, competition or dilution experiments) was found to be the main factor determining reversibility or irreversibility of the protein corona. The NP radius may also have a strong influence on the protein corona, impacting the occurrence of both multilayers and reversibility. Of course, the results of the analysis we provide are prone to evolve in the near future, thanks to the development of new techniques and the improvements of already existing ones.

We focused our statistical analysis of the recent literature on a few relevant parameters, but others could also play a role, such as the particles shape, type of material, and surface chemistry, or other experimental parameters such as the washing medium, the concentration ratio between NPs and proteins, or the presence/absence of flow during adsorption[109, 301-304]. A recent report has shown that the composition of the protein corona of NPs incubated in serum is donor-specific[305], which highlights the difficulty to extract general guidelines about the protein corona from the great variety of NPs and conditions studied. The development of high-throughput techniques would therefore be a great asset to better understand the effect of each parameter via large-scale experiments.

At last, the fact that protein corona studies with large nanoparticles are scarce also emphasizes the need for techniques adapted to large objects (radius > 100 nm). Such nanoparticles are indeed much used for clinical applications: liposomes have already been translated to the clinic for drug delivery[306], and other objects such as extracellular vesicles and virus-like particles have gained much interest these past years[307, 308]. Only few recent articles have analyzed the protein corona of these biologically-derived objects, paving the way for future studies[168, 309-312].

While the literature focused on the protein corona, the presence of other types of biomolecules in the corona has been largely overlooked, even though metabolites such as lipids, amino acids

and nucleotides have been shown to adsorb on NPs as well[186, 313]. The term “biomolecular corona” should therefore be more appropriate to describe NP interactions with a biological medium. Heterogeneity of the corona within a NP population is another key aspect that has been raised[314], but has not found much echo, probably due to the lack of techniques enabling single-particle analysis. Yet, great disparities can exist between NPs in a same sample[315], which should accordingly impact the biological behavior of these NPs.

All these unanswered scientific questions highlight the need for new techniques. In particular, the recent development of nanocytometry offers exciting perspectives to explore the properties of the protein corona. We expect that this technique will have a significant impact on the field, as it combines the benefits of a high-throughput technique, it is adapted to large particles and provides single-particle information. Other promising techniques are also emerging in protein corona research. For instance, to analyze heterogeneity, magnetic levitation can separate homogeneously-coated subpopulations of NPs[315], while single-particle analysis of the protein corona can be performed via single-particle nanoplasmonic sensing[316, 317] or microscopy techniques such as immunogold labeling[128] and super-resolution microscopy[318]. The use of microfluidic devices will help to create dynamic environments better mimicking biological environments[319, 320]. Over time, integrated microfluidic platforms, such as the on-chip electrical monitoring setup recently developed by Srivastava *et al.*, could provide inexpensive and simple tools to analyze the protein corona[321].

Chapitre 4 – « Deciphering *in vitro* and *in vivo* the protein corona formation and dynamics by differential dynamic microscopy»

Pierre-Luc Latreille [1], Jean-Michel Rabanel [1,2,] Marine Le Goas [1], Sina Salimi [1], Jochen Arlt [3], Shunmoogum A. Patten [2], Wilson C.K. Poon [3], Charles Ramassany [2], Patrice Hildgen [1], Vincent A. Martinez [3], Xavier Banquy [1]

1) Faculty of Pharmacy, Université de Montréal, PO Box 6128, Succursale Centre-ville, Montréal, Québec H3C 3J7, Canada

2) INRS, Centre Armand Frappier Santé Biotechnologie 531 Boul des Prairies, Laval, Québec H7V 1B7 Canada

3) School of Physics and Astronomy, The University of Edinburgh, Peter Guthrie Tait Road, Edinburgh, EH9 3FD, UK

Dans ce chapitre, nous avons développé et validé un cadre théorique de DDM en fluorescence pour permettre la mesure *in Situ* de l'adsorption de protéines. Nous évaluons l'impact de la concentration en NPs sur l'affinité des protéines aux NPs et la question de réversibilité est abordée. La DDM est utilisée pour des solutions protéines plus complexes comme le sérum bovin et on applique finalement la DDM pour mesure la désorption de protéines dans un système *in Vivo*, le poisson-zèbre.

En **Annexe 2**, se trouvent les informations supplémentaires cités dans le cadre de ce chapitre.

Ce manuscrit est présentement en préparation. Ces travaux seront envisagés être soumis au journal scientifique « *Science Advance* » en septembre 2021.

4.1 Introduction

Nanomedicine offers new possibilities to increase the pharmaceutical efficacy of currently available drugs as well as to unleash novel therapeutic strategies as what we are currently witnessing with the advent of gene therapy. During their travel in the blood stream, drug nanocarriers interact with blood proteins and often experience physical transformations of their size, shape, or aggregation, as well as chemical transformations at their surface. The interaction of free proteins with a NP's surface leads to the formation of the protein corona (PC), a protein shell which structure and composition play a major role in the fate of nanoparticles in any living body. For instance, the presence of ApoE and clusterin proteins in the PC has been associated with slower clearance from the blood stream[111]. Adsorption of other specific proteins has also been linked to enhanced brain translocation[322], hepatocyte targeting[323], reduced macrophage uptake[65], or an overall altered cellular uptake[58, 59]. Though, for nanomedicine, one issue is the possibility for the PC to completely negate the effect of targeting ligands[32].

Besides its importance on NPs properties, attempts to describe the PC's structure and formation mechanism have led to contrasting results. For example, transferrin was reported to form both multilayers and monolayers on a chemically identical system of sulfated polystyrene NPs[31 70]. Bovine serum albumin (BSA) has also been subject to such contrasting results, where monolayers[199, 324] and multilayers[162, 192, 193] were both reported on metal NPs. Reversibility of protein adsorption on NPs has also been the subject of controversies. Indeed, we demonstrated in a recent review that PC reversibility assays were heavily dependent on the type of experiment (dilution vs competition, see "Chapitre 3"). These recent examples represent only a small fraction of the large body of studies from which no consensus has yet emerged on whether 1) protein adsorption on NPs surfaces should be considered as a reversible or irreversible phenomenon and 2) if the PC is structured as a mono- or multilayer shell.

Most techniques used to study the formation of the PC (*e.g.* mass spectrometry[61], fluorescence[24], UV-absorbance[58]) use separation steps (*e.g* centrifugation, size exclusion)[131] that can alter the PC structure and composition. Other techniques are only mostly effective for small NPs (r_H < 20 nm) as the quantification methodology requires the measurement of the size growth of NPs caused

by protein adsorption, that is for instance dynamic light scattering[74, 113, 117, 122], fluorescence correlation spectroscopy[66, 69, 70, 73] or even analytical ultracentrifugation[78, 190]. However, we suggest here the use of DDM to measure characterise the PC without the need to physically separate protein adsorbed NPs from the protein free in solution. DDM has been used to assess the dynamics of particles[93] and bacteria[94, 96, 98, 325] in different imaging modalities such as confocal[98] or standard microscopy using fluorescence[100], phase contrast[97, 326, 327], bright-field[93, 328] and even dark-field[101]. Here we propose a new theoretical framework that enables the use of DDM in fluorescence imaging mode to quantify *in situ* protein adsorption while simultaneously measuring particle size and aggregation. In this design, the proteins were fluorescently labeled, and NPs were not fluorescent. Upon protein adsorption onto unlabeled NPs, fluorescence signal is emitted from the NPs surface and free proteins. This emission produced measurable fluorescence fluctuations (due to the NPs Brownian diffusion) that are used to quantify the adsorption reaction from the measurement of separate contributions of free and adsorbed proteins. As shown below, due to its high selectivity and sensitivity for adsorbed proteins, DDM provided unique information regarding the PC formation mechanism and its relation to NPs aggregation and stabilization both *in vitro* and *in vivo*. Using this approach, we highlight the affinity dependence of protein adsorption on NPs, a scaling that is observed with all proteins studied. Using more complex protein solutions, the methodology developed enable the identification of the Vroman effect at equilibrium in serum. We also push further and demonstrate that, under favorable conditions, the approach has a viable translational potential for quantitative *in vivo* measurements of protein desorption.

4.2 Results and Discussions

4.2.1 DDM measures protein adsorption, particle size, and aggregates' fractal dimension simultaneously and *in situ*

The experimental setup used to perform DDM experiments in the fluorescence imaging mode consists of a standard epifluorescence microscope equipped with a sCMOS camera. The processing workflow starting from the experimental design to the data acquisition and analysis is illustrated in FigureA. In brief, a fluorescently labelled protein solution of concentration C_p^0 is

mixed with a NP suspension and the resulting mixture is introduced in a rectangular glass capillary of 400 μm in thickness and observed under the microscope. When illuminated at the excitation wavelength of the fluorescent protein, the emitted fluorescence light is detected by the camera sensor and time series of images are recorded. The motion of the free and adsorbed proteins creates localized fluctuations in the emitted intensity which are evaluated by autocorrelation analysis of the image time series after a 2D Fourier transformation and proper (time and azimuthal) averaging[94, 97, 326]. This process allows to obtain the differential image correlation function $g(q, \tau)$ with q being the spatial frequency and τ the lag time between pairs of images. Under appropriate imaging conditions, the function $g(q,\tau)$ is related to the intermediate scattering function (ISF) $f(q,\tau)$ which describes the dynamics of the NPs [93, 94, 97]:

$$g(q,\tau) = A(q)[1 - f(q,\tau)] + B(q) \quad (4.1)$$

where $A(q)$ and $B(q)$ are the signal amplitude and the instrumental noise, respectively. For purely diffusive Brownian NPs the ISF takes the form $f(q,\tau) = \exp(-Dq^2\tau)$, where D is the diffusion coefficient of the NPs. The signal amplitude $A(q)$ is the convolution of the particle scattering properties and the optical transfer function $T(q)$ which is characteristic of the optical setup. Its mathematical expression can be derived as[97, 98, 329]:

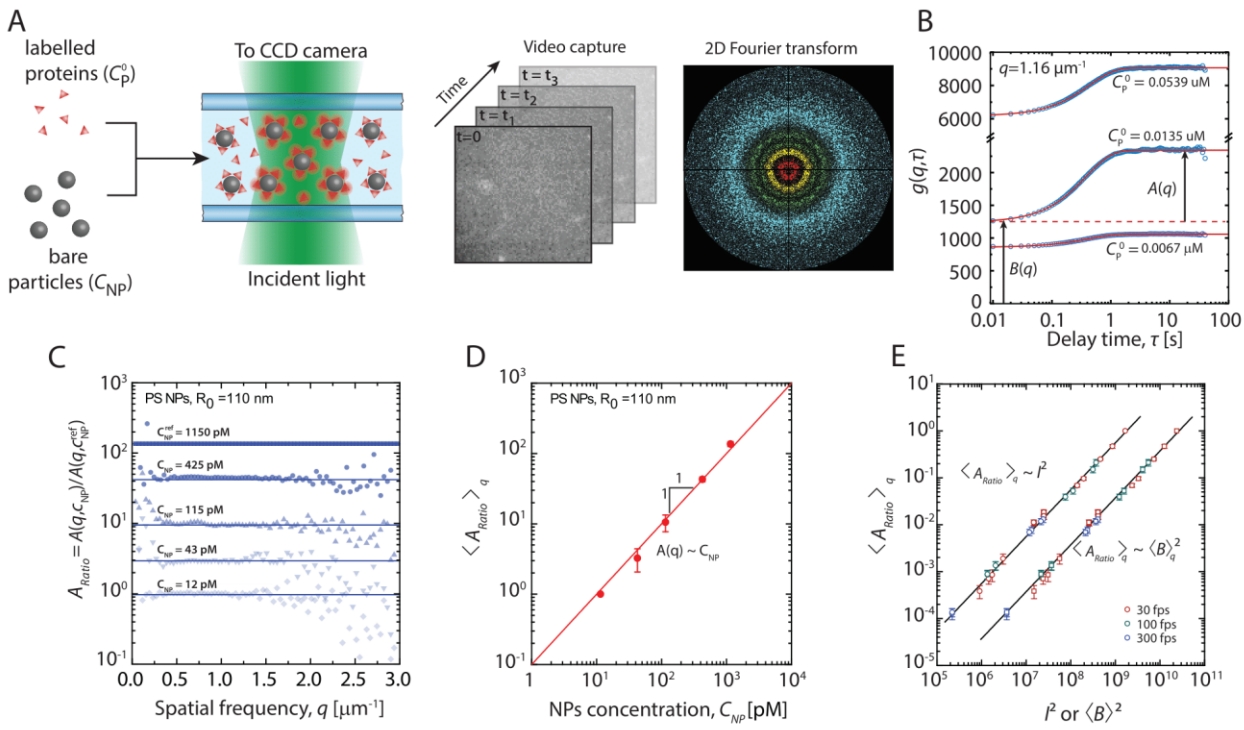

Figure 4.1. Quantification of adsorbed proteins using DDM. A) The workflow to assess proteins adsorbed on NPs starts by mixing the NPs with labelled proteins and letting them adsorb. The suspension is then transferred into a glass capillary for fluorescence microscopy imaging. Time series of images are then analyzed following the process described in the text to extract the 2D spectral transform and the autocorrelation function; B) Examples of autocorrelation function g(q,⍰) obtained at different protein concentrations showing the values of parameters $A(q)$ and $B(q)$ used for the quantification of the amount of protein adsorbed; C) Experimental evidence showing that the parameter A_{ratio} , which is directly proportional to the amount of adsorbed protein, is independent of the spatial frequency q and can therefore be averaged over q; D) Experimental validation of the linear relationship between A_{ratio} and the concentration of particles in the medium as predicted by Eq. 4.2; E) Validation of the power law dependence of A_{ratio} with the average total fluorescence intensity, independently of the frame rate used for the acquisition.

$$A(q) = 2C_{NP}^0 I_0^2 P(q) S(q) T(q) \qquad (4.2)$$

Where C_{NP}^0 is the number density of NPs in the field of view, I_0 is the intensity emitted per particle, $P(q)$ and $S(q)$ are the NP's form factor and suspension structure factor, respectively. Figure 4.1B

represents the evolution of $g(q,\tau)$ and its main parameters for a suspension of PS NPs of hydrodynamic radius R_0 = 110 nm in the presence of increasing concentrations of fluorescent proteins. In the situation where the protein is fluorescently labelled and adsorbs on the NP, the intensity of the NP, I_0, is directly related to the number of proteins adsorbed per particle, Γ, by $I_0 = \Gamma I_p$ with I_p being the intensity of a single protein. Based on these considerations, Eq. 4.2can be expanded to obtain an expression for Γ:

$$\Gamma = \left(\frac{A(q,C_p^0)}{A(q)^{ES}}\frac{C_{NP}^{ES}}{C_{NP}}\right)^{1/2}\frac{I_0^{ES}}{I_p} \tag{4.3}$$

Where $A\left(q,C_p^0\right)$ is the signal amplitude recorded at a total protein concentration C_p^0, and the superscript ES refers to the External Standard used to normalize the amplitude signal. The external standard is a suspension of fluorescently labelled PS NPs, identical in shape, size, and material to the probed NPs. In the absence of aggregation upon protein adsorption, the term $A_{ratio} = A\left(q,C_p^0\right)/A(q)^{ES}$ is independent of q as can be seen in Figure 4.1C and can therefore be averaged over q (as $P(q)$, $S(q)$, $T(q)$ from Eq. 4.2 cancels out in dilute conditions). If the use of an ES is not possible, A_{ratio} can still be quantified using a relative method. In that case, the expression for Γ is:

$$\Gamma = \Gamma_{\text{ref}}\left(\frac{A(q,C_p^0)}{A(q,C_p^0)^{ref}}\frac{C_{NP}^{ref}}{C_{NP}}\right)^{1/2} \tag{4.4}$$

Where the superscript refers to the reference state. The factor Γ_{ref} is measured by an orthogonal method, for example UV absorbance spectroscopy (see Figure 4.2A(ii) and Fig. S1). Both approaches, ES or reference state, where validated and used indistinctively.

In Figure 4.1D, we experimentally validated the scaling $A_{ratio} \propto C_{NP}$ using suspensions of fluorescently labelled PS particles identical to the particles used for the protein adsorption experiments. As shown in the Figure 4.1D, a linear relationship between A_{ratio} and C_{NP} was observed over two orders of magnitude of C_{NP}, from 11.5 pM (diluted regime, $\phi \approx 2.7\text{x}10^{-4}$) up to 1150 pM (multiple scattering regime, $\phi \approx 2.7\text{x}10^{-2}$). The same experiment was performed with phase contrast and brightfield imaging, and turbidity was found to impact the A_{Ratio} measurement at C_{NP}=425 pM (see SI section 2 and Fig.S2). As a result, the window of the linear response with

concentration is far larger in the fluorescence imaging mode. Indeed, with epifluorescence, the light does not have to go through all of the sample, therefore allowing to perform DDM analysis at high particle concentrations, well into the multiple scattering regime[98] and therefore capable of testing a very large range of concentrations. This attribute of DDM is not shared by other light-scattering techniques, especially DLS (and other related techniques) or fluorescence correlation spectroscopy (FCS).

The scaling of A_{ratio} with I_0^2 was also validated using the same fluorescently labelled NPs and modulating I_0 by changing the imaging speed or the intensity from the light source (see Figure 4.1E). We also verified that the impact of the experimental measurement conditions such as the size of the camera region of interest and the binning on measured values of $A(q)$ could be accurately described and predicted based on their effect (see SI section 2 and Fig. S2D&E).

If usually C_{NP} is known beforehand, it is not the case for I_0 and I_p and these parameters must be quantified in order to obtain Γ from Eq.4.3. The intensity per protein is simply obtained by considering that the time- and pixel-averaged intensity per frame, I_{av}, is directly proportional to I_p (or I_0 for the external standard). On a useful note, to speed up the measurement process described here, one can take notice that I_{av} and $B_{\text{av}} = \langle B \rangle_q$ are linearly dependent (see Figure 4.1**Figure**E and Fig. S2F) which allows to use B_{av} as a substitute to I_{av} which is often tedious to compute.

4.2.2 Monitoring of protein-particle interactions *in situ*

The methodology presented here was applied to the adsorption of fluorescently labelled LYZ protein (LYZ-RITC) on PS spheres of radius R_0 = 110 nm in buffered solution (pH = 7.4). The measured adsorption isotherm was obtained for a total protein concentration, C_p^0, ranging from 0.05 to 100 μM, using either the relative quantification method or the ES renormalization (see Figure 4.2A (ii)). Also shown in Figure 4.2A is the evolution of the particle size with the total protein concentration, which indicates the presence of strong NPs aggregation in a relatively narrow range of C_p^0 (1-4 μM). Presence of aggregates is also confirmed by a strong q-dependence of the A_{ratio} as shown on panel (i) in Figure 4.2B. In this concentration window, Eq. 4.3 must be extended in order to take into account the presence of the aggregates. Assuming fractal

aggregates of fractal dimension d_f, Eq. 4.3 is modified by multiplying the right-hand term of the equation by $1/\sqrt{N}$, N being the number of NPs per agregate which is given by $N = \left(\frac{R_N}{R_0}\right)^{d_f}$ where R_0 and R_N are the radius of a single NP and an aggregate of N NPs, respectively. The fractal dimension d_f can be quantified directly via DDM using Eq. 4.2 and using the Fisher-Burford model[328, 330] which provides an expression of the structure factor

$$S(q) = \left[1 + \frac{2(qR_G)^2}{3d_f}\right]^{-d_f/2} \quad (4.5)$$

that is based on the radius of gyration R_G of the aggregate.

Since d_f can be quantitatively assessed *in situ* by DDM, we have taken care of validating its quantification using different independent methods (see Fig. S3). As shown in Figure 4.2A (i), in the strong aggregation regime, d_f = 1.61±0.19, suggesting that aggregates are formed via a diffusion limited colloid aggregation (DLCA) mechanism[328, 331]. Figure 4.2B (ii) also provides an example of time evolution of d_f in the strong aggregation regime. As can be seen, d_f reaches a plateau value $d_f \approx 1.5$ within 10 min and was stable for almost an hour, after which signs of sedimentation were observed. The aggregation of NPs induced by the adsorption of proteins has been reported for sulfated PS particles in the presence of transferrin protein[70], but the impact of aggregation on protein adsorption has not been elucidated. The data shown in Figure 4.2A demonstrate that protein adsorption is not affected by particle aggregation and that adsorbed protein concentration follows a Langmuir adsorption isotherm in the whole range of C_p^0. Comparison of the kinetics of aggregation with the kinetics of protein adsorption clearly shows that LYZ adsorbs rapidly after 1-2 minutes of incubation (see Fig S4) whereas aggregation still evolves more than 50 minutes after incubation (see Figure 4.2B (i) and Figure S3C). Such an observation is also consistent with a DLCA aggregation mechanism where aggregates have extended low density and linear structures with small numbers of contact points between particles, which likely preserves surface accessibility for protein adsorption.

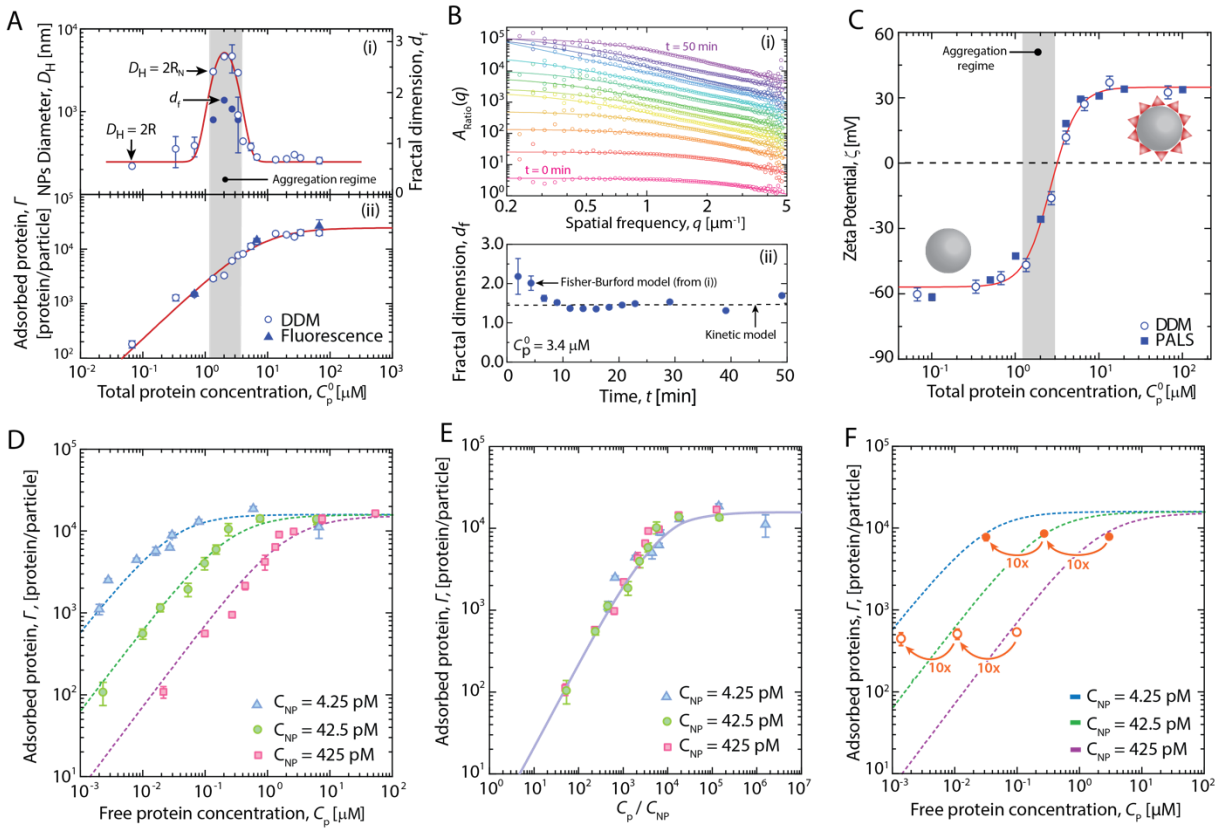

Figure 4.2. Quantification of LYZ on NPs, aggregation and fractal dimension. A) Adsorption isotherm and particle size measurement of PS NPs and LYZ mixtures. In the strong aggregation regime highlighted in grey, aggregates fractal dimension was quantified simultaneously by DDM; B) Protein adsorption triggers NPs aggregation. The aggregates fractal dimension, df, can be monitored by DDM; C) Quantification of adsorbed protein amounts by DDM shows excellent agreement with PALS providing an additional validation of the quantification method; D) Adsorption isotherms of LYZ on PS NPs at different particle concentrations were well described by the Hill adsorption model; E) Adsorption isotherms shown in D renormalized by the concentration of NPs collapse into a single master curve; F) Dilution of proteins / NPs mixture shows that the amount of adsorbed proteins after dilution is always consistent with the amount expected by an adsorption isotherm performed at the same dilution.

Since LYZ is a positively charged protein adsorbing on a negatively charged PS particle, changes in the particle surface potential are expected to occur along the protein adsorption isotherm. In

Figure 4.2C, measurements of the particles' zeta potential, ζ, performed via Phase Analysis Light Scattering (PALS), were compared to theoretical values of ζ calculated using the simple expression[209] $\zeta = \left(\frac{\Gamma}{\Gamma_{\max}}\right)\Delta\zeta + \zeta_0$ where zeta potential change $\Delta\zeta$=100 mV, the NPs zeta potential ζ_0=-65 mV , Γ_{max}=18000 where Γ and Γ_{max} were experimental values obtained by DDM. The excellent agreement between the two methods represents an additional orthogonal validation of the DDM approach to accurately quantify Γ. It also shows that particle aggregation occurred at a protein surface coverage ranging between 2800±200 and 8100±100 LYZ/NPs (16% and 45% respectively). At such surface coverage, the calculated NP effective surface charge is about half the surface charge of the bare particle indicating that full electrostatic screening has not occurred at the onset of aggregation. Therefore the aggregation process of the particle is likely governed by the bridging of the LYZ protein between two particles, "glueing" them strongly together and limiting self restructuration of the aggregate over time.

As we mentioned, fluorescence imaging allows to perform DDM analysis at high particle concentrations when turbidity becomes significant. However, at high concentrations of fluorescent protein, fluorescence quenching is an important limitation as it depends mostly on molecular interactions[157]. After establishing the range of fluorescence signal linearity, we observed that non linearity can have a significant impact on adsorbed protein quantification and could lead to overestimate the adsorbed amounts (see Fig. S5 and S6). It is therefore crucial to keep the concentration of fluorescence protein within the linear regime of concentrations. For LYZ, the concentrations used for adsorption isotherms were limited to C_p^0= 0.0067 – 67.4 µM and C_{NP}= 4.25 – 425 pM to ensure unbiaised quantitative results.

Figure 4.2D shows three adsorption isotherms measured at three different C_{NP}. The measured Γ values are well described by a Hill-type adsorption isotherm for all C_{NP}. The Hill-adsorption isotherm is derived from the equilibrium between a NP and n proteins P (NP + nP $\leftrightarrow$ P_nNP) and can be written as[106]:

$$\frac{\Gamma}{\Gamma_{max}} = \frac{(C_p)^n}{K_D + (C_p)^n} \qquad (4.6)$$

Where K_D is the dissociation constant of the P_nNP complex and n the Hill coefficient often described as the cooperativity index. In the case that n = 1, Eq. 4.6 becomes the Langmuir isotherm. Consequently, the cooperativity index was first set to 1 and was set as a free parameter only if the fitting results were poor. Fitting of the experimental isotherms with Eq. 4.6 were all successfully performed with n=1, *i.e.* using the simple Langmuir isotherm model. Interestingly, a strong dependence of K_D with C_{NP} was observed, where K_D increased significantly from 0.028 ± 0.006 µM to 2.263 ± 0.418 µM for C_{NP} between 4.25 and 425 pM. A value of Γ_{max} = 15 800 ± 1000 proteins/NP was found for all three isotherms and could correspond to a fully covered (~100%) protein monolayer. The theoretical value of the full coverage was estimated considering that LYZ is a prolate ellipsoid of dimensions 2.8x2.8x5.0nm[146, 332] and adsorbs at the positive electrostatic end of its structure[333] with an effective surface footprint area of 7.84 nm². Again, aggregation was observed at all NPs concentrations at constant C_P/C_{NP} ratio (or Γ), but it was strongly increasing with C_{NP}. The full extent of NPs aggregation and fractal dimension analysis can be found in Figure S7.

As already observed by Milani *et al.* [31], renormalizing the free protein concentration C_p by C_{NP} leads to a single master curve (see Figure 4.2E). The scaling $K_D \sim C_{NP}$ observed across different protein-particle systems has interesting consequences regarding the reversibility of the adsorption process. Reversibility is often tested by diluting the particle suspension after adsorption equilibrium has been reached. In such situation, both C_P and C_{NP} decrease but their ratio C_P / C_{NP} remains constant. If Γ is monitored at each dilution, it can be seen in Figure 4.2F that its value does not change significantly, independently of the starting position on the adsorption isotherm (either close to the saturation plateau or in the low protein concentration regime). Absence of desorption upon dilution challenges the very concept of adsorption equilibrium and has not been yet fully understood[69, 70]. The existence of the scaling of K_D with C_{NP} could provide a simple answer to this puzzle. Diluting the suspension in order to trigger desorption would indeed cause a change in K_D and therefore modifiy the adsorption isotherm as well. In Figure 4.2F are represented the different adsorption isotherms obtained in Figure 4.2D as well as the values of Γ obtained when starting from C_{NP} = 425 pM and consecutively diluting 10X so that the suspension reach the subsequent adsorption isotherms at the predicted C_{NP}. As can

be seen, the Γ values obtained by dilution fall exactly on the isotherms obtained independently at the same corresponding C_{NP}. This correspondence between adsorption isotherms and dilution experiments confirms that dilution does not perturb the initial equilibrium and therefore adsorption is not *a priori* irreversible. In fact, this behavior was not only seen with transferrin (Milani et al.[31]) and LYZ (our experiments) as discussed so far. For instance, the investigation of serum and BSA adsorption on PS NPs in the next section (Figure 4.3) demonstrated this same behavior as well, indicating that the phenomenon might be more universal than being anecdotal cases. Indeed, in serum and BSA, the complete rescaling of the isotherm with the C_P/C_{NP} x-axis of the different experiments with changing C_{NP} and C^0_P demonstrate this effect as well.

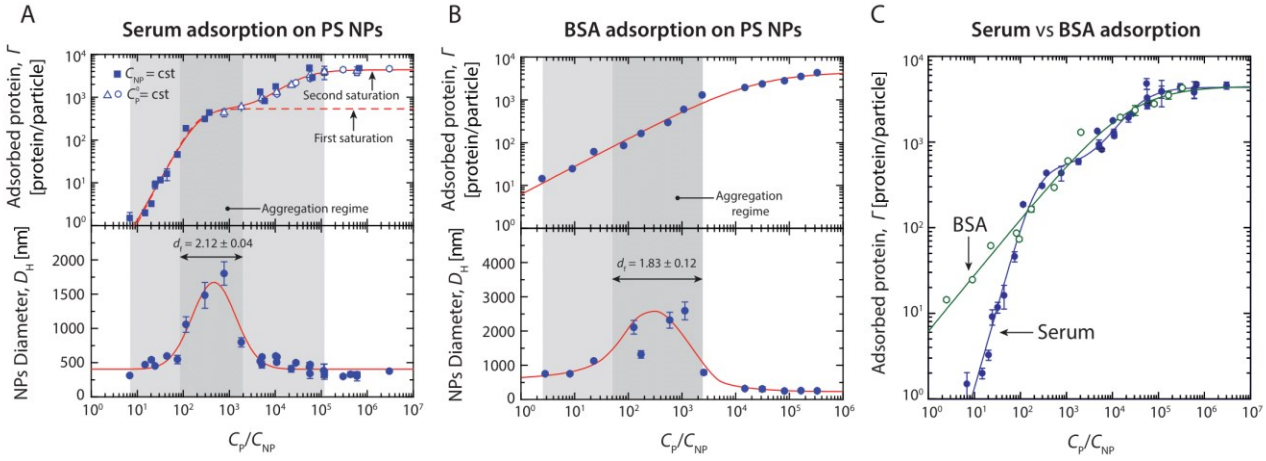

Figure 4.3. Quantification of adsorbed serum proteins. A) Adsorption isotherm, particle size and fractal dimension of PS NPs / serum mixtures show multiple saturation plateaux reminiscent of significant variations in the PC composition along the isotherm; B) The BSA adsorption isotherm can be described by the Hill isotherm and exhibits strong aggregation as all the other proteins tested; C) Superposition of the serum and BSA adsorption isotherms shows strong overlapping in the high concentration region. In that region, the serum PC is expected to be largely composed of BSA. The 4-most dilute experiments (100 < CP/CNP) were tested at CNP=425 pM, whereas all other experiments were tested at CNP=42.5 pM of BSA in panel B.

4.2.3 The complex adsorption mechanism of serum and BSA on PS NPs

Biological fluids such as blood contain numerous proteins (about 3000 different proteins[57]) with very different structure, and molecular size which its composition might change across individuals and organs. Understanding the adsorption mechanism of such complex systems is a formidable task that several studies have embraced. Proteomic analysis is certainly the most common approach to dissect the composition of the protein corona in biological fluids, but it is often limited due to complex sample preparation methods wich all require separation of the particles from the biological fluid. DDM analysis can provide new insights on the formation of the PC in the presence of complex protein mixtures with minimal sample preparation. We used fluorescently labelled complete bovine serum and performed an adsorption isotherm on PS NPs using DDM. The measured values for Γ represented in Figure 4.3 are effective values normalized by the molar mass of its major constituent BSA . They were obtained at constant C_{NP} or constant C_p^0, and are therefore represented as a function of the ratio C_P/C_{NP}. Since the measured adsorbed amount Γ is an effective concentration of BSA, values of the adsorption plateaus, dissociation constants and aggregation regimes should be interpreted with caution and with the proper context. The adsorption isotherm of bovine serum (expressed as effective BSA proteins per NP) exhibits two distinct adsorption regimes, clearly indicating changes in the PC composition depending on the total protein concentration. Both processes were simply fitted by a two steps adsorption model, each described by Eq. 4.6, to extract apparent affinities and saturation values. The first plateau was reached at $\Gamma_{max\text{-}1}$ = 540 ± 40 BSA/NP and the second plateau was observed at $\Gamma_{max\text{-}2}$ = 4370 ± 270 BSA/NP. The first adsorption step (at low C_P/C_{NP} values) seems to correspond to the adsorption of high affinity ($K_{D\text{-}1}$ = 220 ± 120 BSA/NP) large protein(s) such as fibrinogen, immunoglobulins, or some apolipoproteins. The second adsorption step (at high C_P/C_{NP} values) can be ascribed to the adsorption of smaller protein(s) with weaker affinity ($K_{D\text{-}2}$ = 28500 ± 5600 BSA/NP), a phenomenon reminiscent of the Vroman effect found at equilibrium[137, 334]. Simultaneous measurement of particle size showed that serum proteins induced strong aggregation of the NPs for 100 < C_P/C_{NP} < 2000 (dark grey region in Figure 4.3A). Outside this range, particle diameter was still significantly larger than 200 nm indicating the presence of small aggregates (light grey region in Figure 4.3A) rather than multiple layers of proteins adsorbed on

particles. Quantitative assessment of the fractal dimension of the aggregates was only possible in the strong aggregation regime due to limitations arising from the size of the particle aggregates. In this regime, a value of d_f = 2.13±0.13 was found (see Fig. S7), which seems to be indicative of a reaction-limited colloid aggregation mechanism[328, 331].

To gain more insights into the composition of the serum PC just described, we measured in a separate experiment the adsorption isotherm of BSA on PS NPs. We found that the isotherm could be fitted with a Hill model with a K_D=22700±12000 BSA/NP a saturation of Γ_{max}=4500±600 BSA/NP , and an anti-cooperative behavior with n=0.66±0.07 (Figure 4.3B). Given that the albumin has a structure of an equilateral triangular prism, with sides of ~8 nm and a thickness of ~3 nm[335, 336], the number of BSA to reach the full coverage of a monolayer can be estimated. With the consideration that BSA would adopt a side-on orientation when adsorbed on PS NPs, the theoretical full coverage Γ_{max} = 4535 BSA/NP is in perfect agreement with our measurements. Note that the anti-cooperative behavior of BSA adsorption of n = 0.66±0.07 is also in agreement with other reports for albumin adsorption (on negatively charged NPs), irrespective of the size or chemical composition of the NPs[66, 67, 69, 72]. Protein adsorption induced strong particle aggregation between 50 < C_P/C_{NP} < 2200, a range that is similar to serum (see Figure 4.3A). Interestingly, the fractal dimension measured in this aggregation regime was lower compared to serum and equal to d_f = 1.85±0.10, indicative of a DLCA mechanism.

In Figure 4.3C, both serum and BSA adsorption isotherms were superimposed and revealed a strong overlap in the high protein concentration range, which covers the second saturation regime of the serum isotherm ($C_P/C_{NP} > 10^3$). In this regime both isotherms exhibited a value of K_D ≈ 25000 proteins/NPs. Such overlapping between both isotherms indicates that, in this adsorption regime (high number of proteins/NPs), the composition of the PC in serum is largely dominated by albumine (or by proteins with similar molar mass and affinity) as both final saturation values Γ_{max} approach ~ 4500 proteins/NPs. On the other hand, for $C_P/C_{NP} < 10^3$, BSA isotherm presents a higher amount of adsorbed proteins compared to serum. Because of the complex composition of serum, it is likely that in this adsorption regime the PC composition shifted from BSA to larger proteins with stronger affinities. This was also reflected in the difference of aggregates structure and mechanism, where BSA generated a loose structure from a diffusion-limited mechanism

(DLCA) compared to the more compact structure produceded by reaction-limited aggregation (RLCA) for serum (d_f (serum) > d_f (BSA)). As demonstrated, aggregation is triggered by the adsorption of the proteins, hence a shift in the aggregation mechanism is likely to indicate a shift in the type of proteins adsorbed. In the very low adsorption regime, C_P/C_{NP} = 10, the adsorption of BSA is more than an order of magnitude higher than serum, indicating that the adsorbed proteins from serum have a very different affinity and interaction with the NPs compared to BSA. This can be further confirmed by the initial Hill coefficient of serum n = 1.97 ± 0.70, which is significantly larger than BSA n = 0.66 ± 0.07, suggesting a different binding mechanism. Similar values of the Hill coefficients were also measured in a series of experiments by FCS with BSA and serum on negatively charged quantum dots in the first adsorption step[69]. Wang *et al.* reported Hill coefficients for serum (n=1.8±0.2) and HSA (n=0.6±0.1) in perfect agreement with our observations. Further, the ratio between K_D measured in HSA *vs* serum in their experiments ($K_{D\text{-}HSA}/K_{D\text{-}serum}$ ≈ 90) is also in good agreement with our experiments ($K_{D\text{-}BSA}/K_{D\text{-}serum}$ ≈ 100). All together these experiments confirm that the PC composition is strongly dependent on the serum concentration used in the suspending media. This phenomenon observed at equilibrium is also known as the general Vroman effect. It was first reported on flat surfaces[137, 334] but only few studies have shown some evidence of this effect on NPs[337, 338].

4.2.4 Monitoring the PC exchange kinetics *in vitro* and *in vivo*

The versatility of the DDM setup allows to perform time-dependent experiments of protein adsorption in different settings. In Figure 4.4A we show adsoption kinetic curves of LYZ on PS particles in three different experimental configurations. The first two configurations are competitive assays where NPs were precoated with either labelled (Figure 4.4A (i)) or unlabelled (Figure 4.4A (ii)) LYZ and exposed to a medium containing the corresponding unlabelled or labelled protein. The results of these two tests showed the exchange of the preadsorbed proteins with proteins from the medium and confirmed the reversibility of the adsorption process, even for a strongly adsorbing protein such as LYZ, in agreement with the earlier observations from the adsorption isotherm and the dilution experiment . A simple exponential decay model, based on a pseudo-first order kinetics, was used to model both adsorption and desorption experiments. Because the total protein concentration (labelled and unlabelled) was constant in both

experiments, it was expected that both exchange rate constants of adsorption and desorption *k* match. Indeed, the measured value for adsorption, k = 0.020±0.002 min^{-1} was in agreement with the obtained value for desorption of k = 0.030±0.005 min^{-1} considering the experimental error. Interestingly, the competition kinetics was significantly much slower (~30x) than the adsorption kinetics of free LYZ (see Fig. S4). This suggested that upon first contact with a biological fluid, NPs get covered with a layer of proteins within seconds, while competing proteins (slower or further away from the NP) in may take minutes to hours to adsorb and reach equilibrium. However, it was also expected that both plateau values would converge towards a common value of proteins/NP, though experiments showed that the expected complete re-equilibrium was not achieved during the experimental time-window.

The third assay is a dilution assay where precoated particles with labelled LYZ were mixed with uncoated nanoparticles. The concentration of proteins used for this experiment was below the saturation limit of the particles, therefore almost all the proteins were adsorbed and very few were still free in the medium (~10%). Addition of bare particles triggered a decrease of the amount of proteins per particle, indicative of a slow redistribution of the proteins througout the NP suspension. After 200 minutes, a plateau value was reached at Γ = 720 proteins/NP, which was still higher than the value expected if complete and homogeneous redistribution of the proteins had occurred (450 proteins/NP). Therefore, even after 200 minutes, it appears that the initially uncoated NPs that were introduced in the suspension still had a lower amount of adsorbed proteins compared to the NPs that were precoated. This observation is also in line with both previous experiments (adsorption and desorption), where the time to reach equilibrium was longer than the experimental observation time. Further, this could also suggest that even though protein adsorption is a dynamic and reversible process, history effects can create inhomogeneities in PC composition throughout the NPs suspension which can take significant amount of time before reaching equilibrium or that equilibrium state changed over time.

From quantitatively assessing the exchange rate of proteins at different fluorescent protein concentration can also yield the equilibrium constant. Using the same design as in Figure 4.4A (ii), NPs precoated with unlabelled LYZ (at $\Gamma = \Gamma_{max}$) were incubated with a solution of LYZ-RITC and their exchange was followed by DDM. In Figure 4.4B is shown the number of labelled proteins

adsorbed per NP over time. The kinetics of the exchange between labelled and unlabelled proteins is analyzed as in the previous experiment to extract the exchange rate constant, *k*. As previously shown[66], *k* is related to the adsorption and desorption rates constants, k_{on} and k_{off}, via the expression $k = k_{off} + C_p^0 k_{on}$. Figure 4.4C shows the results of this analysis for C_{NP} = 42.5 pM. The ratio of the constants is by definition equal to the dissociation constant K_D, which was already measured via the adsorption isotherm ($K_D = k_{off}/k_{on}$). The value of K_D obtained via the exchange kinetics assay presented in Figure 4.4B and C was K_D = 1.0±0.2 μM, in fair agreement with the value of 0.26±0.05 μM obtained from the adsorption isotherms shown in Figure 4.2D. The slight discrepancy from adsorption kinetics and equilibrium may however arise from a slight difference in affinity that was observed between the labelled and the unlabelled LYZ, which was also observed in other systems[207]. The agreement between these two independent experimental values confirmed that the measured adsorption isotherms relate to a true thermodynamic equilibrium characterized by a dynamic protein exchange at the surface of the NP.

These *in vitro* experiments reconcile kinetic and thermodynamic properties of the PC formation and offer a solid ground to describe the PC in more complex, yet real, environments. Indeed, some reports have suggested that *in vivo* the PC composition evolves with time[63, 64], while other reports have suggested that the PC constitutes the fingerprint of the NPs, its biological identity[113, 122]. To provide more insights into PC dynamics *in vivo*, we used DDM to follow the composition of the PC in zebrafish larvae.

The zebrafish larvae is a powerful model for PC studies using DDM since the transparency of the larvae allows intravital imaging. NPs precoated with labelled serum proteins were injected in the bloodstream of 48-hour post-fertilization larvae and imaged in the Caudal Venous Plexus (CVP) (Figure 4.4D). The CVP has a characteristic dense and tortuous capillary network through which the bloodstream flow speed is far slower (av. speed of ~30 μm/s) than the flow in the main artery (av. speed >100 μm/s), as estimated by video imaging. The low flow speed combined with the presence of macrophage cells on the lining of the subcaudal venous capillaries facilitate the capture of any circulating foreign body such as NPs by either macrophages or vascular endothelial cells[55], a dominant mechanism found in the clearance of "hard nanomaterials" by the liver[55]. CVP is indeed often compared to hepatic sinusoids, which are composed of liver sinusoidal endothelial

cells (LSECs) and Kupffer cells[339, 340]. Vascular endothelial cells in the CVP area are functionally equivalent to LSECs (*i.e.* cells having scavenger receptors on their surface)[340]. Our experiments are in good agreement as an accumulation of NPs was observed over time in the CVP region (see Supplementary Figure 8).

Only a few minutes after NPs injection, NPs appeared as immobilized in the CVP on the lining of the capillaries in the form of small patches (see arrows in Figure 4.4D). Circulating NPs were scarce and did not contribute to $A(q)$ as their ballistic motion was many orders of magnitude faster than immobilized NPs. Besides being immobilized, NPs still exhibited diffusive Brownian motion at the surface of the capillaries based on the measured ISFs (see Figure 4.4F and G) from which the diffusion coefficient, D, of the NPs was extracted for both pre- and post- injection. The diffusion coefficient of the NPs were three orders of magnitudes lower for immobilized NPs compared their diffusion in water of D_w=2.1 μm²/s (Figure 4.4G). Recently, Kwapiszewska *et al.* have shown that the value of the effective viscosity, $\eta_{eff}=D_w/D$ for NPs of similar size located in the cytosol of different cell lines is at least two orders of magnitude larger than the value we measured for the immobilized NPs[341]. Also, other reports have shown that cell membrane viscosity is about two to three orders of magnitude higher than water, which is more in line with our observations[342-344]. Based on these observations, our results therefore support the notion that the NPs were located at the surface of the capillary lining to which they adhered most probably via receptor-mediated interactions as their accumulation were predominantly in the CVP. Therefore, their dynamics at the cell surface is expected to be coupled to the dynamics of the receptor in the plasmatic cell membrane which is dominated by Brownian motion (*i.e.* diffusive behavior[345]).

After their capture, NPs dynamics was followed by DDM and the amount of adsorbed proteins was measured as a ratio to the first measurement as previously described (Eq. 4.1 to 4.4). As can be seen in the different snapshots shown in Figure 4.4D, the fluorescence intensity was initially concentrated in the NPs patches and inside the blood capillaries. Over time, it invaded inter-capillary regions, probably indicating a fast diffusion of free fluorescent proteins outside of the blood capillaries, whereas NPs remained confined within the bloodstream. Some of the free proteins may be the result of desorption, but NPs were injected along with the large free fraction of proteins as well. The protein exchange kinetics at the PC interface exhibited a single

exponential decay over 3 hours of observation (Figure 4.4E). Three different zebrafish larvae were included in the analysis and data were clustered for clarity (see Figure S9 for individual measurements). In the region of interest, no significant variation of the total fluorescence intensity was observed over the time of experiment (Figure 4.4D), confirming that the number of captured particles did not increase during image acquisition. Fluctuations in signal intensity can be thus solely attributed to the desorption of fluorescent proteins. Over this time window (~3 hours), the number of labelled proteins pre-adsorbed on the NPs decreased by 40 %, indicating a slow exchange of characteristic time $\tau_{desorption}$= 67 ± 28 minutes with unlabelled circulating blood proteins. It is important to note that the observed decay was monitored post-immobilization of the NPs and therefore does not provide any information regarding the PC dynamics of circulating NPs immediately after injection. Interestingly, it is possible to infer that the rate at which NPs were immobilized by the CVP (τ < 10 min) was greater than the rate the proteins were exchanged in this experiment. As a result, it is unlikely that circulating the zebrafish larvae proteins had any effect over the behavior of the NPs, rather the pre-adsorbed serum proteins likely dictated the fate of the NPs. Similar to what was observed *in vitro* with LYZ, serum protein exchange at the surface of the NPs *in vivo* was not complete even after the three hours of experimental observation. The existence of a fraction of proteins exhibiting very slow to no exchange with the surrounding biological medium is likely at the origin of the "biological memory effect"[346], also called "hardening" of the PC[113, 117, 122]. These *in vitro* and *in vivo* experiments show clearly that this effect is a unique feature of the PC and is observable in single protein solutions and complex mixtures as well.

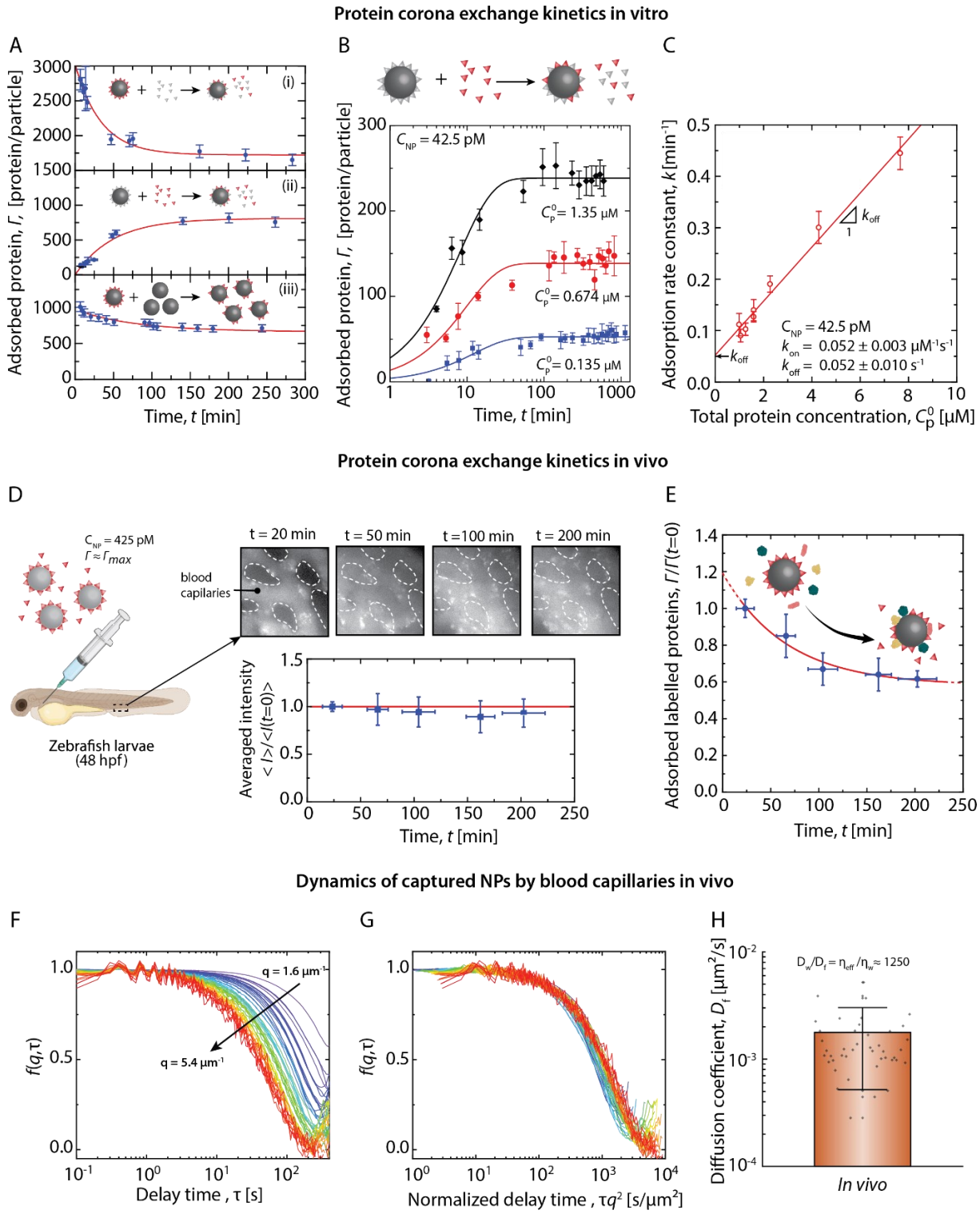

Figure 4.4. Kinetics of the PC formation in vitro and in vivo. A) Monitoring protein exchange at the PC interface can be performed by DDM in different configurations to test the reversibility of protein adsorption; B) Monitoring of protein exchange at the PC interface in the presence of

labelled LYZ at different concentrations; C) Evolution of the adsorption rate with the protein content allows to extract adsorption constants; D) Imaging of NPs in zebrafish larvae post-injection shows quick and stable immobilization of the NPs on the lining of the blood capillaries of the subcaudal region; E) Time evolution of the PC composition of NPs immobilized in the CVP area of the zebrafish larvae; F) Dynamics of the immobilized NPs shows a single process on the whole range of spatial frequency; G) The renormalization of the ISF by τq^2 leads to a master curve demonstrating the diffusive nature of the motion of the immobilized NPs; H) The extracted diffusion coefficient of the immobilized NPs is consistent with the NPs being adsorbed at the cells surface but not internalized.

4.3 Conclusion

Using a series of *in vitro* and *in vivo* assays, we have shown that DDM is a powerful technique to study proteins-particles interactions *in situ* and quantitatively. *In vitro*, protein adsorption on NPs was quantitatively assessed even in presence of NPs aggregation, which was systematically observed for all the proteins and mixture of proteins (serum) studied. Using this approach, it was possible to observe the rescaling of protein adsorption isotherms with the particle concentration and to demonstrate through competition experiments and dilution experiments that adsorption remained reversible, as observed in our earlier review (See “Chapitre 3”). We also evidenced changes in the PC composition contingent to the serum concentration, a phenomenon reminiscent of the Vroman effect at equilibrium. The most plausible interpretation of the experimental data is consistent with reports on planar surfaces[137, 334], where large proteins are adsorbed at “high dilution” (low C_P/C_{NP}) while at higher serum concentration (high C_P/C_{NP}) albumins or other proteins of similar molar mass and affinities are predominant.

Also, all the protein-NPs systems and conditions tested generated monolayers of adsorbed proteins. The measurements at saturation were in reasonably good agreement with the formation of a monolayer of proteins based on their 3D structures. These results are in agreement with the large body of evidence produced by Nienhaus’ group[66, 67, 69, 70, 73, 347], where mostly monolayers were found. Though we are not refuting that multilayers cannot happens. We could argue that the multilayer phenomenon might simply not be as ubiquitous as previously

hypothesize. In fact, it is possible that the "multilayer" might be a manifestation of a sparse layer where protein-protein interactions occur similar to Zhang *et al.*[348] picture (and even sparser) making it difficult to clearly observe, rather than a full dense layer picture from Milani *et al*.[31] or Piella *et al*.[117].

Further, we showed the potential of DDM to study PC formation and composition dynamics *in vivo* in the zebrafish using the same methodological approach developed and used for *in vitro* experiments. *In vivo* experiments demonstrated the partial exchange of proteins in the PC, a phenomenon also observed *in vitro* for the same particles. The existence of a long-lived protein layer which exhibits very slow exchange dynamics constitute one of the first quantitative experimental observation of the so-called biological memory effect and reveals that such effect is long lived but dynamic in nature. On the basis of these results, it is expected that the different phenomena observed *in vitro* and *in vivo* (protein adsorption scaling, equilibrium Vroman effect and memory effect) have a significant impact on the biological behavior of NPs, through the alteration of the composition of the PC. For instance, a recent study by Ouyang *et al.* demonstrated that the number and concentration of injected NPs is playing a massive role over targeting efficiency and tumor delivery, a parameter not often emphasized by studies[349]. Interestingly, we report a similar correlation with the PC adsorption, where the C_{NP} scaling of the adsorption could have severe implication on reproducibility and biodistribution if not considered. These results combined to Ouyang *et al.*[349] work should assert the importance of understanding the effects of NPs concentration and quantity in nanomedicine.

We finally emphasize that the nature of DDM methodology makes a powerful alliance of quantitative video analysis and visual inspection of video imaging. With its successful application to *in vivo* systems, we expect move forward with a series of improvement for direct *in situ* quantification of *in vivo* processes with the aim of moving toward a better quantification of nanomedicine behavior in living organisms.

4.4 Materials and methods

4.4.1 Materials

Plain PS NPs of R_H=110 nm, R_H=30 nm (Duke Standards, Thermofisher) and plain PS NPs of R_H=100 nm (Polysciences) were used after 1-week dialysis (SpectraPor® membrane, 50 kDa MWCO) in MilliQ® water to remove any potential traces of surfactant. Fluorescent PS NPs of R_H=110 nm (Polysciences) were used after a purification step by exclusion chromatography. LYZ (Sigma-Aldrich), BSA (Sigma-Aldrich),serum proteins (Gibco™, Thermofisher), and the fluorescent labelling agent, RITC (Sigma-Aldrich), were all used as is.

4.4.2 Protein labelling

The labelling procedure of proteins was based on published reports[24, 350]. Serum proteins from foetal bovine serum (FBS), BSA and LYZ were labelled with rhodamine B isothiocyanate (RITC) using a molar ratio of 5:1 RITC per equivalent proteins (assuming a concentration of proteins of 40 mg/mL BSA equivalent for serum). Proteins were mixed with carbonate buffer ($NaHCO_3$ 0.2M, pH = 8.35) to which RITC dissolved in 10% v/v DMSO was added. The coupling reaction was carried at room temperature for one hour under gentle stirring and then transferred at 4°C overnight. The resulting solution was dialysed (SpectraPor® membrane, 1000 Da MWCO) against PBS for 3 hours and then centrifuged (30 min at 10000 x g) to remove any aggregates. The sample was further purified on sephadex G-20 columns (GE Healthcare, PD-10) to remove any excess of free RITC. Aliquots were kept at -20°C until use. For LYZ, protein concentrations in the final stock solution were determined by UV-vis spectrophotometry. Serum proteins and BSA concentrations were measured based on BCA assays, Pierce Protein Assay working at 660 nm (Thermo Scientific). Labelling efficiencies were determined based on the spectrophotometric absorbance at 554 nm of the fluorescent protein solutions. The resulting values were ~40% for LYZ and ~80% for both serum and BSA.

4.4.3 Fluorescence spectroscopy quantification

A calibration curve spanning from 0.017 to 3.7 µM was used to quantify adsorption of adsorbed LYZ-RITC on PS NPs. The fluorescence was quantified using a microplate reader (Tecan Infinite®

200 PRO) using an excitation wavelength of 545 nm and an emission wavelength of 590 nm. For each sample, PS NPs incubated with LYZ-RITC were purified by one centrifugation (30 min at 20000 x g). Supernatants (50 µL) were mixed with a solution of 10 mM HEPES (50 µL) and then distributed in a 96-well plate for fluorescence measurement.

4.4.4 Differential dynamic microscopy

An upright microscope (Olympus BX61, Japan) equipped with a high-speed camera (Hamamatsu OrcaFlash 4.0 V3, Japan) was used for the acquisition of videos. Videos were recorded using fluorescence imaging using ×20 objective (Olympus UPLANSAPO, NA= 0.5), at a framerate ranging from 10 to 100 frames per second, with an image binning of 1 × 1 or 4 × 4, and within a region of interest of 512 × 512 pixels. Fluorescence illumination was produced by a mercury burner and double band pass filters (FITC + TRITC) were installed. A neutral density filter blocking 94% of the incoming intensity was also installed to adjust the fluorescent intensity and minimize photobleaching. These parameters were adjusted to maximize the signal intensity and to fully capture the particle dynamics over an adequate q range and timescale for each experiment. Images were recorded on glass capillaries (Vitrocom, Canada) of 0.4 mm thickness filled with nanoparticle suspension (~180 µL) and sealed using petroleum jelly. Videos were recorded at five different positions for each capillary and processed results were averaged over these positions.

4.4.5 Zeta potential measurement

Zeta potential measurements were performed using PALS analysis on a Zetasizer NanoZS device (Malvern Instruments, UK). Measurements were performed at a single scattering angle $\theta = 173^{o}$, at temperature of 21°C and NaCl concentration of 4 mM.

4.4.6 DDM *in vivo*

Experiments in zebrafish larvae were performed in compliance with the guidelines of the Canadian Council for Animal Care and the local ethics committee. Wild-type zebrafish, Tupfel long-fin (TL) strain, were maintained at 28°C and kept under a 12/12 h light/dark cycle at the animal facility of the Centre National de Biologie Expérimentale (CNBE), Laval, Canada. PTU was added to fertilized eggs at 24 hours post-fertilization (hpf) to prevent larvae pigmentation. NPs

were injected in 48 hpf larvae as previously described[351]. Briefly, 48 hpf larvae were placed on the side in Low Melting Point Agarose in 35 mm glass bottom Petri dishes. Zebrafish larvae were injected using a micropipette (10 cm Borosilicate Glass Micropipette with filament, Sutter Instrument, USA) pulled on a Micropipette Puller Model P97 (Sutter Instrument, USA). The injection in the duct of Cuvier was controlled with a nanoinjector FemtoJet 4i (Eppendorf, USA). Volume injected was 4 nL and the NPs concentration was set at 425 pM and the serum protein concentration at 13 µM equivalent BSA. Videos of NPs dynamics inside the blood circulation were recorded immediately after particle injections in larvae using a Zeiss inverted microscope equipped with a Plan-Apochromat 20x/0.8 M27 objective, a LED illumination lamp (X-cite 120LED, Excelitas Technologies) set close to minimum intensities (1-5%) and mounted with a Hamamatsu Orca Flash4.0 V3 camera. Camera frame rate was set between 10-30 fps depending on the experimental requirement.

Chapitre 5 – Dynamique des colloïdes et pénétration tissulaire

Tel qu'établi précédemment, un des grands défis de la nanomédecine porte sur l'optimisation de la pénétration tumorale et tissulaire. Paradoxalement, de « grandes » NPs (~100 nm) sont utilisées pour exploiter l'effet EPR des tumeurs et y favoriser leur accumulation, au dépend de leur capacité de pénétration par diffusion. Comme il est connu que ces NPs plus grandes s'accumulent en périphérie des tumeurs sans jamais y pénétrer profondément[352], plusieurs moyens ont été étudiés pour améliorer leur pénétration tumorale. Une bonne partie de ces efforts ont visé à améliorer les propriétés de diffusion des NPs, bien que ce mode de pénétration soit remis en question par l'équipe du Pr W. Chan qui a montré que le mode prédominant d'entrée des particules dans la tumeur étaient les voies trans- ou intracellulaires à travers l'endothélium vasculaire[353]. Cependant, les mécanismes de transport dominants qui favorisent la pénétration tumorale font encore débats, ce qui ne permet pas de statuer sur la stratégie à adopter[40]. En fait, l'importance de la voie paracellulaire (par diffusion) et trans- et intracellulaire (par transcytose) ont toutes deux étés démontrées par les travaux de Jain[43, 44, 352, 354, 355] et Chan[353], respectivement. Puisqu'il n'y a pas de consensus absolu, nous avons simplement concentré nos travaux sur l'évaluation des paramètres affectant la diffusion des NPs dans les environnements denses, semblables à une matrice extracellulaire tumorale.

5.1 Optimisation de la diffusion des colloïdes dans la matrice extracellulaire

5.1.2 Exploitation de la physiologie tumorale

Plusieurs tentatives pour améliorer la diffusion des NPs dans les tumeurs ont été étudiées. Une première série d'approches portait sur la biologie et la physiologie des tumeurs. Tel que décrit précédemment, une tumeur possède généralement une structure dense et un réseau désorganisé de capillaires sanguins[43, 44]. Cette structure produit une pression hydrostatique qui limite la diffusion de molécules au cœur de la tumeur et créant conséquemment une zone

hypoxique en raison d'une diminution des échanges gazeux des cellules tumorales[356]. Une approche tentée pour favoriser la pénétration des molécules était de normaliser ce réseau vasculaire pour ensuite rétablir l'équilibre hydrostatique et réduire cette zone d'hypoxie. Cette approche fût un grand succès pour les petites molécules, c'est-à-dire les agents antitumoraux seuls. Cependant, cette approche a pour conséquence de renormaliser l'importante fenestration du réseau vasculaire tumoral, limitant ainsi l'importance de l'effet EPR[354, 357]. Cette approche, combinée à celle de la nanomédecine, aura permis de constater que seules les petites NPs (~10 nm) sont avantagées par cette méthode, alors que les plus grandes ne le seront pas ou que très peu[354, 358]. À l'opposé de l'approche de normalisation du réseau vasculaire tumoral, une autre stratégie consiste à perméabiliser les vaisseaux sanguins des tumeurs à l'aide de NPs multifonctionnelles pour y favoriser leur accumulation[359].

5.1.2 Exploitation des propriétés physicochimiques des NPs

Une autre série d'approches consiste à optimiser les propriétés des NPs pour favoriser leur diffusion dans un milieu extracellulaire dense. Plusieurs stratégies ont effectivement été testées pour atteindre cet objectif. D'abord, la forme des NPs a été étudiée. Il a en effet été démontré que l'anisotropie de la forme (sphère *vs* bâtonnet) peut modifier les propriétés de transport des NPs dans une matrice dense interconnectée de pores[360]. Par exemple, il a été montré que des macromolécules linéaires avaient une plus grande mobilité dans des gels, en comparaison aux macromolécules globulaires et aux bâtonnets[82].

Les propriétés de surface des NPs constituent un autre groupe de paramètres qui permettent d'influencer la capacité des NPs à diffuser dans les matrices extracellulaires. Cette approche préconise la modification des matériaux d'origine de la surface des NPs en y ajoutant des groupes fonctionnels à base de polymères. Ces modifications permettent de limiter les interactions avec les composantes de la matrice extracellulaire en altérant le potentiel de surface des NPs ou en introduisant une surface hydrophile pour limiter les interactions hydrophobes. Par exemple, le PEG est un polymère neutre qui une fois à la surface des NPs (PEGylation des surfaces) permet de diminuer le potentiel de surface des NPs[142]. De plus, le PEG a été investigué pour son effet sur la diffusivité des NPs dans des fluides biologiques. Il a ainsi été démontré que la PEGylation des NPs

améliore leur pénétration dans les mucus gastriques[90], vaginaux[90, 91] et pulmonaires[89], en plus d'améliorer leur transport cytoplasmique[361]. Bien qu'il ne s'agisse pas de preuves directes, le PEG semble cependant diminuer les interactions entre les particules et la matrice des mucus, tendance qui semble dépendante de la densité de PEG à la surface des NPs[91]. Il est logique qu'une diminution des interactions des NPs avec la matrice extracellulaire se traduise par une diffusion facilitée à l'intérieur de celle-ci. Il a également été observé que la distribution spatiale des charges à la surface des NPs, comme pour la PEGylation, peut aussi avoir un impact sur le transport des NPs *in vivo* en altérant les interactions non spécifiques avec la matrice extracellulaire[*362*].

D'autres approches ont aussi fait appel à des NPs sensibles pour des stimulus externes comme par exemple, des NPs conçues pour se dégrader en de plus petits fragments lorsqu'elles rencontrent un environnement tumoral[363]. Cependant, il est à considérer que l'élaboration de ce type de NPs nécessite une complexification de leur structure et de leur production, ce qui limite grandement les chances de succès auprès des agences réglementaires[5, 364]. Un autre exemple de cette approche utilise l'effet plasmon des NPs d'or pour générer de la chaleur sous un laser infrarouge. Cela a pour effet de dénaturer le collagène se retrouvant dans la matrice extracellulaire pour ainsi y améliorer la pénétration de ces NPs[365]. De la même manière, dégrader la matrice extracellulaire à partir d'enzymes greffés à la surface de NPs est aussi une approche qui est étudiée pour améliorer la pénétration de la nanomédecine dans les tumeurs[366].

5.2 L'impact des propriétés mécaniques des NPs en nanomédecine

Les propriétés mécaniques des NPs et leurs rôles en nanomédecine ont fait récemment l'objet de nombreuses études[367]. Les propriétés mécaniques des NPs dictent leur capacité à se déformer sous l'effet du stress ou d'une force. De multiples études se sont penchées sur l'impact de la déformabilité des NPs en ce qui a trait à leurs interactions avec les différents systèmes biologiques. Par exemple, des microgels à base de poly(N-isopropylacrylamide) (pNIPAM) ayant un diamètre de 1 µm ont montré une capacité à traverser une membrane ayant des pores de 100 nm et des microgels de 100 nm de diamètre ont pénétré une membrane ayant des pores de 10 nm sous une faible pression de 0.5 psi[368]. Cette capacité impressionnante de ces NPs à pénétrer

des barrières physiques a rapidement suscité l'intérêt de nombreux chercheurs, qui souhaitaient les appliquer à la nanomédecine.

D'autres investigations ont par la suite permis de déterminer que les propriétés mécaniques des NPs permettaient de moduler leurs interactions cellulaires, leur pénétration tissulaire et même certains de leurs paramètres pharmacocinétiques. En effet, certaines études rapportent que la prolongation de la durée en circulation, la modification de la biodistribution et des mécanismes de clairance des NPs seraient causés par leur capacité à se déformer[369-371]. Pour les NPs « molles », d'autres études pointent vers une diminution de leurs interactions avec les cellules[371] et une amélioration globale de la pénétration et du transport dans le milieu tumoral[372, 373]. Bien que plusieurs observations comme l'amélioration de la pénétration tumorale puissent s'expliquer par le caractère déformable de ces NPs, aucune preuve directe n'a permis d'expliquer ce phénomène jusqu'à maintenant. En se basant sur cette problématique, nous nous sommes donc intéressés à étudier par DDM l'impact de la déformabilité sur les propriétés de diffusion des NPs dans un milieu biologique simulé.

5.3 Hypothèse et objectifs spécifiques : Dynamique des colloïdes et pénétration tissulaire

Ainsi, en se basant sur les capacités de la DDM décrite en introduction, nous croyons que l'utilisation de celle-ci nous permettra d'investiguer l'impact de la déformabilité des NPs sur leur diffusion dans des matrices extracellulaires modèles.

D'abord, nous ferons la démonstration que la DDM peut mesurer la diffusion des NPs dans des conditions idéales, c'est à dire dans l'eau. Ensuite, nous évaluerons la diffusion de ces NPs dans un système plus complexe, représentant la matrice extracellulaire. Pour ce faire, un gel d'agarose mimera la structure de la matrice extracellulaire et des NPs dures à base de polystyrène ou d'or serviront de modèle. Nous évaluerons les différentes contributions des paramètres hydrodynamiques, électrostatiques et mécaniques dans la diffusion de NPs à travers une matrice dense, et ce, à partir de modèles mathématiques. Des NPs à base de poly(N-isopropylacrylamide) (pNIPAM) serviront de modèles de NPs molles. Leur diffusion sera mesurée et ensuite comparée

à celles des NPs dures. À partir des différences observées, nous tenterons d'élucider certains mécanismes de transport dans des milieux denses et confinés.

Pour ces travaux portant sur les mécanismes de diffusion des NPs molles et dures, les résultats obtenus ont fait l'objet d'une publication. Ainsi, les travaux présentés dans le chapitre 6 ont été publiés dans le journal Nature Communications[326] .

Chapitre 6 – « Spontaneous Shrinking of Soft Nanoparticles Boosts their Diffusion in Confined Media»

Pierre-Luc Latreille[1], Vahid Adibnia[1], Antone Nour[1], Jean-Michel Rabanel[1], Augustine Lalloz[1], Jochen Arlt[2], Wilson C.K. Poon[2], Patrice Hildgen[1], Vincent A. Martinez[2], Xavier Banquy[1]

1) Faculty of Pharmacy, Université de Montréal, PO Box 6128, Succursale Centre-ville, Montréal, Québec H3C 3J7, Canada

2) School of Physics and Astronomy, The University of Edinburgh, Peter Guthrie Tait Road, Edinburgh, EH9 3FD, UK

Dans cet article, nous avons utilisé la DDM pour étudier le rôle de la déformabilité des NPs sur leur diffusion dans des gels d'agarose. Les propriétés de diffusion d'une librairie de NPs molles de pNIPAM et des NPs dures de polystyrènes et d'or de différentes tailles, sont présentées et caractérisées par DDM, puis évaluées et comparées à l'aide d'un modèle mathématique de diffusion. Nous avons tenté de déterminer si les avantages attribués à la déformabilité dans des études *in Vivo* pouvaient aussi être reproduits dans des conditions plus contrôlées, comme un gel d'agarose.

En **Annexe 3**, se trouvent les informations supplémentaires (SI) cités dans le cadre de ce chapitre.

Les travaux présentés dans ce chapitre ont été présentés dans le journal scientifique « *Nature Communications* » :

Latreille, P.-L.; Adibnia, V.; Nour, A.; Rabanel, J.-M.; Lalloz, A.; Arlt, J.; Poon, W. C. K.; Hildgen, P.; Martinez, V. A.; Banquy, X., Spontaneous shrinking of soft nanoparticles boosts their diffusion in confined media. Nature Communications. 2019, 10 (1), 4294.

6.1 Introduction

Understanding the intricate laws governing transport of nanomaterials, especially nanoparticles, through a porous medium has major implications in many different fields such as filtration technology, separation and water sanitation process[374, 375], geophysics[376, 377], biophysics[378] and medicine[40]. For example, a major challenge encountered in nanomedicine development is improving NPs transport within interstitial tissues [40]. Interstitial tissues typically contain gel-like networks of entangled polymer chains with mesh sizes in the range of tens to hundreds of nanometers[379], posing a critical constraint on the diffusion of nanomedicine. Large NPs (diameter >100 nm) get trapped and cannot diffuse deep in the tissue, limiting their therapeutic efficacy. A straightforward solution is to use sufficiently small NPs, so that the surrounding network does not have any effect on them, and they diffuse without any constrictions in the background liquid media[380, 381]. However, in several cases, it has been shown that NPs larger than the medium characteristic pore size can be far better drug carriers than smaller particles. For example, polymeric micelles with diameters ranging between 100-160 nm demonstrated long plasmatic circulation time and strong accumulation into tumors, whereas significantly less amount of smaller micelles penetrated inside tumoral tissues, even though these small micelles travelled much deeper in the tissues[382]. Strategies to facilitate NPs deep tissue penetration include NPs surface modification [56], local transformation of the connective tissue or extracellular matrix[365], and design of smart NPs responsive to local physicochemical stimulations[383, 384]. Although these strategies have been effective in several cases, they are often designed for very specific situations, and cannot be integrated into one multipurpose drug delivery system[13]. Therefore, to date, improving NPs penetration through biological barriers is still an outstanding technological challenge.

Soft hydrogel NPs, *i.e.* NPs synthesized by crosslinking a hydrophilic polymer, possess attractive attributes as drug delivery systems. Recent *in vivo* studies showed increased circulation time[371], lower immunogenicity[371] and increased tissue penetration[385] using hydrogel NPs compared to their hard counterparts. Longer circulation time is believed to result from two distinct mechanisms: a facilitated escape from the reticulo-endothelial system and a decreased uptake from the immune system, specifically from macrophages.[371] These observations suggest that soft

NPs can diffuse through biological barriers and penetrate interstitial tissues more efficiently compared to hard NPs with their deformable nature.[368, 372, 386] Few mechanisms for the improved penetration of soft NPs have been proposed. Hendrickson *et al.* reported that hydrogel NPs can cross permeable membranes with pore size much smaller than the NPs diameter under high enough hydrostatic pressure[368], a behavior that was ascribed to pressure-induced deformation of the NPs. Yu *et al.* reported that semi-elastic NPs can adopt an ellipsoidal shape when immersed in a hydrogel matrix, interacting strongly with the NPs and diffusing faster than hard spheres.[372]

To elucidate the diffusion mechanism of NPs in a porous medium, we compared the dynamics of soft and hard NPs in agarose hydrogels as a model system. We provide evidence that soft NPs diffuse much faster than hard spheres when dispersed in a hydrogel matrix. Such behaviour is reminiscent to their capacity to dynamically adjust their size under the influence of long-range interactions with their environment.

6.2 Results

6.2.1 Hard and soft NPs diffusivity in water

We used poly(N-isopropylacrylamide) (pNIPAM) hydrogel NPs as model soft hydrogel NPs. These particles have an elastic modulus ranging between 1-10 kPa and are known to be highly deformable under external stimuli such as pH, temperature, and osmotic pressure.[387-389] The diffusion coefficient of these NPs in agarose gels was compared to that of hard NPs (elastic moduli in the GPa range) made of polystyrene[390] (PS) or gold[391] (Au) of similar hydrodynamic radius.

Differential dynamic microscopy (DDM) was used to assess the dynamics of these particles in agarose solutions and gels. DDM allows high precision measurement of unlabelled NPs diffusion in a transparent media based on video microscopy [93, 94, 97]. This technique uses low-resolution movies to obtain the differential image correlation function $g(q,\tau)$, *i.e.,* the power spectrum of the difference between images pairs separated by a delay time τ, at a spatial frequency $q = 2\pi/L$, with L being the length-scale of interest. Under appropriate imaging conditions, the experimentally measured function $g(q,\tau)$ is related to the intermediate scattering function (ISF) $f(q,\tau)$ [15] as

$$g(q,\tau) = A(q)\,[1 - f(q,\tau)] + B(q), \quad (6.1)$$

where $A(q)$ and $B(q)$ are the signal amplitude and instrumental noise, respectively. For diffusing spherical NPs, the ISF takes the generalized exponential form of $f(q,\tau) = e^{-(\tau/\tau_R)^{\beta}}$, where τ_R is the relaxation time and β is the stretch exponent. For non-interacting monodisperse diffusing particles, β = 1, while interactions between particles and media and suspension polydispersity systematically lead to β < 1. From the relaxation time, τ_R, the effective diffusion coefficient $D = 1/q^2\tau_R$, and thus the hydrodynamic radius, r_H, can be estimated using the Stokes-Einstein (SE) equation $D = k_B T/6\eta r_H$, with k_B being the Boltzmann constant, T the absolute temperature and η the medium viscosity.

The dynamics of hard and soft NPs was first characterized in water as a reference medium. Figure 6.1A shows typical ISFs and their associated relaxation times (Fig. 1B) obtained by DDM in dilute hard and soft NP suspensions at volume fractions ϕ < 0.3%. Data reveals that $\tau_R(q)$ follows a power-law decay with an exponent of -2, and the stretching factor is systematically superior to 0.9, as expected for pure diffusion of nanospheres. The NP hydrodynamic radius in diluted suspension, r^0_H, was quantified using the SE equation and cumulant analysis[97, 392]. Figure 6.1C shows that r^0_H values are quantitatively very close to values obtained by dynamic light scattering (DLS), R^0_H, which were obtained by the same cumulant analysis. A good agreement within 3 % between r^0_H and R^0_H was obtained.

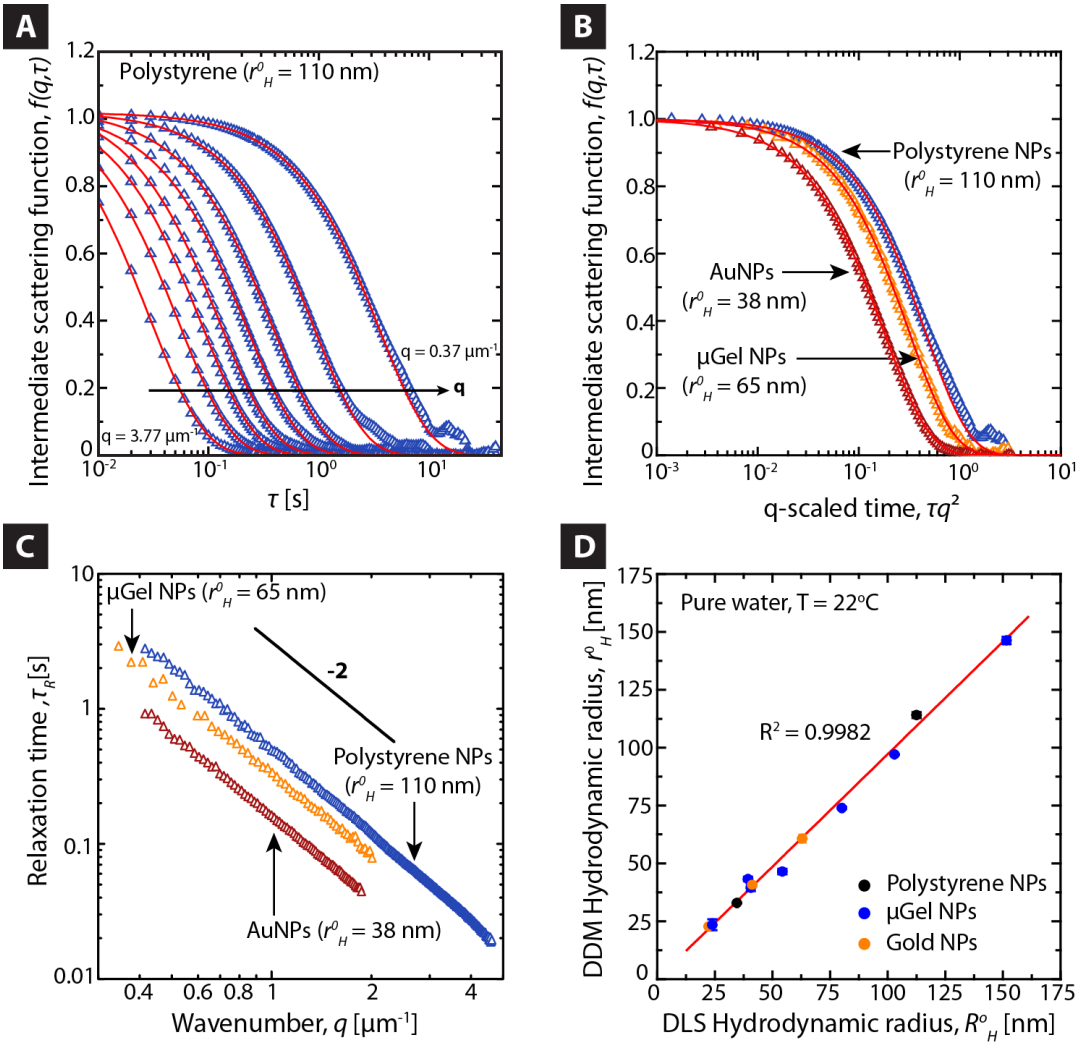

Figure 6.1. Dynamics of soft and hard nanoparticles in pure water at volume fractions φ < 0.1%. (A) DDM intermediate scattering functions extracted from $g(q,\tau)$ functions using Equation 6.1, showing the dynamics over a large sample of q. (B) Intermediate scattering functions as a function of the spatial-frequency-scaled time for hard NPs (blue triangle, q = 0.37 μm^{-1}, red triangle q = 0.57 μm^{-1}) and soft NP (orange triangle, q = 0.63 μm^{-1}). (C) Relaxation time τ_R vs q for different soft and hard NPs radii. Data shows the typical scaling relation between τ_R vs q with an exponent of -2. (C) Comparaison of the hydrodynamic radius obtained from DDM (r^0_H) and DLS (R^0_H). The red line is a linear least square fit to the data (slope = 0.972 ± 0.012) with its corresponding R^2 value. Numerical values for hydrodynamic radius are provided in Supplementary Table 1.

6.2.2 Hard and soft NPs diffusivity in agarose solutions and gels

Next, the effect of confinement on NPs dynamics in agarose solutions and gels of varying agarose concentrations, C_{ag}, was investigated. The diffusion coefficient of soft NPs with r^0_H = 25 – 130 nm was measured in parallel to hard NPs of similar radius r^0_H = 22 – 110 nm at ϕ < 0.3 % as shown in Figure 6.2. The extraction process of $\tau_R(q)$ from representative ISFs for all C_{ag} is shown in Supplementary Fig. 1 and described in Supplementary Notes 1. We confirmed for hard and soft NPs that $\tau_R(q)$ follows the general scaling relationship $\tau_R \sim q^{-2}$, over the range of agarose concentrations investigated, therefore allowing the calculation of an effective diffusion coefficient D_G of the NPs in the gels (see Supplementary Fig. 2 & 3). Alongside with $\tau_R(q)$, a stretch factor, $\beta \approx 0.7$, was measured in agarose gels, indicating that NPs have a quasi-diffusive motion hindered by the gel matrix, while $\beta \approx 1$ in agarose solutions (Supplementary Fig. 4).

Below the gelation point of agarose (C_{ag} = 0.05 – 0.1%w/w), no difference between the diffusion coefficient of hard and soft NPs was observed (see Fig. 2). In this C_{ag} interval, the diffusion coefficients of hard and soft NPs measured by DDM quantitatively matched theoretical calculations using the standard form of the SE equation, $D_G = k_B T/6\eta r_H^0$, suggesting that the decrease in the diffusion coefficient measured in liquid agarose with increasing C_{ag} can be solely attributed to the increase in viscosity of the medium. At C_{ag} = 0.1 %w/w, which is close to the sol-gel transition of agarose (see Supplementary Fig. 5, Supplementary Methods 1 & Supplementary Notes 2 for corresponding rheology experiments), D_G of soft and hard NPs with r^0_H > 75 nm significantly deviated from SE predictions (see Fig. 2, green symbols), highlighting the appearance of interactions between NPs and the polymer matrix. For spherical diffusers in dilute and semi-dilute polymer solutions, Phillies *et al*.[393, 394] have proposed a general expression for the reduced diffusion coefficient $D_G/D_0 = \exp(-\mu\, C_{ag}^{\nu})$, where D_0 is the diffusion coefficient of the NP in pure water and $\mu \sim r_H^{\delta}\, M_w^{\gamma}$. Here, M_w is the agarose molecular weight, γ, ν and δ are scaling factors (M_w^{γ} is constant in our experiments). Analysis of the data using Phillies equation provides a value of $\delta = 0.8 \pm 0.16$ for both hard and soft spheres. If agarose chains were freely moving in solution, a value of δ = 0 would have been expected. [393, 394] Therefore, in this regime agarose chains are strongly interacting with NPs and alter their dynamics. More importantly, the fact that similar

scaling parameter, $v \approx 0.75$, was found for hard and soft NPs indicates that their dynamics can be fully predicted knowing r_H, which determines the value of μ.

In the gel regime ($C_{ag} \geq 0.5$ % w/w), the diffusion of the soft and hard NPs was slowed down by the polymer matrix due to gel-NPs interactions, but soft NPs were found to exhibit significantly faster diffusion compared to hard NPs (see Fig. 2, red and black symbols). Comparing the diffusion coefficient D_G of hard and soft NPs of similar size (r^0_H = 62 and 50 nm, respectively), D_G of soft NPs was found to be nearly 2 orders of magnitude higher than hard NPs (D_G = 0.853 μm^2/s for soft NPs compared to D_G = 0.013 μm^2/s for hard NPs in C_{ag} = 0.5 % w/w agarose, see Fig. 2). Such a large difference in dynamics was ascribed to a change in particle size under the influence of long-range electrostatic interactions.

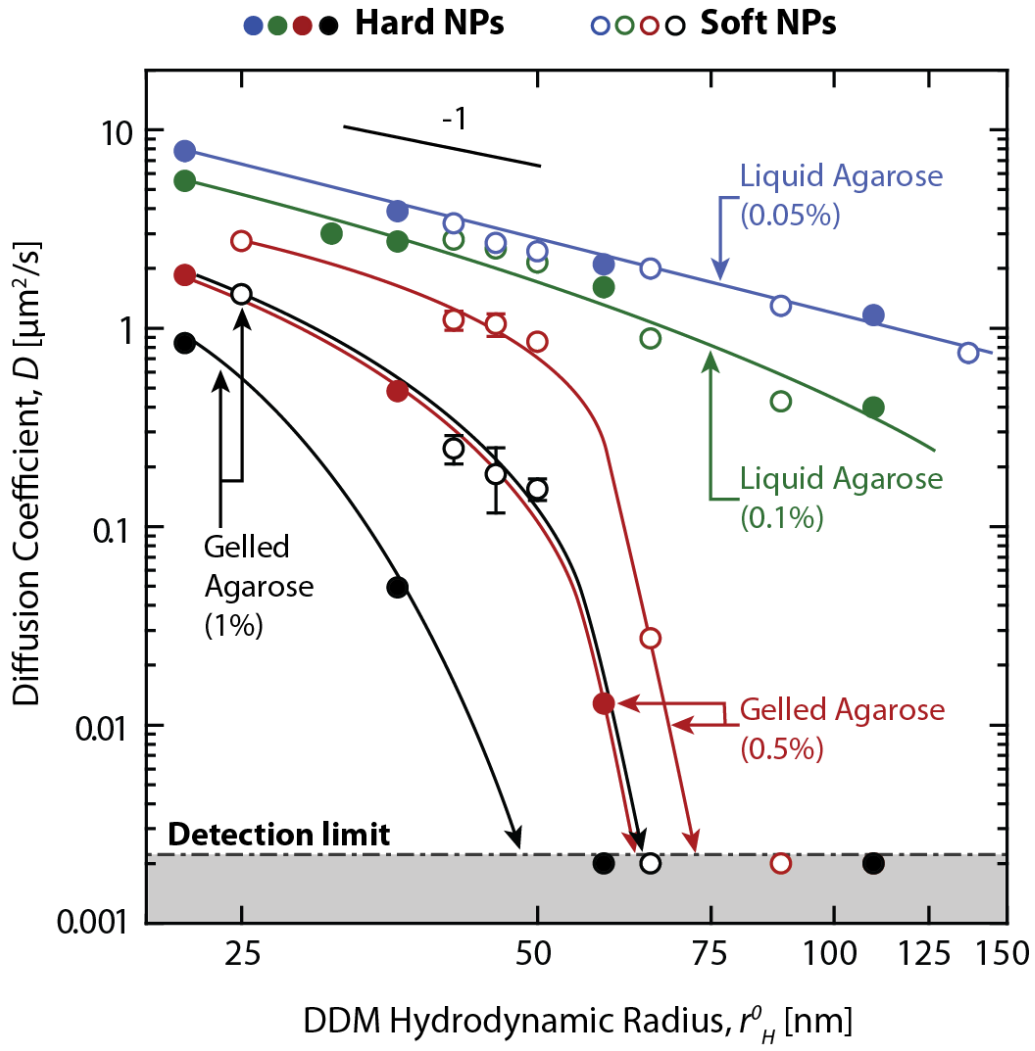

Figure 6.2. Diffusion of hard and soft NPs in agarose. Diffusion is compared at different concentrations of agarose (C_{ag} = 0.05, 0.1, 0.5, 1% w/w) versus the hydrodynamic radius r^0_H measured in water by DDM. Solid lines are guides to the eye, while the grey area shows the region below the detection limit, also indicating NP immobilization. Each point is presented with an error bar that corresponds to an average of 5-7 DDM measurements on one sample and its standard deviation.

6.2.3 Osmotic pressure in agarose gels

To confirm this hypothesis, osmotic deswelling of the soft NPs, originating from the presence of free (un-crosslinked or dangling) agarose chains, was first ruled out. [395-397] The osmotic pressure, Π_{osm}, inside C_{ag} = 1% w/w agarose gels was estimated by the dialysis bag method[398-400] to be 89 Pa (see Supplementary Methods 2 and Supplementary Notes 3 for details), which is of the same order as $\Pi_{osm} \approx$ 0.4 kPa reported for C_{ag} = 1 % w/w molten agarose solutions [395-397] at T = 37°C. This value is about two orders of magnitude smaller than the osmotic pressure needed to induce a 30 % change in NPs radius in presence of Ficoll^{TM} 400 solutions (Π_{osm}= 9.1 kPa, see Supplementary Fig. 6) [389, 401, 402], eliminating the potential contribution of osmotic stress from free agarose molecules to the change in particle size originating.

6.2.4 Hydrodynamic and electrostatic contributions to diffusivity

To quantify the possible contributions of electrostatic and hydrodynamic interactions to the dynamics of the NPs in the gels, the theoretical framework developed by Kang *et al.*[381] was used to analyze the data presented in Fig. 2. In this framework, hydrodynamic and electrostatic interactions are considered to be the sole interactions controlling the diffusion of spherical NPs in a percolating network of randomly oriented cylinders. The reduced diffusivity D_G/D_0 is expressed as the product of two separate terms, one for each interaction, as shown in Equation 6.4

$$\frac{D_G}{D_0} = \frac{1}{1+\alpha_{iso}^{h}\varphi_f}\frac{1}{1+\alpha_{iso}^{s}\varphi_f}. \quad (6.4)$$

The hydrodynamic interaction term is represented by the parameter α_{iso}^{h}, while electrostatic interactions are contained in α_{iso}^{s}. The parameter φ_f represents the agarose volume fraction, which varies between 0.0049 and 0.0098 in Figure 6.2. The coefficient α_{iso}^{h} for hydrodynamic interactions is expressed as a function of the hydrodynamic screening length κ^{-1} and the dimensions of both the particles and the cylinders in Equation 6.5,

$$\alpha_{iso}^{h} = -\frac{\kappa r_H^0}{(\kappa d_f)^2\, ln\{\kappa d_f\}}\left[\frac{64}{10} - \frac{85}{10\,000}\kappa L - \frac{33}{10\,000}(\kappa L)^2\right], \quad (6.5)$$

where L is the length and d_f is the diameter of the cylinders (the agarose fibres in the present case, L = 500 nm [403], d_f = 3.8 nm [404, 405]). The coefficient α_{iso}^{S} for electrostatic interactions is expressed in terms of the Debye-Hückel screening length κ_Q^{-1} in Equation 6.6,

$$\alpha_{iso}^{S} = \frac{2}{3}\left(1+\frac{2r_H^0}{d_f}\right)^2\left[1+2\frac{l_B}{L}\frac{Z_c Z_f}{\left[1+\kappa_Q r_H^0\right]\left[1+\frac{\kappa_Q d_f}{2}\right]}\frac{22}{\left(\kappa_Q\left[r_H^0+\frac{d_f}{2}\right]\right)^2+25\kappa_Q\left[r_H^0+\frac{d_f}{2}\right]+10}\right], \quad (6.6)$$

where l_B is the Bjerrum length, Z_C and Z_f are the surface charge of the colloid and the agarose fibres, respectively. The surface charge Z_C of the colloids was estimated from zeta potential measurements (see Supplementary Table 1 & Supplementary Notes 4 for details) using Makino *et al.* equation [200]. The surface charge of the agarose fibres Z_f was determined using Buffle *et al.* and Johnson *et al*. considerations [405] [84], which gave a value of Z_f = -40. The hydrodynamic screening length, κ^{-1} was calculated based on $\kappa^{-1} = \mathrm{A}\varphi_f^{-\mu}$, with the hydrodynamic constant A = 0.33 and the de Gennes polymer constant μ = 0.75 for soft polymer chains [406, 407].

Figure 6.3A shows the evolution of the reduced diffusivity of hard NPs (ϕ < 0.01 %) as a function of the agarose volume fraction in the gel, φ_f. The reported theoretical curves (Equation 6.4), which were obtained with no fitting parameter, accurately describe the experimental data, confirming the validity of the estimated values used for the gel pore structure and for colloids and agarose fibres surface charges. Using the same set of parameters for the agarose gel and the corresponding parameters for the soft NPs did not lead to a similar agreement between theory and experiments (Fig. 3B). The measured diffusion coefficients were systematically higher than the predicted values, if the soft NPs radius was kept constant and equal to r^0_H. It is interesting to note that the electrostatic interaction contribution by itself cannot account for the observed discrepancy. Indeed, increasing (or decreasing) the values of Z_f or Z_C significantly decreases the predicted reduced diffusivity and does not provide any conciliation with experimental data (see Fig. 3B). On the other hand, using r_H as the sole free parameter in Equation 6.4 allows obtaining excellent agreement between theoretical and experimental values at high C_{ag} (see Fig. 3C). At low C_{ag}, the particles are highly swollen and have a different r_H compared to the NPs at high C_{ag} which is not accounted for in the Kang *et al.* model. The r_H values obtained for all the tested soft NPs were significantly smaller than r^0_H at high agarose volume fractions, indicating shrinkage of the

NPs due to confinement. At φ_f = 4.98x10^{-3}, the shrinking ratio $\alpha = r_H/r_H^0$ was within 0.59 to 0.77, depending on the soft NPs size, which is consistent with α = 0.67 ± 0.12 obtained when exposing the soft NPs to 50 mg/mL Ficoll® solutions. Soft hydrogel NPs have been reported to exhibit a stiff core and a fuzzy corona (~ 1/3 of the NP radius), resulting from the radial decay of crosslinker concentration from their center[402, 408]. Therefore, it is reasonable to conclude that the measured value of $\alpha \approx 2/3$ in agarose gels and Ficoll® solutions is the result of compressing the fuzzy corona.

The discussed experiments above were performed in pure water after extensive dialysis to remove ions (see materials and methods). The measured conductivity in the gel indicated an equivalent monovalent ion concentration of 10^{-4} M, which corresponds to a Debye length $\kappa_Q^{-1} \approx$ 30 nm (see Supplementary Table 2), indicating that long range repulsive electrostatic interactions are present between the particles and the hydrogel matrix. Tuning the value of κ_Q^{-1} using monovalent ions had a strong impact on the dynamics of the soft NPs and hard NPs. By increasing the salt concentration ([NaCl] = 10^{-1} M, $\kappa_Q^{-1} \approx$ 1 nm), the diffusion coefficient of the soft NPs was found to exactly follow the theoretical values predicted by Equation 6.4 using r^0_H (and not r_H, see Supplementary Fig. 7), after accounting for the changes in gel structural parameters. Equation 6.4 predicts an increase in the reduced diffusivity D_G/D_0 of ~ 60 – 200 % (depending on the particle size and charge) when increasing salt concentration from 10^{-4} to 10^{-1} M, assuming no change in the particle size. However experimentally D_G/D_0 increased only by 10 % for the soft NPs, which can only indicate that the NP size has dramatically increased in the gel (see Supplementary Notes 5). Note that prior to these tests, it was verified by time-dependent measurements of r_H in saline solutions (no agarose) that no aggregation of the soft NPs occurs up to 1M NaCl in water. Also, adhesive interactions between the hydrogel NPs and agarose can be ruled out since no change in r_H ($r_H = r^0_H$) was measured in liquid agarose solutions, indicating that agarose chains do not adsorb on the NPs. Therefore, the presented results confirmed that in high salinity solutions, the soft NPs embedded in agarose gel fully recovered their original size ($r_H = r^0_H$).

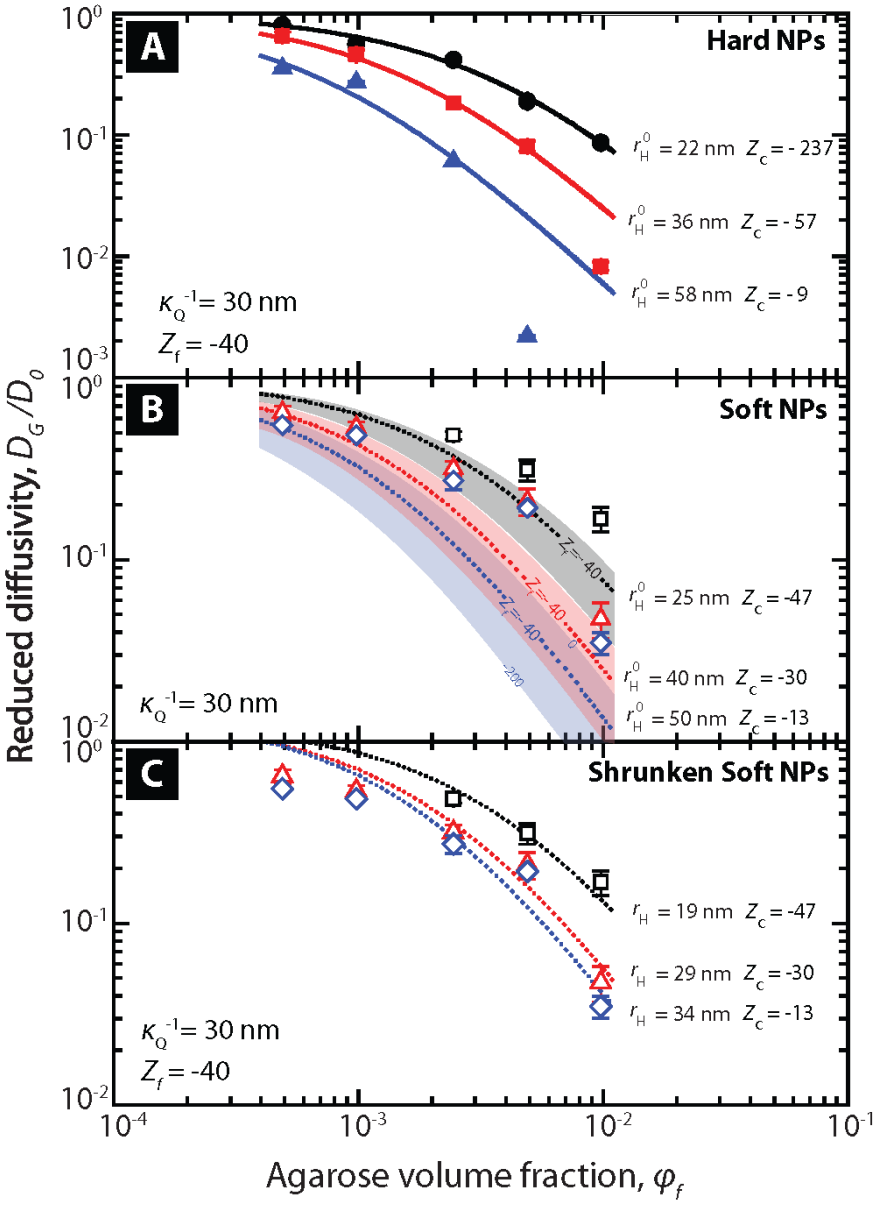

Figure 6.3. Experimental reduced diffusivities and theoretical prediction using Kang *et al.* model. (A) Data for hard NPs; (B) Reduced diffusivity of soft NPs. The theoretical curves were produced considering no change in particle size ($r_H = r^0_H$). Also presented are different simulated curves, using Equation 6.4, fallen into the highlighted areas calculated for different values of Z_f to demonstrate that electrostatic interactions alone cannot account for the increased diffusivity of soft NPs. (C) Reduced diffusivity of soft NPs (dotted lines) calculated assuming $r_H = \alpha r^0_H$. Data points and their error bars correspond to the average of 5-7 DDM measurements on one sample and their standard deviation.

6.2.5 Electrostatic interactions in the EDL

Therefore, it appears that the observed change in the diffusion coefficient, thereby in the particle size, is mediated by long range electrostatic interactions between the NPs and the agarose fibres, since interactions between particles is non-existent in suspensions at such low ϕ (see Supplementary Methods 3 and Supplementary Fig. 8). Agarose gel fibres are negatively charged (Z_f = -40 charge per fibre), which creates an ion cloud surrounding fibres similar to the ion cloud surrounding the NPs to form the so-called electrostatic double layer (EDL).[409, 410]

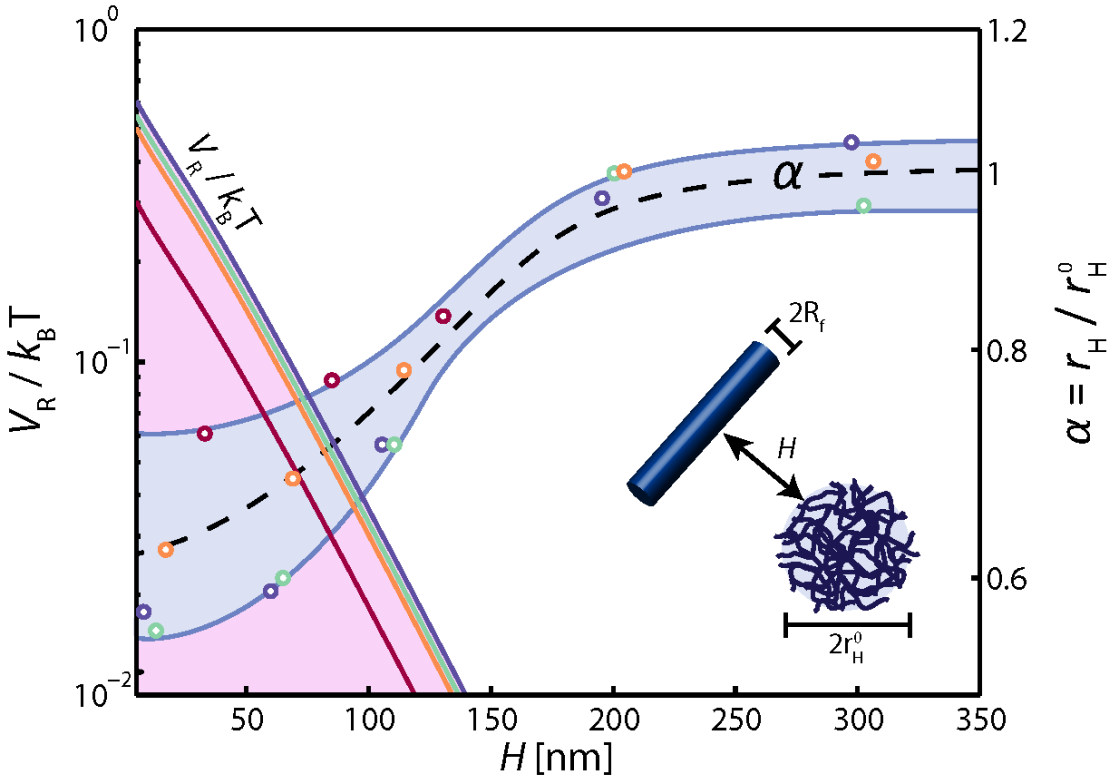

Figure 6.4. Electrostatic interactions in the EDL. Theoretical reduced interaction potential, V_R/k_BT, between a sphere and a fibre (left axis) and experimentally measured NPs shrinking ratio, α, (right axis) as a function of the surface-to-surface distance H. Experimental values for α were collected at different agarose concentrations C_{ag}, which were used to calculate H (see Supplementary Notes 6). The different colors used for the symbols (circles refer to α) and curves (which refer to V_R/k_BT) correspond to different values of r^0_H (red: r^0_H = 25 nm, orange r^0_H = 40 nm, blue r^0_H = 45 nm, green r^0_H = 50 nm).

In support of this hypothesis, the overlapping of soft NPs and agarose fibres EDLs was investigated by calculating the electrostatic interaction potential between a single agarose fibre and a soft NP (Fig. 4). The electrostatic interaction potential V_R between a spherical NP and an infinite cylinder in water was calculated using [411]

$$V_R = -4\epsilon\sqrt{2\pi\kappa R_f}\int_0^{r_H^0} x\sqrt{\frac{x}{\left({r_H^0}^2-x^2\right)(R_f+x)}}\left\{\begin{array}{l}\left(\frac{\psi_{0C}+\psi_{0f}}{2}\right)^2 Li_{1/2}\left[-e^{-\kappa_Q(H+r_H^0-x)}\right]\\ +\left(\frac{\psi_{0C}-\psi_{0f}}{2}\right)^2 Li_{1/2}\left[-e^{-\kappa_Q(H+r_H^0-x)}\right]\end{array}\right\}dx, \quad (6.7)$$

where R_f is the cylinder radius (agarose fibre), ε is the water permittivity, L_i is the polylogarithm function, H is the particle to fibre surface-to-surface distance and ψ_0 is the surface potential of the NPs (C) or the fibres (F) whose expression for the NPs is given by

$$\psi_0 = \frac{4k_BT}{e}tanh\frac{e\psi_d}{4k_BT}, \quad (6.8)$$

where ψ_d is the zeta potential and k_BT is the thermal energy. For the fibre, the surface charge density, σ, is related to the surface potential through:[412]

$$\sigma = \frac{2\epsilon\kappa_Q k_BT}{e}\sinh\left(\frac{e\psi_0}{2k_BT}\right)\left[1+\left(\frac{1}{\beta^2}-1\right)\frac{1}{cosh^2\left(\frac{e\psi_0}{4k_BT}\right)}\right]^{1/2}. \quad (6.9)$$

Here,

$$\beta = \frac{K_0\,(\kappa_Q d_f/2)}{K_1\,(\kappa_Q d_f/2)}, \quad (6.10)$$

where $K_n(z)$ is the modified Bessel function of the second kind of order n.

Plugging the experimental parameters in Equation 6.7, theoretical interaction potential curves were generated for NPs of different sizes in agarose gels of different C_{ag} (which defines the pore size in Supplementary Table 3 and the separation distance H as detailed in Supplementary Notes 6) and compared to the shrinking ratios r_H/r^0_H measured by DDM. As shown in Fig. 4, the shrinking ratio, α, of the soft NPs decreases from 1 to 0.6 when the particle-cylinder distance reaches the critical distance at which the repulsive electrostatic interaction begins (onset of interaction). This

transition occurs for *H* ranging between 100 and 150 nm depending on the value of r^0_H. The close correspondence between the onset of shrinking and the onset of electrostatic interaction is consistent with the hypothesis that EDL overlapping plays a major role in the shrinking of the NPs. The predicted value of the repulsive potential may appear rather small to create the required osmotic pressure for NPs shrinking in the gel, but it should be noted that the present calculation is accounting for the interaction between only one fibre and the NP. It is expected that many other fibres can simultaneously interact with the NP to create a much stronger pressure capable of triggering particle shrinking. The energy, *U*, required to compress an elastic nanosphere of elastic modulus *E* =1-10 kPa to 66% of its original size is U = 1-10 k_BT (see Supplementary Notes 7 for the calculations), which would approximately correspond to the interaction energy between 10-100 fibres and the NP.

6.3 Discussion

We have shown that hydrogel NPs shrinking occurs under confinement in gels, and found that such behaviour is due to the interactions between overlapping electrical double layers. Thanks to their deformable nature, hydrogels NPs shrink and diffuse 1 or 2 orders of magnitude faster than hard NPs under weak interaction pressure. Such peculiar ability may be triggered not only by electrostatic interactions, which in the present study were tuned by saline concentration, but in principle by any long-range interaction force. Different examples of such long range forces exist in the biological realm, especially those involving thermal fluctuations such as undulation forces originating from cell membrane undulation or steric polymer forces from for example pericellular glycosylated moieties [413, 414]. For example, compressive forces originating from membrane undulations[413] are proportional to $(k_BT)^2/k_bH^3$, (where k_b = 0.1-10 k_BT is the membrane bending modulus, and *H* is the separation distance) are of the order of 10^{-1} – 10^3 Pa for *H* in the range of 100 - 20 nm, which is sufficient to trigger soft NP compression. In the same line, considering a typical contour length of glycosylated moieties of 50-700 nm[415] and in some cases up to 11 µm[416], the Alexander – de Gennes steric interaction pressure generated by these moieties on a particle is written as $P(H) = 100\Gamma^{3/2}k_BT\exp(-\pi H/t)$, with Γ being the number of chains per unit area, and *t* the effective thickness of an adsorbed layer of moieties. Considering average values of 400 nm

and 0.001 nm^{-2} for t and Γ[417], the resulting steric pressure is of the order of 10^2 – 10^5 Pa, again sufficient to produce soft NP shrinking.

By taking advantage of their distinct ability to diffuse faster in complex crowded media, soft NPs can be invaluable assets when used as drug carriers for example. The results presented in this study echo the ever-increasing *in vivo* evidences showing that soft deformable NPs[370, 371] have the unusual capacity to penetrate more deeply into soft porous tissues. The soft NP shrinkage in this study was attributed to the pressure from the long-range electrostatic interactions. Although electrostatic interactions are short-range *in vivo*, other long-range interactions in biological environment could generate similar pressures. Therefore, careful attention should be paid to the design of the NPs mechanical properties and deformability in order to control their biological fate.

6.4 Methods

6.4.1 Chemicals

N-Isopropylacrylamide (NIPAM), N,N'-methylene-bis(acrylamide) (BisA), methacrylic acid (MAA) with 250 ppm inhibitor MEHQ and sodium dodecyl sulfate (SDS) approximately 95% were purchased from Sigma–Aldrich (Oakville, ON, Canada). Ficoll™ 400 (molecular weight ≈ 400 kDa) and agarose (low melting point) were purchased from Fisher Scientific (Montréal, QC, Canada).

6.4.2 Hard Nanoparticles preparation

Gold NPs of hydrodynamic radius R_H = 45, 75 and 125 nm (core diameter of 20, 50 and 100 nm) were purchased from Nanocomposix (San Diego, CA, USA). PS NPs (R_H = 60 and 220 nm) were purchased from Nanospheres. Silica NPs (Ludox TM-40) were purchased from Sigma–Aldrich (Oakville, ON, Canada). The nanoparticles were diluted with Milli-Q® water as needed.

6.4.3 Microgel synthesis

Microgel synthesis was performed as previously reported[418, 419]. Typically, the reaction was held in a three-neck flask under argon flow and mechanical stirring (approx. 300 rpm). NIPAM was dissolved with MAA (NIPAM:MAA ratio of 100:0 and 95:5), BisA (5.3 mol% total monomer), and

SDS in degassed water. Microgels smaller than r^0_H = 92.5 nm were synthesized without MAA and the largest microgel (r^0_H = 140 nm) with 5% molar MAA.

SDS concentration 0.87, 1.73, 3.47, 4.33, 8.67 mmol/L was used to tune microgel sizes (smaller microgels were produced by increasing SDS concentration). The reaction was initiated at 65°C by adding APS (2.7 mmol/L) with a subsequent rise in the temperature to 75°C for 4h30. Upon completion, the NPs suspension was removed from the flask and allowed to cool at room temperature. Each batch was dialyzed three times using Spectra/Por Tube-A-Lyzer Dynamic Dialysis Device (100 kDa MWCO) against Milli-Q water (~ 60-70 mL of particle suspension for 20 L of water for each dialysis cycle). NPs concentration within each batch was determined by freeze-drying 1.5 mL of the microgel suspension and weighting its dry mass. Colloidal microgels were stored at 4°C until further use.

6.4.4 Dynamic light scattering

DLS data presented in Fig. 1 were obtained with a Malvern Zetasizer NanoZS (Malvern Instruments, UK). Experiments were performed at a single scattering angle ϑ=173° at a temperature of 22°C for dilute suspensions (ϕ < 0.5%, details of the calculation in Supplementary Methods 4). Using Malvern software (cumulant analysis), the NP hydrodynamic radius (R^0_H) was obtained by identifying the peak of the intensity-weighted particle radius distribution.

6.4.5 Differential dynamic microscopy (DDM)

An upright microscope (Olympus BX81, Japan) equipped with a high acquisition speed camera (Hamamatsu Orca-Flash 4.0 V3, Japan) was used for the acquisition of videos of NPs suspensions. Videos were recorded using phase-contrast imaging using 20X or 40X magnification (Olympus Plan, NA = 0.4 (Ph1) and NA = 0.65 (Ph2) respectively), a framerate ranging from 20 to 300 frames per seconds, and an image binning of 1x1 or 2x2 within a region of interest of 512 x 512 pixels. These parameters were adjusted to optimize the signal amplitude and to access particle dynamics over an adequate q range and time-scale for each NP. Images were recorded in glass capillaries (Vitrocom, Canada) of thickness 0.4 mm filled with nanoparticle suspension (~180 µL) and sealed using petroleum jelly. Videos were recorded at least 5 times at three different positions for each capillary.

In some instances, the presence of a second decay in the autocorrelation function was observed at longer time, presumably due to larger aggregates or very slow relaxation of the gel. For these specific measurements, we used a double generalized exponential model to extract the short-time process:

$$g(q,\tau) = A1(q)\left(1 - e^{-\left(\frac{\tau}{\tau_{R1}}\right)^{\beta 1}}\right) + A2(q)\left(1 - e^{-\left(\frac{\tau}{\tau_{R2}}\right)^{\beta 2}}\right) + B(q), \quad (6.11)$$

with indices 1 and 2 corresponding to the short and long-time processes, respectively.

6.4.6 NPs diffusion measurements in agarose

To prepare NP suspensions in agarose, stock solutions of agarose were prepared at a concentration of 40 mg mL^{-1}. Agarose was dissolved in hot water using a common microwave oven. The stock solution was diluted accordingly to prepare agarose solutions of 0.05, 0.1, 0.5 and 1% (w/v) using warm diluted suspensions of NPs. The resulting suspensions was injected in a rectangular capillary as described and was let to cool-down at room temperature for at least 24 hours. Preliminary data was obtained during the cooling time to ensure that the gel was stabilized, and that the particles were not aggregating.

Chapitre 7 – Discussion générale

Dans cette thèse, diverses utilisations de la DDM ont été explorées afin de caractériser le comportement des NPs en milieu biologique. L'exploitation du formalisme DDM pour caractériser les interactions entre les protéines et les NPs dans des fluides biologiques aura permis de surmonter les défis analytiques précédemment rencontrés. Dans cette discussion, nous évaluerons les résultats présentés dans cette thèse quant à leur validité, leurs limitations et leur impact scientifique. Nous présenterons cette discussion en trois parties distinctes qui reflèteront les trois grands sujets présentés dans cette thèse.

Nous débuterons avec l'étude des mécanismes de diffusion dans les gels, au cours de laquelle nous avons fait l'observation que les NPs « molles » se déforment sous l'influence d'interactions électrostatiques, résultant en une diffusion plus rapide comparativement aux NPs « rigides ».

Ensuite, nous poursuivrons en évaluant la portée des observations réalisées dans le cadre de la caractérisation de la CP pour y évaluer l'impact des techniques de quantifications.

Nous terminerons cette discussion en évaluant l'étude des interactions protéines-NPs par DDM. En effet, cette technique aura permis d'identifier de multiples phénomènes dont l'influence de la concentration en protéines sur l'affinité de l'adsorption et l'effet Vroman à l'équilibre. Nous avons aussi pu établir les fondations de la méthodologie pour l'étude par DDM de ces interactions *in vivo*.

7.1 Étude des mécanismes de diffusion dans les gels

Dans le chapitre 6, l'étude de la diffusion de NPs dans un gel d'agarose a été présentée. Nous avons montré la validité de la mesure de diffusion des NPs dans l'eau par DDM. La mesure de la diffusion ou par extension le rayon hydrodynamique a été comparé à celui obtenu par DLS, une autre technique déjà bien établie. Nous avons ainsi montré que la DDM permettait une mesure équivalente à celle de la DLS pour la mesure de la diffusion des NPs. L'analyse des cumulants a

aussi permis de montrer la correspondance entre mesures DDM et DLS pour l'évaluation de l'indice de polydispersité des suspensions de NPs.

Nous avons ensuite utilisé des gels d'agarose pour modéliser une matrice extracellulaire et étudier la diffusion de NPs de tailles variables possédant différentes propriétés mécaniques (molles et dures). Nous avons remarqué que les NPs molles peuvent se déplacer beaucoup plus rapidement que les NPs dures, dans le même environnement. Dans certaines conditions, cette différence de diffusion était de 100 fois.

Nous avons investigué l'impact de la pression osmotique du gel sur les NPs, mais les mesures montrent que celle-ci est trop faible pour faire dégonfler les NPs.

Les contributions électrostatiques et hydrodynamiques ont aussi été étudiées à l'aide du modèle de diffusion de Kang *et al*[381]. Toutefois, les contributions électrostatiques du modèle de Kang *et al.* ne permettent pas d'expliquer la supériorité de diffusion observée chez les NPs molles, comparativement aux NPs dures (Figure 6.3). Or, seule la contribution hydrodynamique permettrait d'offrir une explication valable pour la variation du coefficient de diffusion observée entre les différents types de NPs. En effet, uniquement les NPs molles peuvent voir leur taille diminuer et donc influencer la contribution hydrodynamique. En utilisant cette approche, il a été possible d'estimer un rétrécissement d'environ 33% du rayon initial des NPs molles.

Bien que le modèle de Kang *et al.* suggère que les interactions électrostatiques ne sont pas responsables de la diffusion supérieure des NPs molles, ces dernières pourraient cependant être responsable de leur réduction de taille. Nous avons finalement proposé que cette réduction de taille pouvait être d'origine électrostatique. En effet, en calculant l'énergie d'interaction électrostatique entre une fibre d'agarose et une NP molle, il a été possible d'estimer qu'environ 10 à 100 fibres seraient nécessaires dans l'environnement d'une NP pour produire le dégonflement qui a été précédemment observé. Il serait raisonnable de considérer cette hypothèse sachant que le gel d'agarose est un vaste réseau de fibres et de pores interconnectés[86, 396, 403, 404, 420]. Enfin, nous avons fait la démonstration de ce mécanisme en utilisant un gel d'agarose pour lequel les portées électrostatiques étaient contrôlées (~1 nm) par ajout de NaCl.

Il a été possible de remarquer que dans ce gel, les NPs molles se comportaient de la même manière que les NPs dures (Annexe 3, Figure S7).

À partir de cette étude, nous avons montré que des NPs molles peuvent facilement être influencées par les interactions électrostatiques dans les milieux denses. Cependant, il est connu que les portées électrostatiques sont plus faibles *in vivo* comparativement à celles testées *in vitro*. En effet, pour des conditions *in vivo,* une force ionique estimée à 154 mM réduit les portées des interactions électrostatiques inferieures à 1 nm. Il s'agit, néanmoins, de l'une des premières démonstrations de la supériorité des NPs déformables en terme de diffusion en l'absence d'une force externe tel que montré par Hendrickson *et al.*[368]. De plus, cette étude permet de supporter l'hypothèse suggérant que l'amélioration de la pénétration des NPs molles serait majoritairement dictée par leur capacité à se déformer, ce qui aurait pour effet d'accroitre leur coefficient de diffusion dans les matrices extracellulaires. La réduction de taille des NPs molles leur permettrait de pénétrer de plus petits pores, modifiant ainsi leur pharmacocinétique et biodistribution[369-371].

7.1.1 Interprétation du rétrécissement des NPs molles et modélisation de leur diffusion

Il est à noter que l'interprétation du rétrécissement des NPs molles repose, en partie, sur des présuppositions du modèle de diffusion. Tout d'abord, le modèle de Kang *et al.*[381] est un modèle qui tient compte de plusieurs contributions en faisant intervenir plusieurs paramètres dont le sens physique est bien défini. En effet, dans ce modèle on y considère la taille et la charge des NPs, les dimensions et la charge des fibres du gel, de même que les portées hydrodynamiques et électrostatiques. Un modèle incluant autant de paramètres peut rapidement devenir très complexe et difficile à utiliser. De plus, dans le cas de l'agarose, puisqu'il s'agit d'un vaste réseau de fibres entre-mêlées[396, 403], la notion de « fibre » utilisée dans le modèle de diffusion peut s'avérer difficile à définir. Couplé à des estimations basées sur la littérature, ces zones grises peuvent rapidement faire croitre l'erreur associée au modèle de diffusion. Ce sont principalement les paramètres structuraux du gel, tels que la charge et la dimension, qui seront les plus susceptibles de générer des incertitudes. À l'inverse, les paramètres associés à la NP elle-même,

plus facilement accessible, soit la taille et la charge, peuvent être facilement déterminés par DLS ou PALS, améliorant ainsi la fiabilité du modèle de diffusion.

L'interprétation du rétrécissement des NPs molles se base aussi sur la présupposition que l'influence des propriétés électrostatiques du modèle de Kang *et al.* soit juste. Dans le contexte du modèle, les interactions électrostatiques ne permettaient pas d'expliquer l'augmentation de la diffusivité des NPs molles. Cependant, si le modèle sous-estimait l'ampleur des interactions électrostatiques, il serait possible de remettre en doute l'hypothèse du dégonflement. Cependant, ce genre d'évaluation nécessite des efforts et des ressources qui sortent du cadre du présent projet. Il existe un réel manque de consensus par rapport aux phénomènes influençant la diffusion des NPs dans les solutions de polymères et les gels. Bon nombre de modèles ont pour objectif de décrire quantitativement ou semi-quantitativement la diffusion dans ces milieux[421]. Toutefois, tel qu'argumenté par Phillies, il peut être ardu de déterminer le modèle de diffusion décrivant quantitativement la réalité[196]. En effet, un large éventail d'évidences serait nécessaire pour qu'un tel travail soit concluant.

Il est intéressant de noter que le rétrécissement des NPs molles pouvait tout autant être évalué par des modèles de diffusion simples. Par exemple, en utilisant les modèle de Ogston[422] et de Phillies[196, 393, 394] nous avons pu estimer une réduction de taille d'environ 30-40% de la taille initiale, une valeur semblable à celle estimée à partir du modèle de Kang *et al*[381]. Toutefois, ces deux modèles plus simples présentent des lacunes, qui ne devraient pas être négligées lors de la sélection du modèle.

Le modèle d'Ogston ne considère ni les interactions hydrodynamiques ni les interactions électrostatiques, mais plutôt le déplacement stochastique d'un objet de taille donnée dans un réseau aléatoirement orienté de fibres[421]. Toutefois, le modèle est reconnu pour diverger des mesures expérimentales aux grandes concentrations de gel (ou polymères) et pour les tailles plus grandes de NPs[421], ce que nous avons également observé.

Le modèle de Phillies bien que complet a été la cible de plusieurs critiques, notamment en ce qui a trait à son manque de clarté et l'absence de justifications théoriques[421]. Malgré le fait que ce modèle empirique permette l'interprétation de plusieurs phénomènes de transport (viscosité,

sédimentation, diffusion, etc.), le manque de sens physique pour certains de ses paramètres le rend difficilement « universel », malgré certaines tentatives de justification[196, 393].

Avec le modèle de Kang *et al.*, nous avons aussi observé des divergences du modèle par rapport aux données expérimentales pour les NPs les plus ralenties dans le gel. Cette observation suggère alors une limitation quant à la zone de validité du modèle pour le gel d'agarose.

L'interprétation de la réduction en taille des NPs molles pourrait soulever d'autres questions. Serait-il possible que le dégonflement observé soit en réalité, un effet hydrodynamique des NPs molles dont le modèle de Kang *et al*. ne considère pas? Il a été démontré que la structure poreuse des microgels pouvait avoir un impact sur les interactions hydrodynamiques lorsque les expériences étaient conduites à des fractions volumiques de >20% [423]. Nos expériences ont été réalisées à des fractions volumiques de 1%, en considérant le gel d'agarose et les NPs. Il est donc difficile d'établir si ce facteur pourrait avoir influencé nos résultats.

7.1.2 Diffusion, sous-diffusion et autres interprétations

À partir des données de diffusion générées par DDM, il pourrait être tentant d'évaluer le mécanisme de transport dominant des NPs dans les gels. Dans le contexte d'un déplacement purement diffusif, la distribution de probabilité des déplacements est gaussienne et le déplacement moyen carré est proportionnel au temps, $<\Delta x^2(t)>\sim t^1$. Dans une diffusion dite « anormale » ou sous-diffusive, le déplacement moyen carré est proportionnel au temps selon t^α, ou $\alpha < 1$. En DDM, il est possible de calculer le déplacement moyen $<\Delta x^2(t)>$ à partir de la DICF, sachant que l'ISF prend la forme $f(q,\tau)=\exp(-q^2<\Delta x^2(t)>/4)$ lorsque la distribution des probabilités de déplacement est gaussienne[424]. C'est de cette relation, entre le $<\Delta x^2(t)>$ et l'ISF qui prend généralement la forme de $f(q,\tau)=\exp(-[\tau/\tau_R(q)]^\beta)$, qu'est apparu le critère de sous-diffusion $\beta < 1$.

Il est important de noter que pour évaluer si le transport dans un gel d'agarose est sous-diffusif ou anormal, certaines conditions doivent être *à priori* respectées pour s'assurer que $\beta<1$ signifie bel et bien un phénomène de sous-diffusion. D'abord, $f(q,\tau)$ assume que la distribution des distances de déplacements des NPs soit gaussienne, que les interactions entre les NPs soient négligeables et que la distribution de taille des NPs soit monodisperse[95, 196]. En effet, tel que mentionné dans le chapitre 6.2.1, une importante polydispersité des NPs peut aussi engendrer

un β<1. Dans ce cas, cette mesure ne permettrait pas de tirer des conclusions définitives sur le type de diffusion observée. Cependant, une analyse de la dépendance spatiale de $\tau_R(q)$ peut aussi être un indicateur d'une diffusion anormale, si $\tau_R(q) \sim q^{-a}$ pour $a \neq 2$[87].

Contrairement à Banks *et al*.[87], nous n'avons pas été en mesure de trouver un marqueur direct de la sous-diffusion ou de la diffusion anormale des NPs dans des gels d'agarose. La seule exception à cette observation était lorsque la diffusion des NPs était massivement réduite (a<2). Ces exceptions ont été principalement observés pour les NPs dures (r^0_H=38 et 58 nm) lorsque la réduction de leur coefficient de diffusion D_G/D_0<0.01. L'observation de a<2 pour ces NPs pourrait dans ce cas-ci être la résultante d'obstruction significative du gel sur le transport des NPs, causant effectivement un transport sous-diffusif des NPs dans le gel.

7.1.3 Effets de la polydispersité

Nous avons précédemment mentionné que la distribution de taille des NPs pouvait avoir une influence sur les paramètres mesurés en DDM. En fait, il est possible que la polydispersité des NPs utilisées dans le cadre de nos expériences soit l'unique responsable de la décroissance du facteur β de l'ISF d'environ 0.95 dans l'eau à 0.7 dans l'agarose concentrée. Il est possible de voir numériquement cet effet à l'œuvre.

Nous allons voir qu'il est possible de reproduire l'effet du facteur β de l'ISF en utilisant uniquement des paramètres théoriques pour la distribution de taille, de l'effet d'un gel sur le coefficient de diffusion. Bien entendu, d'autres modèles ou paramètres pourraient être utilisés, cette simulation n'est qu'à titre d'exemple illustratif.

Si l'on assume une distribution (en nombre) de taille de NPs de forme log-normale[425], on peut reconstruire des fonctions d'autocorrélation en assumant que l'intensité du signal est proportionnelle au rayon, R^6 (basé sur la diffusion de la lumière d'une sphère[95, 103]). Ainsi, on peut décrire la fonction d'autocorrélation par DDM, comme en DLS, par la somme de chacune des contributions des NPs de la distribution[196]

$$G(q,\tau) = \sum_{i=0,1,2\ldots}^{R} P(R_i) R_i^6 (1 - \exp(-D(R) q^2 \tau)) \qquad (7.1)$$

pour laquelle, $D(R)$ est la relation entre le coefficient de diffusion des NPs et la taille des NPs et $P(R_i)$ est la distribution log-normale en taille des NPs de la forme[425]

$$P(R) = \exp\left(-\frac{(ln\,R - ln\,R_{ave})^2}{2(\sigma^2)}\right). \quad (7.2)$$

Ici, σ est équivalent à la polydispersité des NPs alors que R_{ave} est la taille médiane des NPs. Les distributions de tailles testées sont pour σ = 0.1, σ = 0.2 et σ = 0.3, tel que montré à la Figure 7.1A. On assume que le coefficient de diffusion suit une loi exponentielle en fonction de la taille, tel de défini par le modèle de Phillies *et al*.[196, 393, 394]

$$D(R) = D_0(R)\exp(-Rc^{\nu}) \quad (7.3)$$

pour laquelle $D_0(R)$ est le coefficient de diffusion des NPs dans l'eau (proportionnel à $1/R$) et c^{ν} est la concentration du gel à la puissance d'une constante que nous utiliserons pour simuler la réduction des coefficients de diffusion causé par un gel ou une solution de polymère. On assume ainsi que chaque NPs se déplace de manière purement diffusive et que l'impact de la concentration du milieu (c^{ν}) sur leurs déplacements est simplement affecté par le rayon des NPs.

On peut ainsi construire les fonctions d'autocorrélation $g(q,\tau)$ à partir des fonctions de distribution de tailles $P(R)$ de l'équation 7.2 et de l'impact de c^{ν} sur la diffusion de l'équation 7.3, en testant différentes valeurs de c^{ν}, soit 0, 0.66, 1.0, 1.33, 2.0, 2.66 et 4 x10^{-2}. Les fonctions d'autocorrélation obtenues par ce calcul sont présentées à la Figure 7.1B où nous avons assumé que D_0(100nm)q^2 = 1 s^{-1}. On peut finalement extraire les différents coefficients de diffusion D et facteurs d'étirements β, tel que nous l'avions fait dans le chapitre 6 par l'équation 6.1, où $f(q,\tau)=\exp(-[\tau/\tau_R]^{\beta})$ et $\tau_R=(Dq^2)^{-1}$.

De manière intéressante, on remarque une diminution du facteur β plus c^{ν} augmente, ce qui se traduit en une augmentation de l'étirement des fonctions $g(q,\tau)$, tel que l'on peut l'observer à la Figure 7.1B et 7.1C. En analysant la Figure 7.1C, on peut remarquer une diminution de β semblable à celle que nous avions observée expérimentalement avec l'agarose, soit de 1 à 0.7. Dans ces simulations, la décroissance de β provient uniquement de l'effet de polydispersité qui lui est accentué par la différence de diffusivité des NPs dans le milieu, tel que décrit par l'équation 7.3. Cet exemple représente bien la complexité des analyses des mécanismes de diffusion dans les gels et l'importance de considérer la polydispersité de tailles dans ces analyses.

Il est aussi possible de remarquer l'impact de la polydispersité sur les mesures de coefficients de diffusion. En effet, à partir de ces fonctions d'autocorrélation, il est possible de calculer le rayon hydrodynamique R_H pour c^v=0. Une forte déviation par rapport à la moyenne de la distribution de taille initiale peut être observée pour σ > 0.2. On peut observer jusqu'à 80% d'erreur par rapport à la moyenne théorique lorsque σ=0.3. Toutefois, cette dernière était attendue. Évidemment, cet effet est amplifié puisque nous avons établi que la contribution de la taille des NPs sur l'intensité du signal était de R^6. Toutefois, même si cette contribution est réduite à R^4, l'erreur reste tout de même élevée, pour ~50% (153 nm pour σ=0.3). Or on peut se poser la question suivante :

« *Est-ce que la polydispersité peut influencer la mesure du coefficient de diffusion dans un gel?* »

La réponse ici est oui, cependant, il est possible de considérer ce paramètre dans l'analyse. Par exemple, dans le panneau de droite de la Figure 7.1C, on peut voir l'impact de la polydispersité sur la mesure de D_g/D_0. Plus la polydispersité est grande, plus la mesure du coefficient de diffusion est faible. Si l'on modélise les données par $D_g/D_0=\exp(-Rc^v)$, on retrouve R=100 nm tel qu'attendu pour la courbe monodisperse (σ→0). Si on fait le même test pour σ=0.1, 0.2 et 0.3, on retrouve R=108, 137 et 200 nm, respectivement. Ces valeurs sont donc proches de celles trouvées pour c^v=0. En fait, on trouve une erreur maximale de 20% dans la mesure, malgré des coefficients de diffusion qui divergent de plus de 10x par rapport à la valeur monodisperse.

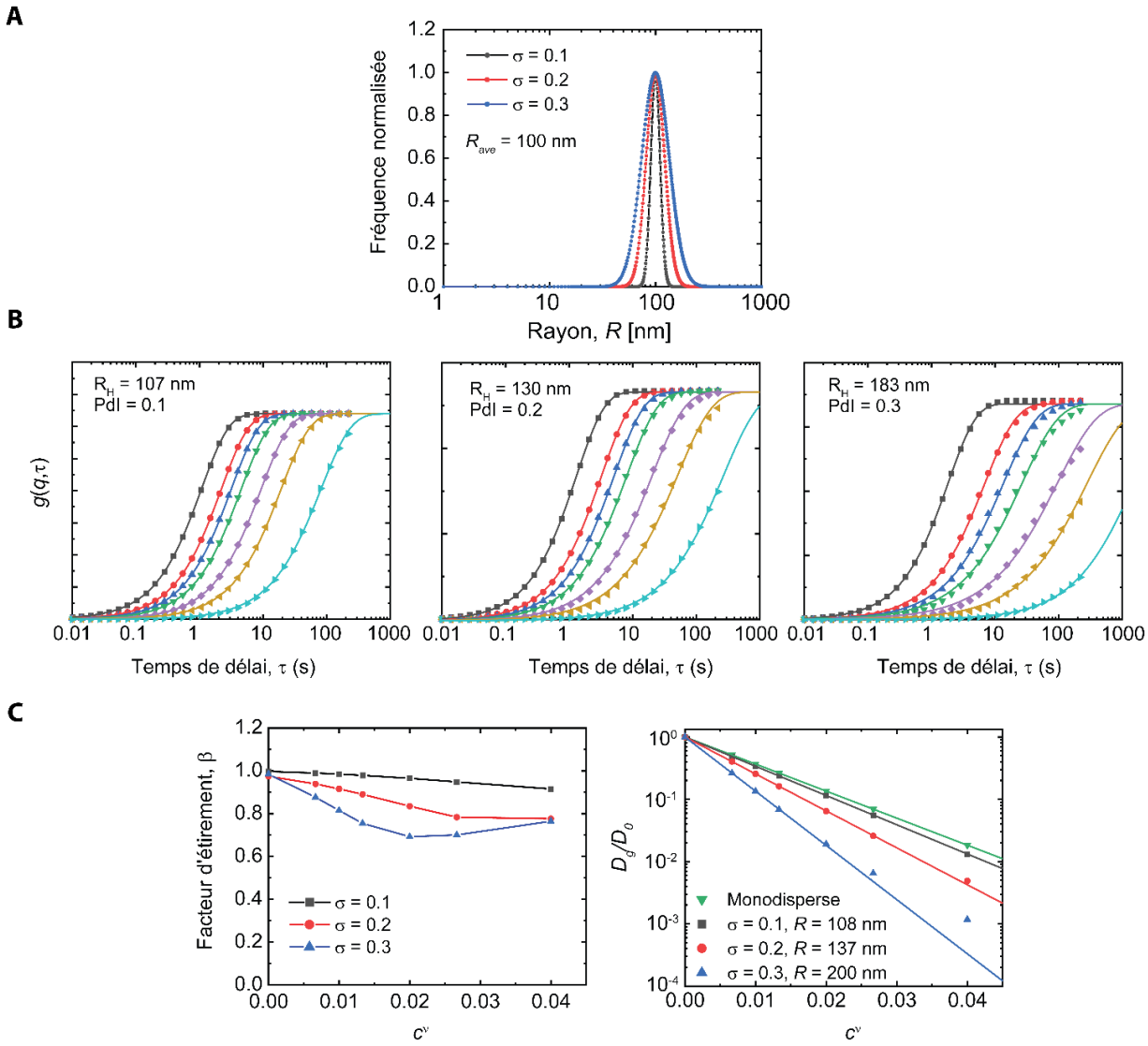

Figure 7.1. Simulation des fonctions d'autocorrélations DDM à partir d'une distribution de taille. Les distributions de tailles sont données par une distribution log-normale centrée à *R*=100 nm pour différentes polydispersités σ (A). Les fonctions d'autocorrélation sont construites à partir des équations 7.1-7.3 et sont modélisées par le modèle de l'exponentielle étirée (B). Les couleurs représentent différentes valeurs de c^v = 0 (noir), 0.66 (rouge), 1.0 (bleu), 1.33 (vert), 2.0 (violet), 2.66 (orange) et 4 (turquoise) x10^{-2}. Les tailles données (R_H) sont celles calculées à partir des fonctions d'autocorrélation pour c^v = 0. Paramètres extraits des fonctions d'autocorrélation en B pour les différentes polydispersité (C). Dans le panneau de droite, D_g/D_0 est modélisé par $D_g/D_0 = \exp(-Rc^v)$ où *R* y est laissé comme paramètre libre. Les valeurs de *R* obtenues sont données dans le graphique.

Ce que nous pouvons conclure de cette analyse est que le meilleur moyen pour minimiser les erreurs systématiques dans l'étude de la diffusion de NPs dans des matrices complexes, comme les gels, est de comparer les coefficients de diffusion avec les mesures de tailles obtenues par la même technique. Nous avons évalué dans le chapitre 6, la dépendance entre les coefficients de diffusion et la taille des NPs, tous deux mesurés par DDM. En procédant ainsi, on conserve la même sensibilité aux différentes tailles. En plus, il est possible d'assurer que la décroissance apparente de la taille des NPs molles dans les gels ne peut pas être causée par une différence de polydispersité. En effet, ces dernières ont des indices de polydispersité plus élevés que pour les NPs dures. Selon notre analyse, en l'absence d'effet de « dégonflement » nous aurions dû observer une augmentation du rayon des NPs molles et non l'inverse. Si tel est le cas, cet effet de polydispersité contribuerait plutôt à atténuer la différence de diffusion observée entre les NPs dures et molles.

Il est connu que la polydispersité de NPs déformable peut influencer ses propriétés de cristallisation à forte concentration et favoriser le dégonflement des NPs plus larges[402]. Bien que la dureté (module élastique) peut varier en fonction de la taille des NPs[390, 426], l'effet de la taille et de la polydispersité sur le dégonflement de NPs molles n'est pas toujours clair[427]. Il est donc difficile de conclure quant à l'effet de la polydispersité sur le dégonflement des NPs molles dans nos travaux.

7.1.4 Gels, matrice extracellulaire et milieu interstitiel tumoral

Pour l'étude de la diffusion de NPs dans les matrices biologiques simulées, nous avons fait le choix de mimer la matrice extracellulaire en utilisant l'agarose. Bien que ce type de gel ait déjà été employé dans plusieurs études ayant des buts similaires[82, 84, 85, 405], nous décrirons dans cette section l'impact de ce choix sur la portée des résultats.

Premièrement, l'agarose est un polysaccaride dont la structure se base principalement sur l'alternance entre deux unités, le *D*-galactose et le 3,6-anhydro-L-galactopyranose[396]. Les chaînes moléculaires d'agarose ainsi formées, possèdent une température de transition qui dépend de leur composition en galactose et galactopyranose. Cette température de transition permet la gélation de l'agarose dans l'eau. En effet, au-delà de cette température de transition (entre 30 et

50°C) les chaines se retrouveront sous forme soluble dans l'eau. En-deçà de cette température de transition, des ponts hydrogènes intra- et intermoléculaires assemblent les chaînes moléculaires d'agarose en fibrilles qui forment le gel d'agarose[396]. Le gel sera formé de ces fibrilles enchevêtrées formant une structure poreuse[403, 404]. L'agarose peut donc, par sa structure, être utilisée pour mimer la matrice extracellulaire des tissus ou le milieu interstitiel tumoral[82, 405] tout en limitant la présence de groupement chargés et d'interactions non-spécifiques[84].

Ces propriétés ont donc été exploitées dans le cadre de notre étude. En utilisant l'agarose, nous avons réduit les probabilités d'interactions non-spécifiques entre les NPs et le gel, en plus de limiter l'impact des interactions électrostatiques, puisque l'agarose est naturellement faiblement chargée de par sa composition moléculaire[84]. Limiter les probabilités d'interactions entre le gel et les NPs était primordial afin de réduire le nombre de paramètres à considérer lors de l'analyse, et par la même occasion limiter l'introduction de biais. De plus, quantifier ces interactions non-spécifiques pourrait s'avérer être une tâche difficile, d'autant plus que l'implication de ces dernières sur les coefficients de diffusion seraient peu connues. Pour cette raison, le gel d'agarose étant reconnu pour ses faibles interactions non-spécifiques, était le candidat idéal pour simplifier l'élucidation des différences entre les mécanismes de diffusion des NPs dures et molles.

Toutefois, ce choix de limiter la complexité du modèle a été fait aux dépens du réalisme de la matrice extracellulaire limitant ainsi l'extrapolation directe de nos résultats à des situations observées *in vivo*. En effet, la matrice extracellulaire est beaucoup plus complexe qu'un simple gel d'agarose. Les principales composantes de la matrice extracellulaire sont des protéines structurales telles que le collagène et l'élastine, des polysaccarides tels que l'acide hyaluronique, ainsi que des protéoglycanes[43]. En raison de sa complexité structurale et de sa composition unique, la matrice extracellulaire pourrait engendrer un plus large éventail d'interactions (spécifiques, non-spécifiques, adhésives, etc) avec les NPs que le modèle d'agarose.

7.1.5 Des essais de diffusion plus réalistes

Afin de réaliser des essais de diffusion qui se rapprochent plus étroitement de la réalité de la matrice extracellulaire (ou bien du milieu interstitiel tumoral), il serait logique de se baser sur sa composition. À titre d'exemple, des matrices de collagènes ont souvent été utilisées pour

modéliser la matrice extracellulaire[365, 428]. Le Matrigel, constitué d'extraits de matrice extracellulaire tumorale, peut aussi servir de modèle pour recréer le plus fidèlement possible la nature complexe de la matrice extracellulaire[429, 430]. Par exemple, ce dernier est fréquemment utilisé comme support de matrice extracellulaire pour le génie tissulaire. Il est cependant à noter que le Matrigel, en raison de sa nature biologique, peut être sujet à de fortes variabilités de composition biochimiques et structurales pouvant affecter, entre autres, ses propriétés mécaniques[429]. Pour illustrer la pertinence biologique de cette matrice, une récente étude par Le Goas *et al*. portant sur l'impact des propriétés de surface des NPs sur leur diffusivité dans le Matrigel[430]. L'approche a permis de simuler correctement la diffusion de NPs en périphérie des tumeurs en comparant avec des extraits *in vivo*. De plus, les traits caractéristiques d'une diffusion anormale des NPs dans le Matrigel a été observée, soit un comportement sous-diffusif attribué à des interactions non-spécifiques avec la matrice.

On peut faire le parallèle avec une étude de Roth *et al*., pour laquelle notre laboratoire a contribué, portant sur l'élaboration d'hydrogels présentant des sites d'affinité pour des NPs[431]. Dans cette étude, des hydrogels à base d'alginate ont été modifiés afin d'incorporer à leur surface le peptide « K », formant un complexe superhélice en présence d'un autre peptide dit « E ». Le peptide « E » a donc été ajouté à la surface de NPs d'or en guise de « ligand » pour le peptide « K », greffés sur le gel. Le gel possédant des domaines d'affinité pour les NPs, il devient alors possible d'étudier leur impact sur la diffusion des NPs. Nous avons évalué la diffusion par deux méthodologies distinctes : d'abord la diffusion brownienne par DDM et ensuite macroscopiquement par libération des NPs initialement incorporées dans le gel. En DDM, une différence notable a pu être observée au niveau des coefficients de diffusion entre les NPs avec et sans peptide « E ». Toutefois, le facteur d'étirement β des fonctions d'autocorrélations n'ont pas indiqué de diffusion anormale. D'autre part, un mécanisme de libération ne pouvant être expliqué par un simple processus de diffusion a été détecté dans le cadre des essais de diffusion par libération, mettant en évidence les interactions entre les peptides « E » et « K ». De manière intéressante, les résultats de Le Goas *et al.* pour la diffusion de NPs dans le Matrigel ont aussi été obtenus à partir d'une mesure macroscopique de la diffusion[430]. On peut ainsi remarquer que les

observations macroscopiques et les observations microscopiques par DDM sont qualitativement en accord, mais divergent quant à l'interprétation des différences.

Il serait donc intéressant de répondre à cette question : Est-ce que des mesures de diffusion microscopiques par DDM peuvent prédire ou expliquer les essais de diffusion macroscopique, ou bien, ces deux expériences sont complémentaires?

7.1.6 D'autres paramètres à étudier

Toujours dans un souci de reproduire le plus fidèlement possible les conditions que l'on retrouve *in vivo*, d'autres moyens ont été explorés dans le but de recréer des environnements biologiques. Premièrement, nous avons exploré l'utilisation des puces microfluidiques pour reproduire un environnement vascularisé. Pour ce faire, une puce microfluidique contenant des gels de chitosane, structurés d'un réseau complexe de capillaires semblables à ceux du réseau vasculaire des tissus [327], a été utilisée. Ce réseau de capillaires a ensuite été utilisé pour fournir du milieu de culture à des fibroblastes situés dans des chambres, à proximité des capillaires. Ce type de puce microfluidique a permis de mesurer par DDM la diffusion de NPs dans les différents compartiments du gel. Par exemple, la diffusion des NPs dans un des capillaires se rapprochait beaucoup de celle de l'eau alors que la diffusion des NPs dans le gel de chitosan était significativement ralentie. Il serait intéressant de pousser encore plus loin l'utilisation de ce modèle et de reproduire les flux sanguins physiologiques, pour ensuite mesurer l'importance de ce stress sur la matrice extracellulaire, les tissus et leur impact sur le transport des NPs, similairement à ce qui a été rapporté par Chen *et al*[432].

Finalement, il serait intéressant de mesurer l'impact de la déformabilité des NPs en fonction de leur forme, par exemple, des bâtonnets mous. Certaines observations proposent que la forme de bâtonnet permettrait d'augmenter la pénétration tissulaire[82, 360], il serait intéressant de vérifier s'il serait possible d'optimiser encore plus la diffusion des NPs en exploitant leur caractère déformable. Des molécules d'ADN relativement molles diffusent plus rapidement que des sphères dans des gels dû à un mécanisme de transport appelé « reptation »[82]. Il serait possible de penser que des nanovecteurs allongés et mous à base de polymères, tels que ceux proposés par

Johnson *et al.*[433] ou Xie *et al.*[434], pourraient prendre avantage de ce mécanisme de transport pour faciliter leur pénétration dans les pores de la matrice extracellulaire.

7.2 Identification des lacunes technologiques et expérimentales de la caractérisation des interactions protéines-NPs

Dans le chapitre 3, nous avons présenté une revue des différentes techniques permettant de caractériser la CP tant au niveau de leur utilité que de leurs avantages et limitations, toujours dans un contexte d'interactions nano-bio. Nous avons aussi, à partir des résultats générés par ces nombreuses techniques, déterminé leur contribution respective dans la résolution de certaines controverses attribuables à la CP. Nous avons remarqué avec cette revue que certains aspects de la CP font encore débat dans la littérature. Des hypothèses de nature opposée, notamment en lien avec la structure d'adsorption (mono *vs* multicouches) et la réversibilité de la CP, sont deux exemples de controverses retrouvées dans la littérature.

Le but ici était donc de vérifier si l'origine de ces observations opposées pouvait s'expliquer soit par l'utilisation d'une technique inadaptée pour la mesure des interactions protéines-NPs, soit par les composantes intrinsèques du système à l'étude (NPs, protéines, etc.).

Tout d'abord, nous avons procédé à la revue des principes théoriques, des différentes techniques d'analyse de la CP et de leurs limitations respectives. Certaines techniques se basent sur le changement de taille des NPs causé par l'adsorption des protéines. Pour ces techniques, c'est la sensibilité à la mesure du changement en taille qui déterminera la précision de leur mesure. D'autres techniques ne permettent pas de quantifier la quantité de protéines à la surface des NPs et vont plutôt mesurer l'affinité des protéines ou bien mesurer la composition relative des protéines adsorbées. Certaines techniques nécessitent une méthode d'extraction spécifique pour séparer les protéines libres des protéines adsorbées sur les NPs (*ex situ*) alors que d'autres peuvent faire ces mesures dans le milieu original (*in situ*). Nous avons donc tenté de catégoriser les techniques en fonction de leurs limitations et leur principe de quantification, afin d'identifier leur implication potentielle dans la mesure de multicouches et dans l'évaluation de la réversibilité par analyse statistique.

7.2.1 Absence de biais technique-dépendant

Dans cette analyse, les techniques regroupées par leur principe de quantification n'ont montré aucune différence entre-elles, autant pour la capacité de détection de multicouches de protéines que pour la réversibilité des interactions. De plus, la nature *ex situ* et *in situ* des techniques ne semble pas non plus influencer les deux phénomènes étudiés. Ces deux observations tendent donc à montrer que la performance à mesurer les multicouches de protéines et la réversibilité ne dépend pas, *à priori*, de la technique utilisée, ce qui va à l'encontre de certaines hypothèses émises dans la littérature[70, 73, 130]. En principe, il serait possible de supposer que les techniques utilisées pour caractériser l'adsorption des protéines ont été appliquées à l'intérieur de leurs limites.

7.2.2 L'impact de la taille des NPs

Il est intéressant de noter que la taille des NPs est le seul paramètre ayant montré un impact sur l'adsorption de protéines. Effectivement, une plus forte récurrence de multicouches et d'adsorption réversible a été observée pour les NPs plus larges, indépendamment du type de technique utilisée pour les caractériser. Tel que mentionné, certaines techniques se basent sur la mesure de la taille des NPs pour mesurer l'adsorption des protéines sur les NPs. Sachant que la sensibilité de ce type de techniques varie selon la taille initiale des NPs, il aurait été raisonnable de croire que cette variation provienne d'un biais technique. Même en retirant les études utilisant des mesures basées sur la taille des NPs pour caractériser la présence de multicouches, l'impact de la taille est resté présent, signifiant qu'il ne s'agit pas d'un effet dépendant de l'approche expérimentale utilisée.

Plusieurs études indépendantes relatent des différences significatives au niveau de l'adsorption de protéines en fonction de la taille des NPs. Par exemple, l'étude de Lacerda *et al*. a montré que l'affinité de certaines protéines envers les NPs augmentait en fonction de la taille de ces dernières[252]. Cependant, ce ne sont pas toutes les études qui montrent une croissance significative de l'affinité en fonction de la taille, certaines montrent une corrélation plutôt modeste entre ces deux paramètres[239]. Malgré cette divergence d'opinion, il n'en demeure pas moins que plusieurs études confirment que la taille des NPs a un rôle à jouer dans la

composition[107, 108, 163] et l'épaisseur de la CP[117] ainsi que dans les changements conformationnels des protéines une fois adsorbées[242]. Ces effets pourraient en fait contribuer à expliquer nos observations, mais l'absence d'explication mécanistique de l'impact de la taille souligne notre manque de connaissance par rapport aux interactions protéines-NPs.

Il est tout de même important de considérer que très peu d'études se sont penchées sur l'étude des NPs de plus de 50 nm de rayon. Ce manque de données sur les NPs plus larges contribuent donc à diminuer l'impact statistique de ces observations. C'est d'ailleurs pour cette raison qu'un effort devra être déployé pour combler ce vide, soit en développant de nouvelles techniques ou bien simplement en utilisant celles qui ne sont pas limitées par les plus grandes tailles (ITC, UV/Fluorescence, cytométrie de flux).

7.2.3 L'approche expérimentale à la désorption

Il est connu que pour tester la désorption d'un objet sur une surface, on peut soit le diluer ou bien le mettre en compétition avec un autre objet. Ces deux approches, pour évaluer la désorption se basent essentiellement sur la perturbation de l'équilibre d'adsorption (Loi thermodynamique de Le Chatelier). Il a été montré dans notre analyse que l'approche employée pour étudier la désorption des protéines sur les NPs pouvait avoir un impact important sur le résultat obtenu. En effet, les études ayant évalué la réversibilité de l'adsorption en utilisant la méthode de la dilution reportent davantage une adsorption irréversible comparé aux études utilisant la méthode de compétition. Quoique cette observation puisse refléter un problème méthodologique, nous pensons plutôt qu'elle serait reliée à une particularité mécanistique de l'adsorption protéine-NPs. Il est possible que certaines protéines s'adsorbent avec des mécanismes d'adsorption plus complexe sur les NPs comme ce fut démontré sur des surfaces macroscopiques[300]. Ceci pourrait potentiellement expliquer que dans certains cas, la simple dilution ne perturbe pas significativement l'équilibre pour causer la désorption. Si cette hypothèse s'avère exacte, des mécanismes d'adsorption plus complexes permettraient probablement d'expliquer pourquoi les protéines du sérum peuvent changer de composition dans le temps[63, 64], sans toutefois se désorber sous l'effet d'une dilution[69].

7.2.4 Limitations et possibilités futures

Finalement, bien que l'étude n'ait pu permettre l'identification de biais directement reliés aux techniques utilisées pour l'étude des phénomènes de réversibilité et d'adsorption en multicouches, elle souligne toutefois certains paramètres d'importance. D'abord, un manque flagrant d'études de la CP sur les NPs de plus de 50 nm a été identifié et s'expliquerait principalement par les limitations rencontrées avec l'utilisation des techniques usuelles. La méthode d'évaluation de la réversibilité a aussi été identifiée comme facteur pouvant impacter la nature des résultats. Cette étude contribue donc à mettre en avant les différents manquements et les avenues potentielles qui permettraient d'approfondir concrètement nos connaissances en lien avec les interactions protéines-NPs.

Bien entendu, nous n'avons pas couvert la totalité des paramètres qui peuvent influencer l'occurrence de multicouches de protéines et l'irréversibilité de l'adsorption. Une étude semblable a déjà permis l'évaluation de l'impact de certaines techniques et du potentiel zêta sur la mesure de l'affinité des protéines et des NPs[106]. Effectivement, notre analyse suppose que ces paramètres sont distribués de manière homogène à travers nos groupes. C'est pourquoi il pourrait être intéressant d'optimiser l'étude, en orientant cette fois notre analyse vers les propriétés des NPs ou bien des protéines. Il serait ainsi possible d'étudier l'effet du potentiel zêta, de la chimie de surface, du type de NP et des protéines étudiées sur l'occurrence des multicouches et de la réversibilité de l'adsorption à partir de notre ensemble de données.

7.3 Étude des interactions protéines-NPs par DDM

L'objectif principal de cette étude était de développer une méthodologie DDM robuste pour quantifier *in situ* l'adsorption de protéines. Cette méthode aura permis d'explorer les différentes hypothèses en lien avec la CP, notamment la présence de multicouches et la réversibilité de l'adsorption.

Tout d'abord, un modèle théorique a été développé et validé pour la quantification de l'adsorption de protéines dans diverses conditions. Ce système modèle était composé de la protéine lysozyme (positivement chargée) et de NPs à base de polystyrène (négativement chargées).

La validité de la mesure d'adsorption par DDM a été validée par le biais de deux méthodes externes : la mesure du potentiel zêta et la quantification par spectroscopie de fluorescence. Les différentes techniques se sont montrées équivalentes pour la mesure de l'adsorption de protéines. Avantageusement, la DDM permet également de mesurer *in situ* la taille des NPs et la structure des agrégats protéines-NPs en utilisant, respectivement, la mesure du coefficient de diffusion et de la dimension fractale[328]. Les mesures de tailles ont révélé que l'agrégation était présente dans tous les systèmes étudiés. En effet, il est déjà connu que l'adsorption de protéines à la surface de NPs favorise leur agrégation[70, 164, 198]. Cependant, cet aspect n'a que très rarement été abordé dans la littérature. Ainsi avec la DDM, nous proposons une méthodologie de caractérisation systématique de la taille et de la structure des agrégats. Avec cette caractérisation, il sera alors possible d'élucider les mécanismes d'agrégation et d'étudier les conséquences de l'agrégation de NPs dans les fluides biologiques.

Il est à noter que l'agrégation systématique de NPs en présence de protéines complexifie l'analyse de l'adsorption. Tel qu'expliqué précédemment, pour que la DDM puisse offrir une mesure quantitative de l'adsorption, il est impératif de déterminer le nombre d'agrégation *N*, *i.e* le nombre de NPs par agrégat. C'est pour cette raison que nous nous sommes tournés vers la mesure de la dimension fractale. Bien que cette dernière permette la normalisation de la mesure d'adsorption, elle introduit tout de même une erreur non-négligeable sur cette mesure. En effet, on estime que pour des agrégats de taille dix fois supérieure à celle des NPs seules, l'erreur de la mesure de taille et de la dimension fractale contribuerait à une incertitude d'environ 30% sur la mesure d'adsorption de protéines. Ainsi, dans ces conditions « *extrêmes* », la DDM permet de quantifier l'adsorption de protéines aux NPs avec une précision intéressante. À notre connaissance, aucune autre technique n'a clairement démontré la capacité à quantifier *in situ* l'adsorption de protéines dans des conditions d'agrégation.

7.3.1 Isothermes d'adsorption, affinité et notions d'équilibre

À partir de la méthodologie développée, nous avons été en mesure d'évaluer l'adsorption du lysozyme à la surface des NPs de polystyrène. La mesure d'adsorption a été réalisée à l'équilibre, ce qui a permis la construction d'isothermes d'adsorption, permettant le calcul de l'affinité du

couple lysozyme-NPs. Il est à noter que dans le cadre d'études similaires, l'influence de la concentration en NPs n'a que très rarement été abordé[31, 66, 67, 69, 72, 74, 162]. En mesurant l'affinité entre les protéines et les NPs pour différentes concentrations à partir d'isothermes d'adsorption, il a été observé que l'affinité diminuait avec l'augmentation de la concentration en NPs. Cette observation avait aussi été faite par Milani *et al.* Les auteurs avaient toutefois conclu que l'adsorption mesurée était irréversible[31], ce qui n'est pas le cas ici. En effet, la mesure de l'affinité par isotherme d'adsorption, basée sur le calcul de la quantité de protéines libres, implique nécessairement une adsorption réversible et à l'équilibre. Si les sites d'adsorption n'étaient pas tous saturés et que l'adsorption était irréversible, on se serait attendu à une déplétion des protéines libres. Or, nous n'avons pas fait cette observation dans le cadre de nos expériences. Par ailleurs, nous avons montré que les protéines fluorescentes adsorbées pouvaient être déplacées par cette même protéine, cette fois-ci, non fluorescente. Ces deux démonstrations montrent donc la réversibilité de l'adsorption, et ce, malgré la proportionnalité observée entre l'affinité protéine-NPs et la concentration en NPs.

Il est important de remarquer que cette observation implique un phénomène bien particulier. Lorsque la solution contenant les protéines et les NPs est diluée, on n'observe aucune perturbation de l'équilibre. Nous pouvons dresser un parallèle avec l'observation que nous avions faite précédemment, où nous avions identifié un biais dans l'approche à la désorption. Ici, on rapporte exactement le même phénomène, où l'approche par compétition permet de désorber les protéines alors que la dilution, elle, ne perturbe pas l'équilibre et ne cause pas de désorption de protéines.

On attribue donc l'origine de ce comportement unique à un mécanisme d'adsorption un peu plus complexe, qui permettrait en fait d'unifier nos observations expérimentales aux observations faites dans d'autres études. Cependant, pour le moment nous ne connaissons pas un mécanisme d'adsorption précis qui permettrait d'expliquer en détail nos observations. C'est pour cette raison qu'une simple dilution ne suffit pas pour identifier un système irréversible, puisqu'elle pourrait ne pas perturber l'équilibre et désorber les protéines à la surface des NPs.

7.3.2 L'effet Vroman sur les NPs

Par la suite, nous avons souhaité caractériser l'adsorption de protéines à partir de solutions plus représentatives de la complexité des fluides biologiques. C'est pourquoi l'adsorption des protéines du sérum bovin sur les NPs de polystyrène a été étudiée. En parallèle, l'adsorption de l'albumine a aussi été étudiée, puisqu'elle constitue la protéine majoritaire du sérum bovin. En mesurant l'adsorption des protéines du sérum sur les NPs, nous avons démontré deux régimes bien distincts. En faibles concentrations dans le sérum, les protéines s'adsorbent de manière coopérative, *i.e.* chaque protéine adsorbée facilite l'adsorption de sa proche voisine, s'exprimant par un facteur de Hill, n >1. Cette tendance semble s'estomper à de plus fortes concentrations, aboutissant à une adsorption comparable à celle de l'albumine au niveau de l'affinité et du nombre occupé par NPs.

Nous avons donc évalué si les deux régimes d'adsorption dans le sérum étaient bien réels et s'ils pouvaient provenir d'un changement dans la composition de la CP. Dans cette analyse, la DDM ne fait pas la distinction entre les différentes protéines du sérum et il sera assumé que toutes les protéines du sérum sont identiques à l'albumine. Si c'était réellement le cas, nous n'aurions pas pu observer deux régimes d'adsorption distincts. Il est possible que toutes protéines du sérum ne possèdent pas le même ratio de fluorophore par masse molaire, où par exemple 1 fluorophore serait greffés par albumine (~66 kDa) et par IgG (~150 kDa). Cette hétérogénéité pourrait être à l'origine de l'observation du changement de composition de la CP dans le sérum par DDM. On note aussi une agrégation qui survient proche de la transition des deux régimes d'adsorption, C_P/C_{NP} entre 10^2 et 10^3. Tel qu'estimé précédemment, l'erreur maximale à la mesure est d'environ 30% pour les conditions d'agrégations mesurées ($R_{agg}/R_0 \approx 10 \pm 1$ et $d_f = 2.13 \pm 0.13$). *À priori*, seul un changement de la composition en protéines permettrait d'expliquer les différences des niveaux d'adsorption observées entre les 2 régimes d'adsorption, tel qu'un écart de 10 fois, pour le régime très dilué vers $C_P/C_{NP} = 10$.

Cet effet est similaire à l'effet « Vroman à l'équilibre », pour lequel on observe une différence dans la composition des protéines à la surface de matériaux en fonction de la dilution du sérum[137, 334]. Il serait possible que cet effet soit aussi observable avec les NPs. Nous avons expliqué que des protéines volumineuses pouvaient s'adsorber initialement sur les NPs, à faible concentration de

sérum, pour ensuite être remplacées par de plus petites protéines à forte concentration. Il est suggéré que les protéines ayant une masse molaire élevée causeraient une saturation de la surface des NPs, se traduisant par un faible nombre de protéines pouvant être adsorbées. Toutefois, à de plus fortes concentrations de sérum, des protéines ayant de plus faibles masses molaires, comparables à l'albumine, constitueraient la plus grande partie de la CP et y permettrait une adsorption en plus grand nombre.

Les preuves de l'existence de l'effet Vroman à l'équilibre pour les NPs se font peu nombreuses et des traits caractéristiques de cet effet n'ont été rapportés que tout récemment [337, 338]. Il pourrait être intéressant de valider le phénomène en utilisant deux protéines connues pour contribuer à l'effet Vroman, par exemple le fibrinogène et l'albumine[136, 137, 140, 334], marquées de fluorophores différents. Par DDM, il serait possible de mesurer séquentiellement l'adsorption de chacune de ces protéines soit à l'équilibre ou durant leur évolution dans le temps. De cette manière, il serait possible d'approfondir nos connaissances des mécanismes responsables de l'adsorption des protéines dans des conditions contrôlées et proches de la réalité.

7.3.3 Vue d'ensemble de la couronne de protéine

Une dernière mention d'intérêt doit être portée sur la structure de la CP. La technique DDM développée permet la mesure quantitative du nombre de protéines par NPs. Avec cette mesure, il a donc été possible d'évaluer si la structure des CPs observées étaient en fait des monocouches ou bien des multicouches de protéines. Une partie du chapitre 3 a été consacrée précisément à l'évaluation de la sensibilité des méthodes pour cette mesure. Le travail de revue a révélé que 70% des CPs étudiées étaient structurées en monocouches. De plus, le travail présenté dans le chapitre 4 montre uniquement la présence de monocouches lors de l'adsorption du lysozyme, des protéines du sérum et de l'albumine. Tel que décrit dans le chapitre 2, les protéines n'interagissent que très peu entre elles, ce qui confère aux différentes composantes du sang une stabilité colloïdale par exemple. Pour que ces interactions soient suffisamment nombreuses pour permettre une structure en multicouche à la surface des NPs, elles devraient donc être accompagnées d'une dénaturation importante des protéines [73]. Une récente étude de Zhang *et al.* a montré qu'à la surface des NPs, des protéines du sérum pouvaient s'attacher à plusieurs

protéines, ce qui contribuerait à produire plusieurs couches de protéines[348]. S'il est vrai que les protéines peuvent interagir entre-elles à la surface des NPs, ce phénomène n'empêcherait pas non plus les protéines de s'organiser en monocouches. Il est intéressant de noter qu'une récente étude a tenté de caractériser la composition de la CP dure et molle du sérum sur des NPs de silice et de polystyrène. Dans les travaux de Mohammad-Beigi *et al.*, l'analyse détaillée de cette composition révèle que la totalité des protéines fortement et faiblement adsorbées recouvrent approximativement une seule couche[150]. Il est à noter que bien que ces interactions soient peu probables, nous n'excluons pas qu'elles existent. Il se pourrait que les interactions protéines-protéines menant à la formation de multicouches soient plus rares que ce qui était imaginé initialement. Par exemple, ceci permettrait d'expliquer pourquoi ces observations sont aussi difficiles à générer et à reproduire.

7.3.4 Les opportunités de la DDM *in vivo*

Enfin, une avancée importante a été réalisée dans le domaine de l'analyse de la CP en mesurant la désorption de protéines *in vivo* dans un poisson zèbre par DDM. Cette expérience aura permis de mettre en évidence le potentiel de la technique pour étudier les interactions nano-bio *in situ* dans un organisme vivant. À notre connaissance, très peu de techniques pourraient permettre de telles mesures. Une des seules approches développées dans cette optique repose sur la RMN, mais se limite actuellement à des études *in vitro*[75, 229]. Nous avons donc, à notre connaissance, décrit la première mesure *in situ* de la réversibilité de la CP dans un organisme vivant.

La durée caractéristique de désorption était d'environ 1h, pendant laquelle la moitié des protéines se sont désorbées. Nous pouvons comparer nos résultats à ceux d'études évaluant la cinétique de la composition de la CP par protéomique. Pour des NPs de polystyrène négativement chargé dans le sérum humain, Tenzer *et al*. ont montré que le changement en composition de la CP peut s'effectuer entre 30 et 60 minutes, ce qui est en accord avec nos observations[63]. Ces résultats contribuent à confirmer la validité de notre observation par DDM.

Il est cependant à noter que les mesures DDM dans le poisson zèbre ont été réalisées dans des conditions idéales et très contraignantes. Tout d'abord, la concentration en NPs dans le champ de vision devait rester la même tout au long de la cinétique. Il était donc impératif de limiter le

mouvement des appareils de microscopie. Aussi, le photoblanchiment des fluorophores devait être limité au maximum, en minimisant, par exemple, l'intensité d'excitation. Finalement, la dynamique devait être suffisamment lente pour permettre la mesure de l'amplitude du signal DDM. Dans notre cas, les NPs ont été capturées par les cellules endothéliales du poisson zèbre, ce qui limitait la vitesse de diffusion des NPs facilitant ainsi la mesure de l'amplitude du signal.

Bien entendu, il s'agit des premiers développements de la DDM *in vivo.* Il sera nécessaire d'améliorer le contrôle des différents paramètres afin d'optimiser la mesure. Cette évolution logique de la DDM dans l'univers *in vivo* permettra d'explorer des systèmes toujours plus complexes et plus représentatifs de la réalité. En effet, on peut considérer le poisson zèbre, et ces nombreux capillaires sanguins, comme un modèle plus complexe de la puce microfluidique utilisée pour les études *in vitro*. Par exemple, de récents développements en DDM ont permis d'étudier la dynamique diffusive de NPs dans les flux convectifs générés par microfluidique[435]. Il pourrait enfin être envisageable de véritablement transposer ces développements de la DDM à l'étude des phénomènes *in vivo.*

Chapitre 8 – Conclusion et perspectives

Deux thématiques distinctes de la nanomédecine ont été abordées dans le cadre de cette thèse, soit les interactions des NPs avec les fluides biologiques et leur diffusion dans des matrices extracellulaires simulées. Nous avons d'abord identifié un intérêt marqué pour le développement de nouvelles techniques permettant la caractérisation des nanotechnologies dans leurs interactions avec les composantes du vivant. L'hypothèse centrale de ces travaux était qu'il serait possible de développer et d'utiliser la DDM pour caractériser les différentes interactions propres à la nanomédecine. Nous avons donc fait usage de la DDM pour contribuer à l'avancement de notre compréhension des phénomènes d'adsorption de protéines sur les NPs et des paramètres affectant la diffusion de NPs dans des modèles de tissus interstitiels.

Tout d'abord, nous avons développé une méthodologie robuste pour la quantification de l'adsorption de protéines sur des NPs. Cette méthodologie est très avantageuse puisqu'elle ne nécessite que l'utilisation d'un microscope muni d'une caméra sensible ayant une bonne vitesse d'acquisition. La technique ainsi développée aura permis la quantification de l'adsorption de protéines, et ce, même dans des conditions peu favorables, telles qu'en présence de NPs agrégées, d'une composition complexe de protéines et même d'un système *in vivo*. À l'aide d'une revue de la littérature et d'une méta-analyse, nous avons pu préciser le rôle que pourrait jouer la DDM dans l'étude de l'interaction des NPs avec les composantes des fluides biologiques. Il a été possible, par la suite, d'orienter nos recherches afin de répondre à des questions importantes pour la caractérisation de la CP, en lien avec la formation de multicouches de protéines et la réversibilité de l'adsorption de protéines. Il a été remarqué que pour les différentes protéines étudiées, le lysozyme, la BSA et les protéines du sérum, s'adsorbaient en monocouches. Bien que cette observation soit opposée à ce que certains ont rapportées dans la littérature[74, 113, 162], nos résultats expérimentaux sont supportés par ceux de notre méta-analyse où l'on a remarqué une occurrence de monocouches dans environ 70% des cas. L'exploration de la réversibilité de l'adsorption par DDM a d'ailleurs permis de mettre en évidence que les mécanismes d'adsorption ne sont pas toujours aussi simples que ce que les modèles standards pourraient nous laisser croire. Les conclusions de la méta-analyse abondaient dans ce même sens.

Enfin, nous pouvons conclure que l'approche par DDM pour l'étude des interactions des fluides biologiques avec les NPs aura permis d'unifier plusieurs observations et conclusions qui avaient été faites par le passé. Les travaux présentés illustrent toute l'importance de comprendre les mécanismes moléculaires impliqués dans l'adsorption de protéines sur les NPs. Dans des travaux futurs, il serait important d'élucider ces mécanismes hypothétiques par une approche, d'une part théorique, et d'autre part expérimentale. De plus, nous suggérons d'exploiter davantage la DDM dans le cadre de l'étude de l'adsorption de protéines dans des systèmes *in vivo* pour ainsi poursuivre son optimisation et permettre l'élucidation de phénomènes, qui à première vue, peuvent sembler très complexes.

Ensuite, nous avons montré la capacité de la DDM à étudier les propriétés de diffusion des nanotechnologies dans des gels d'agarose, simulant une matrice extracellulaire. Nous avons choisi d'évaluer l'importance de la déformabilité des NPs dans des milieux confinés. Cela a permis de tester l'hypothèse qui a été émise par plusieurs études *in vivo*, voulant que les NPs peuvent se déformer pour améliorer leur pénétration tissulaire et modifier leurs paramètres pharmacocinétiques [369-371, 436]. Les mesures de diffusion DDM auront permis de confirmer, avec l'aide de modèles mathématiques, que les NPs « molles » pouvaient se dégonfler sous le confinement du gel d'agarose, leur permettant une diffusion plus rapide que celle des NPs « dures ».

Nous avons finalement montré qu'il était possible d'évaluer par DDM l'impact des différentes propriétés des NPs influençant leur diffusion dans des matrices extracellulaires simulées. Nous croyons qu'il serait bénéfique d'employer cette technique pour évaluer la pénétration des NPs dans les tissus interstitiels. Par exemple, il serait intéressant d'évaluer les mécanismes prédominants dans la pénétration tissulaire, et ce, dans des conditions plus réalistes. Il serait alors possible d'évaluer si la forme, la déformabilité et une combinaison de ces deux paramètres sont affectés différemment. De plus, nous avons noté de légères différences entre les résultats obtenus avec l'approche macroscopique et microscopique pour la mesure de diffusion par DDM. Il serait intéressant d'évaluer si une unification de ces résultats serait possible et si la DDM serait en mesure d'élucider les différents modes de transports dans une matrice complexe et poreuse, similaire à un gel.

Enfin, cette thèse rappelle l'importance des techniques de quantification pour générer de l'information de haute qualité et permettre l'avancement des connaissances en lien avec un sujet d'intérêt. Nous croyons avoir mis en place, dans notre laboratoire, un outil de caractérisation versatile qui permettra de contribuer à l'avancement de plusieurs projets en lien avec les nanotechnologies. Il est attendu que de la DDM puisse contribuer à la bonification de nos connaissances dans le domaine de la nanomédecine et d'ainsi favoriser la transition de ces projets vers la clinique.

Références bibliographiques

1. Wouters, O. J.; McKee, M.; Luyten, J., Estimated Research and Development Investment Needed to Bring a New Medicine to Market, 2009-2018. *JAMA* **2020,** *323* (9), 844-853.
2. Simoens, S.; Huys, I., R&D Costs of New Medicines: A Landscape Analysis. **2021,** *8* (1891).
3. Schuhmacher, A.; Gassmann, O.; Hinder, M., Changing R&D models in research-based pharmaceutical companies. *Journal of Translational Medicine* **2016,** *14* (1), 105.
4. Mitragotri, S.; Burke, P. A.; Langer, R., Overcoming the challenges in administering biopharmaceuticals: formulation and delivery strategies. *Nature Reviews Drug Discovery* **2014,** *13* (9), 655-672.
5. Park, K., Facing the Truth about Nanotechnology in Drug Delivery. *ACS Nano* **2013,** *7* (9), 7442-7447.
6. Li, J.; Mooney, D. J., Designing hydrogels for controlled drug delivery. *Nat. Rev. Mater.* **2016,** *1* (12), 16071.
7. Dash, A.; Cudworth, G., Therapeutic applications of implantable drug delivery systems. *J. Pharmacol. Toxicol. Methods* **1998,** *40* (1), 1-12.
8. Prausnitz, M. R.; Langer, R., Transdermal drug delivery. *Nat. Biotechnol.* **2008,** *26* (11), 1261-1268.
9. Peer, D.; Karp, J. M.; Hong, S.; Farokhzad, O. C.; Margalit, R.; Langer, R., Nanocarriers as an emerging platform for cancer therapy. *Nat. Nanotechnol.* **2007,** *2* (12), 751-760.
10. Farokhzad, O. C.; Langer, R., Impact of Nanotechnology on Drug Delivery. *ACS Nano* **2009,** *3* (1), 16-20.
11. LaVan, D. A.; McGuire, T.; Langer, R., Small-scale systems for in vivo drug delivery. *Nat. Biotechnol.* **2003,** *21* (10), 1184-1191.
12. Kim, B. Y. S.; Rutka, J. T.; Chan, W. C. W., Nanomedicine. *N Engl J Med* **2010,** *363* (25), 2434-2443.
13. Pelaz, B.; Alexiou, C.; Alvarez-Puebla, R. A.; Alves, F.; Andrews, A. M.; Ashraf, S.; Balogh, L. P.; Ballerini, L.; Bestetti, A.; Brendel, C.; Bosi, S.; Carril, M.; Chan, W. C. W.; Chen, C.; Chen, X.; Chen, X.; Cheng, Z.; Cui, D.; Du, J.; Dullin, C.; Escudero, A.; Feliu, N.; Gao, M.; George, M.; Gogotsi, Y.; Grünweller, A.; Gu, Z.; Halas, N. J.; Hampp, N.; Hartmann, R. K.; Hersam, M. C.; Hunziker, P.; Jian, J.; Jiang, X.; Jungebluth, P.; Kadhiresan, P.; Kataoka, K.; Khademhosseini, A.; Kopeček, J.; Kotov, N. A.; Krug, H. F.; Lee, D. S.; Lehr, C.-M.; Leong, K. W.; Liang, X.-J.; Ling Lim, M.; Liz-Marzán, L. M.; Ma, X.; Macchiarini, P.; Meng, H.; Möhwald, H.; Mulvaney, P.; Nel, A. E.; Nie, S.; Nordlander, P.; Okano, T.; Oliveira, J.; Park, T. H.; Penner, R. M.; Prato, M.; Puntes, V.; Rotello, V. M.; Samarakoon, A.; Schaak, R. E.; Shen, Y.; Sjöqvist, S.; Skirtach, A. G.; Soliman, M. G.; Stevens, M. M.; Sung, H.-W.; Tang, B. Z.; Tietze, R.; Udugama, B. N.; VanEpps, J. S.; Weil, T.; Weiss, P. S.; Willner, I.; Wu, Y.; Yang, L.; Yue, Z.; Zhang, Q.; Zhang, Q.; Zhang, X.-E.; Zhao, Y.; Zhou, X.; Parak, W. J., Diverse Applications of Nanomedicine. *ACS Nano* **2017,** *11* (3), 2313-2381.
14. Chou, L. Y. T.; Chan, W. C. W., No signs of illness. *Nat. Nanotechnol.* **2012,** *7* (7), 416-417.
15. Murphy, C. J.; Chang, H. H.; Falagan-Lotsch, P.; Gole, M. T.; Hofmann, D. M.; Hoang, K. N. L.; McClain, S. M.; Meyer, S. M.; Turner, J. G.; Unnikrishnan, M.; Wu, M.; Zhang, X.; Zhang, Y. S., Virus-Sized Gold Nanorods: Plasmonic Particles for Biology. *Acc. Chem. Res.* **2019,** *52* (8), 2124-2135.
16. Matsumura, Y.; Maeda, H., A New Concept for Macromolecular Therapeutics in Cancer Chemotherapy: Mechanism of Tumoritropic Accumulation of Proteins and the Antitumor Agent Smancs. *Cancer Res.* **1986,** *46* (12 Part 1), 6387.
17. Shi, J.; Kantoff, P. W.; Wooster, R.; Farokhzad, O. C., Cancer nanomedicine: progress, challenges and opportunities. *Nature Reviews Cancer* **2016,** *17*, 20.

18. Hobbs, S. K.; Monsky, W. L.; Yuan, F.; Roberts, W. G.; Griffith, L.; Torchilin, V. P.; Jain, R. K., Regulation of transport pathways in tumor vessels: Role of tumor type and microenvironment. **1998,** *95* (8), 4607-4612.
19. Bae, Y. H.; Park, K., Targeted drug delivery to tumors: Myths, reality and possibility. *J. Control. Release.* **2011,** *153* (3), 198-205.
20. Shi, Y.; van der Meel, R.; Chen, X.; Lammers, T., The EPR effect and beyond: Strategies to improve tumor targeting and cancer nanomedicine treatment efficacy. *Theranostics* **2020,** *10* (17), 7921-7924.
21. Petersen, G. H.; Alzghari, S. K.; Chee, W.; Sankari, S. S.; La-Beck, N. M., Meta-analysis of clinical and preclinical studies comparing the anticancer efficacy of liposomal versus conventional non-liposomal doxorubicin. *J. Control. Release.* **2016,** *232*, 255-264.
22. Gref, R.; Minamitake, Y.; Peracchia, M. T.; Trubetskoy, V.; Torchilin, V.; Langer, R., Biodegradable long-circulating polymeric nanospheres. *Science* **1994,** *263* (5153), 1600.
23. Gabizon, A.; Catane, R.; Uziely, B.; Kaufman, B.; Safra, T.; Cohen, R.; Martin, F.; Huang, A.; Barenholz, Y., Prolonged Circulation Time and Enhanced Accumulation in Malignant Exudates of Doxorubicin Encapsulated in Polyethylene-glycol Coated Liposomes. *Cancer Res.* **1994,** *54* (4), 987.
24. Rabanel, J.-M.; Faivre, J.; Tehrani, S. F.; Lalloz, A.; Hildgen, P.; Banquy, X., Effect of the Polymer Architecture on the Structural and Biophysical Properties of PEG–PLA Nanoparticles. *ACS Appl. Mater. Interfaces* **2015,** *7* (19), 10374-10385.
25. Fletcher, J. I.; Haber, M.; Henderson, M. J.; Norris, M. D., ABC transporters in cancer: more than just drug efflux pumps. *Nature Reviews Cancer* **2010,** *10* (2), 147-156.
26. Patel, N. R.; Pattni, B. S.; Abouzeid, A. H.; Torchilin, V. P., Nanopreparations to overcome multidrug resistance in cancer. *Adv. Drug Del. Rev.* **2013,** *65* (13), 1748-1762.
27. Conde, J.; de la Fuente, J.; Baptista, P., Nanomaterials for reversion of multidrug resistance in cancer: a new hope for an old idea? **2013,** *4* (134).
28. Bertrand, N.; Wu, J.; Xu, X.; Kamaly, N.; Farokhzad, O. C., Cancer nanotechnology: The impact of passive and active targeting in the era of modern cancer biology. *Adv. Drug Del. Rev.* **2014,** *66*, 2-25.
29. Jiang, X.; Xin, H.; Gu, J.; Xu, X.; Xia, W.; Chen, S.; Xie, Y.; Chen, L.; Chen, Y.; Sha, X.; Fang, X., Solid tumor penetration by integrin-mediated pegylated poly(trimethylene carbonate) nanoparticles loaded with paclitaxel. *Biomaterials* **2013,** *34* (6), 1739-1746.
30. Jiang, W.; Kim, B. Y. S.; Rutka, J. T.; Chan, W. C. W., Nanoparticle-mediated cellular response is size-dependent. *Nat. Nanotechnol.* **2008,** *3* (3), 145-150.
31. Milani, S.; Bombelli, F. B.; Pitek, A. S.; Dawson, K. A.; Radler, J., Reversible versus irreversible binding of transferrin to polystyrene nanoparticles: soft and hard corona. *ACS Nano* **2012,** *6* (3), 2532-41.
32. Salvati, A.; Pitek, A. S.; Monopoli, M. P.; Prapainop, K.; Bombelli, F. B.; Hristov, D. R.; Kelly, P. M.; Aberg, C.; Mahon, E.; Dawson, K. A., Transferrin-functionalized nanoparticles lose their targeting capabilities when a biomolecule corona adsorbs on the surface. *Nat. Nanotechnol.* **2013,** *8* (2), 137-143.
33. Derfus, A. M.; Chan, W. C. W.; Bhatia, S. N., Intracellular delivery of quantum dots for live cell labeling and organelle tracking. *Adv. Mater.* **2004,** *16* (12), 961-+.
34. Dawson, M.; Krauland, E.; Wirtz, D.; Hanes, J., Transport of Polymeric Nanoparticle Gene Carriers in Gastric Mucus. *Biotechnol. Prog.* **2004,** *20* (3), 851-857.
35. Lai, S. K.; Wang, Y.-Y.; Hanes, J., Mucus-penetrating nanoparticles for drug and gene delivery to mucosal tissues. *Adv. Drug Del. Rev.* **2009,** *61* (2), 158-171.
36. Chou, L. Y. T.; Ming, K.; Chan, W. C. W., Strategies for the intracellular delivery of nanoparticles. *Chem. Soc. Rev.* **2011,** *40* (1), 233-245.
37. Suk, J. S.; Xu, Q.; Kim, N.; Hanes, J.; Ensign, L. M., PEGylation as a strategy for improving nanoparticle-based drug and gene delivery. *Adv. Drug Del. Rev.* **2016,** *99*, 28-51.
38. Kulkarni, J. A.; Witzigmann, D.; Thomson, S. B.; Chen, S.; Leavitt, B. R.; Cullis, P. R.; van der Meel, R., The current landscape of nucleic acid therapeutics. *Nat. Nanotechnol.* **2021,** *16* (6), 630-643.

39. Saraiva, C.; Praça, C.; Ferreira, R.; Santos, T.; Ferreira, L.; Bernardino, L., Nanoparticle-mediated brain drug delivery: Overcoming blood–brain barrier to treat neurodegenerative diseases. *J. Control. Release.* **2016,** *235*, 34-47.
40. Rabanel, J. M.; Aoun, V.; Elkin, I.; Mokhtar, M.; Hildgen, P., Drug-loaded nanocarriers: passive targeting and crossing of biological barriers. *Curr. Med. Chem.* **2012,** *19* (19), 3070-102.
41. Goulatis, L. I.; Shusta, E. V., Protein engineering approaches for regulating blood–brain barrier transcytosis. *Curr. Opin. Struct. Biol.* **2017,** *45*, 109-115.
42. Behzadi, S.; Serpooshan, V.; Tao, W.; Hamaly, M. A.; Alkawareek, M. Y.; Dreaden, E. C.; Brown, D.; Alkilany, A. M.; Farokhzad, O. C.; Mahmoudi, M., Cellular uptake of nanoparticles: journey inside the cell. *Chem. Soc. Rev.* **2017,** *46* (14), 4218-4244.
43. Jain, R. K., Transport of Molecules in the Tumor Interstitium: A Review. *Cancer Res.* **1987,** *47* (12), 3039-3051.
44. Jain, R. K., Transport of molecules across tumor vasculature. *Cancer and Metastasis Reviews* **1987,** *6* (4), 559-593.
45. Sweeney, M. D.; Zhao, Z.; Montagne, A.; Nelson, A. R.; Zlokovic, B. V., Blood-Brain Barrier: From Physiology to Disease and Back. *Physiol. Rev.* **2018,** *99* (1), 21-78.
46. Barenholz, Y., Doxil® — The first FDA-approved nano-drug: Lessons learned. *J. Control. Release.* **2012,** *160* (2), 117-134.
47. Ventola, C. L., Progress in Nanomedicine: Approved and Investigational Nanodrugs. *P t* **2017,** *42* (12), 742-755.
48. Mitchell, M. J.; Billingsley, M. M.; Haley, R. M.; Wechsler, M. E.; Peppas, N. A.; Langer, R., Engineering precision nanoparticles for drug delivery. *Nature Reviews Drug Discovery* **2021,** *20* (2), 101-124.
49. Wilhelm, S.; Tavares, A. J.; Dai, Q.; Ohta, S.; Audet, J.; Dvorak, H. F.; Chan, W. C. W., Analysis of nanoparticle delivery to tumours. *Nat. Rev. Mater.* **2016,** *1* (5), 16014.
50. Anselmo, A. C.; Mitragotri, S., Nanoparticles in the clinic: An update. **2019,** *4* (3), e10143.
51. Akinc, A.; Maier, M. A.; Manoharan, M.; Fitzgerald, K.; Jayaraman, M.; Barros, S.; Ansell, S.; Du, X.; Hope, M. J.; Madden, T. D.; Mui, B. L.; Semple, S. C.; Tam, Y. K.; Ciufolini, M.; Witzigmann, D.; Kulkarni, J. A.; van der Meel, R.; Cullis, P. R., The Onpattro story and the clinical translation of nanomedicines containing nucleic acid-based drugs. *Nat. Nanotechnol.* **2019,** *14* (12), 1084-1087.
52. Creech, C. B.; Walker, S. C.; Samuels, R. J., SARS-CoV-2 Vaccines. *JAMA* **2021,** *325* (13), 1318-1320.
53. Nemet, I.; Kliker, L.; Lustig, Y.; Zuckerman, N.; Erster, O.; Cohen, C.; Kreiss, Y.; Alroy-Preis, S.; Regev-Yochay, G.; Mendelson, E.; Mandelboim, M., Third BNT162b2 Vaccination Neutralization of SARS-CoV-2 Omicron Infection. **2021**.
54. Du, B.; Yu, M.; Zheng, J., Transport and interactions of nanoparticles in the kidneys. *Nat. Rev. Mater.* **2018,** *3* (10), 358-374.
55. Tsoi, K. M.; MacParland, S. A.; Ma, X.-Z.; Spetzler, V. N.; Echeverri, J.; Ouyang, B.; Fadel, S. M.; Sykes, E. A.; Goldaracena, N.; Kaths, J. M.; Conneely, J. B.; Alman, B. A.; Selzner, M.; Ostrowski, M. A.; Adeyi, O. A.; Zilman, A.; McGilvray, I. D.; Chan, W. C. W., Mechanism of hard-nanomaterial clearance by the liver. *Nature Materials* **2016,** *15* (11), 1212-1221.
56. Liu, X.; Li, H.; Chen, Y.; Jin, Q.; Ren, K.; Ji, J., Mixed-Charge Nanoparticles for Long Circulation, Low Reticuloendothelial System Clearance, and High Tumor Accumulation. *Adv. Healthc. Mater.* **2014,** *3* (9), 1439-1447.
57. Schwenk, J. M.; Omenn, G. S.; Sun, Z.; Campbell, D. S.; Baker, M. S.; Overall, C. M.; Aebersold, R.; Moritz, R. L.; Deutsch, E. W., The Human Plasma Proteome Draft of 2017: Building on the Human Plasma PeptideAtlas from Mass Spectrometry and Complementary Assays. *J. Proteome Res.* **2017,** *16* (12), 4299-4310.

58. Walkey, C. D.; Olsen, J. B.; Song, F.; Liu, R.; Guo, H.; Olsen, D. W.; Cohen, Y.; Emili, A.; Chan, W. C., Protein corona fingerprinting predicts the cellular interaction of gold and silver nanoparticles. *ACS Nano* **2014,** *8* (3), 2439-55.
59. Ritz, S.; Schottler, S.; Kotman, N.; Baier, G.; Musyanovych, A.; Kuharev, J.; Landfester, K.; Schild, H.; Jahn, O.; Tenzer, S.; Mailander, V., Protein corona of nanoparticles: distinct proteins regulate the cellular uptake. *Biomacromolecules* **2015,** *16* (4), 1311-21.
60. Monopoli, M. P.; Aberg, C.; Salvati, A.; Dawson, K. A., Biomolecular coronas provide the biological identity of nanosized materials. *Nat. Nanotechnol.* **2012,** *7* (12), 779-86.
61. Docter, D.; Distler, U.; Storck, W.; Kuharev, J.; Wunsch, D.; Hahlbrock, A.; Knauer, S. K.; Tenzer, S.; Stauber, R. H., Quantitative profiling of the protein coronas that form around nanoparticles. *Nat. Protoc.* **2014,** *9* (9), 2030-2044.
62. Liu, R.; Jiang, W.; Walkey, C. D.; Chan, W. C. W.; Cohen, Y., Prediction of nanoparticles-cell association based on corona proteins and physicochemical properties. *Nanoscale* **2015,** *7* (21), 9664-9675.
63. Tenzer, S.; Docter, D.; Kuharev, J.; Musyanovych, A.; Fetz, V.; Hecht, R.; Schlenk, F.; Fischer, D.; Kiouptsi, K.; Reinhardt, C.; Landfester, K.; Schild, H.; Maskos, M.; Knauer, S. K.; Stauber, R. H., Rapid formation of plasma protein corona critically affects nanoparticle pathophysiology. *Nat. Nanotechnol.* **2013,** *8* (10), 772-U1000.
64. Pisani, C.; Gaillard, J. C.; Odorico, M.; Nyalosaso, J. L.; Charnay, C.; Guari, Y.; Chopineau, J.; Devoisselle, J. M.; Armengaud, J.; Prat, O., The timeline of corona formation around silica nanocarriers highlights the role of the protein interactome. *Nanoscale* **2017,** *9* (5), 1840-1851.
65. Schöttler, S.; Becker, G.; Winzen, S.; Steinbach, T.; Mohr, K.; Landfester, K.; Mailänder, V.; Wurm, F. R., Protein adsorption is required for stealth effect of poly(ethylene glycol)- and poly(phosphoester)-coated nanocarriers. *Nat. Nanotechnol.* **2016,** *11*, 372.
66. Röcker, C.; Pötzl, M.; Zhang, F.; Parak, W. J.; Nienhaus, G. U., A quantitative fluorescence study of protein monolayer formation on colloidal nanoparticles. *Nat. Nanotechnol.* **2009,** *4*, 577.
67. Maffre, P.; Brandholt, S.; Nienhaus, K.; Shang, L.; Parak, W. J.; Nienhaus, G. U., Effects of surface functionalization on the adsorption of human serum albumin onto nanoparticles - a fluorescence correlation spectroscopy study. *Beilstein J Nanotechnol* **2014,** *5*, 2036-47.
68. Pelaz, B.; del Pino, P.; Maffre, P.; Hartmann, R.; Gallego, M.; Rivera-Fernandez, S.; de la Fuente, J. M.; Nienhaus, G. U.; Parak, W. J., Surface Functionalization of Nanoparticles with Polyethylene Glycol: Effects on Protein Adsorption and Cellular Uptake. *ACS Nano* **2015,** *9* (7), 6996-7008.
69. Wang, H.; Shang, L.; Maffre, P.; Hohmann, S.; Kirschhofer, F.; Brenner-Weiss, G.; Nienhaus, G. U., The Nature of a Hard Protein Corona Forming on Quantum Dots Exposed to Human Blood Serum. *Small* **2016,** *12* (42), 5836-5844.
70. Wang, H.; Ma, R.; Nienhaus, K.; Nienhaus, G. U., Formation of a Monolayer Protein Corona around Polystyrene Nanoparticles and Implications for Nanoparticle Agglomeration. *Small* **2019,** *15* (22), e1900974.
71. Madathiparambil Visalakshan, R.; Gonzalez Garcia, L. E.; Benzigar, M. R.; Ghazaryan, A.; Simon, J.; Mierczynska-Vasilev, A.; Michl, T. D.; Vinu, A.; Mailander, V.; Morsbach, S.; Landfester, K.; Vasilev, K., The Influence of Nanoparticle Shape on Protein Corona Formation. *Small* **2020,** *16* (25), e2000285.
72. Mahmoudi, M.; Abdelmonem, A. M.; Behzadi, S.; Clement, J. H.; Dutz, S.; Ejtehadi, M. R.; Hartmann, R.; Kantner, K.; Linne, U.; Maffre, P.; Metzler, S.; Moghadam, M. K.; Pfeiffer, C.; Rezaei, M.; Ruiz-Lozano, P.; Serpooshan, V.; Shokrgozar, M. A.; Nienhaus, G. U.; Parak, W. J., Temperature: the "ignored" factor at the NanoBio interface. *ACS Nano* **2013,** *7* (8), 6555-62.
73. Shang, L.; Nienhaus, G. U., *In Situ* Characterization of Protein Adsorption onto Nanoparticles by Fluorescence Correlation Spectroscopy. *Acc. Chem. Res.* **2017,** *50* (2), 387-395.
74. Cui, M. H.; Liu, R. X.; Deng, Z. Y.; Ge, G. L.; Liu, Y.; Xie, L. M., Quantitative study of protein coronas on gold nanoparticles with different surface modifications. *Nano Research* **2014,** *7* (3), 345-352.

75. Carril, M.; Padro, D.; del Pino, P.; Carrillo-Carrion, C.; Gallego, M.; Parak, W. J., *In Situ* detection of the protein corona in complex environments. *Nat. Commun.* **2017,** *8* (1), 1542.
76. Prozeller, D.; Morsbach, S.; Landfester, K., Isothermal titration calorimetry as a complementary method for investigating nanoparticle–protein interactions. *Nanoscale* **2019,** *11* (41), 19265-19273.
77. Lo Giudice, M. C.; Herda, L. M.; Polo, E.; Dawson, K. A., *In Situ* characterization of nanoparticle biomolecular interactions in complex biological media by flow cytometry. *Nat. Commun.* **2016,** *7* (1), 13475.
78. Bekdemir, A.; Stellacci, F., A centrifugation-based physicochemical characterization method for the interaction between proteins and nanoparticles. *Nat. Commun.* **2016,** *7* (1), 13121.
79. Jain, R. K., Barriers to drug delivery in solid tumors. *Sci. Am.* **1994,** *271* (1), 58-65.
80. Jain, R. K.; Stylianopoulos, T., Delivering nanomedicine to solid tumors. *Nature Reviews Clinical Oncology* **2010,** *7* (11), 653-664.
81. Maeda, H.; Wu, J.; Sawa, T.; Matsumura, Y.; Hori, K., Tumor vascular permeability and the EPR effect in macromolecular therapeutics: a review. *J. Control. Release.* **2000,** *65* (1), 271-284.
82. Pluen, A.; Netti, P. A.; Jain, R. K.; Berk, D. A., Diffusion of Macromolecules in Agarose Gels: Comparison of Linear and Globular Configurations. *Biophysical Journal* **1999,** *77* (1), 542-552.
83. Ramanujan, S.; Pluen, A.; McKee, T. D.; Brown, E. B.; Boucher, Y.; Jain, R. K., Diffusion and Convection in Collagen Gels: Implications for Transport in the Tumor Interstitium. *Biophysical Journal* **2002,** *83* (3), 1650-1660.
84. Fatin-Rouge, N.; Milon, A.; Buffle, J.; Goulet, R. R.; Tessier, A., Diffusion and Partitioning of Solutes in Agarose Hydrogels: The Relative Influence of Electrostatic and Specific Interactions. *The Journal of Physical Chemistry B* **2003,** *107* (44), 12126-12137.
85. Fatin-Rouge, N.; Starchev, K.; Buffle, J., Size Effects on Diffusion Processes within Agarose Gels. *Biophysical Journal* **2004,** *86* (5), 2710-2719.
86. Fatin-Rouge, N.; Wilkinson, K. J.; Buffle, J., Combining Small Angle Neutron Scattering (SANS) and Fluorescence Correlation Spectroscopy (FCS) Measurements To Relate Diffusion in Agarose Gels to Structure. *The Journal of Physical Chemistry B* **2006,** *110* (41), 20133-20142.
87. Banks, D. S.; Tressler, C.; Peters, R. D.; Höfling, F.; Fradin, C., Characterizing anomalous diffusion in crowded polymer solutions and gels over five decades in time with variable-lengthscale fluorescence correlation spectroscopy. *Soft Matter* **2016,** *12* (18), 4190-4203.
88. Chenouard, N.; Smal, I.; de Chaumont, F.; Maška, M.; Sbalzarini, I. F.; Gong, Y.; Cardinale, J.; Carthel, C.; Coraluppi, S.; Winter, M.; Cohen, A. R.; Godinez, W. J.; Rohr, K.; Kalaidzidis, Y.; Liang, L.; Duncan, J.; Shen, H.; Xu, Y.; Magnusson, K. E. G.; Jaldén, J.; Blau, H. M.; Paul-Gilloteaux, P.; Roudot, P.; Kervrann, C.; Waharte, F.; Tinevez, J.-Y.; Shorte, S. L.; Willemse, J.; Celler, K.; van Wezel, G. P.; Dan, H.-W.; Tsai, Y.-S.; de Solórzano, C. O.; Olivo-Marin, J.-C.; Meijering, E., Objective comparison of particle tracking methods. *Nat. Methods* **2014,** *11* (3), 281-289.
89. Suk, J. S.; Lai, S. K.; Wang, Y.-Y.; Ensign, L. M.; Zeitlin, P. L.; Boyle, M. P.; Hanes, J., The penetration of fresh undiluted sputum expectorated by cystic fibrosis patients by non-adhesive polymer nanoparticles. *Biomaterials* **2009,** *30* (13), 2591-2597.
90. Lai, S. K.; O'Hanlon, D. E.; Harrold, S.; Man, S. T.; Wang, Y. Y.; Cone, R.; Hanes, J., Rapid transport of large polymeric nanoparticles in fresh undiluted human mucus. *Proc Natl Acad Sci U S A* **2007,** *104* (5), 1482-7.
91. Wang, Y.-Y.; Lai, S. K.; Suk, J. S.; Pace, A.; Cone, R.; Hanes, J., Addressing the PEG Mucoadhesivity Paradox to Engineer Nanoparticles that "Slip" through the Human Mucus Barrier. *Angew. Chem. Int. Ed. Engl.* **2008,** *47* (50), 9726-9729.
92. Maisel, K.; Ensign, L.; Reddy, M.; Cone, R.; Hanes, J., Effect of surface chemistry on nanoparticle interaction with gastrointestinal mucus and distribution in the gastrointestinal tract following oral and rectal administration in the mouse. *J. Control. Release.* **2015,** *197*, 48-57.

93. Cerbino, R.; Trappe, V., Differential Dynamic Microscopy: Probing Wave Vector Dependent Dynamics with a Microscope. *Physical Review Letters* **2008,** *100* (18), 188102.
94. Wilson, L. G.; Martinez, V. A.; Schwarz-Linek, J.; Tailleur, J.; Bryant, G.; Pusey, P. N.; Poon, W. C. K., Differential Dynamic Microscopy of Bacterial Motility. *Physical Review Letters* **2011,** *106* (1), 018101.
95. Berne, B. J.; Pecora, R., *Dynamic Light Scattering with Applications to Biology, Chemistry and Physics*. Dover: 2000.
96. Martinez, Vincent A.; Besseling, R.; Croze, Ottavio A.; Tailleur, J.; Reufer, M.; Schwarz-Linek, J.; Wilson, Laurence G.; Bees, Martin A.; Poon, Wilson C. K., Differential Dynamic Microscopy: A High-Throughput Method for Characterizing the Motility of Microorganisms. *Biophysical Journal* **2012,** *103* (8), 1637-1647.
97. Reufer, M.; Martinez, V. A.; Schurtenberger, P.; Poon, W. C. K., Differential Dynamic Microscopy for Anisotropic Colloidal Dynamics. *Langmuir* **2012,** *28* (10), 4618-4624.
98. Lu, P. J.; Giavazzi, F.; Angelini, T. E.; Zaccarelli, E.; Jargstorff, F.; Schofield, A. B.; Wilking, J. N.; Romanowsky, M. B.; Weitz, D. A.; Cerbino, R., Characterizing Concentrated, Multiply Scattering, and Actively Driven Fluorescent Systems with Confocal Differential Dynamic Microscopy. *Physical Review Letters* **2012,** *108* (21), 218103.
99. Pal, A.; Martinez, V. A.; Ito, T. H.; Arlt, J.; Crassous, J. J.; Poon, W. C. K.; Schurtenberger, P., Anisotropic dynamics and kinetic arrest of dense colloidal ellipsoids in the presence of an external field studied by differential dynamic microscopy. *Sci Adv* **2020,** *6* (3), eaaw9733.
100. He, K.; Spannuth, M.; Conrad, J. C.; Krishnamoorti, R., Diffusive dynamics of nanoparticles in aqueous dispersions. *Soft Matter* **2012,** *8* (47), 11933-11938.
101. Bayles, A. V.; Squires, T. M.; Helgeson, M. E., Dark-field differential dynamic microscopy. *Soft Matter* **2016,** *12* (8), 2440-2452.
102. Giavazzi, F.; Crotti, S.; Speciale, A.; Serra, F.; Zanchetta, G.; Trappe, V.; Buscaglia, M.; Bellini, T.; Cerbino, R., Viscoelasticity of nematic liquid crystals at a glance. *Soft Matter* **2014,** *10* (22), 3938-3949.
103. Safari, M. S.; Poling-Skutvik, R.; Vekilov, P. G.; Conrad, J. C., Differential dynamic microscopy of bidisperse colloidal suspensions. *npj Microgravity* **2017,** *3* (1), 21.
104. Sentjabrskaja, T.; Zaccarelli, E.; De Michele, C.; Sciortino, F.; Tartaglia, P.; Voigtmann, T.; Egelhaaf, S. U.; Laurati, M., Anomalous dynamics of intruders in a crowded environment of mobile obstacles. *Nat. Commun.* **2016,** *7* (1), 11133.
105. Jacob, J. D. C.; He, K.; Retterer, S. T.; Krishnamoorti, R.; Conrad, J. C., Diffusive dynamics of nanoparticles in ultra-confined media. *Soft Matter* **2015,** *11* (38), 7515-7524.
106. Huhn, J.; Fedeli, C.; Zhang, Q.; Masood, A.; Del Pino, P.; Khashab, N. M.; Papini, E.; Parak, W. J., Dissociation coefficients of protein adsorption to nanoparticles as quantitative metrics for description of the protein corona: A comparison of experimental techniques and methodological relevance. *Int. J. Biochem. Cell Biol.* **2016,** *75*, 148-61.
107. Lundqvist, M.; Stigler, J.; Elia, G.; Lynch, I.; Cedervall, T.; Dawson, K. A., Nanoparticle size and surface properties determine the protein corona with possible implications for biological impacts. *Proc. Natl. Acad. Sci. U.S.A.* **2008,** *105* (38), 14265-70.
108. Tenzer, S.; Docter, D.; Rosfa, S.; Wlodarski, A.; Kuharev, J.; Rekik, A.; Knauer, S. K.; Bantz, C.; Nawroth, T.; Bier, C.; Sirirattanapan, J.; Mann, W.; Treuel, L.; Zellner, R.; Maskos, M.; Schild, H.; Stauber, R. H., Nanoparticle Size Is a Critical Physicochemical Determinant of the Human Blood Plasma Corona: A Comprehensive Quantitative Proteomic Analysis. *ACS Nano* **2011,** *5* (9), 7155-7167.
109. Walkey, C. D.; Olsen, J. B.; Guo, H.; Emili, A.; Chan, W. C., Nanoparticle size and surface chemistry determine serum protein adsorption and macrophage uptake. *J. Am. Chem. Soc.* **2012,** *134* (4), 2139-47.
110. Tonigold, M.; Simon, J.; Estupiñán, D.; Kokkinopoulou, M.; Reinholz, J.; Kintzel, U.; Kaltbeitzel, A.; Renz, P.; Domogalla, M. P.; Steinbrink, K.; Lieberwirth, I.; Crespy, D.; Landfester, K.; Mailänder, V.,

Pre-adsorption of antibodies enables targeting of nanocarriers despite a biomolecular corona. *Nat. Nanotechnol.* **2018,** *13* (9), 862-869.
111. Bertrand, N.; Grenier, P.; Mahmoudi, M.; Lima, E. M.; Appel, E. A.; Dormont, F.; Lim, J. M.; Karnik, R.; Langer, R.; Farokhzad, O. C., Mechanistic understanding of *in Vivo* protein corona formation on polymeric nanoparticles and impact on pharmacokinetics. *Nat. Commun.* **2017,** *8* (1), 777.
112. Walczyk, D.; Bombelli, F. B.; Monopoli, M. P.; Lynch, I.; Dawson, K. A., What the cell "sees" in bionanoscience. *J. Am. Chem. Soc.* **2010,** *132* (16), 5761-8.
113. Casals, E.; Pfaller, T.; Duschl, A.; Oostingh, G. J.; Puntes, V., Time evolution of the nanoparticle protein corona. *ACS Nano* **2010,** *4* (7), 3623-32.
114. Linse, S.; Cabaleiro-Lago, C.; Xue, W. F.; Lynch, I.; Lindman, S.; Thulin, E.; Radford, S. E.; Dawson, K. A., Nucleation of protein fibrillation by nanoparticles. *Proc. Natl. Acad. Sci. U.S.A.* **2007,** *104* (21), 8691-6.
115. Dawson, K. A.; Yan, Y., Current understanding of biological identity at the nanoscale and future prospects. *Nat. Nanotechnol.* **2021,** *16* (3), 229-242.
116. Walkey, C. D.; Chan, W. C., Understanding and controlling the interaction of nanomaterials with proteins in a physiological environment. *Chem. Soc. Rev.* **2012,** *41* (7), 2780-99.
117. Piella, J.; Bastus, N. G.; Puntes, V., Size-Dependent Protein-Nanoparticle Interactions in Citrate-Stabilized Gold Nanoparticles: The Emergence of the Protein Corona. *Bioconjug. Chem.* **2017,** *28* (1), 88-97.
118. Wang, H.; Lin, Y.; Nienhaus, K.; Nienhaus, G. U., The protein corona on nanoparticles as viewed from a nanoparticle-sizing perspective. *Wiley Interdiscip. Rev. Nanomed. Nanobiotechnol.* **2018,** *10* (4), e1500.
119. Goy-López, S.; Juárez, J.; Alatorre-Meda, M.; Casals, E.; Puntes, V. F.; Taboada, P.; Mosquera, V., Physicochemical Characteristics of Protein–NP Bioconjugates: The Role of Particle Curvature and Solution Conditions on Human Serum Albumin Conformation and Fibrillogenesis Inhibition. *Langmuir* **2012,** *28* (24), 9113-9126.
120. Weber, C.; Simon, J.; Mailander, V.; Morsbach, S.; Landfester, K., Preservation of the soft protein corona in distinct flow allows identification of weakly bound proteins. *Acta Biomater.* **2018,** *76*, 217-224.
121. Docter, D.; Westmeier, D.; Markiewicz, M.; Stolte, S.; Knauer, S. K.; Stauber, R. H., The nanoparticle biomolecule corona: lessons learned - challenge accepted? *Chem. Soc. Rev.* **2015,** *44* (17), 6094-121.
122. Casals, E.; Pfaller, T.; Duschl, A.; Oostingh, G. J.; Puntes, V. F., Hardening of the nanoparticle-protein corona in metal (Au, Ag) and oxide (Fe3O4, CoO, and CeO2) nanoparticles. *Small* **2011,** *7* (24), 3479-86.
123. Vitali, M.; Casals, E.; Canals, F.; Colomé, N.; Puntes, V., Simple spectroscopic determination of the hard protein corona composition in AuNPs: albumin at 75. *Nanoscale* **2020,** *12* (29), 15832-15844.
124. Zhang, X. N.; Shi, H. M.; Zhang, R. T.; Zhang, J. T.; Xu, F. X.; Qiao, L.; Yu, S. N., The Competitive Dynamic Binding of Some Blood Proteins Adsorbed on Gold Nanoparticles. *Part. Part. Syst. Charact.* **2019,** *36* (1), 1800257.
125. Khan, S.; Gupta, A.; Verma, N. C.; Nandi, C. K., Kinetics of protein adsorption on gold nanoparticle with variable protein structure and nanoparticle size. *J. Chem. Phys.* **2015,** *143* (16), 164709.
126. Caputo, D.; Papi, M.; Coppola, R.; Palchetti, S.; Digiacomo, L.; Caracciolo, G.; Pozzi, D., A protein corona-enabled blood test for early cancer detection. *Nanoscale* **2017,** *9* (1), 349-354.
127. Cedervall, T.; Lynch, I.; Lindman, S.; Berggard, T.; Thulin, E.; Nilsson, H.; Dawson, K. A.; Linse, S., Understanding the nanoparticle-protein corona using methods to quantify exchange rates and affinities of proteins for nanoparticles. *Proc. Natl. Acad. Sci. U.S.A.* **2007,** *104* (7), 2050-2055.

128. Kelly, P. M.; Aberg, C.; Polo, E.; O'Connell, A.; Cookman, J.; Fallon, J.; Krpetic, Z.; Dawson, K. A., Mapping protein binding sites on the biomolecular corona of nanoparticles. *Nat. Nanotechnol.* **2015,** *10* (5), 472-9.
129. Lundqvist, M.; Augustsson, C.; Lilja, M.; Lundkvist, K.; Dahlbäck, B.; Linse, S.; Cedervall, T., The nanoparticle protein corona formed in human blood or human blood fractions. *PLOS ONE* **2017,** *12* (4), e0175871.
130. Winzen, S.; Schoettler, S.; Baier, G.; Rosenauer, C.; Mailaender, V.; Landfester, K.; Mohr, K., Complementary analysis of the hard and soft protein corona: sample preparation critically effects corona composition. *Nanoscale* **2015,** *7* (7), 2992-3001.
131. Weber, C.; Morsbach, S.; Landfester, K., Possibilities and Limitations of Different Separation Techniques for the Analysis of the Protein Corona. *Angew. Chem. Int. Ed. Engl.* **2019,** *58* (37), 12787-12794.
132. Langmuir, I., The Adsorption of Gases on Plane Surfaces of Glass, Mica and Platinum. *J. Am. Chem. Soc.* **1918,** *40* (9), 1361-1403.
133. Swenson, H.; Stadie, N. P., Langmuir's Theory of Adsorption: A Centennial Review. *Langmuir* **2019,** *35* (16), 5409-5426.
134. Weiss, J. N., The Hill equation revisited: uses and misuses. *FASEB J.* **1997,** *11* (11), 835-41.
135. Ayawei, N.; Ebelegi, A. N.; Wankasi, D., Modelling and Interpretation of Adsorption Isotherms. *J. Chem.* **2017,** *2017*, 3039817.
136. Vroman, L., Effect of Adsorbed Proteins on the Wettability of Hydrophilic and Hydrophobic Solids. *Nature* **1962,** *196*.
137. Slack, S. M.; Horbett, T. A., The Vroman Effect. In *Proteins at Interfaces II*, American Chemical Society: 1995; Vol. 602, pp 112-128.
138. Vilanova, O.; Mittag, J. J.; Kelly, P. M.; Milani, S.; Dawson, K. A.; Radler, J. O.; Franzese, G., Understanding the Kinetics of Protein-Nanoparticle Corona Formation. *ACS Nano* **2016,** *10* (12), 10842-10850.
139. Langevin, D.; Lozano, O.; Salvati, A.; Kestens, V.; Monopoli, M.; Raspaud, E.; Mariot, S.; Salonen, A.; Thomas, S.; Driessen, M.; Haase, A.; Nelissen, I.; Smisdom, N.; Pompa, P. P.; Maiorano, G.; Puntes, V.; Puchowicz, D.; Stepnik, M.; Suarez, G.; Riediker, M.; Benetti, F.; Micetic, I.; Venturini, M.; Kreyling, W. G.; Van Der Zande, M.; Bouwmeester, H.; Milani, S.; Radler, J. O.; Mulhopt, S.; Lynch, I.; Dawson, K., Inter-laboratory comparison of nanoparticle size measurements using dynamic light scattering and differential centrifugal sedimentation. *Nanoimpact* **2018,** *10*, 97-107.
140. Jung, S.-Y.; Lim, S.-M.; Albertorio, F.; Kim, G.; Gurau, M. C.; Yang, R. D.; Holden, M. A.; Cremer, P. S., The Vroman Effect: A Molecular Level Description of Fibrinogen Displacement. *J. Am. Chem. Soc.* **2003,** *125* (42), 12782-12786.
141. Kumar, S.; Yadav, I.; Aswal, V. K.; Kohlbrecher, J., Structure and Interaction of Nanoparticle-Protein Complexes. *Langmuir* **2018,** *34* (20), 5679-5695.
142. Rabanel, J. M.; Hildgen, P.; Banquy, X., Assessment of PEG on polymeric particles surface, a key step in drug carrier translation. *J. Control. Release.* **2014,** *185*, 71-87.
143. Monopoli, M. P.; Wan, S. H. A.; Bombelli, F. B.; Mahon, E.; Dawson, K. A., Comparisons of Nanoparticle Protein Corona Complexes Isolated with Different Methods. *Nano Life* **2014,** *03* (04), 1343004.
144. Stoscheck, C. M., Quantitation of protein. In *Methods Enzymol.*, 1990/01/01 ed.; 1990; Vol. 182, pp 50-68.
145. Kumar, S.; Aswal, V. K.; Kohlbrecher, J., SANS and UV-vis spectroscopy studies of resultant structure from lysozyme adsorption on silica nanoparticles. *Langmuir* **2011,** *27* (16), 10167-73.
146. Yadav, I.; Aswal, V. K.; Kohlbrecher, J., Size-dependent interaction of silica nanoparticles with lysozyme and bovine serum albumin proteins. *Phys. Rev. E* **2016,** *93* (5), 052601.

147. Yadav, I.; Kumar, S.; Aswal, V. K.; Kohlbrecher, J., Structure and Interaction in the pH-Dependent Phase Behavior of Nanoparticle–Protein Systems. *Langmuir* **2017,** *33* (5), 1227-1238.
148. Kratz, F.; Muller, C.; Korber, N.; Umanskaya, N.; Hannig, M.; Ziegler, C., Characterization of protein films on dental materials: Bicinchoninic acid assay (BCA) studies on loosely and firmly adsorbed protein layers. *Phys. Status Solidi A* **2013,** *210* (5), 964-967.
149. Eren, N. M.; Narsimhan, G.; Campanella, O. H., Protein adsorption induced bridging flocculation: the dominant entropic pathway for nano-bio complexation. *Nanoscale* **2016,** *8* (6), 3326-36.
150. Mohammad-Beigi, H.; Hayashi, Y.; Zeuthen, C. M.; Eskandari, H.; Scavenius, C.; Juul-Madsen, K.; Vorup-Jensen, T.; Enghild, J. J.; Sutherland, D. S., Mapping and identification of soft corona proteins at nanoparticles and their impact on cellular association. *Nat. Commun.* **2020,** *11* (1), 4535.
151. Goppert, T. M.; Muller, R. H., Protein adsorption patterns on poloxamer- and poloxamine-stabilized solid lipid nanoparticles (SLN). *Eur. J. Pharm. Biopharm.* **2005,** *60* (3), 361-72.
152. Gagner, J. E.; Qian, X.; Lopez, M. M.; Dordick, J. S.; Siegel, R. W., Effect of gold nanoparticle structure on the conformation and function of adsorbed proteins. *Biomaterials* **2012,** *33* (33), 8503-16.
153. Marucco, A.; Fenoglio, I.; Turci, F.; Fubini, B. In *Interaction of fibrinogen and albumin with titanium dioxide nanoparticles of different crystalline phases*, Journal of Physics: Conference Series, IOP Publishing: 2013; p 012014.
154. Ferhan, A. R.; Jackman, J. A.; Sut, T. N.; Cho, N. J., Quantitative Comparison of Protein Adsorption and Conformational Changes on Dielectric-Coated Nanoplasmonic Sensing Arrays. *Sensors* **2018,** *18* (4).
155. Bastus, N. G.; Piella, J.; Puntes, V., Quantifying the Sensitivity of Multipolar (Dipolar, Quadrupolar, and Octapolar) Surface Plasmon Resonances in Silver Nanoparticles: The Effect of Size, Composition, and Surface Coating. *Langmuir* **2016,** *32* (1), 290-300.
156. Saha, K.; Agasti, S. S.; Kim, C.; Li, X.; Rotello, V. M., Gold Nanoparticles in Chemical and Biological Sensing. *Chem. Rev.* **2012,** *112* (5), 2739-2779.
157. Lakowicz, J. R., *Principles of Fluorescence Spectroscopy*. 3 ed.; Springer US: 2006; p 954.
158. Hlady, V.; Buijs, J.; Jennissen, H. P., [26] Methods for studying protein adsorption. In *Methods Enzymol.*, Elsevier: 1999; Vol. 309, pp 402-429.
159. Park, S. J., Protein-Nanoparticle Interaction: Corona Formation and Conformational Changes in Proteins on Nanoparticles. *Int. J. Nanomedicine* **2020,** *15*, 5783-5802.
160. Welsch, N.; Lu, Y.; Dzubiella, J.; Ballauff, M., Adsorption of proteins to functional polymeric nanoparticles. *Polymer* **2013,** *54* (12), 2835-2849.
161. Welsch, N.; Dzubiella, J.; Graebert, A.; Ballauff, M., Protein binding to soft polymeric layers: a quantitative study by fluorescence spectroscopy. *Soft Matter* **2012,** *8* (48), 12043-12052.
162. Waghmare, M.; Khade, B.; Chaudhari, P.; Dongre, P., Multiple layer formation of bovine serum albumin on silver nanoparticles revealed by dynamic light scattering and spectroscopic techniques. *J. Nanopart. Res.* **2018,** *20* (7), 185.
163. García-Álvarez, R.; Hadjidemetriou, M.; Sánchez-Iglesias, A.; Liz-Marzán, L. M.; Kostarelos, K., In vivo formation of protein corona on gold nanoparticles. The effect of their size and shape. *Nanoscale* **2018,** *10* (3), 1256-1264.
164. Monopoli, M. P.; Walczyk, D.; Campbell, A.; Elia, G.; Lynch, I.; Bombelli, F. B.; Dawson, K. A., Physical-chemical aspects of protein corona: relevance to in vitro and in vivo biological impacts of nanoparticles. *J. Am. Chem. Soc.* **2011,** *133* (8), 2525-34.
165. Hadjidemetriou, M.; Al-Ahmady, Z.; Kostarelos, K., Time-evolution of in vivo protein corona onto blood-circulating PEGylated liposomal doxorubicin (DOXIL) nanoparticles. *Nanoscale* **2016,** *8* (13), 6948-57.
166. Lesniak, A.; Fenaroli, F.; Monopoli, M. P.; Aberg, C.; Dawson, K. A.; Salvati, A., Effects of the presence or absence of a protein corona on silica nanoparticle uptake and impact on cells. *ACS Nano* **2012,** *6* (7), 5845-57.

167. Wan, S.; Kelly, P. M.; Mahon, E.; Stockmann, H.; Rudd, P. M.; Caruso, F.; Dawson, K. A.; Yan, Y.; Monopoli, M. P., The "sweet" side of the protein corona: effects of glycosylation on nanoparticle-cell interactions. *ACS Nano* **2015,** *9* (2), 2157-66.
168. Pitek, A. S.; Wen, A. M.; Shukla, S.; Steinmetz, N. F., The Protein Corona of Plant Virus Nanoparticles Influences their Dispersion Properties, Cellular Interactions, and *in Vivo* Fates. *Small* **2016,** *12* (13), 1758-69.
169. Tabb, D. L.; Vega-Montoto, L.; Rudnick, P. A.; Variyath, A. M.; Ham, A. J.; Bunk, D. M.; Kilpatrick, L. E.; Billheimer, D. D.; Blackman, R. K.; Cardasis, H. L.; Carr, S. A.; Clauser, K. R.; Jaffe, J. D.; Kowalski, K. A.; Neubert, T. A.; Regnier, F. E.; Schilling, B.; Tegeler, T. J.; Wang, M.; Wang, P.; Whiteaker, J. R.; Zimmerman, L. J.; Fisher, S. J.; Gibson, B. W.; Kinsinger, C. R.; Mesri, M.; Rodriguez, H.; Stein, S. E.; Tempst, P.; Paulovich, A. G.; Liebler, D. C.; Spiegelman, C., Repeatability and reproducibility in proteomic identifications by liquid chromatography-tandem mass spectrometry. *J. Proteome Res.* **2010,** *9* (2), 761-76.
170. Berg, M.; Parbel, A.; Pettersen, H.; Fenyo, D.; Bjorkesten, L., Reproducibility of LC-MS-based protein identification. *J. Exp. Bot.* **2006,** *57* (7), 1509-14.
171. Blume, J. E.; Manning, W. C.; Troiano, G.; Hornburg, D.; Figa, M.; Hesterberg, L.; Platt, T. L.; Zhao, X.; Cuaresma, R. A.; Everley, P. A.; Ko, M.; Liou, H.; Mahoney, M.; Ferdosi, S.; Elgierari, E. M.; Stolarczyk, C.; Tangeysh, B.; Xia, H.; Benz, R.; Siddiqui, A.; Carr, S. A.; Ma, P.; Langer, R.; Farias, V.; Farokhzad, O. C., Rapid, deep and precise profiling of the plasma proteome with multi-nanoparticle protein corona. *Nat. Commun.* **2020,** *11* (1), 3662.
172. Bourmaud, A.; Gallien, S.; Domon, B., A quality control of proteomic experiments based on multiple isotopologous internal standards. *EuPA Open Proteom.* **2015,** *8*, 16-21.
173. Collins, B. C.; Hunter, C. L.; Liu, Y.; Schilling, B.; Rosenberger, G.; Bader, S. L.; Chan, D. W.; Gibson, B. W.; Gingras, A. C.; Held, J. M.; Hirayama-Kurogi, M.; Hou, G.; Krisp, C.; Larsen, B.; Lin, L.; Liu, S.; Molloy, M. P.; Moritz, R. L.; Ohtsuki, S.; Schlapbach, R.; Selevsek, N.; Thomas, S. N.; Tzeng, S. C.; Zhang, H.; Aebersold, R., Multi-laboratory assessment of reproducibility, qualitative and quantitative performance of SWATH-mass spectrometry. *Nat. Commun.* **2017,** *8* (1), 291.
174. Klatt, J. N.; Depke, M.; Goswami, N.; Paust, N.; Zengerle, R.; Schmidt, F.; Hutzenlaub, T., Tryptic digestion of human serum for proteomic mass spectrometry automated by centrifugal microfluidics. *Lab Chip* **2020,** *20* (16), 2937-2946.
175. Poulos, R. C.; Hains, P. G.; Shah, R.; Lucas, N.; Xavier, D.; Manda, S. S.; Anees, A.; Koh, J. M. S.; Mahboob, S.; Wittman, M.; Williams, S. G.; Sykes, E. K.; Hecker, M.; Dausmann, M.; Wouters, M. A.; Ashman, K.; Yang, J.; Wild, P. J.; deFazio, A.; Balleine, R. L.; Tully, B.; Aebersold, R.; Speed, T. P.; Liu, Y.; Reddel, R. R.; Robinson, P. J.; Zhong, Q., Strategies to enable large-scale proteomics for reproducible research. *Nat. Commun.* **2020,** *11* (1), 3793.
176. Saadatkhah, N.; Garcia, A. C.; Ackermann, S.; Leclerc, P.; Latifi, M.; Samih, S.; Patience, G. S.; Chaouki, J., Experimental methods in chemical engineering: Thermogravimetric analysis—TGA. *The Canadian Journal of Chemical Engineering* **2020,** *98* (1), 34-43.
177. Weidner, A.; Grafe, C.; von der Luhe, M.; Remmer, H.; Clement, J. H.; Eberbeck, D.; Ludwig, F.; Muller, R.; Schacher, F. H.; Dutz, S., Preparation of Core-Shell Hybrid Materials by Producing a Protein Corona Around Magnetic Nanoparticles. *Nanoscale Res. Lett.* **2015,** *10* (1), 1-11.
178. Gräfe, C.; von der Lühe, M.; Weidner, A.; Globig, P.; Clement, J. H.; Dutz, S.; Schacher, F. H., Protein corona formation and its constitutional changes on magnetic nanoparticles in serum featuring a polydehydroalanine coating: effects of charge and incubation conditions. *Nanotechnology* **2019,** *30* (26), 265707.
179. Lehman, S. E.; Mudunkotuwa, I. A.; Grassian, V. H.; Larsen, S. C., Nano-Bio Interactions of Porous and Nonporous Silica Nanoparticles of Varied Surface Chemistry: A Structural, Kinetic, and Thermodynamic Study of Protein Adsorption from RPMI Culture Medium. *Langmuir* **2016,** *32* (3), 731-42.

180. Yallapu, M. M.; Chauhan, N.; Othman, S. F.; Khalilzad-Sharghi, V.; Ebeling, M. C.; Khan, S.; Jaggi, M.; Chauhan, S. C., Implications of protein corona on physico-chemical and biological properties of magnetic nanoparticles. *Biomaterials* **2015,** *46*, 1-12.
181. Clemments, A. M.; Muniesa, C.; Landry, C. C.; Botella, P., Effect of surface properties in protein corona development on mesoporous silica nanoparticles. *RSC Adv.* **2014,** *4* (55), 29134-29138.
182. Lin, C. Y.; Yang, C. M.; Linden, M., Influence of serum concentration and surface functionalization on the protein adsorption to mesoporous silica nanoparticles. *RSC Adv.* **2019,** *9* (58), 33912-33921.
183. Franqui, L. S.; De Farias, M. A.; Portugal, R. V.; Costa, C. A. R.; Domingues, R. R.; Souza Filho, A. G.; Coluci, V. R.; Leme, A. F. P.; Martinez, D. S. T., Interaction of graphene oxide with cell culture medium: Evaluating the fetal bovine serum protein corona formation towards in vitro nanotoxicity assessment and nanobiointeractions. *Mater. Sci. Eng. C* **2019,** *100*, 363-377.
184. Clemments, A. M.; Botella, P.; Landry, C. C., Protein Adsorption From Biofluids on Silica Nanoparticles: Corona Analysis as a Function of Particle Diameter and Porosity. *ACS Appl. Mater. Interfaces* **2015,** *7* (39), 21682-9.
185. Vidaurre-Agut, C.; Rivero-Buceta, E.; Romani-Cubells, E.; Clemments, A. M.; Vera-Donoso, C. D.; Landry, C. C.; Botella, P., Protein Corona over Mesoporous Silica Nanoparticles: Influence of the Pore Diameter on Competitive Adsorption and Application to Prostate Cancer Diagnostics. *ACS Omega* **2019,** *4* (5), 8852-8861.
186. Chetwynd, A. J.; Zhang, W.; Thorn, J. A.; Lynch, I.; Ramautar, R., The Nanomaterial Metabolite Corona Determined Using a Quantitative Metabolomics Approach: A Pilot Study. *Small* **2020,** *16* (21), e2000295.
187. Hong, R.; Han, G.; Fernandez, J. M.; Kim, B. J.; Forbes, N. S.; Rotello, V. M., Glutathione-mediated delivery and release using monolayer protected nanoparticle carriers. *J. Am. Chem. Soc.* **2006,** *128* (4), 1078-1079.
188. Brown, P. H.; Balbo, A.; Schuck, P., Characterizing Protein-Protein Interactions by Sedimentation Velocity Analytical Ultracentrifugation. **2008,** *81* (1), 18.15.1-18.15.39.
189. Lebowitz, J.; Lewis, M. S.; Schuck, P., Modern analytical ultracentrifugation in protein science: A tutorial review. **2002,** *11* (9), 2067-2079.
190. Bekdemir, A.; Liao, S. Y.; Stellacci, F., On the effect of ligand shell heterogeneity on nanoparticle/protein binding thermodynamics. *Colloids Surf. B* **2019,** *174*, 367-373.
191. Schaefer, J.; Schulze, C.; Marxer, E. E. J.; Schaefer, U. F.; Wohlleben, W.; Bakowsky, U.; Lehr, C. M., Atomic Force Microscopy and Analytical Ultracentrifugation for Probing Nanomaterial Protein Interactions. *ACS Nano* **2012,** *6* (6), 4603-4614.
192. Davidson, A. M.; Brust, M.; Cooper, D. L.; Volk, M., Sensitive Analysis of Protein Adsorption to Colloidal Gold by Differential Centrifugal Sedimentation. *Anal. Chem.* **2017,** *89* (12), 6807-6814.
193. Wang, R. M.; Chen, L.; Li, D. X.; Liu, R. X.; Ge, G. L., Concurrent Detection of Protein Adsorption on Mixed Nanoparticles by Differential Centrifugal Sedimentation. *Part. Part. Syst. Charact.* **2017,** *34* (12), 1700134.
194. Valle, A.; Perez-Socas, L. B.; Canet, L.; Hervis, Y. D.; de Armas-Guitart, G.; Martins-de-Sa, D.; Lima, J. C. B.; Souza, A. C. B.; Barbosa, J. A. R. G.; de Freitas, S. M.; Pazos, I. F., Self-homodimerization of an actinoporin by disulfide bridging reveals implications for their structure and pore formation. *Scientific Reports* **2018,** *8* (1), 6614.
195. Scotti, A.; Liu, W.; Hyatt, J. S.; Herman, E. S.; Choi, H. S.; Kim, J. W.; Lyon, L. A.; Gasser, U.; Fernandez-Nieves, A., The CONTIN algorithm and its application to determine the size distribution of microgel suspensions. *J. Chem. Phys.* **2015,** *142* (23), 234905.
196. Phillies, G. D. J., *Phenomenology of Polymer Solution Dynamics*. 2011.
197. Moerz, S. T.; Kraegeloh, A.; Chanana, M.; Kraus, T., Formation Mechanism for Stable Hybrid Clusters of Proteins and Nanoparticles. *ACS Nano* **2015,** *9* (7), 6696-705.

198. Kristin Mohr, M. S., Grit Baier, Susanne Schöttler, Patricia Okwieka, Stefan Tenzer, Katharina Landfester, Volker Mailänder, Manfred Schmidt, Ralf Georg Meyer, Aggregation Behavior of Polystyrene-Nanoparticles in Human Blood Serum and its Impact on the in vivo Distribution in Mice. *Journal of Nanomedicine & Nanotechnology* **2014,** *5* (2), 10.
199. Balog, S.; Rodriguez-Lorenzo, L.; Monnier, C. A.; Obiols-Rabasa, M.; Rothen-Rutishauser, B.; Schurtenberger, P.; Petri-Fink, A., Characterizing nanoparticles in complex biological media and physiological fluids with depolarized dynamic light scattering. *Nanoscale* **2015,** *7* (14), 5991-7.
200. Makino, K.; Ohshima, H., Electrophoretic mobility of a colloidal particle with constant surface charge density. *Langmuir* **2010,** *26* (23), 18016-9.
201. Cai, C.; Bakowsky, U.; Rytting, E.; Schaper, A. K.; Kissel, T., Charged nanoparticles as protein delivery systems: A feasibility study using lysozyme as model protein. *Eur. J. Pharm. Biopharm.* **2008,** *69* (1), 31-42.
202. Elson, E. L.; Magde, D., Fluorescence correlation spectroscopy. I. Conceptual basis and theory. *Biopolymers* **1974,** *13* (1), 1-27.
203. Magde, D.; Elson, E. L.; Webb, W. W., Fluorescence correlation spectroscopy. II. An experimental realization. *Biopolymers* **1974,** *13* (1), 29-61.
204. Lanzanò, L.; Scipioni, L.; Di Bona, M.; Bianchini, P.; Bizzarri, R.; Cardarelli, F.; Diaspro, A.; Vicidomini, G., Measurement of nanoscale three-dimensional diffusion in the interior of living cells by STED-FCS. *Nat. Commun.* **2017,** *8* (1), 65.
205. Chiantia, S.; Ries, J.; Schwille, P., Fluorescence correlation spectroscopy in membrane structure elucidation. *Biochim. Biophys. Acta Biomembr.* **2009,** *1788* (1), 225-33.
206. Treuel, L.; Brandholt, S.; Maffre, P.; Wiegele, S.; Shang, L.; Nienhaus, G. U., Impact of protein modification on the protein corona on nanoparticles and nanoparticle-cell interactions. *ACS Nano* **2014,** *8* (1), 503-13.
207. Winzen, S.; Koynov, K.; Landfester, K.; Mohr, K., Fluorescence labels may significantly affect the protein adsorption on hydrophilic nanomaterials. *Colloids Surf. B* **2016,** *147*, 124-128.
208. Sousa, A. A., A Note on the use of Steady-State Fluorescence Quenching to Quantify Nanoparticle-Protein Interactions. *J. Fluoresc.* **2015,** *25* (6), 1567-75.
209. Yin, M.-M.; Chen, W.-Q.; Lu, Y.-Q.; Han, J.-Y.; Liu, Y.; Jiang, F.-L., A model beyond protein corona: thermodynamics and binding stoichiometries of the interactions between ultrasmall gold nanoclusters and proteins. *Nanoscale* **2020,** *12* (7), 4573-4585.
210. Shahabadi, N.; Maghsudi, M.; Shiri, F., Application of a fluorescent biosensor based-on magneto-γ-Fe2 O3 -methyldopa nanoparticles for adsorption of human serum albumin. *Luminescence* **2016,** *31* (4), 937-44.
211. Yuan, M.; Zhong, R.; Yun, X.; Hou, J.; Du, Q.; Zhao, G.; Zhang, F., A fluorimetric study on the interaction between a Trp-containing beta-strand peptide and amphiphilic polymer-coated gold nanoparticles. *Luminescence* **2016,** *31* (1), 47-53.
212. Yin, M. M.; Dong, P.; Chen, W. Q.; Xu, S. P.; Yang, L. Y.; Jiang, F. L.; Liu, Y., Thermodynamics and Mechanisms of the Interactions between Ultrasmall Fluorescent Gold Nanoclusters and Human Serum Albumin, γ-Globulins, and Transferrin: A Spectroscopic Approach. *Langmuir* **2017,** *33* (21), 5108-5116.
213. Ross, P. D.; Subramanian, S., Thermodynamics of protein association reactions: forces contributing to stability. *Biochemistry* **1981,** *20* (11), 3096-3102.
214. Xu, X. Y.; Mao, X. Y.; Wang, Y. F.; Li, D. D.; Du, Z. Y.; Wu, W. H.; Jiang, L.; Yang, J.; Li, J. J., Study on the interaction of graphene oxide silver nanocomposites with bovine serum albumin and the formation of nanoparticle-protein corona. *Int. J. Biol. Macromol.* **2018,** *116*, 492-501.
215. Lai, L.; Lin, C.; Xu, Z. Q.; Han, X. L.; Tian, F. F.; Mei, P.; Li, D. W.; Ge, Y. S.; Jiang, F. L.; Zhang, Y. Z.; Liu, Y., Spectroscopic studies on the interactions between CdTe quantum dots coated with different ligands and human serum albumin. *Spectrochim. Acta A Mol. Biomol. Spectrosc.* **2012,** *97*, 366-76.

216. Boulos, S. P.; Davis, T. A.; Yang, J. A.; Lohse, S. E.; Alkilany, A. M.; Holland, L. A.; Murphy, C. J., Nanoparticle-protein interactions: a thermodynamic and kinetic study of the adsorption of bovine serum albumin to gold nanoparticle surfaces. *Langmuir* **2013,** *29* (48), 14984-96.
217. Lippé, R.; Glaunsinger, B. A., Flow Virometry: a Powerful Tool To Functionally Characterize Viruses. *J. Virol.* **2018,** *92* (3), e01765-17.
218. Welsh, J. A.; Holloway, J. A.; Wilkinson, J. S.; Englyst, N. A., Extracellular Vesicle Flow Cytometry Analysis and Standardization. *Front. Cell Dev. Biol.* **2017,** *5* (78).
219. Rodrigues, V.; Baudier, J. B.; Chantal, I., Development of a bead-based multiplexed assay for simultaneous quantification of five bovine cytokines by flow cytometry. *Cytometry A* **2017,** *91* (9), 901-907.
220. Liptrott, N. J.; Giardiello, M.; Hunter, J. W.; Tatham, L.; Tidbury, L. R.; Siccardi, M.; Rannard, S.; Owen, A., Flow cytometric analysis of the physical and protein-binding characteristics of solid drug nanoparticle suspensions. *Nanomedicine* **2015,** *10* (9), 1407-21.
221. Guindani, C.; Frey, M. L.; Simon, J.; Koynov, K.; Schultze, J.; Ferreira, S. R. S.; Araújo, P. H. H.; Oliveira, D.; Wurm, F. R.; Mailänder, V.; Landfester, K., Covalently Binding of Bovine Serum Albumin to Unsaturated Poly(Globalide-Co-ε-Caprolactone) Nanoparticles by Thiol-Ene Reactions. *Macromol. Biosci.* **2019,** *19* (10), 1900145.
222. Wan, S.; Egri, G.; Oddo, L.; Cerroni, B.; Dahne, L.; Paradossi, G.; Salvati, A.; Lynch, I.; Dawson, K. A.; Monopoli, M. P., Biological in situ characterization of polymeric microbubble contrast agents. *Int. J. Biochem. Cell Biol.* **2016,** *75*, 232-243.
223. Assfalg, M.; Ragona, L.; Pagano, K.; D'Onofrio, M.; Zanzoni, S.; Tomaselli, S.; Molinari, H., The study of transient protein-nanoparticle interactions by solution NMR spectroscopy. *Biochim. Biophys. Acta Proteins Proteom.* **2016,** *1864* (1), 102-14.
224. Wang, A. L.; Vangala, K.; Vo, T.; Zhang, D. M.; Fitzkee, N. C., A Three-Step Model for Protein-Gold Nanoparticle Adsorption. *J. Phys. Chem. C* **2014,** *118* (15), 8134-8142.
225. Woods, K. E.; Perera, Y. R.; Davidson, M. B.; Wilks, C. A.; Yadav, D. K.; Fitzkee, N. C., Understanding Protein Structure Deformation on the Surface of Gold Nanoparticles of Varying Size. *J. Phys. Chem. C* **2016,** *120* (49), 27944-27953.
226. Wang, A. L.; Perera, Y. R.; Davidson, M. B.; Fitzkee, N. C., Electrostatic Interactions and Protein Competition Reveal a Dynamic Surface in Gold Nanoparticle-Protein Adsorption. *J. Phys. Chem. C* **2016,** *120* (42), 24231-24239.
227. Pagès, G.; Gilard, V.; Martino, R.; Malet-Martino, M., Pulsed-field gradient nuclear magnetic resonance measurements (PFG NMR) for diffusion ordered spectroscopy (DOSY) mapping. *Analyst* **2017,** *142* (20), 3771-3796.
228. Porsch, C.; Zhang, Y. N.; Ostlund, A.; Damberg, P.; Ducani, C.; Malmstrom, E.; Nystrom, A. M., *In Vitro* Evaluation of Non-Protein Adsorbing Breast Cancer Theranostics Based on 19F-Polymer Containing Nanoparticles. *Part. Part. Syst. Charact.* **2013,** *30* (4), 381-390.
229. Padro, D.; Cienskowski, P.; Lopez-Fernandez, S.; Chakraborty, I.; Carrillo-Carrion, C.; Feliu, N.; Parak, W. J.; Carril, M., Toward Diffusion Measurements of Colloidal Nanoparticles in Biological Environments by Nuclear Magnetic Resonance. *Small* **2020,** *16* (36), e2001160.
230. Kari, O. K.; Rojalin, T.; Salmaso, S.; Barattin, M.; Jarva, H.; Meri, S.; Yliperttula, M.; Viitala, T.; Urtti, A., Multi-parametric surface plasmon resonance platform for studying liposome-serum interactions and protein corona formation. *Drug Deliv. Transl. Res.* **2017,** *7* (2), 228-240.
231. Zen, F.; Karanikolas, V. D.; Behan, J. A.; Andersson, J.; Ciapetti, G.; Bradley, A. L.; Colavita, P. E., Nanoplasmonic Sensing at the Carbon-Bio Interface: Study of Protein Adsorption at Graphitic and Hydrogenated Carbon Surfaces. *Langmuir* **2017,** *33* (17), 4198-4206.
232. Miclaus, T.; Bochenkov, V. E.; Ogaki, R.; Howard, K. A.; Sutherland, D. S., Spatial mapping and quantification of soft and hard protein coronas at silver nanocubes. *Nano Lett.* **2014,** *14* (4), 2086-93.

233. Kabiri, M.; Unsworth, L. D., Application of isothermal titration calorimetry for characterizing thermodynamic parameters of biomolecular interactions: peptide self-assembly and protein adsorption case studies. *Biomacromolecules* **2014,** *15* (10), 3463-73.
234. Parikh, V.; Gupta, P., Thermodynamic analysis of r-hGH-polymer surface Interaction using isothermal titration calorimetry. *Growth Horm. IGF Res.* **2018,** *42-43*, 86-93.
235. Thomson, J. A.; Ladbury, J. E., *Isothermal titration calorimetry: a tutorial*. 2nd ed.; John Wiley & Sons, Ltd: 2004; Vol. 2, p 37-58.
236. Ladbury, J. E.; Chowdhry, B. Z., Sensing the heat: the application of isothermal titration calorimetry to thermodynamic studies of biomolecular interactions. *Chem. Biol.* **1996,** *3* (10), 791-801.
237. Huang, R.; Lau, B. L. T., Biomolecule-nanoparticle interactions: Elucidation of the thermodynamics by isothermal titration calorimetry. *Biochim. Biophys. Acta Gen. Subj.* **2016,** *1860* (5), 945-956.
238. Goobes, G.; Goobes, R.; Shaw, W. J.; Gibson, J. M.; Long, J. R.; Raghunathan, V.; Schueler-Furman, O.; Popham, J. M.; Baker, D.; Campbell, C. T.; Stayton, P. S.; Drobny, G. P., The structure, dynamics, and energetics of protein adsorption-lessons learned from adsorption of statherin to hydroxyapatite. *Magn. Reson. Chem.* **2007,** *45 Suppl 1* (S1), S32-47.
239. Lindman, S.; Lynch, I.; Thulin, E.; Nilsson, H.; Dawson, K. A.; Linse, S., Systematic investigation of the thermodynamics of HSA adsorption to N-iso-propylacrylamide/N-tert-butylacrylamide copolymer nanoparticles. Effects of particle size and hydrophobicity. *Nano Lett.* **2007,** *7* (4), 914-20.
240. Das, P.; Chaudhari, S. K.; Das, A.; Kundu, S.; Saha, C., Interaction of flavonols with human serum albumin: a biophysical study showing structure-activity relationship and enhancement when coated on silver nanoparticles. *J. Biomol. Struct. Dyn.* **2019,** *37* (6), 1414-1426.
241. Liu, S. J.; Han, Y. C.; Qiao, R. R.; Zeng, J. F.; Jia, Q. J.; Wang, Y. L.; Gao, M. Y., Investigations on the Interactions between Plasma Proteins and Magnetic Iron Oxide Nanoparticles with Different Surface Modifications. *J. Phys. Chem. C* **2010,** *114* (49), 21270-21276.
242. Nasir, I.; Lundqvist, M.; Cabaleiro-Lago, C., Size and surface chemistry of nanoparticles lead to a variant behavior in the unfolding dynamics of human carbonic anhydrase. *Nanoscale* **2015,** *7* (41), 17504-15.
243. Leavitt, S.; Freire, E., Direct measurement of protein binding energetics by isothermal titration calorimetry. *Curr. Opin. Struct. Biol.* **2001,** *11* (5), 560-566.
244. Chakraborti, S.; Joshi, P.; Chakravarty, D.; Shanker, V.; Ansari, Z. A.; Singh, S. P.; Chakrabarti, P., Interaction of Polyethyleneimine-Functionalized ZnO Nanoparticles with Bovine Serum Albumin. *Langmuir* **2012,** *28* (30), 11142-11152.
245. Henzler, K.; Haupt, B.; Lauterbach, K.; Wittemann, A.; Borisov, O.; Ballauff, M., Adsorption of β-Lactoglobulin on Spherical Polyelectrolyte Brushes: Direct Proof of Counterion Release by Isothermal Titration Calorimetry. *J. Am. Chem. Soc.* **2010,** *132* (9), 3159-3163.
246. Marichal, L.; Degrouard, J.; Gatin, A.; Raffray, N.; Aude, J.-C.; Boulard, Y.; Combet, S.; Cousin, F.; Hourdez, S.; Mary, J.; Renault, J.-P.; Pin, S., From Protein Corona to Colloidal Self-Assembly: The Importance of Protein Size in Protein–Nanoparticle Interactions. *Langmuir* **2020,** *36* (28), 8218-8230.
247. Devineau, S.; Zanotti, J.-M.; Loupiac, C.; Zargarian, L.; Neiers, F.; Pin, S.; Renault, J. P., Myoglobin on Silica: A Case Study of the Impact of Adsorption on Protein Structure and Dynamics. *Langmuir* **2013,** *29* (44), 13465-13472.
248. Kelly, S. M.; Jess, T. J.; Price, N. C., How to study proteins by circular dichroism. *Biochim. Biophys. Acta Proteins Proteom.* **2005,** *1751* (2), 119-39.
249. Jiang, X.; Jiang, J.; Jin, Y.; Wang, E.; Dong, S., Effect of colloidal gold size on the conformational changes of adsorbed cytochrome c: probing by circular dichroism, UV-visible, and infrared spectroscopy. *Biomacromolecules* **2005,** *6* (1), 46-53.
250. Wangoo, N.; Suri, C. R.; Shekhawat, G., Interaction of gold nanoparticles with protein: A spectroscopic study to monitor protein conformational changes. *Appl. Phys. Lett.* **2008,** *92* (13), 133104.

251. Treuel, L.; Malissek, M.; Gebauer, J. S.; Zellner, R., The Influence of Surface Composition of Nanoparticles on their Interactions with Serum Albumin. *Chemphyschem* **2010,** *11* (14), 3093-3099.
252. Lacerda, S. H. D.; Park, J. J.; Meuse, C.; Pristinski, D.; Becker, M. L.; Karim, A.; Douglas, J. F., Interaction of Gold Nanoparticles with Common Human Blood Proteins. *ACS Nano* **2010,** *4* (1), 365-379.
253. Ge, C. C.; Du, J. F.; Zhao, L. N.; Wang, L. M.; Liu, Y.; Li, D. H.; Yang, Y. L.; Zhou, R. H.; Zhao, Y. L.; Chai, Z. F.; Chen, C. Y., Binding of blood proteins to carbon nanotubes reduces cytotoxicity. *Proc. Natl. Acad. Sci. U.S.A.* **2011,** *108* (41), 16968-16973.
254. Alex, S. A.; Chakraborty, D.; Chandrasekaran, N.; Mukherjee, A., A comprehensive investigation of the differential interaction of human serum albumin with gold nanoparticles based on the variation in morphology and surface functionalization. *RSC Adv.* **2016,** *6* (58), 52683-52694.
255. Wang, X.; Wang, M.; Lei, R.; Zhu, S. F.; Zhao, Y.; Chen, C., Chiral Surface of Nanoparticles Determines the Orientation of Adsorbed Transferrin and Its Interaction with Receptors. *ACS Nano* **2017,** *11* (5), 4606-4616.
256. Laera, S.; Ceccone, G.; Rossi, F.; Gilliland, D.; Hussain, R.; Siligardi, G.; Calzolai, L., Measuring protein structure and stability of protein-nanoparticle systems with synchrotron radiation circular dichroism. *Nano Lett.* **2011,** *11* (10), 4480-4.
257. Wang, L.; Li, J.; Pan, J.; Jiang, X.; Ji, Y.; Li, Y.; Qu, Y.; Zhao, Y.; Wu, X.; Chen, C., Revealing the binding structure of the protein corona on gold nanorods using synchrotron radiation-based techniques: understanding the reduced damage in cell membranes. *J. Am. Chem. Soc.* **2013,** *135* (46), 17359-68.
258. Ma, W. W.; Saccardo, A.; Roccatano, D.; Aboagye-Mensah, D.; Alkaseem, M.; Jewkes, M.; Di Nezza, F.; Baron, M.; Soloviev, M.; Ferrari, E., Modular assembly of proteins on nanoparticles. *Nat. Commun.* **2018,** *9* (1), 1489.
259. Sanchez-Guzman, D.; Giraudon-Colas, G.; Marichal, L.; Boulard, Y.; Wien, F.; Degrouard, J.; Baeza-Squiban, A.; Pin, S.; Renault, J. P.; Devineau, S., In Situ Analysis of Weakly Bound Proteins Reveals Molecular Basis of Soft Corona Formation. *ACS Nano* **2020,** *14* (7), 9073-9088.
260. Cristian, R. E.; Mohammad, I. J.; Mernea, M.; Sbarcea, B. G.; Trica, B.; Stan, M. S.; Dinischiotu, A., Analyzing the Interaction between Two Different Types of Nanoparticles and Serum Albumin. *Materials* **2019,** *12* (19), 3183.
261. Basu, A.; Kundu, S.; Basu, C.; Ghosh, S. K.; Sur, R.; Mukherjee, A., Biopolymer nanoparticle surface chemistry dictates the nature and extent of protein hard corona. *J. Mol. Liq.* **2019,** *282*, 169-176.
262. Vasti, C.; Bedoya, D. A.; Rojas, R.; Giacomelli, C. E., Effect of the protein corona on the colloidal stability and reactivity of LDH-based nanocarriers. *J. Mater. Chem. B* **2016,** *4* (11), 2008-2016.
263. Wang, M.; Fu, C.; Liu, X.; Lin, Z.; Yang, N.; Yu, S., Probing the mechanism of plasma protein adsorption on Au and Ag nanoparticles with FT-IR spectroscopy. *Nanoscale* **2015,** *7* (37), 15191-6.
264. Podila, R.; Chen, R.; Ke, P. C.; Brown, J. M.; Rao, A. M., Effects of surface functional groups on the formation of nanoparticle-protein corona. *Appl. Phys. Lett.* **2012,** *101* (26), 263701.
265. Szekeres, G. P.; Kneipp, J., SERS Probing of Proteins in Gold Nanoparticle Agglomerates. *Front. Chem.* **2019,** *7*, 30.
266. Grass, S.; Treuel, L., Mechanistic aspects of protein corona formation: insulin adsorption onto gold nanoparticle surfaces. *J. Nanopart. Res.* **2014,** *16* (2), 2254.
267. Treuel, L.; Malissek, M.; Grass, S.; Diendorf, J.; Mahl, D.; Meyer-Zaika, W.; Epple, M., Quantifying the influence of polymer coatings on the serum albumin corona formation around silver and gold nanoparticles. *J. Nanopart. Res.* **2012,** *14* (9), 1102.
268. Engel, M. F.; Visser, A. J.; van Mierlo, C. P., Conformation and orientation of a protein folding intermediate trapped by adsorption. *Proc. Natl. Acad. Sci. U.S.A.* **2004,** *101* (31), 11316-21.
269. Kogot, J. M.; Parker, A. M.; Lee, J.; Blaber, M.; Strouse, G. F.; Logan, T. M., Analysis of the dynamics of assembly and structural impact for a histidine tagged FGF1-1.5 nm Au nanoparticle bioconjugate. *Bioconjug. Chem.* **2009,** *20* (11), 2106-13.

270. Wang, A.; Vo, T.; Le, V.; Fitzkee, N. C., Using hydrogen-deuterium exchange to monitor protein structure in the presence of gold nanoparticles. *J. Phys. Chem. B* **2014,** *118* (49), 14148-56.
271. Heyduk, T., Measuring protein conformational changes by FRET/LRET. *Curr. Opin. Biotechnol.* **2002,** *13* (4), 292-296.
272. Raoufi, M.; Hajipour, M. J.; Kamali Shahri, S. M.; Schoen, I.; Linn, U.; Mahmoudi, M., Probing fibronectin conformation on a protein corona layer around nanoparticles. *Nanoscale* **2018,** *10* (3), 1228-1233.
273. Qu, S.; Sun, F.; Qiao, Z.; Li, J.; Shang, L., In Situ Investigation on the Protein Corona Formation of Quantum Dots by Using Fluorescence Resonance Energy Transfer. *Small* **2020,** *16* (21), 1907633.
274. Li, S.; Zhao, X.; Mo, Y.; Cummings, P. T.; Heller, W. T., Human serum albumin interactions with C60 fullerene studied by spectroscopy, small-angle neutron scattering, and molecular dynamics simulations. *J. Nanopart. Res.* **2013,** *15* (7), 1769.
275. Mehan, S.; Chinchalikar, A. J.; Kumar, S.; Aswal, V. K.; Schweins, R., Small-angle neutron scattering study of structure and interaction of nanoparticle, protein, and surfactant complexes. *Langmuir* **2013,** *29* (36), 11290-9.
276. Marichal, L.; Giraudon-Colas, G.; Cousin, F.; Thill, A.; Labarre, J.; Boulard, Y.; Aude, J. C.; Pin, S.; Renault, J. P., Protein-Nanoparticle Interactions: What Are the Protein-Corona Thickness and Organization? *Langmuir* **2019,** *35* (33), 10831-10837.
277. Brandes, N.; Welzel, P. B.; Werner, C.; Kroh, L. W., Adsorption-induced conformational changes of proteins onto ceramic particles: Differential scanning calorimetry and FTIR analysis. *J. Colloid Interface Sci.* **2006,** *299* (1), 56-69.
278. Yin, H.; Chen, R.; Casey, P. S.; Ke, P. C.; Davis, T. P.; Chen, C. Y., Reducing the cytotoxicity of ZnO nanoparticles by a pre-formed protein corona in a supplemented cell culture medium. *RSC Adv.* **2015,** *5* (90), 73963-73973.
279. Hadjidemetriou, M.; Al-Ahmady, Z.; Mazza, M.; Collins, R. F.; Dawson, K.; Kostarelos, K., *In Vivo* Biomolecule Corona around Blood-Circulating, Clinically Used and Antibody-Targeted Lipid Bilayer Nanoscale Vesicles. *ACS Nano* **2015,** *9* (8), 8142-56.
280. Kokkinopoulou, M.; Simon, J.; Landfester, K.; Mailander, V.; Lieberwirth, I., Visualization of the protein corona: towards a biomolecular understanding of nanoparticle-cell-interactions. *Nanoscale* **2017,** *9* (25), 8858-8870.
281. Stewart, M.; Mulenos, M. R.; Steele, L. R.; Sayes, C. M., Differences among Unique Nanoparticle Protein Corona Constructs: A Case Study Using Data Analytics and Multi-Variant Visualization to Describe Physicochemical Characteristics. *Appl. Sci.* **2018,** *8* (12), 2669.
282. Lara, S.; Alnasser, F.; Polo, E.; Garry, D.; Lo Giudice, M. C.; Hristov, D. R.; Rocks, L.; Salvati, A.; Yan, Y.; Dawson, K. A., Identification of Receptor Binding to the Biomolecular Corona of Nanoparticles. *ACS Nano* **2017,** *11* (2), 1884-1893.
283. Kuschnerus, I.; Lau, M.; Giri, K.; Bedford, N.; Biazik, J.; Ruan, J. F.; Garcia-Bennett, A., Effect of a protein corona on the fibrinogen induced cellular oxidative stress of gold nanoparticles. *Nanoscale* **2020,** *12* (10), 5898-5905.
284. Henzler, K.; Rosenfeldt, S.; Wittemann, A.; Harnau, L.; Finet, S.; Narayanan, T.; Ballauff, M., Directed motion of proteins along tethered polyelectrolytes. *Phys. Rev. Lett.* **2008,** *100* (15), 158301.
285. Henzler, K.; Haupt, B.; Rosenfeldt, S.; Harnau, L.; Narayanan, T.; Ballauff, M., Interaction strength between proteins and polyelectrolyte brushes: a small angle X-ray scattering study. *Phys. Chem. Chem. Phys.* **2011,** *13* (39), 17599-605.
286. Yadav, I.; Kumar, S.; Aswal, V. K.; Kohlbrecher, J., Small-angle neutron scattering study of differences in phase behavior of silica nanoparticles in the presence of lysozyme and bovine serum albumin proteins. *Phys. Rev. E Stat Nonlin. Soft Matter Phys.* **2014,** *89* (3), 032304.

287. Kihara, S.; van der Heijden, N. J.; Seal, C. K.; Mata, J. P.; Whitten, A. E.; Koper, I.; McGillivray, D. J., Soft and Hard Interactions between Polystyrene Nanoplastics and Human Serum Albumin Protein Corona. *Bioconjug. Chem.* **2019,** *30* (4), 1067-1076.
288. Pinals, R. L.; Yang, D.; Rosenberg, D. J.; Chaudhary, T.; Crothers, A. R.; Iavarone, A. T.; Hammel, M.; Landry, M. P., Protein Corona Composition and Dynamics on Carbon Nanotubes in Blood Plasma and Cerebrospinal Fluid. *bioRxiv* **2020**, 2020.01.13.905356.
289. Pilkington, E. H.; Gustafsson, O. J. R.; Xing, Y.; Hernandez-Fernaud, J.; Zampronio, C.; Kakinen, A.; Faridi, A.; Ding, F.; Wilson, P.; Ke, P. C.; Davis, T. P., Profiling the Serum Protein Corona of Fibrillar Human Islet Amyloid Polypeptide. *ACS Nano* **2018,** *12* (6), 6066-6078.
290. Liu, X.; Yan, C.; Chen, K. L., Adsorption of Human Serum Albumin on Graphene Oxide: Implications for Protein Corona Formation and Conformation. *Environ. Sci. Technol.* **2019,** *53* (15), 8631-8639.
291. Wang, Y.; Sun, Y.; Li, M.; Xiong, L.; Xu, X.; Ji, N.; Dai, L.; Sun, Q., The formation of a protein corona and the interaction with α-amylase by chitin nanowhiskers in simulated saliva fluid. *Food Hydrocoll.* **2020,** *102*, 105615.
292. Hampitak, P.; Melendrez, D.; Iliut, M.; Fresquet, M.; Parsons, N.; Spencer, B.; Jowitt, T. A.; Vijayaraghavan, A., Protein interactions and conformations on graphene-based materials mapped using a quartz-crystal microbalance with dissipation monitoring (QCM-D). *Carbon* **2020,** *165*, 317-327.
293. Pino, P. d.; Pelaz, B.; Zhang, Q.; Maffre, P.; Nienhaus, G. U.; Parak, W. J., Protein corona formation around nanoparticles – from the past to the future. *Mater. Horiz.* **2014,** *1* (3), 301-313.
294. Ilinskaya, A. N.; Dobrovolskaia, M. A., Interaction Between Nanoparticles and Plasma Proteins: Effects on Nanoparticle Biodistribution and Toxicity. In *Polymer Nanoparticles for Nanomedicines: A Guide for their Design, Preparation and Development*, Vauthier, C.; Ponchel, G., Eds. Springer International Publishing: Cham, 2016; pp 505-520.
295. Shalaby, S. W.; Burg, K. J. L., *Absorbable and Biodegradable Polymers*. CRC Press: Boca Raton, 2003; p 304.
296. Hoshyar, N.; Gray, S.; Han, H.; Bao, G., The effect of nanoparticle size on *in Vivo* pharmacokinetics and cellular interaction. *Nanomedicine* **2016,** *11* (6), 673-692.
297. Kaufman, E. D.; Belyea, J.; Johnson, M. C.; Nicholson, Z. M.; Ricks, J. L.; Shah, P. K.; Bayless, M.; Pettersson, T.; Feldotö, Z.; Blomberg, E., Probing Protein Adsorption onto Mercaptoundecanoic Acid Stabilized Gold Nanoparticles and Surfaces by Quartz Crystal Microbalance and ζ-Potential Measurements. *Langmuir* **2007,** *23*.
298. Satzer, P.; Svec, F.; Sekot, G.; Jungbauer, A., Protein adsorption onto nanoparticles induces conformational changes: Particle size dependency, kinetics, and mechanisms. *Eng. Life Sci.* **2016,** *16* (3), 238-246.
299. Latour, R. A., The langmuir isotherm: A commonly applied but misleading approach for the analysis of protein adsorption behavior. *J. Biomed. Mater. Res. A* **2015,** *103* (3), 949-958.
300. Rabe, M.; Verdes, D.; Seeger, S., Understanding protein adsorption phenomena at solid surfaces. *Adv. Colloid Interface Sci.* **2011,** *162* (1), 87-106.
301. Caracciolo, G.; Pozzi, D.; Capriotti, A. L.; Cavaliere, C.; Foglia, P.; Amenitsch, H.; Laganà, A., Evolution of the Protein Corona of Lipid Gene Vectors as a Function of Plasma Concentration. *Langmuir* **2011,** *27* (24), 15048-15053.
302. Brückner, M.; Simon, J.; Jiang, S.; Landfester, K.; Mailänder, V., Preparation of the protein corona: How washing shapes the proteome and influences cellular uptake of nanocarriers. *Acta Biomater.* **2020,** *114*, 333-342.
303. Yu, K.; Andruschak, P.; Yeh, H. H.; Grecov, D.; Kizhakkedathu, J. N., Influence of dynamic flow conditions on adsorbed plasma protein corona and surface-induced thrombus generation on antifouling brushes. *Biomaterials* **2018,** *166*, 79-95.

304. Jayaram, D. T.; Pustulka, S. M.; Mannino, R. G.; Lam, W. A.; Payne, C. K., Protein Corona in Response to Flow: Effect on Protein Concentration and Structure. *Biophys. J.* **2018,** *115* (2), 209-216.
305. Ju, Y.; Kelly, H. G.; Dagley, L. F.; Reynaldi, A.; Schlub, T. E.; Spall, S. K.; Bell, C. A.; Cui, J.; Mitchell, A. J.; Lin, Z.; Wheatley, A. K.; Thurecht, K. J.; Davenport, M. P.; Webb, A. I.; Caruso, F.; Kent, S. J., Person-Specific Biomolecular Coronas Modulate Nanoparticle Interactions with Immune Cells in Human Blood. *ACS Nano* **2020,** *14* (11), 15723-15737.
306. Hassan, S.; Prakash, G.; Ozturk, A.; Saghazadeh, S.; Sohail, M. F.; Seo, J.; Dockmeci, M.; Zhang, Y. S.; Khademhosseini, A., Evolution and Clinical Translation of Drug Delivery Nanomaterials. *Nano Today* **2017,** *15*, 91-106.
307. György, B.; Hung, M. E.; Breakefield, X. O.; Leonard, J. N., Therapeutic Applications of Extracellular Vesicles: Clinical Promise and Open Questions. *Annu. Rev. Pharmacol. Toxicol.* **2015,** *55* (1), 439-464.
308. Koudelka, K. J.; Pitek, A. S.; Manchester, M.; Steinmetz, N. F., Virus-Based Nanoparticles as Versatile Nanomachines. *Annu. Rev. Virol.* **2015,** *2* (1), 379-401.
309. Ezzat, K.; Pernemalm, M.; Pålsson, S.; Roberts, T. C.; Järver, P.; Dondalska, A.; Bestas, B.; Sobkowiak, M. J.; Levänen, B.; Sköld, M.; Thompson, E. A.; Saher, O.; Kari, O. K.; Lajunen, T.; Sverremark Ekström, E.; Nilsson, C.; Ishchenko, Y.; Malm, T.; Wood, M. J. A.; Power, U. F.; Masich, S.; Lindén, A.; Sandberg, J. K.; Lehtiö, J.; Spetz, A.-L.; El Andaloussi, S., The viral protein corona directs viral pathogenesis and amyloid aggregation. *Nat. Commun.* **2019,** *10* (1), 2331.
310. Singh, P.; Szigyártó, I. C.; Ricci, M.; Zsila, F.; Juhász, T.; Mihály, J.; Bősze, S.; Bulyáki, É.; Kardos, J.; Kitka, D.; Varga, Z.; Beke-Somfai, T., Membrane Active Peptides Remove Surface Adsorbed Protein Corona From Extracellular Vesicles of Red Blood Cells. *Front. Chem.* **2020,** *8*.
311. Zackova Suchanova, J.; Hejtmankova, A.; Neburkova, J.; Cigler, P.; Forstova, J.; Spanielova, H., The Protein Corona Does Not Influence Receptor-Mediated Targeting of Virus-like Particles. *Bioconjug. Chem.* **2020,** *31* (5), 1575-1585.
312. Varga, Z.; Fehér, B.; Kitka, D.; Wacha, A.; Bóta, A.; Berényi, S.; Pipich, V.; Fraikin, J.-L., Size Measurement of Extracellular Vesicles and Synthetic Liposomes: The Impact of the Hydration Shell and the Protein Corona. *Colloids Surf. B* **2020,** *192*, 111053.
313. Lee, J. Y.; Wang, H.; Pyrgiotakis, G.; DeLoid, G. M.; Zhang, Z.; Beltran-Huarac, J.; Demokritou, P.; Zhong, W., Analysis of lipid adsorption on nanoparticles by nanoflow liquid chromatography-tandem mass spectrometry. *Anal. Bioanal. Chem.* **2018,** *410* (24), 6155-6164.
314. Forest, V.; Pourchez, J., The nanoparticle protein corona: The myth of average. *Nano Today* **2016,** *11* (6), 700-703.
315. Ashkarran, A. A.; Dararatana, N.; Crespy, D.; Caracciolo, G.; Mahmoudi, M., Mapping the heterogeneity of protein corona by ex vivo magnetic levitation. *Nanoscale* **2020,** *12* (4), 2374-2383.
316. Frost, R.; Wadell, C.; Hellman, A.; Molander, S.; Svedhem, S.; Persson, M.; Langhammer, C., Core–Shell Nanoplasmonic Sensing for Characterization of Biocorona Formation and Nanoparticle Surface Interactions. *ACS Sens.* **2016,** *1* (6), 798-806.
317. Alekseeva, S.; Nedrygailov, I. I.; Langhammer, C., Single Particle Plasmonics for Materials Science and Single Particle Catalysis. *ACS Photonics* **2019,** *6* (6), 1319-1330.
318. Feiner-Gracia, N.; Beck, M.; Pujals, S.; Tosi, S.; Mandal, T.; Buske, C.; Linden, M.; Albertazzi, L., Super-Resolution Microscopy Unveils Dynamic Heterogeneities in Nanoparticle Protein Corona. *Small* **2017,** *13* (41), 1701631.
319. Digiacomo, L.; Palchetti, S.; Giulimondi, F.; Pozzi, D.; Chiozzi, R. Z.; Laura Capriotti, A.; Laganà, A.; Caracciolo, G., The biomolecular corona of gold nanoparticles in a controlled microfluidic environment. *Lab Chip* **2019**.
320. Weiss, A. C. G.; Krüger, K.; Besford, Q. A.; Schlenk, M.; Kempe, K.; Förster, S.; Caruso, F., *In Situ* Characterization of Protein Corona Formation on Silica Microparticles Using Confocal Laser Scanning Microscopy Combined with Microfluidics. *ACS Appl. Mater. Interfaces* **2019,** *11* (2), 2459-2469.

321. Srivastava, I.; Khan, M. S.; Dighe, K.; Alafeef, M.; Wang, Z.; Banerjee, T.; Ghonge, T.; Grove, L. M.; Bashir, R.; Pan, D., On-Chip Electrical Monitoring of Real-Time "Soft" and "Hard" Protein Corona Formation on Carbon Nanoparticles. *Small Methods* **2020,** *4* (7), 2000099.
322. Kim, H. R.; Gil, S.; Andrieux, K.; Nicolas, V.; Appel, M.; Chacun, H.; Desmaële, D.; Taran, F.; Georgin, D.; Couvreur, P., Low-density lipoprotein receptor-mediated endocytosis of PEGylated nanoparticles in rat brain endothelial cells. *Cell. Mol. Life Sci.* **2007,** *64* (3), 356-364.
323. Dong, Y.; Love, K. T.; Dorkin, J. R.; Sirirungruang, S.; Zhang, Y.; Chen, D.; Bogorad, R. L.; Yin, H.; Chen, Y.; Vegas, A. J.; Alabi, C. A.; Sahay, G.; Olejnik, K. T.; Wang, W.; Schroeder, A.; Lytton-Jean, A. K. R.; Siegwart, D. J.; Akinc, A.; Barnes, C.; Barros, S. A.; Carioto, M.; Fitzgerald, K.; Hettinger, J.; Kumar, V.; Novobrantseva, T. I.; Qin, J.; Querbes, W.; Koteliansky, V.; Langer, R.; Anderson, D. G., Lipopeptide nanoparticles for potent and selective siRNA delivery in rodents and nonhuman primates. *Proc Natl Acad Sci U S A* **2014,** *111* (11), 3955-3960.
324. Dominguez-Medina, S.; Blankenburg, J.; Olson, J.; Landes, C. F.; Link, S., Adsorption of a Protein Monolayer via Hydrophobic Interactions Prevents Nanoparticle Aggregation under Harsh Environmental Conditions. *ACS Sustainable Chemistry & Engineering* **2013,** *1* (7), 833-842.
325. Germain, D.; Leocmach, M.; Gibaud, T., Differential dynamic microscopy to characterize Brownian motion and bacteria motility. *American Journal of Physics* **2016,** *84* (3), 202-210.
326. Latreille, P.-L.; Adibnia, V.; Nour, A.; Rabanel, J.-M.; Lalloz, A.; Arlt, J.; Poon, W. C. K.; Hildgen, P.; Martinez, V. A.; Banquy, X., Spontaneous shrinking of soft nanoparticles boosts their diffusion in confined media. *Nat. Commun.* **2019,** *10* (1), 4294.
327. Adibnia, V.; Mirbagheri, M.; Latreille, P.-L.; Faivre, J.; Cécyre, B.; Robert, J.; Bouchard, J.-F.; Martinez, V. A.; Delair, T.; David, L.; Hwang, D. K.; Banquy, X., Chitosan hydrogel micro-bio-devices with complex capillary patterns via reactive-diffusive self-assembly. *Acta Biomater.* **2019,** *99*, 211-219.
328. Ferri, F.; D'Angelo, A.; Lee, M.; Lotti, A.; Pigazzini, M. C.; Singh, K.; Cerbino, R., Kinetics of colloidal fractal aggregation by differential dynamic microscopy. *The European Physical Journal Special Topics* **2011,** *199* (1), 139-148.
329. Giavazzi, F.; Brogioli, D.; Trappe, V.; Bellini, T.; Cerbino, R., Scattering information obtained by optical microscopy: Differential dynamic microscopy and beyond. *Phys. Rev. E* **2009,** *80* (3), 031403.
330. Haw, M. D.; Poon, W. C. K.; Pusey, P. N., Structure and arrangement of clusters in cluster aggregation. *Phys. Rev. E* **1997,** *56* (2), 1918-1933.
331. Lin, M. Y.; Lindsay, H. M.; Weitz, D. A.; Ball, R. C.; Klein, R.; Meakin, P., Universality in Colloid Aggregation. *Nature* **1989,** *339* (6223), 360-362.
332. Krigbaum, W. R.; Kuegler, F. R., Molecular conformation of egg-white lysozyme and bovine α-lactalbumin in solution. *Biochemistry* **1970,** *9* (5), 1216-1223.
333. Sun, D. P.; Liao, D. I.; Remington, S. J., Electrostatic fields in the active sites of lysozymes. **1989,** *86* (14), 5361-5365.
334. Slack, S. M.; Horbett, T. A., The effects of temperature and buffer on fibrinogen adsorption from blood plasma to glass. *Journal of Biomaterials Science, Polymer Edition* **1991,** *2* (3), 227-237.
335. He, X. M.; Carter, D. C., Atomic structure and chemistry of human serum albumin. *Nature* **1992,** *358* (6383), 209-215.
336. Bujacz, A., Structures of bovine, equine and leporine serum albumin. *Acta Crystallogr D Biol Crystallogr* **2012,** *68* (Pt 10), 1278-89.
337. Partikel, K.; Korte, R.; Mulac, D.; Humpf, H.-U.; Langer, K., Serum type and concentration both affect the protein-corona composition of PLGA nanoparticles. *Beilstein Journal of Nanotechnology* **2019,** *10*, 1002-1015.
338. Gräfe, C.; Weidner, A.; Lühe, M. v. d.; Bergemann, C.; Schacher, F. H.; Clement, J. H.; Dutz, S., Intentional formation of a protein corona on nanoparticles: Serum concentration affects protein corona

mass, surface charge, and nanoparticle–cell interaction. *The International Journal of Biochemistry & Cell Biology* **2016,** *75*, 196-202.
339. Sørensen, K. K.; Simon-Santamaria, J.; McCuskey, R. S.; Smedsrød, B., Liver Sinusoidal Endothelial Cells. In *Comprehensive Physiology*, 2015; pp 1751-1774.
340. Campbell, F.; Bos, F. L.; Sieber, S.; Arias-Alpizar, G.; Koch, B. E.; Huwyler, J.; Kros, A.; Bussmann, J., Directing Nanoparticle Biodistribution through Evasion and Exploitation of Stab2-Dependent Nanoparticle Uptake. *ACS Nano* **2018,** *12* (3), 2138-2150.
341. Kwapiszewska, K.; Szczepański, K.; Kalwarczyk, T.; Michalska, B.; Patalas-Krawczyk, P.; Szymański, J.; Andryszewski, T.; Iwan, M.; Duszyński, J.; Hołyst, R., Nanoscale Viscosity of Cytoplasm Is Conserved in Human Cell Lines. *The Journal of Physical Chemistry Letters* **2020,** *11* (16), 6914-6920.
342. Bicknese, S.; Periasamy, N.; Shohet, S. B.; Verkman, A. S., Cytoplasmic viscosity near the cell plasma membrane: measurement by evanescent field frequency-domain microfluorimetry. *Biophysical Journal* **1993,** *65* (3), 1272-1282.
343. Mika, Jacek T.; Thompson, Alexander J.; Dent, Michael R.; Brooks, Nicholas J.; Michiels, J.; Hofkens, J.; Kuimova, Marina K., Measuring the Viscosity of the Escherichia coli Plasma Membrane Using Molecular Rotors. *Biophysical Journal* **2016,** *111* (7), 1528-1540.
344. Kubánková, M.; Summers, P. A.; López-Duarte, I.; Kiryushko, D.; Kuimova, M. K., Microscopic Viscosity of Neuronal Plasma Membranes Measured Using Fluorescent Molecular Rotors: Effects of Oxidative Stress and Neuroprotection. *ACS Appl. Mater. Interfaces* **2019,** *11* (40), 36307-36315.
345. Sankaran, J.; Manna, M.; Guo, L.; Kraut, R.; Wohland, T., Diffusion, Transport, and Cell Membrane Organization Investigated by Imaging Fluorescence Cross-Correlation Spectroscopy. *Biophysical Journal* **2009,** *97* (9), 2630-2639.
346. Lundqvist, M.; Stigler, J.; Cedervall, T.; Berggård, T.; Flanagan, M. B.; Lynch, I.; Elia, G.; Dawson, K., The Evolution of the Protein Corona around Nanoparticles: A Test Study. *ACS Nano* **2011,** *5*.
347. Maffre, P.; Nienhaus, K.; Amin, F.; Parak, W. J.; Nienhaus, G. U., Characterization of protein adsorption onto FePt nanoparticles using dual-focus fluorescence correlation spectroscopy. *Beilstein Journal of Nanotechnology* **2011,** *2*, 374-383.
348. Zhang, Y.; Wu, J. L. Y.; Lazarovits, J.; Chan, W. C. W., An Analysis of the Binding Function and Structural Organization of the Protein Corona. *J. Am. Chem. Soc.* **2020,** *142* (19), 8827-8836.
349. Ouyang, B.; Poon, W.; Zhang, Y.-N.; Lin, Z. P.; Kingston, B. R.; Tavares, A. J.; Zhang, Y.; Chen, J.; Valic, M. S.; Syed, A. M.; MacMillan, P.; Couture-Senécal, J.; Zheng, G.; Chan, W. C. W., The dose threshold for nanoparticle tumour delivery. *Nature Materials* **2020,** *19* (12), 1362-1371.
350. Bertoli, F.; Garry, D.; Monopoli, M. P.; Salvati, A.; Dawson, K. A., The Intracellular Destiny of the Protein Corona: A Study on its Cellular Internalization and Evolution. *ACS Nano* **2016,** *10* (11), 10471-10479.
351. Rabanel, J.-M.; Piec, P.-A.; Landri, S.; Patten, S. A.; Ramassamy, C., Transport of PEGylated-PLA nanoparticles across a blood brain barrier model, entry into neuronal cells and in vivo brain bioavailability. *J. Control. Release.* **2020,** *328*, 679-695.
352. Stylianopoulos, T.; Jain, R. K., Design considerations for nanotherapeutics in oncology. *Nanomed. Nanotechnol. Biol. Med.* **2015,** *11* (8), 1893-1907.
353. Sindhwani, S.; Syed, A. M.; Ngai, J.; Kingston, B. R.; Maiorino, L.; Rothschild, J.; MacMillan, P.; Zhang, Y.; Rajesh, N. U.; Hoang, T.; Wu, J. L. Y.; Wilhelm, S.; Zilman, A.; Gadde, S.; Sulaiman, A.; Ouyang, B.; Lin, Z.; Wang, L.; Egeblad, M.; Chan, W. C. W., The entry of nanoparticles into solid tumours. *Nature Materials* **2020,** *19* (5), 566-575.
354. Chauhan, V. P.; Stylianopoulos, T.; Martin, J. D.; Popović, Z.; Chen, O.; Kamoun, W. S.; Bawendi, M. G.; Fukumura, D.; Jain, R. K., Normalization of tumour blood vessels improves the delivery of nanomedicines in a size-dependent manner. *Nat. Nanotechnol.* **2012,** *7* (6), 383-388.

355. Chauhan, V. P.; Jain, R. K., Strategies for advancing cancer nanomedicine. *Nature Materials* **2013,** *12*, 958.
356. Jain, R. K., Normalization of Tumor Vasculature: An Emerging Concept in Antiangiogenic Therapy. *Science* **2005,** *307* (5706), 58-62.
357. Carmeliet, P.; Jain, R. K., Principles and mechanisms of vessel normalization for cancer and other angiogenic diseases. *Nature Reviews Drug Discovery* **2011,** *10* (6), 417-427.
358. Stylianopoulos, T.; Jain, R. K., Combining two strategies to improve perfusion and drug delivery in solid tumors. *Proceedings of the National Academy of Sciences* **2013,** *110* (46), 18632.
359. Li, S.; Zhang, Y.; Wang, J.; Zhao, Y.; Ji, T.; Zhao, X.; Ding, Y.; Zhao, X.; Zhao, R.; Li, F.; Yang, X.; Liu, S.; Liu, Z.; Lai, J.; Whittaker, A. K.; Anderson, G. J.; Wei, J.; Nie, G., Nanoparticle-mediated local depletion of tumour-associated platelets disrupts vascular barriers and augments drug accumulation in tumours. *Nature Biomedical Engineering* **2017,** *1* (8), 667-679.
360. P., C. V.; Zoran, P.; Ou, C.; Jian, C.; Dai, F.; G., B. M.; K., J. R., Fluorescent Nanorods and Nanospheres for Real-Time In Vivo Probing of Nanoparticle Shape-Dependent Tumor Penetration. *Angew. Chem. Int. Ed.* **2011,** *50* (48), 11417-11420.
361. Suh, J.; Choy, K. L.; Lai, S. K.; Suk, J. S.; Tang, B. C.; Prabhu, S.; Hanes, J., PEGylation of nanoparticles improves their cytoplasmic transport. *Int. J. Nanomedicine* **2007,** *2* (4), 735-41.
362. Han, H.-S.; Martin, J. D.; Lee, J.; Harris, D. K.; Fukumura, D.; Jain, R. K.; Bawendi, M., Spatial Charge Configuration Regulates Nanoparticle Transport and Binding Behavior In Vivo. **2013,** *52* (5), 1414-1419.
363. Wong, C.; Stylianopoulos, T.; Cui, J.; Martin, J.; Chauhan, V. P.; Jiang, W.; Popovic, Z.; Jain, R. K.; Bawendi, M. G.; Fukumura, D., Multistage nanoparticle delivery system for deep penetration into tumor tissue. *Proc. Natl. Acad. Sci. U.S.A.* **2011,** *108* (6), 2426-31.
364. Syed, A. M.; Sindhwani, S.; Chan, W. C. W., Making vessels more permeable. *Nature Biomedical Engineering* **2017,** *1* (8), 629-631.
365. Raeesi, V.; Chan, W. C. W., Improving nanoparticle diffusion through tumor collagen matrix by photo-thermal gold nanorods. *Nanoscale* **2016,** *8* (25), 12524-12530.
366. Gong, H.; Chao, Y.; Xiang, J.; Han, X.; Song, G.; Feng, L.; Liu, J.; Yang, G.; Chen, Q.; Liu, Z., Hyaluronidase To Enhance Nanoparticle-Based Photodynamic Tumor Therapy. *Nano Lett.* **2016,** *16* (4), 2512-2521.
367. Nayak, S.; Lyon, L. A., Soft Nanotechnology with Soft Nanoparticles. **2005,** *44* (47), 7686-7708.
368. Hendrickson, G. R.; Lyon, L. A., Microgel Translocation through Pores under Confinement. *Angew. Chem. Int. Ed.* **2010,** *49* (12), 2193-2197.
369. Merkel, T. J.; Jones, S. W.; Herlihy, K. P.; Kersey, F. R.; Shields, A. R.; Napier, M.; Luft, J. C.; Wu, H.; Zamboni, W. C.; Wang, A. Z.; Bear, J. E.; DeSimone, J. M., Using mechanobiological mimicry of red blood cells to extend circulation times of hydrogel microparticles. *Proceedings of the National Academy of Sciences* **2011,** *108* (2), 586.
370. Zhang, L.; Cao, Z.; Li, Y.; Ella-Menye, J.-R.; Bai, T.; Jiang, S., Softer Zwitterionic Nanogels for Longer Circulation and Lower Splenic Accumulation. *ACS Nano* **2012,** *6* (8), 6681-6686.
371. Anselmo, A. C.; Zhang, M.; Kumar, S.; Vogus, D. R.; Menegatti, S.; Helgeson, M. E.; Mitragotri, S., Elasticity of Nanoparticles Influences Their Blood Circulation, Phagocytosis, Endocytosis, and Targeting. *ACS Nano* **2015,** *9* (3), 3169-3177.
372. Yu, M.; Xu, L.; Tian, F.; Su, Q.; Zheng, N.; Yang, Y.; Wang, J.; Wang, A.; Zhu, C.; Guo, S.; Zhang, X.; Gan, Y.; Shi, X.; Gao, H., Rapid transport of deformation-tuned nanoparticles across biological hydrogels and cellular barriers. *Nat. Commun.* **2018,** *9* (1), 2607.
373. Guo, P.; Liu, D.; Subramanyam, K.; Wang, B.; Yang, J.; Huang, J.; Auguste, D. T.; Moses, M. A., Nanoparticle elasticity directs tumor uptake. *Nat. Commun.* **2018,** *9* (1), 130.

374. Bianco, C.; Tosco, T.; Sethi, R., A 3-dimensional micro- and nanoparticle transport and filtration model (MNM3D) applied to the migration of carbon-based nanomaterials in porous media. *J. Contam. Hydrol.* **2016,** *193*, 10-20.
375. Babakhani, P.; Bridge, J.; Doong, R.-a.; Phenrat, T., Parameterization and prediction of nanoparticle transport in porous media: A reanalysis using artificial neural network. *Water Resources Research* **2017,** *53* (6), 4564-4585.
376. Goldberg, E.; Scheringer, M.; Bucheli, T. D.; Hungerbühler, K., Critical Assessment of Models for Transport of Engineered Nanoparticles in Saturated Porous Media. *Environ. Sci. Technol.* **2014,** *48* (21), 12732-12741.
377. Liu, H.; Jin, X.; Ding, B., Application of nanotechnology in petroleum exploration and development. *Petroleum Exploration and Development* **2016,** *43* (6), 1107-1115.
378. Liu, Z.; Zhu, Y.; Rao, R. R.; Clausen, J. R.; Aidun, C. K., Nanoparticle transport in cellular blood flow. *Computers & Fluids* **2018,** *172*, 609-620.
379. Stirland, D. L.; Nichols, J. W.; Denison, T. A.; Bae, Y. H., Targeted drug delivery for cancer therapy A2. In *Biomaterials for Cancer Therapeutics*, Park, K., Ed. Woodhead Publishing: 2013; pp 31-56.
380. Adibnia, V.; Hill, R. J., Electroacoustic Spectroscopy of Nanoparticle-Doped Hydrogels. *Macromolecules* **2014,** *47* (22), 8064-8071.
381. Kang, K.; Wilk, A.; Patkowski, A.; Dhont, J. K. G., Diffusion of spheres in isotropic and nematic networks of rods: Electrostatic interactions and hydrodynamic screening. *J. Chem. Phys.* **2007,** *126* (21), 214501.
382. Wang, J.; Mao, W.; Lock, L. L.; Tang, J.; Sui, M.; Sun, W.; Cui, H.; Xu, D.; Shen, Y., The Role of Micelle Size in Tumor Accumulation, Penetration, and Treatment. *ACS Nano* **2015,** *9* (7), 7195-7206.
383. Yuan, Y.-Y.; Mao, C.-Q.; Du, X.-J.; Du, J.-Z.; Wang, F.; Wang, J., Surface Charge Switchable Nanoparticles Based on Zwitterionic Polymer for Enhanced Drug Delivery to Tumor. *Adv. Mater.* **2012,** *24* (40), 5476-5480.
384. Liu, X.; Chen, Y.; Li, H.; Huang, N.; Jin, Q.; Ren, K.; Ji, J., Enhanced Retention and Cellular Uptake of Nanoparticles in Tumors by Controlling Their Aggregation Behavior. *ACS Nano* **2013,** *7* (7), 6244-6257.
385. Na, J. H.; Lee, S.-Y.; Lee, S.; Koo, H.; Min, K. H.; Jeong, S. Y.; Yuk, S. H.; Kim, K.; Kwon, I. C., Effect of the stability and deformability of self-assembled glycol chitosan nanoparticles on tumor-targeting efficiency. *J. Control. Release.* **2012,** *163* (1), 2-9.
386. Smith, M. H.; Lyon, L. A., Multifunctional Nanogels for siRNA Delivery. *Acc. Chem. Res.* **2012,** *45* (7), 985-993.
387. Hoare, T.; Pelton, R., Functionalized Microgel Swelling: Comparing Theory and Experiment. *The Journal of Physical Chemistry B* **2007,** *111* (41), 11895-11906.
388. Karg, M.; Pastoriza-Santos, I.; Rodriguez-González, B.; von Klitzing, R.; Wellert, S.; Hellweg, T., Temperature, pH, and Ionic Strength Induced Changes of the Swelling Behavior of PNIPAM−Poly(allylacetic acid) Copolymer Microgels. *Langmuir* **2008,** *24* (12), 6300-6306.
389. Sierra-Martin, B.; Frederick, J. A.; Laporte, Y.; Markou, G.; Lietor-Santos, J. J.; Fernandez-Nieves, A., Determination of the bulk modulus of microgel particles. *Colloid. Polym. Sci.* **2011,** *289* (5), 721-728.
390. Guo, D.; Li, J.; Xie, G.; Wang, Y.; Luo, J., Elastic Properties of Polystyrene Nanospheres Evaluated with Atomic Force Microscopy: Size Effect and Error Analysis. *Langmuir* **2014,** *30* (24), 7206-7212.
391. Ramos, M.; Ortiz-Jordan, L.; Hurtado-Macias, A.; Flores, S.; Elizalde-Galindo, J. T.; Rocha, C.; Torres, B.; Zarei-Chaleshtori, M.; Chianelli, R. R., Hardness and Elastic Modulus on Six-Fold Symmetry Gold Nanoparticles. *Materials (Basel, Switzerland)* **2013,** *6* (1), 198-205.
392. Safari, M. S.; Vorontsova, M. A.; Poling-Skutvik, R.; Vekilov, P. G.; Conrad, J. C., Differential dynamic microscopy of weakly scattering and polydisperse protein-rich clusters. *Phys. Rev. E Stat Nonlin. Soft Matter Phys.* **2015,** *92* (4), 042712.

393. Phillies, G. D. J., The hydrodynamic scaling model for polymer self-diffusion. *The Journal of Physical Chemistry* **1989,** *93* (13), 5029-5039.
394. Phillies, G. D. J.; Ullmann, G. S.; Ullmann, K.; Lin, T. H., Phenomenological scaling laws for ''semidilute'' macromolecule solutions from light scattering by optical probe particles. *Journal of Chemical Physics* **1985,** *82* (11), 5242-5246.
395. Fujii, T.; Yano, T.; Kumagai, H.; Miyawaki, O., Dynamic Light Scattering Analysis on Critical Behavior of Cluster Size Distribution of Polyacrylamide and Agarose Solutions near the Sol-Gel Transition Point. *Food Sci. Technol. Res.* **2000,** *6* (2), 94-98.
396. Tako, M.; Nakamura, S., Gelation mechanism of agarose. *Carbohydr. Res.* **1988,** *180* (2), 277-284.
397. Xiong, J.-Y.; Narayanan, J.; Liu, X.-Y.; Chong, T. K.; Chen, S. B.; Chung, T.-S., Topology Evolution and Gelation Mechanism of Agarose Gel. *J. Phys. Chem. B* **2005,** *109* (12), 5638-5643.
398. Horkay, F.; Basser, P. J., Ionic and pH effects on the osmotic properties and structure of polyelectrolyte gels. *Journal of polymer science. Part B, Polymer physics* **2008,** *46* (24), 2803-2810.
399. Horkay, F.; Hecht, A. M.; Mallam, S.; Geissler, E.; Rennie, A. R., Macroscopic and microscopic thermodynamic observations in swollen poly(vinyl acetate) networks. *Macromolecules* **1991,** *24* (10), 2896-2902.
400. Faivre, J.; Sudre, G.; Montembault, A.; Benayoun, S.; Banquy, X.; Delair, T.; David, L., Bioinspired microstructures of chitosan hydrogel provide enhanced wear protection. *Soft Matter* **2018,** *14* (11), 2068-2076.
401. Fernández-Nieves, A.; Fernández-Barbero, A.; Vincent, B.; Nieves, F. J. d. l., Osmotic de-swelling of ionic microgel particles. *J. Chem. Phys.* **2003,** *119* (19), 10383-10388.
402. Scotti, A.; Gasser, U.; Herman, E. S.; Pelaez-Fernandez, M.; Han, J.; Menzel, A.; Lyon, L. A.; Fernandez-Nieves, A., The role of ions in the self-healing behavior of soft particle suspensions. *Proc. Natl. Acad. Sci. U.S.A.* **2016,** *113* (20), 5576-81.
403. Griess, G. A.; Guiseley, K. B.; Serwer, P., The relationship of agarose gel structure to the sieving of spheres during agarose gel electrophoresis. *Biophysical Journal* **1993,** *65* (1), 138-148.
404. Waki, S.; Harvey, J. D.; Bellamy, A. R., Study of agarose gels by electron microscopy of freeze-fractured surfaces. *Biopolymers* **1982,** *21* (9), 1909-1926.
405. Johnson, E. M.; Berk, D. A.; Jain, R. K.; Deen, W. M., Diffusion and partitioning of proteins in charged agarose gels. *Biophysical Journal* **1995,** *68* (4), 1561-1568.
406. De Gennes, P. G., Dynamics of Entangled Polymer Solutions. II. Inclusion of Hydrodynamic Interactions. *Macromolecules* **1976,** *9* (4), 594-598.
407. Cukier, R. I., Diffusion of Brownian spheres in semidilute polymer solutions. *Macromolecules* **1984,** *17* (2), 252-255.
408. Jones, C. D.; Lyon, L. A., Synthesis and Characterization of Multiresponsive Core−Shell Microgels. *Macromolecules* **2000,** *33* (22), 8301-8306.
409. Guo, Y.; Li, X.; Fang, Y., The effects of electroendosmosis in agarose electrophoresis. *Electrophoresis* **1998,** *19* (8-9), 1311-3.
410. Jimidar, M. I., Theoretical considerations in performance of various modes of CE. In *Capillary Electrophoresis Methods for Pharmaceutical Analysis*, 1st ed.; Ahuja, S.; Jimidar, M. I., Eds. Academic Press: 2008; Vol. 9, pp 9-530.
411. Li, K.; Chen, Y., Evaluation of DLVO interaction between a sphere and a cylinder. *Colloids Surf., A* **2012,** *415*, 218-229.
412. Ohshima, H., Surface Charge Density/Surface Potential Relationship for a Cylindrical Particle in an Electrolyte Solution. *J. Colloid Interface Sci.* **1998,** *200* (2), 291-297.
413. Israelachvili, J. N., *Intermolecular and Surface Forces*. 3rd Edition ed.; Academic Press: San Diego, 2011; p 710.

414. Leckband, D.; Israelachvili, J., Intermolecular forces in biology. *Quarterly Reviews of Biophysics* **2001,** *34* (2), 105-267.
415. Slayter, H. S.; Codington, J. F., Size and Configuration of Glycoprotein Fragments Cleaved from Tumor Cells by Proteolysis. *J. Biol. Chem.* **1973,** *248* (10), 3405-3410.
416. Ebong, E. E.; Macaluso, F. P.; Spray, D. C.; Tarbell, J. M., Imaging the endothelial glycocalyx in vitro by rapid freezing/freeze substitution transmission electron microscopy. *Arterioscler Thromb Vasc Biol* **2011,** *31* (8), 1908-15.
417. Kabedev, A.; Lobaskin, V., Structure and elasticity of bush and brush-like models of the endothelial glycocalyx. *Scientific Reports* **2018,** *8* (1), 240.
418. Hanauer, N.; Latreille, P. L.; Banquy, X., Mechanistic Insights into the Directed Assembly of Hydrogel Blocks Mediated by Polyelectrolytes or Microgels. *Langmuir* **2017,** *33* (15), 3864-3870.
419. Latreille, P.-L.; Alsharif, S.; Gourgas, O.; Tehrani, S. F.; Roullin, V. G.; Banquy, X., Release kinetics from nano-inclusion-based and affinity-based hydrogels: A comparative study. *Colloids Surf., A* **2017,** *529*, 739-749.
420. Maaloum, M.; Pernodet, N.; Tinland, B., Agarose gel structure using atomic force microscopy: Gel concentration and ionic strength effects. *Electrophoresis* **1998,** *19* (10), 1606-1610.
421. Masaro, L.; Zhu, X. X., Physical models of diffusion for polymer solutions, gels and solids. *Prog. Polym. Sci.* **1999,** *24* (5), 731-775.
422. Ogston, A. G.; Preston, B. N.; Wells, J. D., On the transport of compact particles through solutions of chain-polymers. *Proc. Royal Soc. A* **1973,** *333* (1594), 297-316.
423. Eckert, T.; Richtering, W., Thermodynamic and hydrodynamic interaction in concentrated microgel suspensions: Hard or soft sphere behavior? *J. Chem. Phys.* **2008,** *129* (12), 124902.
424. Edera, P.; Bergamini, D.; Trappe, V.; Giavazzi, F.; Cerbino, R., Differential dynamic microscopy microrheology of soft materials: A tracking-free determination of the frequency-dependent loss and storage moduli. *Physical Review Materials* **2017,** *1* (7), 073804.
425. Söderlund, J.; Kiss, L. B.; Niklasson, G. A.; Granqvist, C. G., Lognormal Size Distributions in Particle Growth Processes without Coagulation. *Physical Review Letters* **1998,** *80* (11), 2386-2388.
426. Scotti, A.; Gasser, U.; Herman, E. S.; Han, J.; Menzel, A.; Lyon, L. A.; Fernandez-Nieves, A., Phase behavior of binary and polydisperse suspensions of compressible microgels controlled by selective particle deswelling. *Phys. Rev. E* **2017,** *96* (3), 032609.
427. Hashmi, S. M.; Dufresne, E. R., Mechanical properties of individual microgel particles through the deswelling transition. *Soft Matter* **2009,** *5* (19), 3682-3688.
428. Sykes, E. A.; Dai, Q.; Sarsons, C. D.; Chen, J.; Rocheleau, J. V.; Hwang, D. M.; Zheng, G.; Cramb, D. T.; Rinker, K. D.; Chan, W. C., Tailoring nanoparticle designs to target cancer based on tumor pathophysiology. *Proc. Natl. Acad. Sci. U.S.A.* **2016,** *113* (9), E1142-51.
429. Aisenbrey, E. A.; Murphy, W. L., Synthetic alternatives to Matrigel. *Nat. Rev. Mater.* **2020,** *5* (7), 539-551.
430. Le Goas, M.; Testard, F.; Taché, O.; Debou, N.; Cambien, B.; Carrot, G.; Renault, J.-P., How Do Surface Properties of Nanoparticles Influence Their Diffusion in the Extracellular Matrix? A Model Study in Matrigel Using Polymer-Grafted Nanoparticles. *Langmuir* **2020,** *36* (35), 10460-10470.
431. Roth, A.; Murschel, F.; Latreille, P.-L.; Martinez, V. A.; Liberelle, B.; Banquy, X.; De Crescenzo, G., Coiled Coil Affinity-Based Systems for the Controlled Release of Biofunctionalized Gold Nanoparticles from Alginate Hydrogels. *Biomacromolecules* **2019**.
432. Chen, Y. Y.; Syed, A. M.; MacMillan, P.; Rocheleau, J. V.; Chan, W. C. W., Flow Rate Affects Nanoparticle Uptake into Endothelial Cells. *Adv. Mater.* **2020,** *32* (24), 1906274.
433. Johnson, J. A.; Lu, Y. Y.; Burts, A. O.; Xia, Y.; Durrell, A. C.; Tirrell, D. A.; Grubbs, R. H., Drug-Loaded, Bivalent-Bottle-Brush Polymers by Graft-through ROMP. *Macromolecules* **2010,** *43* (24), 10326-10335.

434. Xie, G.; Martinez, M. R.; Olszewski, M.; Sheiko, S. S.; Matyjaszewski, K., Molecular Bottlebrushes as Novel Materials. *Biomacromolecules* **2019,** *20* (1), 27-54.
435. Richards, J. A.; Martinez, V. A.; Arlt, J., Particle sizing for flowing colloidal suspensions using flow-differential dynamic microscopy. *Soft Matter* **2021,** *17* (14), 3945-3953.
436. Perry, J. L.; Reuter, K. G.; Kai, M. P.; Herlihy, K. P.; Jones, S. W.; Luft, J. C.; Napier, M.; Bear, J. E.; DeSimone, J. M., PEGylated PRINT Nanoparticles: The Impact of PEG Density on Protein Binding, Macrophage Association, Biodistribution, and Pharmacokinetics. *Nano Lett.* **2012,** *12*.
437. Martinez, V. A.; Thijssen, J. H. J.; Zontone, F.; Megen, W. v.; Bryant, G., Dynamics of hard sphere suspensions using dynamic light scattering and X-ray photon correlation spectroscopy: Dynamics and scaling of the intermediate scattering function. *J. Chem. Phys.* **2011,** *134* (5), 054505.
438. Ioannidis, N.; Bowen, J.; Pacek, A.; Zhang, Z., Manufacturing of agarose-based chromatographic adsorbents – Effect of ionic strength and cooling conditions on particle structure and mechanical strength. *J. Colloid Interface Sci.* **2012,** *367* (1), 153-160.
439. Park, T. G.; Hoffman, A. S., Sodium chloride-induced phase transition in nonionic poly(N-isopropylacrylamide) gel. *Macromolecules* **1993,** *26* (19), 5045-5048.
440. Jiang, L.; Granick, S., Real-Space, in Situ Maps of Hydrogel Pores. *ACS Nano* **2017,** *11* (1), 204-212.

Annexe 1

Supplementary Information for "*Scratching the Surface of the Protein Corona: Challenging Measurements and Unresolved Issues*"

Research methodology for the bibliographic dataset

The bibliographic dataset was constructed using Web of Science through all available databases. The aim was to collect articles measuring protein adsorption or characterizing the protein corona using at least one of the techniques reviewed in section 3. We searched for articles that contained keywords of "*protein corona*" or "*protein adsorption*", compiling a total of ~20 000 articles. We further narrowed down the number of articles to ~ 1500 by adding the key word *nanoparticle*, so that only adsorption on nanoparticles is included. Then, the last keyword was the full name of the technique, *e.g.* "*fluorescence correlation spectroscopy"* or "*isothermal titration calorimetry*", generating ~10-100 articles, depending on the technique. From this pool, each article was carefully examined to determine if it contained information regarding protein adsorption layer(s) and/or reversibility. A total of 109 articles ended up in the dataset. The information extracted from all articles was further categorized, as presented in the table in supplementary information 2.

We categorized as "system" a unique NPs and proteins couple. Therefore, protein solutions that differed in terms of composition (*e.g.* BSA, HSA, IgG, transferrin, hemoglobin, bovine serum, human serum) each generated a different system, even when interacting with a same NP. The same was considered for each NP that presented a different size, surface chemistry, or core material. For example, AuNPs of R = 10 and 50 nm incubated separately in both BSA and transferrin protein solutions would generate 4 unique proteins-NPs systems.

For each system, information such as the NPs size, the incubation medium was extracted from those articles. NPs size is provided as the radius in nm and incubation media are categorized into two distinct groups: single protein solutions (*e.g.* BSA, transferrin, hemoglobin) and mixtures of

proteins (*e.g.* serum, BSA and transferrin, HSA and fibrinogen, plasma). Mono- or multilayer and reversible or irreversible observation were reported only if all criteria were met (see next paragraphs). Data present in the articles have not been subject to reinterpretation or further analyses. Only original interpretations of the authors were used and only accessible evidence was collected to build out dataset.

Definition of mono- and multilayers

A monolayer is defined as a single layer of proteins partially or fully covering the NPs at the saturation of adsorption. Multilayer consequently refers to the adsorption of more than one layer of proteins, but independently of the saturation of the NPs. Reports of mono- or multilayers observations needed to correspond to one of those two different scenarios:

1- In the case that saturation was not reached and that no multilayers was found; the observation was not reported. However, if the saturation was not reached but multilayers was observed, the system was labeled as a multilayer system. If the saturation of adsorption was reached and that only monolayers were observed, then the system was labeled as monolayer.

2- Observation in serum, plasma or other biologically derived fluid were not required to reach saturation if its content were higher than 10% (*e.g.* 10% bovine serum in PBS) because of their physiological relevance. Hence any observations of mono- or multilayers were reported.

Systems where the authors specify that the result could be interpreted as both monolayer and multilayers were not included in the supplementary table. As mentioned, reports where further analysis was needed to extract information were not included as well. However, if the threshold for a monolayer of protein was given and the values of adsorbed proteins were accessible and comparable with the threshold, then the result of mono- or multilayers was included in the supplementary table. Of course, the assessment of surface packing density <1 was also considered as a monolayer and >1 as multilayers, as long as it matched scenario 1 or 2.

Definition of reversibility and irreversibility

Again, authors' interpretations were conserved, but whenever no conclusion was reported regarding the reversibility of adsorption, the protein-NP binding was defined as reversible when either one of the three criteria were met:

1- Adsorbed proteins were capable of desorbing from the NPs following a simple dilution or washing of the free proteins. Complete evaluation of the kinetics was not crucial, but preferred.
2- It was possible to displace adsorbed proteins from the NPs by using another molecule or protein to perturb the initial equilibrium. Complete evaluation of the kinetics was not crucial, but preferred.
3- The desorption constant k_{off} was measured through kinetics experiments and was larger than 10^{-6} s^{-1}.

The adsorption constant k_{on} and desorption constant k_{off} were extracted from articles in which those values were available and were rescaled to make comparison through different systems possible.

Definition of dilution and competition experiments

Categorization of dilution and competition experiments was performed following those 2 definitions.

Dilution: Experiments assessing the reversibility by perturbation of the equilibrium achieved by diluting the NPs-proteins systems or by removing the free proteins through purification steps (*e.g.* centrifugation, chromatographic methods, electrophoresis).

Competition: Experiments assessing the reversibility by perturbation of the equilibrium achieved by introducing a molecule or protein competing for the NPs' surface. This experimental design also includes testing for the Vroman effect, *i.e.* assessing compositional change on the NPs surface over time arising from the competition of different proteins in serum, plasma or a mixture of proteins.

Outliers

The specificity of the Walkey *et al*. study[58] described in section 5.2 resides in the number of systems that were tested for protein adsorption. A total of 105 different AuNPs were analyzed, corresponding to 3 different sizes and 3 major types of coatings (positive, negative and neutral) for a total of 20-40 different types of coatings in total. All those systems were incubated with serum solution and had their protein corona quantified with the BCA assay, all resulting in a monolayer. As the rest of the dataset was constituted of about 300 systems, having 105 systems only coming from one reference would have created an imbalance regarding the importance of other studies, giving 1/4th of the total weight to a single reference. Indeed, the second largest pool of systems from one study was 32 systems, for 2 incubation media (BSA and serum) and 16 different NPs radii[117], a number still far behind Walkey *et al*. study, but with non-repeating types of systems. So, as a compromise and to restore the balance in the statistical analysis, 9 systems were selected to represent the 105 ones: 3 different sizes coupled with 3 representative surface charges (negative, positive, neutral). Since all observations from this study resulted in monolayers, the exact surface coating was expected to have no impact on the result. This simplification should therefore accurately reflect the results of this study without compromising the overall statistical analysis.

Annexe 2

Supplementary Information for "Deciphering in vitro and in vivo the protein corona formation and dynamics by differential dynamic microscopy"

Supplementary note 1: Quantification of fluorescent proteins adsorbed on PS NPs.

Measurement of adsorbed proteins by UV spectroscopy

A calibration curve spanning from C_p^0 = 0.017 to 3.7 µM was used to quantify adsorbed LYZ-RITC on PS NPs. The fluorescence was quantified using a microplate reader (TECAN Spark®) in a 96-well plate. The fluorescence was measured at an excitation wavelength of 545 nm and the emitted fluorescence was measured at 590 nm. Prior to fluorescence measurements, LYZ-RITC incubated with PS NPs were purified following one centrifugation (30 minx x 20000 G). Supernatant was collected and 50 µL mixed with 50 µL HEPES 10 mM then distributed in a 96-well plate for fluorescence measurement.

Supplementary Figure 1

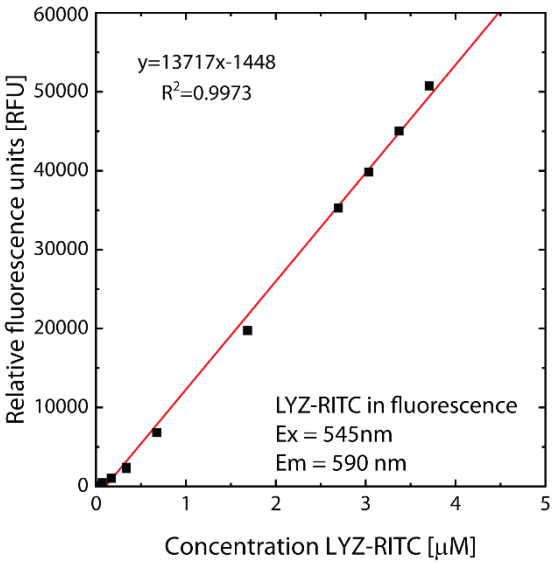

Figure S1. Calibration curve for the quantification of fluorescent LYZ-RITC adsorbed to PS NPs. Error bars are smaller than markers.

Supplementary note 2: Validation of different imaging parameters in fluorescence imaging DDM.

Measurement of particle dynamics by DDM does not depend on the imaging mode

The ISF $f(q,\tau) = \exp(-Dq^2\tau)$, (Eq. 1 of the manuscript) where D is the diffusion coefficient of the NPs was used for the analysis of the DDM data obtained in fluorescence mode imaging, phase contrast and brightfield imaging. In Figure S2A, experimental data are presented for phase contrast and fluorescence imaging of fluorescent particles R_0=110 nm (PSfluo 110 nm), for fluorescence imaging of fluorescent proteins adsorbed on non-fluorescent particles R_0=110 nm (PS 110nm + LYZ-RITC) and fluorescent proteins alone (LYZ-RITC). As can be seen in Figure S2A, the differential image correlation function obtained by DDM is fully described by Eq.1. It is interesting to note that LYZ-RITC alone did not generate a detectable signal due to its high diffusion coefficient and small amplitude signal. Though, the addition of NPs to LYZ-RITC generated a signal whose amplitude was measurable and whose τ-dependence corresponds to the expected NPs dynamics, which is also in agreement with both fluorescence and phase contrast imaging of the PSFluo 110 nm.

The extraction of D from the differential image correlation function for PSfluo in water under different illumination modes serves as a basis to demonstrate the equivalence of the dynamics measured using phase contrast, brightfield and fluorescence. All three illumination modes were tested as a function of concentration of NPs (see Figure S2B). Diffusion coefficients perfectly align around 2.1 µm²/s, illustrating the concentration independence of the measurement up to 1.15 nM of NPs. At 11.5 nM, we observed a massive drop of amplitude caused by strong turbidity of the sample impeding fluorescence signal to measurement and quantification of the diffusion coefficient. Note that the slight increase in diffusion coefficient at 11.5 nM (ϕ ~ 0.03) is likely the mark of rising interparticle interactions. The measured average diffusion coefficient of 2.14 ± 0.06 µm²/s is in good agreement with the theoretical value obtained with the Stokes-Einstein relationship $D = kT/6\pi\eta r_H$ with kT being the thermal energy, η the medium viscosity and r_H the hydrodynamic radius of the NPs being 110 nm, (D = 2.06 µm²/s). Therefore, we can assume that

the measured diffusion coefficient is accurate independently of the illumination mode, in agreement with previous reports[96-98, 100].

Using the same recorded videos that were used in Figure S2B, we can also extract the amplitude signal $A(q)$ as a function of concentration as demonstrated in Figure S2C, where $A(q) \sim C_{NP}$. To better validate experimentally this relation, it is represented as a ratio of two amplitude signals, A_{ratio}, as a function of NPs concentration. As presented in the main text, the red line is a prediction based on the lowest concentrations of NPs which follows perfectly fluorescence experimental data. However, in the case of phase contrast and bright field imaging modes, the sample turbidity massively hinders the light transmission at high NPs concentrations, reducing drastically the amplitude signal.

Effect of ROI and binning on the signal amplitude A(q)

The DDM signal amplitude given in Eq. 2 shows that $A(q) \sim C^0_{NP} I_0^2$ with C^0_{NP} being the number of diffusing objects per unit volume, or in our case, the volume of the voxel. Therefore, $A(q)$ should not depend on the region of interest (ROI), or the volume of observation. Figure S2D shows that $A(q)$ is indeed constant, independently of the ROI. In the case where a binning is applied on an already acquired video, $A(q)$ increases due to the increase of the corresponding voxel. The resulting effective concentration is then $C^0_{NP} \sim C_{NP}/S_{px}$, where S_{px} is the binning of the pixel (1x1=1, 2x2=4, 4x4=16) and C_{NP} is the NPs concentration. By combining these equations, we can normalize the values of $A(q)$ from binned videos using the expression $C_{NP} = A(q)\, S_{px}/ I_0^2$ as demonstrated in the inset of Figure S2E.

Relationship between B(q) and the total average intensity ⟨I⟩

The dependence of the noise term $B(q)$ (arising from the camera) on the total average intensity of the image is shown in Figure S2F. The term $B(q)$ is only dependent (in these conditions) on the total intensity $\langle I \rangle$ recorded by the camera. The relationship between these two terms is linear over almost 4 orders of magnitudes, independently of the illumination mode (fluorescence, phase contrast and bright field). Moreover, as presented in the inset of Figure S2F, dividing $B(q)$ by the total intensity of the image (background subtracted) yielded a constant value $B(q)/\langle I \rangle = 3.97 \pm 0.03$, also independent on the total intensity recorded by the camera. Given the variety of optical

setups and the range of intensities used, it is fair to assume for those conditions that $B(q) \sim \langle I \rangle$ for such DDM experiment.

This linear relationship was expected considering that, in the real space, the error (or noise) associated to the statistical distribution of photon counting typically follows a Poisson distribution. As a result, the random fluctuations of light in a DDM experiment converge to the square root of its mean value (with large enough sampling). Bayles *et* al. derived the noise term in DDM in the Fourier space to be $B(q) = \langle |\Delta I_B(q, \Delta t)|^2 \rangle$, where ΔI_B is the spontaneous (time-independent) background fluctuation[101]. Therefore, assuming that the noise follows a Poisson distribution, the following relationship can be derived $\Delta I_B(q, \Delta t) = \langle I \rangle^{1/2}$ which leads to the linear relationship between $B(q)$ and $\langle I \rangle$, $B(q) = \gamma \langle I \rangle$, where γ is a scaling factor that is related to the camera sensitivity (*e.g.* the camera's quantum efficiency).

Supplementary Figure 2

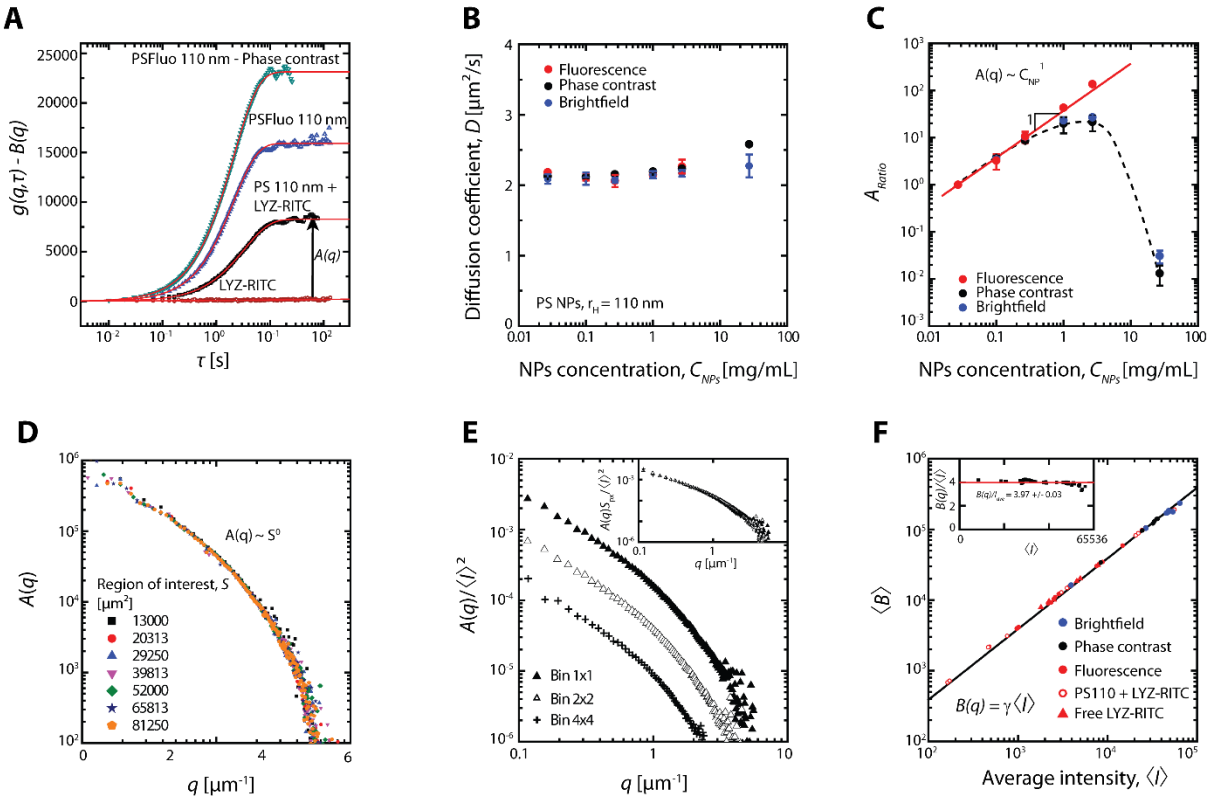

Figure S2. Impact of imaging parameters on the measurement of the dynamics and amplitude function A(q). (A) Differential intensity correlation functions g(q,τ) with subtracted background B(q) of fluorescent PS NPs (PSFluo 110 nm) in phase contrast and fluorescence imaging mode, and of fluorescent lysozyme-RITC with and without non fluorescent PS NPs (PS 110 nm) under fluorescence imaging. (B) Diffusion coefficient of PSFluo 110 nm under fluorescence, phase contrast and brightfield imaging from highly turbid samples (C_{NP} = 11.5 nM) to very dilute samples (C_{NP} = 11.5 pM). (C) Comparison of the linear relationship between A(q) and C_{NP} in different imaging modes. (D) Effect of the size of the ROI on A(q) (E) Effect of video binning on A(q). The resulting A(q) can be normalized by multiplying the amplitude with the factor $\frac{S_{px}}{\langle I \rangle^2}$. (F) Demonstration of the linear relationship between the noise term B(q) and the average intensity of the video $\langle I \rangle^2$ that is conserved through different imaging modes and different imaged objects.

Supplementary note 3: Quantification of the fractal dimension

DDM can reliably measure the fractal dimension d_f of aggregates from the structure factor $S(q)$ contained in the amplitude function $A(q)$, using the Fisher-Burford model. We validated our measurement by comparing DDM results with the ones obtained by turbidity and kinetics methods using different proteins-NPs systems and concentrations.

The Fisher-Burford expression is used to model $S(q)$ at low q and extract d_f and $A_{ratio}(q=0)$ along with the radius of gyration R_G. In Fig. S3A, fittings of the Fisher-Burford expression are shown for different aggregating conditions of PS NPs in presence of LYZ-RITC or serum-RITC. With PS NPs of r_H=110 nm, two systems were studied, with LYZ-RITC (C_{NP}=42.5 pM, C_P^0=0.27 µM) and with serum-RITC (C_{NP}=425 pM, C_P^0=0.26 µM). For NPs of r_H=30 nm, only LYZ-RITC was tested (C_{NP}=2000 pM, C_P^0=1.07 µM).

Turbidity-based determination of the fractal dimension is based on the measurement of scattered light as a function of the wavelength. In the case of non-aggregating NPs, the scattered light (measured as an "absorbance") is expected to follow ~ λ^{-4} based on Rayleigh scattering[328]. Upon aggregation, the scattered light is expected to follow ~ $\lambda^{-(4-df)}$. Due to optical effects of the NPs and its material, the effective exponent from the unaggregated NPs, x_{NP}, is measured and the fractal dimension is expressed as $d_f = x_{NP} - x_{agg}$, where x is the exponent of the power-law behavior of the absorbance as a function of λ [328]. Here, we demonstrate that the value of the fractal dimension obtained by DDM is comparable to the fractal dimension obtained by turbidity measurements for different systems and different fractal aggregates. Turbidity experiments were performed at the same concentration as DDM experiments.

We also extracted the fractal dimension from DDM kinetic experiments[328] as another validation. In short, the kinetics of NPs' radius growth is known to grow as $R_G \sim t^{1/d_f}$ in the case of a diffusion-limited aggregation. In DDM the hydrodynamic radius, R_H, which can be approximated here as R_G, is obtained from the measurement of the diffusion coefficient. Then, by monitoring the increase of R_H as a function of time, it is possible to estimate the fractal dimension. As shown in Fig. S3C, by fitting a power-law to the data, we obtain d_f = 1.47±0.08 in very good agreement with 1.46±0.12 obtained from the average of the Fisher-Burford fits presented in Fig. 2Bii.

Supplementary Figure 3

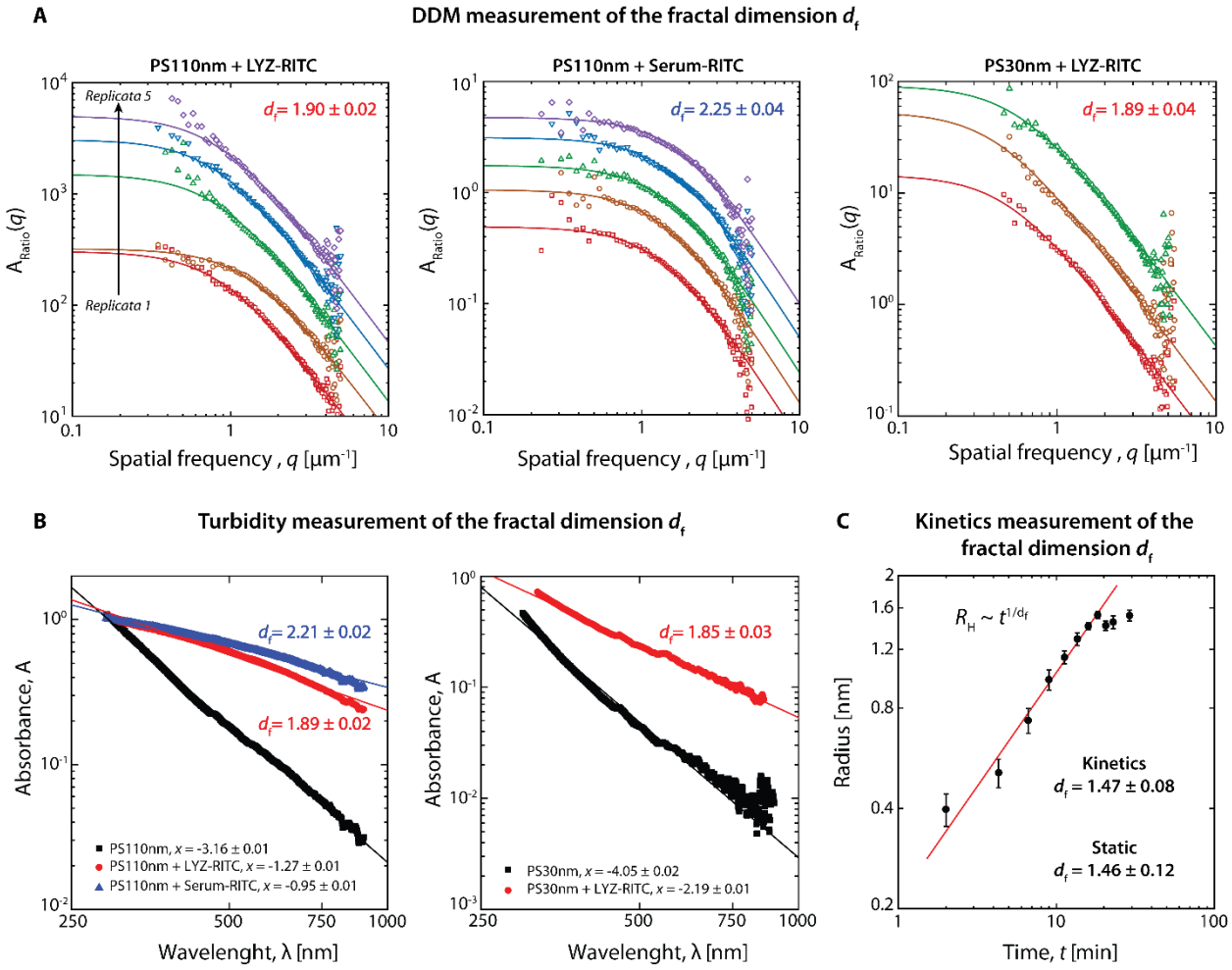

Figure S3. Validation of the determination of the fractal dimension by DDM (A), turbidity (B) and aggregation kinetics (C) measurements. Replicates from 1 to 5 in DDM have been separated by a x2 multiplicative factor (red=1, orange=2, green=4, blue=8 and purple=16). Full lines are global fits to the Fisher-Burford expression in DDM. Full lines are fits to a simple power law for turbidity experiments $A=a\lambda^x$, with a being a fitting parameter. The evolution of the radius was also fit to a simple power law.

Supplementary note 4: Lysozyme adsorption kinetics

Supplementary Figure 4

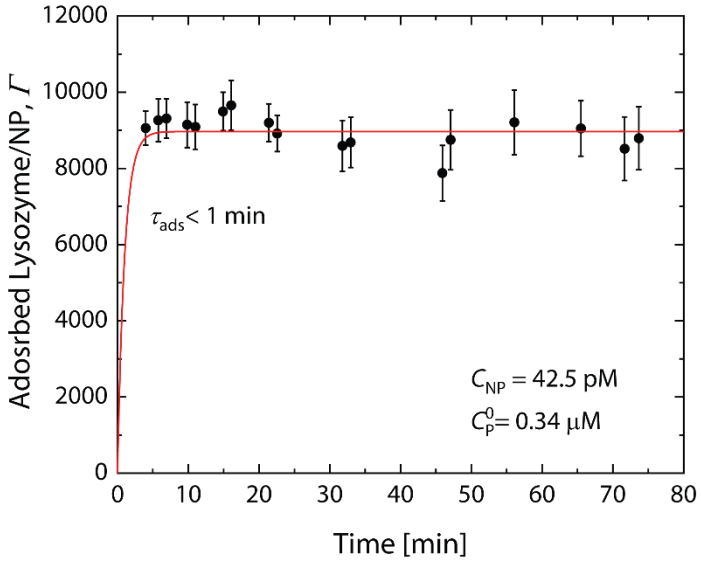

Figure S4. Kinetics of the adsorption of 0.34 μM of lysozyme on 42.5 pM NPs. The full line is an exponential decay of the form $\Gamma=9000(1-\exp(-t/\tau_{ads}))$ with $\tau_{ads}=1$ min, demonstrating that the lysozyme adsorption kinetics is at least faster than the minute timescale.

Supplementary note 5: Fluorescence intensity of labelled proteins and linearity range

The linearity range of the fluorescence signal vs C_p^0 was measured on the microscope used to perform DDM measurements. The fluorescent proteins were injected at different concentrations in a 400 µm thick glass capillary and the focal position was selected 100 µm below the top wall of the capillary. Short video sequences (200 images) were recorded at different framerates (30 or 100 fps). Fluorescence intensity was normalized (multiplied) based on the framerate of the recorded video (normalizing factor: 30fps = 1 ; 100fps = 10/3) and background from a blank capillary was subtracted. A linear regression was fitted over the data and the quenching regime was determined when the experimental intensities were diverging significantly (~20%) below the linear regression (see Figure S5).

Supplementary Figure S5

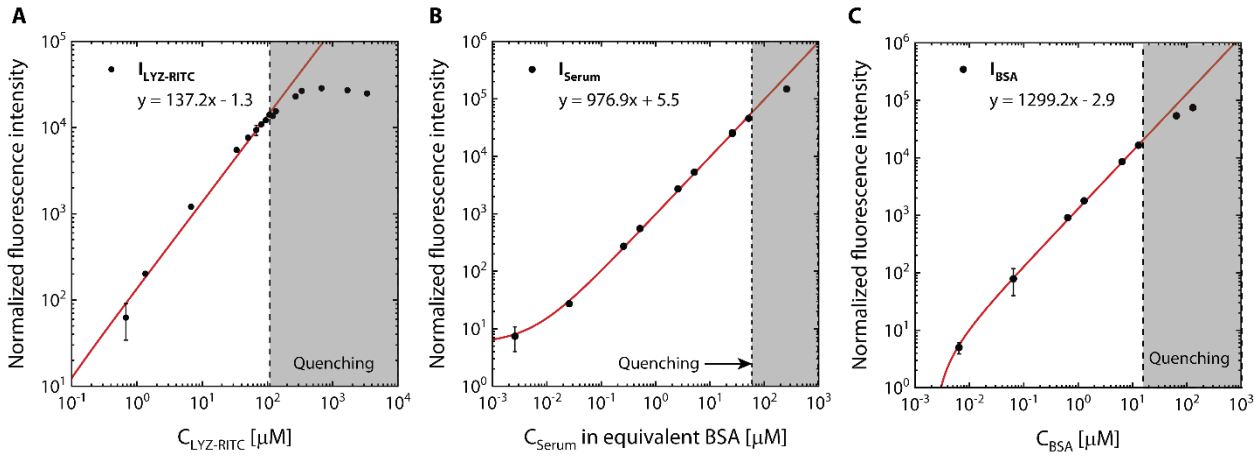

Figure S5. Fluorescence linearity of (A) LYZ-RITC, (B) Serum-RITC and (C) BSA-RITC and their quenching regime obtained by fluorescence microscopy.

Supplementary note 6: Adsorption isotherms

The reconstruction of the adsorption isotherm is valid for both calibration methods described in the main text. The process is performed in three steps. The first step consists in extracting the term $A_{ratio} = A(q, C_p^0) / A(q)^{ES}$ and applying a square root over the resulting value. The second step consists in normalizing the data by a reference intensity in order to eliminate the effect of frame rate. The third step is performed if the NPs are aggregating. Then a renormalization of the signal is necessary using the calculation of the number of NPs per aggregate $N = \left(\frac{R_N}{R_0}\right)^{d_f}$ as described in the main text. Figure S6 shows how the measured signal evolves after each step before reaching the final adsorption isotherm. As can be seen a strong increase of the adsorbed protein amount was observed at high $C_{LYZ\text{-}RITC}$, which coincides with the quenching regime found in Fig. S5. These data illustrate clearly how quenching can lead to an overestimate of the adsorbed protein amount if not appropriately characterized.

Supplementary Figure S6

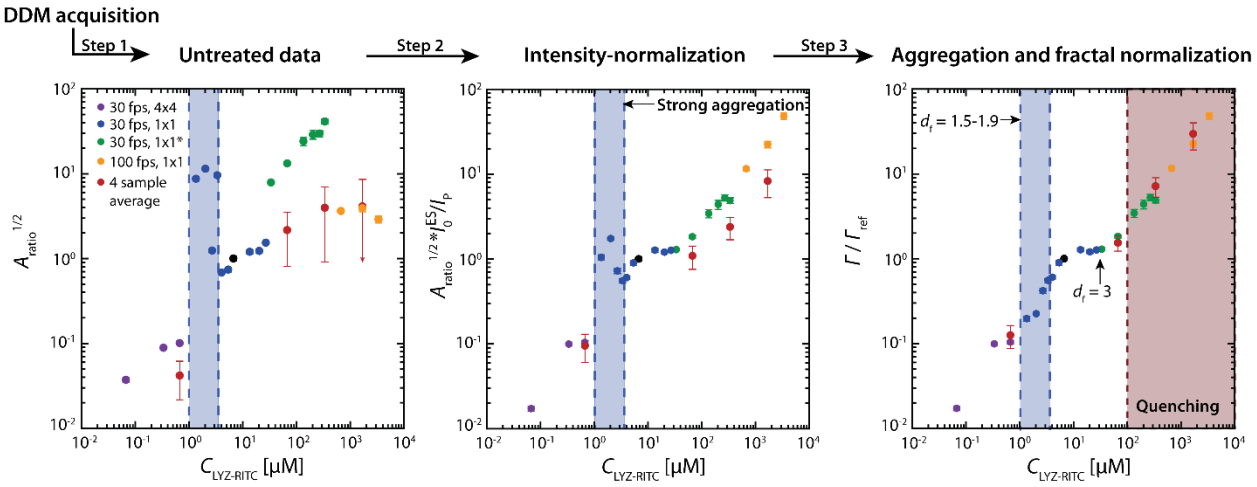

Figure S6. Illustration of the normalization of DDM adsorption data, from the measurement of A_{ratio}, to the intensity normalization and aggregation and fractal dimension normalization. The aggregation zone determined here is the same as on Figure 2A in the main text and the quenching zone shown here is based on the fluorescence linearity in Figure S5.

Supplementary note 7: Fisher-Burford fits for LYZ, Serum, BSA

Measurements of the fractal dimension were performed whenever aggregation was observed and was strong enough to generate large and homogeneous aggregates (clusters visible on the videos). The experimental data provided here are the result of 5 measurements on each sample, each measurement probing a different area of the aggregated suspension. The average fractal dimension of NPs in presence of LYZ-RITC or Serum-RITC indicates that the cluster structure is more compact than in presence of BSA.

Supplementary Figure 7

(see figure on next page)

Figure S7. Fractal dimension analysis of the aggregation peak for (A) LYZ-RITC, (B) Serum-RITC and (C) BSA-RITC. Replicates from 1 to 5 have been separated by a x2 multiplicative factor each (red=1, orange=2, green=4, blue=8 and purple=16). (D) Summary of the extracted d_f for each investigated proteins-NPs couples averaged for all measurable concentrations. The last concentration for BSA (C_{NP} = 425 pM & C_P= 0.0321 µM) has not been taken into the average as it is one example of an aggregate slightly too small and heterogeneous to accurately measure the fractal dimension on this range of concentrations (corresponds to the lighter gray area on Fig. 3B in the manuscript).

A DDM measurement of the fractal dimension d_f in LYZ-RITC

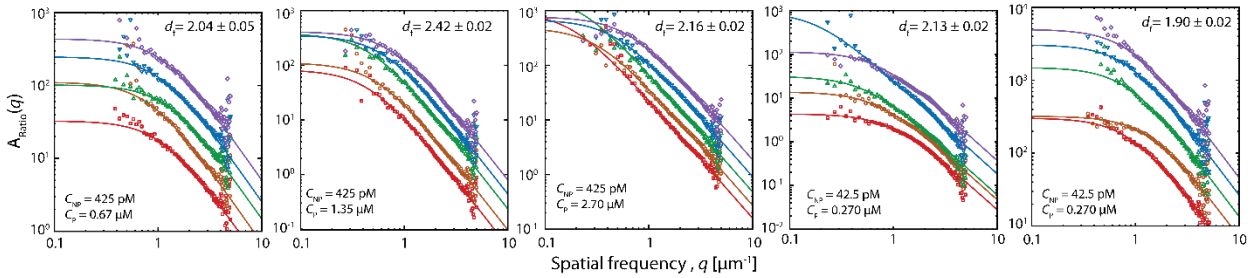

B DDM measurement of the fractal dimension d_f in serum-RITC

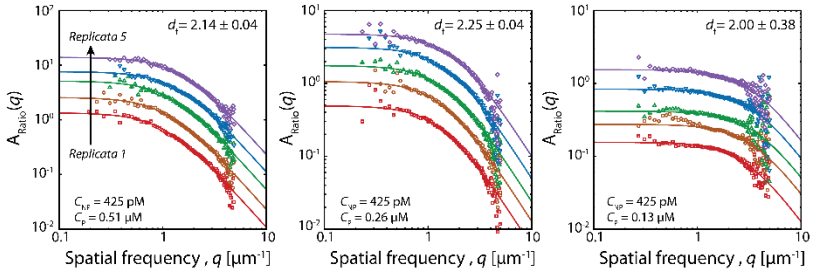

C DDM measurement of the fractal dimension d_f in BSA-RITC

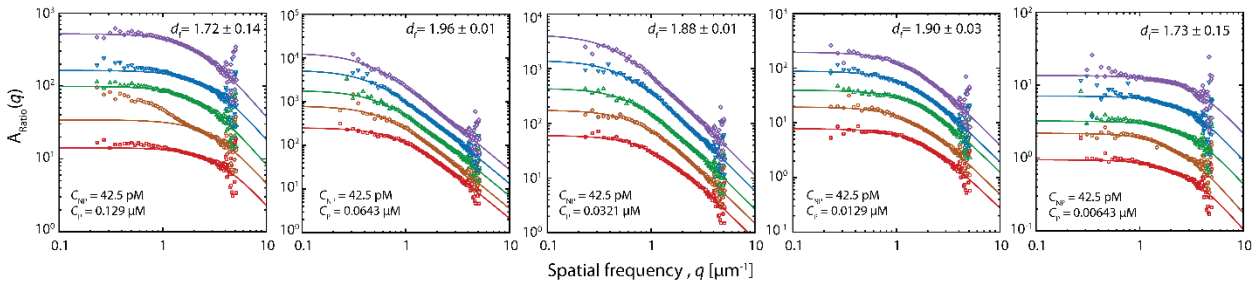

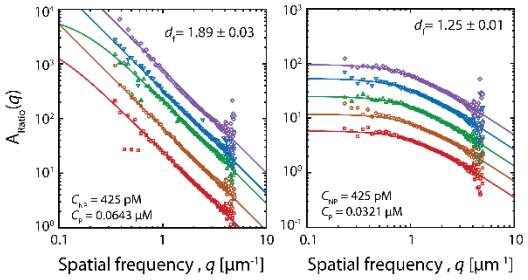

D

Summary of the fractal dimension analysis

Incubated protein	Average fractal dimension, d_f
Lysozyme-RITC[1]	2.13 ± 0.19
Serum-RITC	2.13 ± 0.13
BSA-RITC	1.85 ± 0.10
Lysozyme-RITC[2]	1.61 ± 0.19

1- Incubated with PS NPs (r_h=100 nm) for asorption isotherm experiments
2- Incubated with PS NPs (r_h=110 nm) for adsorption validation experiments

Supplementary note 8: Accumulation of NPs in the zebrafish caudal veinous plexus (CVP)

Supplementary Figure S8

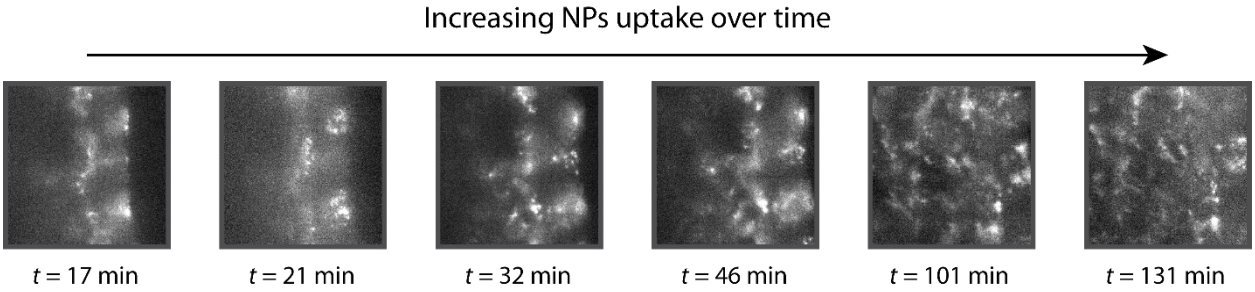

Figure S8. Evidence for NPs accumulation within the time frame of the kinetic experiment (~2 hours). Notice that some drift between videos in this specific case has occurred. The immobilization rate of NPs was found highly variable across individuals and may depend on many other factors (*e.g.* location, blood flow, time after fertilization).

Supplementary note 9: *In vivo* protein exchange kinetics and its fitting parameters

Supplementary Figure S9

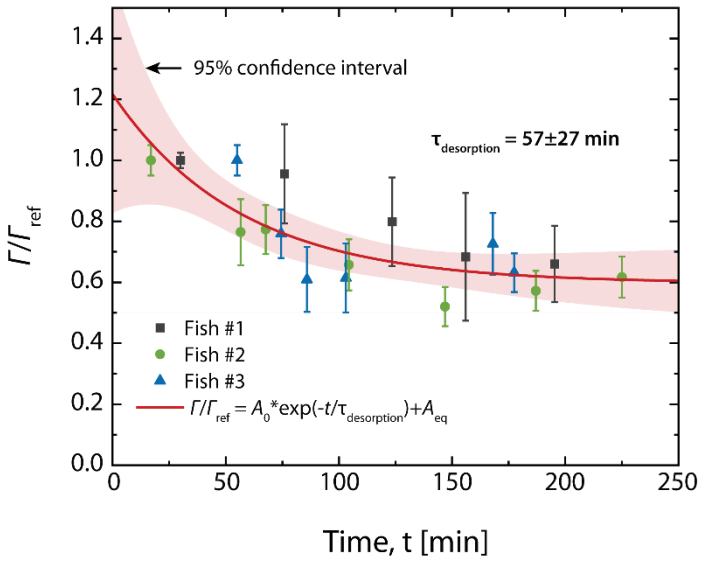

Figure S9. Complete set of data points for the in vivo desorption kinetics presented in Figure 4D of the main text and the global fitting parameters. The light red area corresponds to the 95% confidence interval of the non-linear regression.

Annexe 3

Supplementary Information for "Spontaneous Shrinking of Soft Nanoparticles Boosts their Diffusion in Confined Media"

Supplementary Figures

(See figure on next page)

Supplementary Figure 1. Intermediate scattering function, f(q,τ), extracted from DDM autocorrelation functions, g(q,τ), plotted as a function of q²-scaled time (q²τ) for different particles (A-L) and agarose concentrations present in the main text figure 1, 2 and 3. Each agarose concentration, notably, 0 w/v% (circles), 0.05 w/v% (upward triangles), 0.1 w/v % (squares), 0.25 w/v% (diamonds), 0.5 w/v% (downward triangles) and 1 w/v% (crosses) are presented and fitted according to the generalized exponential $f(q,\tau) = e^{-(\tau/\tau_R)^{\beta}}$. Some ISFs had a second relaxation mode and the ISFs were corrected using Eq. 11 for which the second relaxation process was occurring between τ_{R2} ≈ 10 - 200 s with β_2 ≈ 0.6-2.5. This very slow process was found consistent to a small drift of the sample observed in those few videos. Samples that were affected by the thermal drift were: agarose 0.05% (AuNPs 38 nm, AuNPs 22 nm, µGel 150 nm, µGel 50 nm, µGel 45 nm), agarose 0.1% (µGel 50 nm), agarose 0.25% (AuNPs 58 nm, µGel40) agarose 0.5% (µGel 50 nm, µGel 45 nm, µGel 25 nm), agarose 1% (µGel 25 nm). The presented ISFs here are only representative examples of approximately 60 000 to 100 000 generated ISF in DDM in this study.

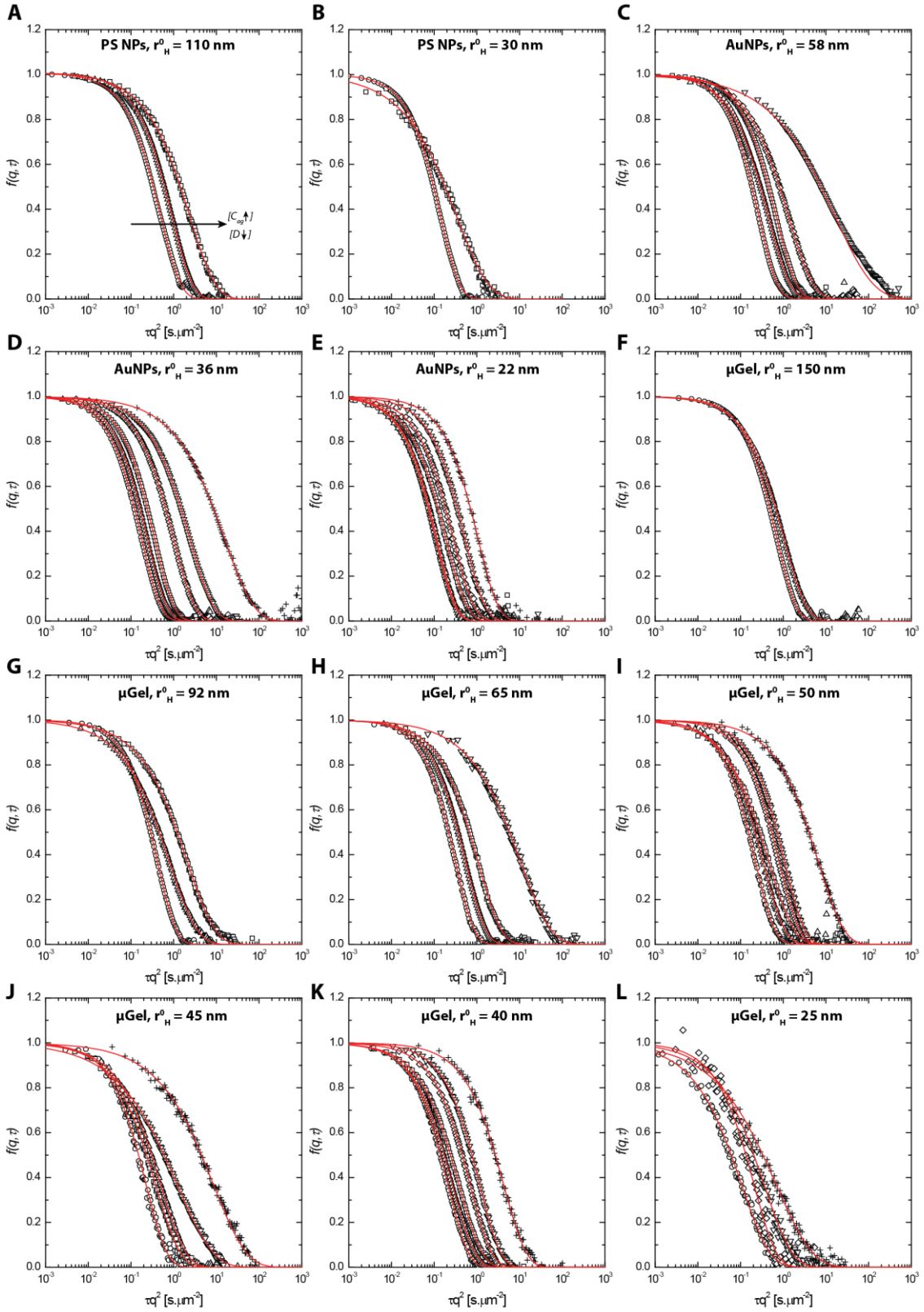
A
PS NPs, r⁰H = 110 nm
[Cagt]
[D]
B
PS NPs, r⁰H = 30 nm
C
AuNPs, r⁰H = 58 nm
D
AuNPs, r⁰H = 36 nm
E
AuNPs, r⁰H = 22 nm
F
µGel, r⁰H = 150 nm
G
µGel, r⁰H = 92 nm
H
µGel, r⁰H = 65 nm
I
µGel, r⁰H = 50 nm
J
µGel, r⁰H = 45 nm
K
µGel, r⁰H = 40 nm
L
µGel, r⁰H = 25 nm
f(q, τ)
τq² [s.µm⁻²]

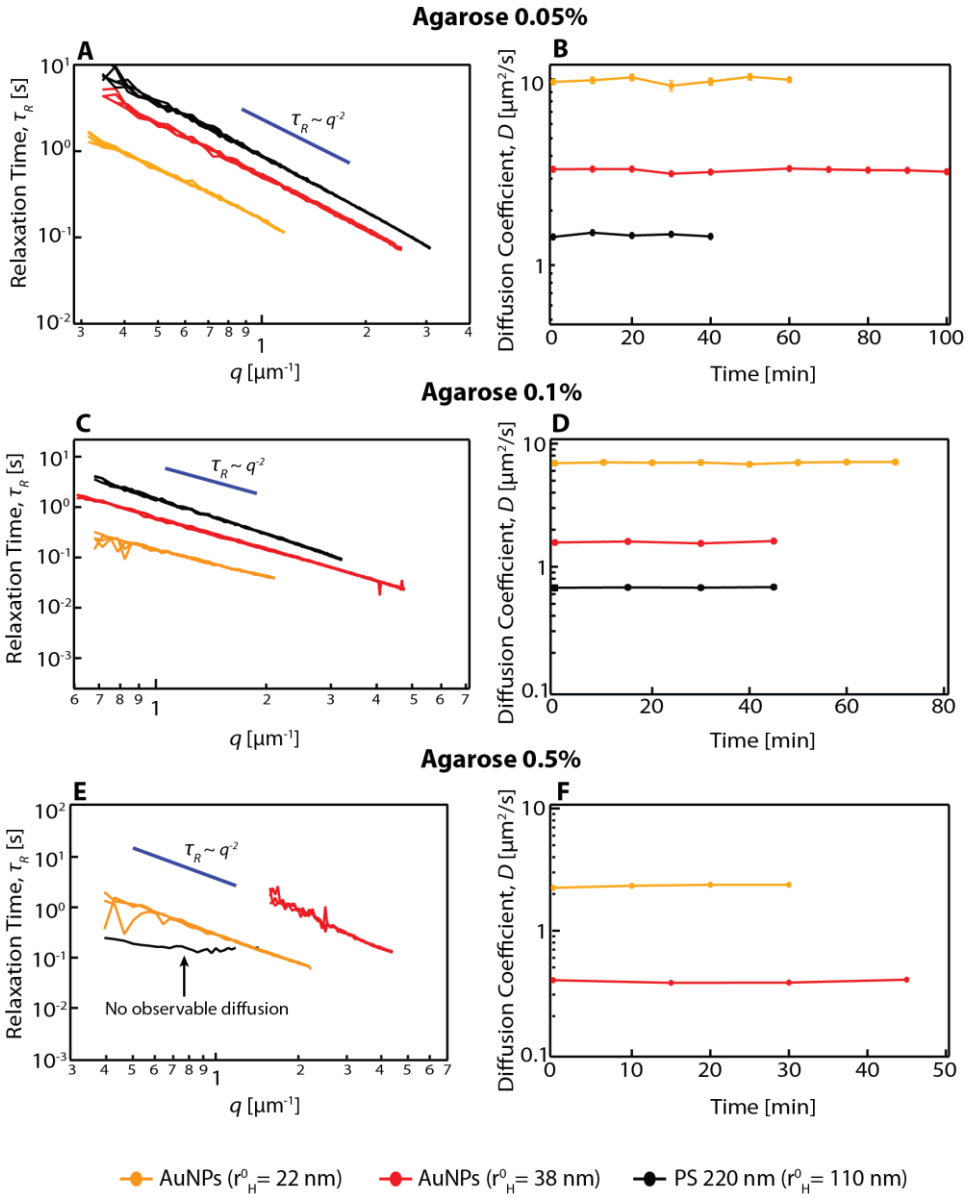

Supplementary Figure 2. DDM measurements of τ_R for hard NPs in agarose gel. (A, C, E and G) Relaxation time expressed as a function of q in agarose. The dynamics of NPs in solution is compared to the expected diffusion behavior $D= \tau_R(q)^{-1}q^{-2}$ (C). (B, D, F) Measurement of the diffusion coefficient of hard NPs 16h after gelation of the agarose gel.

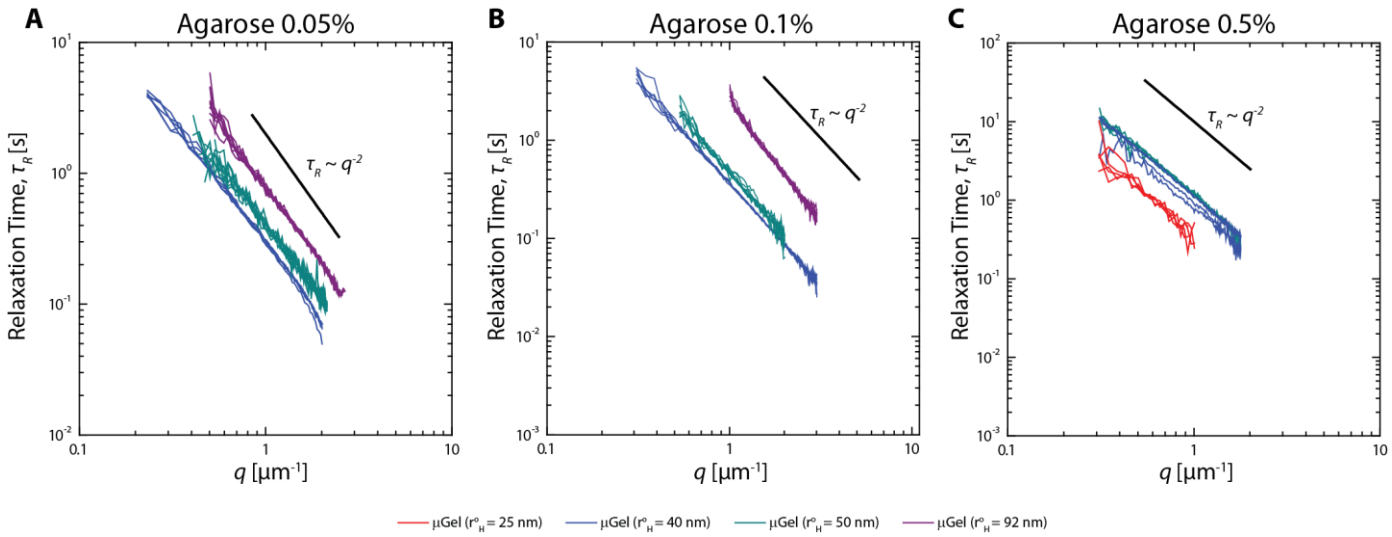

Supplementary Figure 3. DDM measurements of τ_R for soft NPs in agarose gels: A) Cag = 0.05%, B) Cag = 0.1% and C) Cag = 0.5% w/w. Large soft NPs (r^0_H = 92 nm) were not diffusing in agarose at C_{ag} > 0.5%, and were not shown in panel C but were replaced by small soft NPs (r^0_H = 25 nm). Lines in red, blue, teal and purple are NPs with r^0_H = 25, 40, 50 and 92 nm respectively.

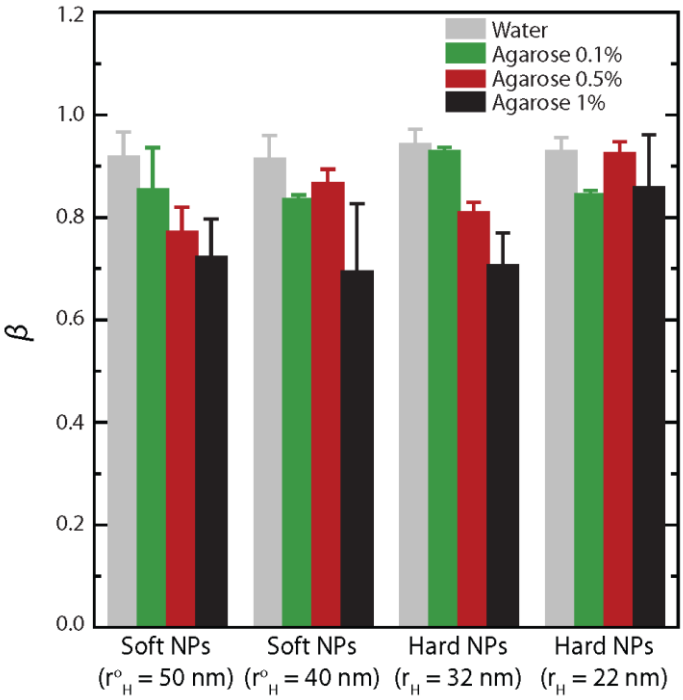

Supplementary Figure 4. Stretch exponent of the ISF for hard and soft NPs in water (gray), agarose Cag = 0.1% (green), 0.5 % (red) and 1 % (black).

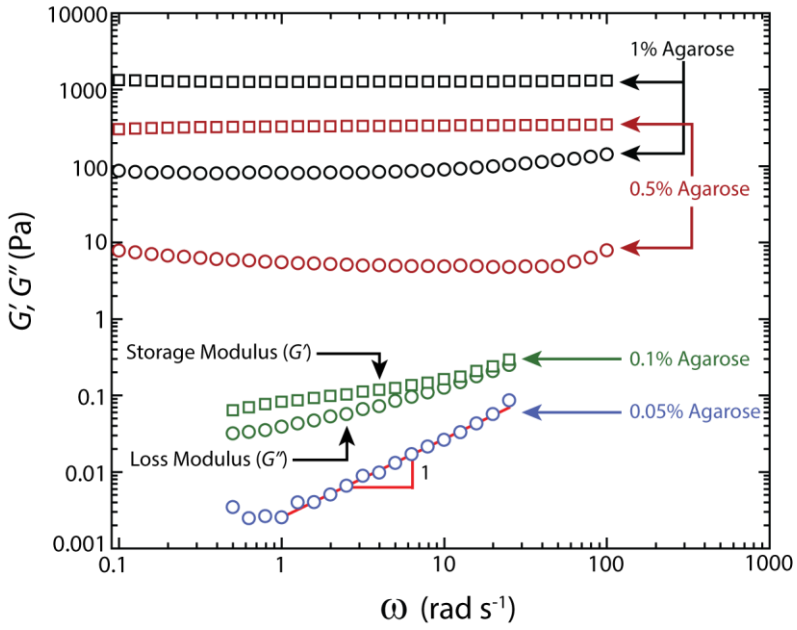

Supplementary Figure 5. Representation of the rheological properties of the agarose solutions and gels in pure water at ambient temperature (T≈22oC). Squares represent the storage modulus (G') and circles represent the loss modulus (G") for each agarose concentrations. Storage modulus data for 0.05% agarose was not shown in this graph because the values were below instruments detection limit.

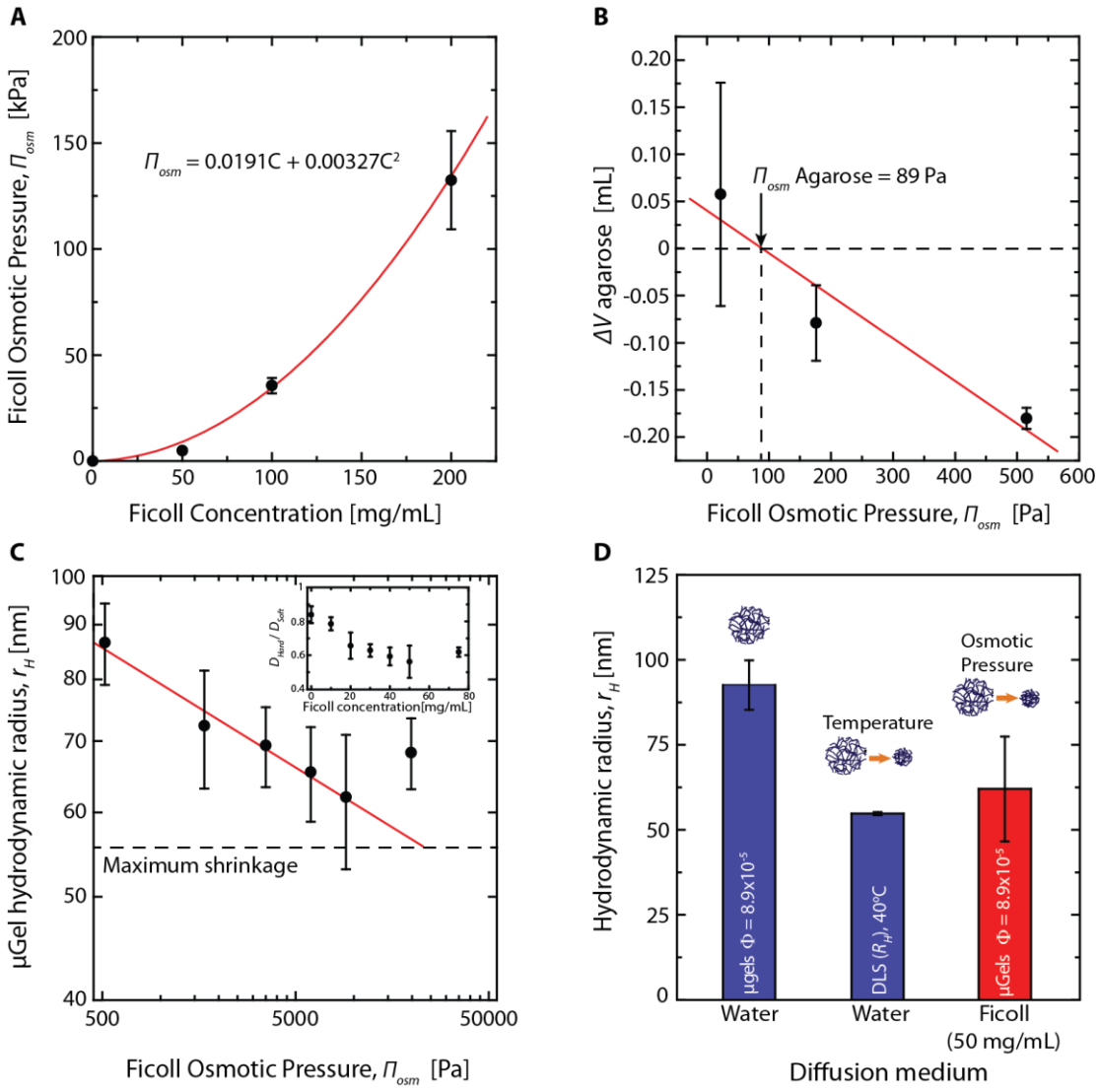

Supplementary Figure 6. Osmotic pressure of agarose gels and the effect of osmotic pressure exerted by Ficoll on soft NPs. (A) Osmotic pressure of Ficoll solutions of different concentrations. (B) Volume change of agarose gel (C_{ag} = 1% w/w) at equilibrium (or 7 days) at different Ficoll osmotic pressure. Red line is a linear fit: $\Delta V = 0.0403 - 0.00045\ \Pi_{osm}$ (C) Shrinkage of microgels with concentration of Ficoll osmotic pressure and in inset, the ratio of the coefficient of diffusion of hard and soft NPs for the different Ficoll concentrations. The red line corresponds to the power law fit: $r_H = 342\ \Pi_{osm}^{-1/9}$ (D) Comparison of different stimuli triggering shrinking of the microgels.

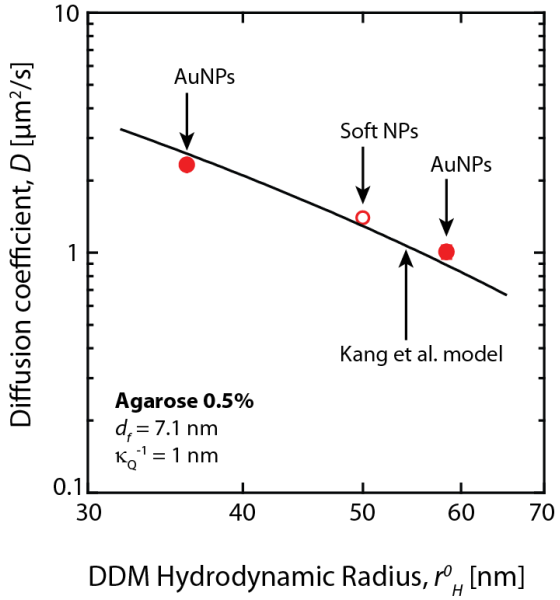

Supplementary Figure 7. Diffusion coefficient of hard and soft nanoparticles in agarose 0.5 % w/w in presence of 10^{-1} M NaCl. The line is the theoretical prediction of Kang et al. (Eq. 4) using r^0_H as the particle radius.

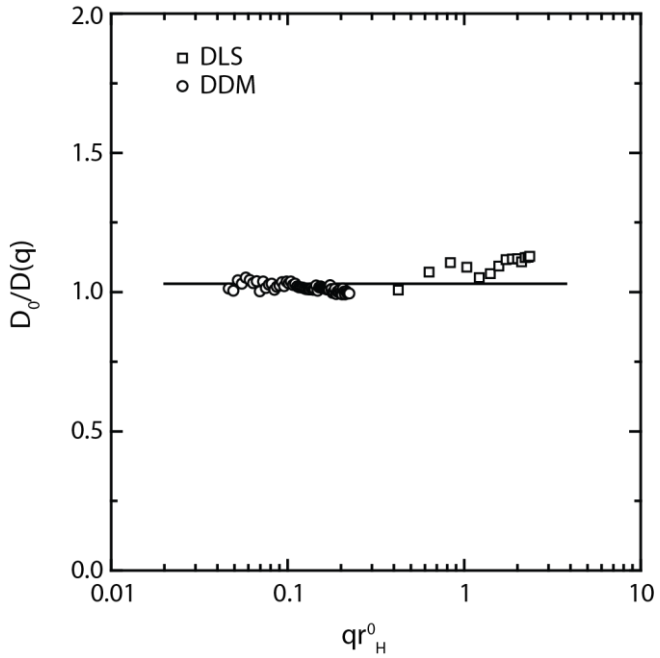

Supplementary Figure 8. Probing the structure factor of microgels by DDM and DLS. Dependence of the dynamics $D_0/D(q)$ for r^0_H = 92 nm microgel at $\phi = 0.03\%$ measured by DDM (circles from 0.04 – 0.25 qr_H^0) and DLS (squares from 0.4 – 3 qr_H^0). Here, q is normalized by the dilute radius r^0_H of the particle and the peak structure factor would be expected to be located at $qr^0_H \approx 1$ which does not appear in this graph.

Supplementary Tables

Supplementary Table 1. Hydrodynamic radius by DDM and DLS and Zeta potential of hard and soft NPs measured by DLS at a 4 mM NaCl concentration

Type of NP	DDM, r^0_H (nm)*	DLS, R^0_H (nm)*	DDM, PdI	DLS, PdI	ZP at 22°C (mV)	ZP at 38°C (mV)
μGel r^o_H = 140 nm	146 ± 2	152 ± 1	0.01	0.07	N/A	N/A
μGel r^o_H = 92 nm	97.0 ± 0.3	103 ± 1	0.03	0.02	-1.6 ± 0.3	-11.8 ± 1.8
μGel r^o_H = 65 nm	74.0 ± 0.5	80.2 ± 0.6	0.04	0.08	-2.7 ± 1.1	-9.0 ± 2.9
μGel r^o_H = 50 nm	46.5 ± 1.1	54.3 ± 0.2	0.16	0.14	-1.3 ± 0.2	-7.2 ± 2.9
μGel r^o_H = 45 nm	43.3 ± 0.9	39.5 ± 0.3	0.18	0.25	-1.4 ± 0.2	-8.4 ± 1.6
μGel r^o_H = 40 nm	40.8 ± 0.7	41.2 ± 0.2	0.13	0.22	-3.1 ± 0.6	-7.6 ± 1.7
μGel r^o_H = 25 nm	23.5 ± 2.4	23.9 ± 0.6	0.26	0.25	N/A	N/A
AuNPs r^o_H = 22 nm	22.8 ± 0.1	22.3 ± 0.1	0.12	0.11	-6.5 ± 1.2	N/A
AuNPs r^o_H = 36 nm	39.5 ± 1.5	40.7 ± 0.3	0.15	0.12	-7.1 ± 1.0	N/A
AuNPs r^o_H = 58 nm	60.7 ± 0.2	63.0 ± 1.3	0.05	0.02	-7.7 ± 0.1	N/A
PS r^o_H = 110 nm	114 ± 1	113 ± 1	0.13	0.02	N/A	N/A
PS r^o_H = 30 nm	32.9 ± 0.1	34.6 ± 0.4	0.02	0.02	N/A	N/A

* Hydrodynamic radius calculated using cumulant analysis as shown in Fig. 1D.

Supplementary Table 2. Conductivity, salt concentration and electrostatic screening length for soft NPs

Medium	**Conductivity** (mS/cm)	**[NaCl]** (M)	κ_Q^{-1} (nm)
MilliQ® water	0.001	8.0 x 10^{-6}	107.9
$r_H^0 = 92.5\ nm$	0.025	2.0 x 10^{-4}	21.6
$r_H^0 = 70\ nm$	0.01	8.0 x 10^{-5}	34.1
$r_H^0 = 50\ nm$	0.008	6.4 x 10^{-6}	38.2
$r_H^0 = 45\ nm$	0.013	1.0 x 10^{-4}	29.9
$r_H^0 = 40\ nm$	0.017	1.4 x 10^{-4}	26.2
$r_H^0 = 25\ nm$	0.027	2.2 x 10^{-4}	20.8

Supplementary Table 3. Structural parameters obtained from Supplementary Equation (5) and DDM measurements

C_{ag} **w/w%**	**Mesh size** ξ **(nm)**
1	116
0.5	220
0.25	311
0.1	491
0.05	695

Supplementary Methods 1 - Rheological measurements

The rheological properties of the agarose hydrogels were measured under oscillatory shear using ARES-G2 rheometer (TA Instruments, U.S.A.). An appropriate amount of agarose was completely dissolved in 100oC MilliQ water. The sample was then injected and sandwiched between parallel plates equipped with a Peltier device for temperature control. The temperature was set at 22oC and evaporation was minimized using a solvent trap provided by the manufacturer. Gelation dynamics were monitored by measuring the storage and loss moduli over time at an angular frequency of 10 rad s-1 and strain amplitudes of 1, 2, 50 and 50 % for 1, 0.5, 0.1 and 0.05 % agarose samples, respectively. The strain amplitudes were verified to be at the linear viscoelastic regime.

Supplementary Methods 2 - Osmotic pressure in Ficoll solution

Osmotic pressure of Ficoll suspension (0, 50, 100 and 200 mg/mL) was measured with freezing depression point osmometer (μOsmette, Precision Systems). Measurements were performed 6 times consecutively with multiple 50 μL aliquots.

Osmotic pressure of agarose was determined by incubating agarose gels (1% w/v) in Ficoll solutions with various concentration / osmotic pressure. Agarose gels were covered with a dialysis membrane of 15 kDa molecular weight to create the pressure on the gels. Agarose was periodically weighted on an analytical balance to screen water gain / loss. The osmotic pressure was determined at the Ficoll concentration at which the volume of agarose does not change, hence the applied external osmotic pressure Π_{ext}, is in equilibrium with the internal osmotic pressure of the agarose.

mechanical properties were at the steady state, a frequency sweep test was performed at the appropriate strains for each sample, following by a strain sweep test at 10 rad s^{-1} frequency.

Supplementary Methods 3 - Structure factor of soft NPs suspension at $\varphi = 0.03\%$

The structure factor of microgels was measured using the DeGennes narrowing method. Diffusion was measured with DDM and DLS at different q values and normalized with D_0 in the dilute regime ($\phi \rightarrow 0$), so that $\tau_R(q,\phi)/\tau_R(q,\phi \rightarrow 0) \sim D_0/D(q) \sim S(q)$ allow to access for the structure factor $S(q)$. Using microgels r_H^0 = 92 nm, we get $S(q) \approx 1$ which is invariant over the studied q range.

DLS data were obtained with an ALV instrument (CGS-3 goniometer and LSE-5004 correlator) as a function of the scattering angle, using a 633 nm laser, to confirm that the increase in diffusion coefficients (interpreted as particle shrinkage in Fig. 2) is not due to a structural effect. Experiments were performed for soft microgels with r^0_H = 92 nm as a function of the concentration (ϕ = [0.009, 3.26%]). The intermediate scattering functions were extracted from measurements of the intensity autocorrelation function[437] at fourteen angles between 20° and 150°. The ISFs were fitted assuming a generalised exponential $f(q,\tau) = e^{-\left(\frac{\tau}{\tau_R}\right)^{\beta}}$. The exponent β was found to be close to 1.

Supplementary Methods 4 - Volume fraction determination of NP suspensions

PS (hard NPs) were compared to microgels (soft NPs) at similar volume fractions. Because microgels can swell or shrink, calculations of ϕ was different for microgels and hard NPs. For hard NPs, we used the following equation to describe ϕ:

$$\phi_{Hard\ NPs} = \frac{w_i \rho_{solv}}{w_i \rho_{solv} + (1 - w_i)\rho_{NP}} \quad (1)$$

And for microgels, we used the approximation provided by Scotti *et al.* as it is valid for low solid volume fractions [402] :

$$\phi_{\mu Gel} = w_i \frac{\rho_{solv}}{\rho_{\mu Gel}} \left(\frac{R_{swollen}}{R_{collapsed}}\right)^3, \quad (2)$$

Where w_i is the mass fraction of the NP, ρ_{solv} is the density of the solvent, ρ_{NP} or $\rho_{\mu Gel}$ is the density of microgels. For microgels, the term $\left(\frac{R_{swollen}}{R_{collapsed}}\right)^3$ is added to consider the swelling of microgels. $R_{swollen}$ is the radius of the swollen microgel and $R_{collapsed}$ is the radius of the microgel shrunk with temperature as measured by DLS.

Supplementary Notes 1 - Examples of DDM measurements in agarose gel.

Intermediate scattering function (ISF), $f(q,\tau)$, shows the dynamics of the particles and can be extracted from the DDM autocorrelation functions, $g(q,\tau)$, as expressed in Eq.1. Extracting $f(q,\tau)$ and applying corrections for sometimes a slow thermal drift in the gel using Eq.11 yields the ISFs reported in Supplementary Fig. 1. All the observed dynamics fits the generalized exponential equation $f(q,\tau) = e^{-(\tau/\tau_R)^{\beta}}$ with the stretched exponent β close to 1 in water, which indicates NPs are not interacting with each other or the media and polydispersity is not significant, and $0.7 < \beta < 1$ in agarose solutions and gels (with few exceptions of $\beta \approx 0.5$-0.6), highlighting particle-gel interactions depending on the NPs type and size (see Supplementary Fig. 4).

After filling a capillary with agarose gel, we noticed a slow gelation process affecting the particle dynamics. To avoid the effect of slow relaxation, we performed DDM experiments as a function of the waiting time, ranging from 15 minutes to 3 days, with t=0 the time at which the capillary was filled with a solution. We found that a resting time of 16h was necessary prior to any DDM measurement in order to reach data at the steady state in the agarose gel. This is expressed in Supplementary Fig. 2 (B, D, F and H), where the diffusion coefficient of hard NPs is independent of time after a relaxation period of 16h. We also show the relaxation time τ_R approximately follows q^{-2}. Similar results were found for soft NPs as well (Supplementary Fig. 3).

Supplementary Notes 2 - Rheological measurements

Agarose was found to display an apparent Newtonian behavior at very low concentrations (0.05%) as shown by the power-law increase in the loss modulus, G'', with frequency in Supplementary Fig. 5. Above this concentration, agarose demonstrates a non-Newtonian behavior at the studied frequency range because of interchain interactions. An expected sol-gel transition occurs close to C_{ag} = 0.1% characterized by the storage and loss moduli following a power-law scaling of the form $G' \sim G'' \sim \omega^n$, where n is a critical relaxation exponent. The sol-gel transition occurs at an agarose concentration between 0.1 and 0.5% evidenced by the independency of G' to ω. The storage moduli of these gels are 330 ± 10 kPa and 1890 ± 220 kPa for C_{ag} = 0.5% and 1% agarose, respectively.

Supplementary Notes 3 - Effect of the osmotic pressure on microgel diffusion

We investigated the soft NP shrinkage as a function of osmotic pressure by adding Ficoll 400 kDa to solution of NP microgels and evaluate the minimum pressure required to shrink the microgels to half their swollen size, as it was observed in agarose (Figure 2).

We measured the diffusion coefficients of soft and hard NPs using DDM and the osmotic pressure as a function of Ficoll concentration (see Supplementary Fig. 6A & C). The mathematical relation between the osmotic pressure and Ficoll concentration (red curve in Supplementary Fig. 6A) was obtained by a second order polynomial fit (expected for a virial expansion). Microgels and PS NPs of about the same size (r^0_H = 92.5 and 110 nm) were used at $\phi_{microgel}$ = 0.0089% and ϕ_{PS} = 0.0014% in Ficoll solutions of 10, 20, 30, 40, 50 and 75 mg/mL in Supplementary Fig. 6C.

As Ficoll concentration increases both osmotic pressure and viscosity increase. However, we found that the ratio $\frac{D_{PS}(\phi_{Ficoll})}{D_{\mu Gel}(\phi_{Ficoll})} = \frac{r_{H_{\mu Gel}}(\phi_{Ficoll})}{r_{H_{PS}}}$ decreases as the Ficoll concentration is increased (inset of Supplementary Fig. 6C) suggesting that the microgel particle shrinks, *i.e.* $r_{H_{\mu Gel}}(\phi_{Ficoll})$ decreases. The viscosity of the solution can be estimated by using the Stokes-Einstein relation and considering the hard PS particle does not change size so that

$$\eta(\phi_{Ficoll}) = \frac{D_{PS}(\phi_{Ficoll}=0)}{D_{PS}(\phi_{Ficoll})\,\eta(\phi_{Ficoll}=0)} \quad (3)$$

This allows extraction of the microgel radius r_H as a function of Ficoll concentration from solely measured quantities using the following expression

$$r_H(\phi_{Ficoll}) = r_H^0 \frac{D_{\mu Gel(H_2O)}}{D_{\mu Gel(\phi_{Ficoll})}} \frac{D_{PS(\phi_{Ficoll})}}{D_{PS(H_2O)}} \quad (4)$$

Evolution of r_H as a function of the measured osmotic pressure confirmed that particles are shrinking as the osmotic pressure is increased. We found that the smallest size attainable by the microgel (r^0_H = 92.5 nm) in Ficoll is $r_H \approx$ 60 nm, which is obtained at a concentration of 50 mg mL^{-1} Ficoll. This concentration yields an osmotic pressure Π_{osm} = 9.1 kPa (see Supplementary Fig. 6A) which shrinks the microgels similarly to other stimuli such as temperature and concentration

(Supplementary Fig. 6D). The measured thermal shrinking observed in this study is consistent with other reports[389, 401].

The osmotic pressure of agarose was calculated from its swelling / deswelling in Ficoll solutions. The concentration of Ficoll at which the agarose gels (C_{ag} = 1% w/w) does not swell / deswell (ΔV = 0) was estimated by a linear fit (Supplementary Fig. 6B). At this point, the internal osmotic pressure, including the elastic and mixing osmotic pressures, is equivalent to the external osmotic pressure. Therefore, the agarose gel (C_{ag} = 1% w/w) has an osmotic pressure of Π_{osm} = 89 Pa equivalent to 3.1 mg mL^{-1} Ficoll, which is too weak to induce any microgel shrinkage.

Supplementary Notes 4 - Zeta potential of hard and soft NPs

Zeta potential was assessed by measuring the electrophoretic mobility of the nanoparticles using DLS for NPs in 4 mM NaCl solutions. Values are presented in Supplementary Table 1 for a range of size for both hard AuNPs and soft microgels at two different temperatures.

Supplementary Notes 5 - Dynamics in saline solutions

We investigated the effect of adding salt on the diffusion of the NPs in agarose gel at C_{ag} = 0.5 % w/w. A larger mesh size of the gel is expected with higher ionic strength solutions [404]. Generally, those ions contribute in reducing water-polymer interactions consequently promoting polymer-polymer interactions and leading to larger chain aggregates as well as pores [438, 439]. With bigger pores, we expect no overlap of the EDL and thus no microgel shrinking. Supplementary Fig. 7 shows the DDM-measured diffusion coefficient D_G of hard Au NPs (two sizes) and soft microgel particle (one size). With salt addition, we found D_G values of the soft particles agree well with the prediction of the Kang et al. model for the hard particles suggesting that the soft microgel particle do not shrink. Using Eq. 4 to calculate the size r_H of microgels, we obtained a size that corresponds to the fully swollen microgels r^0_H observed in the diluted regime.

Supplementary Notes 6 - Calculations of the agarose mesh size and interaction distance H

The mesh size *l* was determined based on the first hard immobilized particle in agarose gels. Because softer gels are not dense enough to trap NPs of 220 nm in diameter, we used the expression

$$l = L\sqrt{C^*_{ag}/C_{ag}} \quad (5)$$

where L is the length of the fiber, C^*_{ag} the overlap concentration of agarose and C_{ag} the concentration of agarose. This approach allows to estimate the mesh size l for $C_{ag} \leq 0.25\%$ w/w using the mesh size of agarose 0.5% as a reference to evaluate $C^*_{ag} = 0.097\%$ w/w. Calculated values of l in Table S3 are in good agreement with previously published values.[440]

In agarose gels, the fiber-particle distance H is obtained using the following expression:

$$H_{Agarose} = \frac{l}{2} - r_H^0 \quad (6)$$

Supplementary Notes 7 - Elastic energy of a spherical particle

The elastic energy U of a soft spherical particle of elastic modulus E is described by its elastic potential energy per unit volume $U_v = 1/2E\xi^2$ with ξ being the strain on the particle so that we have

$$dU = \frac{E}{2}\xi^2 dV \quad (7)$$

and the strain

$$\xi = \left(\frac{R_0 - r}{R_0}\right), \quad (8)$$

where R_0 is the initial radius of the particle and *r* is the shrinked layer of the particle. The potential energy required to compress a soft sphere to a fraction *α* of its original size (*α* being the shrinkage ratio of the particle) is given by:

$$U = \frac{E\pi {R_0}^3}{15}(6\alpha^5 - 15\alpha^4 + 10\alpha^3 - 1). \quad (9)$$

Therefore, for a particle of a weak elastic modulus (E = 1 kPa), initial radius of R_0 = 50 nm, and α = 2/3, we get U/k_BT = 1.34. The required energy for shrinking by α this type of particle then needs only 10-20 agarose fibers within its vicinity, which is reasonable considering the fractal nature of agarose and the non-homogenous fiber distribution in its matrix.